Measurement of the Tau-Pair Cross Section and Charge Asymmetry at the Z° Resonance

Thesis by

Martin Werner Grünewald

In Partial Fulfillment of the Requirements

for the Degree of

Doctor of Philosophy

California Institute of Technology

Pasadena, California

1993

(Submitted December 14, 1992)

Acknowledgment

First of all, I want to thank my parents for strong support during my stay in Pasadena and Geneva, which allowed me to concentrate on graduate studies at Caltech and thesis work at **CERN**.

For the latter, the help of many people from the **L3** collaboration is acknowledged, especially enlightening discussions with:

Harvey Newman as my advisor,

Richard Mount, Martin Pohl, He Sheng Chen and the other members of the **L3** τ-analysis group,

Albrecht Böhm, Frank Linde and the other members the **L3** Z°-parameter group, including

Joachim Rose, Som Ganguli and Atul Gurtu as the experts in fitting to the data, and

Johannes Schwenke on the problem of selecting $\tau^+\tau^-(\gamma)$ events back in 1990.

Sunanda Banerjee, Francis Bruyant, Robert Clare, Vincenzo Innocente, Ghita Rahal-Callot, David Stickland and many others answered patiently all my questions about the features of the **L3**-analysis software.

Technical help from Hans Lubbers, Markus Möller and Gerhard Raven to get a comfortable working environment on three different computer systems has been very valuable. Also, I thank Marcel Merk for the permission to use some of his subdetector drawings.

L3 is a large collaboration and a lot of its members have supported my analysis in one way or another. Many thanks to all of them!

Abstract

This thesis describes a measurement of the production cross section and forward-backward charge asymmetry of the process $e^+e^- \to \tau^+\tau^-(\gamma)$ at center-of-mass energies around the Z° resonance (88 GeV to 94 GeV). These and other measurements made by the $\mathbf{L_3}$ collaboration on production and decay of the Z° boson have been used to determine precisely parameters of the Minimal Standard Model of electroweak and strong interactions, and to place stringent limits on possible new physics beyond it. The data used for the analysis have been collected by the $\mathbf{L_3}$ detector at the $\mathbf{LEP}$ storage ring during the years 1990 and 1991.

The results presented in this work include:

- the production cross section of the process $e^+e^- \to \tau^+\tau^-(\gamma)$ at the peak of the Z° resonance: $\sigma_\tau = 1.481 \pm 0.019\ (stat.) \pm 0.013\ (syst.)$ nb,

- the forward-backward charge asymmetry of the process $e^+e^- \to \tau^+\tau^-(\gamma)$ at the peak of the Z° resonance: $A_{fb}^\tau = 0.014 \pm 0.017\ (stat.) \pm 0.006\ (syst.)$,

- the strong coupling constant at the mass of the charged τ lepton: $\alpha_s(m_\tau) = 0.35 \pm 0.06\ (exp.) \pm 0.03\ (theor.)$,

- the mass of the Z° boson: $m_Z = 91.195 \pm 0.006 \pm 0.007\ (LEP)$ GeV,

- the total width of the Z° boson: $\Gamma_Z = 2.490 \pm 0.010 \pm 0.005\ (LEP)$ GeV,

- the partial decay width of the Z° boson into τ pairs: $\Gamma_\tau = 84.6 \pm 1.2$ MeV,

- the effective axial-vector and vector coupling constants of the neutral weak current for charged τ leptons: $g_A^\tau = -0.5032 \pm 0.0037$ and $g_V^\tau = -0.037 \pm 0.008$,

- the effective weak mixing angle: $\sin^2\overline{\theta}_W = 0.2328 \pm 0.0013$,

- the strong coupling constant at the mass of the Z° boson: $\alpha_s(m_Z) = 0.124 \pm 0.005$,

- the mass of the top quark: $m_t = 152^{+36}_{-46} \pm 20\ (Higgs)$ GeV.

The self-consistency of these measurements increases the confidence that the charged τ lepton behaves as a sequential lepton, with properties as predicted by the Minimal Standard Model.

No indications for any deviations from the Minimal Standard Model have been found.

Contents

List of Figures

List of Tables

Chapter 1

Introduction and Overview

Since 1989, a new generation of precision experiments has been measuring electron-positron annihilations at center-of-mass energies around 91 GeV, large enough to produce the Z° boson. Its properties and corresponding electroweak parameters can be very well determined due to the clean experimental environment at e^+e^- colliders, where at this center-of-mass energy just one Z° particle decaying to some final state and nothing else is produced in an interaction.

The production and decay properties of the Z° boson, which are inferred from measuring the cross section of electron-positron annihilations into various final states, are of principal importance. This thesis concentrates on final states consisting of τ pairs and on the measurement of both total cross section and forward-backward charge asymmetry of the process $e^+e^- \rightarrow \tau^+\tau^-(\gamma)$.[1] The data used for this analysis have been collected by the **L₃** detector at the **LEP** accelerator at **CERN** during the year 1991.

All predicted decay modes of the Z° boson have been investigated by the **L₃** collaboration. Parameters of the Minimal Standard Model of particle physics, especially of its electroweak sector, are precisely determined from the data taken during the years 1990 and 1991. Comparison of the theory with the measurements constitutes a stringent test and consistency check of the theory.

---

[1]The bracketed γ denotes the *possible* presence of radiative photons.

The thesis is organized in chapters and appendices as follows:

Chapter 2 presents the current understanding of the Standard Model of particle physics in its minimal realization. It concentrates on physics at electron-positron colliders in general, and on electroweak physics at the Z° resonance in particular.

Chapter 3 describes the measurement device and experimental setup, i.e., the L_3 detector at the LEP e^+e^- collider.

Chapter 4 gives a detailed overview of the Monte Carlo simulations, consisting of event generation and detector simulation, and of the event reconstruction procedure. Contributions to this area constitute my work on the general infrastructure of L_3 physics analysis. Collection and maintenance of physics (event) generators is done by three people, including myself as the coordinator and responsible at **CERN**. Also, I improved and introduced new versions of the program to simulate the L_3 detector. Technical aspects of this work are further outlined in Appendix E.

Chapter 5 summarizes the measurement of the luminosity of L_3's interaction region.

Chapter 6 describes in detail a selection of $e^+e^- \rightarrow \tau^+\tau^-(\gamma)$ events and a measurement of the production cross section and forward-backward charge asymmetry of this process using the 1991 data. This work is the physics analysis part solely done by myself, and constitutes part of the input for the remaining chapters.

Chapter 7 first describes other L_3 measurements on charged τ leptons, and then proceeds to the determination of Minimal Standard Model parameters from τ data alone.

Chapter 8 first describes results on other Z° boson decay channels measured by L_3, which are relevant for a global analysis in terms of electroweak parameters, and then proceeds to the determination of Minimal Standard Model parameters and limits on new physics.

Chapter 9 summarizes the presented work and concludes with remarks about future prospects in precision electroweak measurements.

Appendix A gives an overview of the important aspect of radiative corrections in the framework of the Minimal Standard Model, and how they can be exploited to gain information about the top quark and Higgs boson.

Appendix B discusses aspects of the decay of the charged τ lepton, which can be observed at electron-positron accelerators.

Appendix C gives an overview of the procedure to calibrate the energy of the **LEP** beams and to handle the remaining uncertainties.

Appendix D summarizes future upgrades of both the **LEP** machine and the **L3** detector.

Appendix E describes the development of the **L3** detector simulation program during the last years (from the **LEP** start-up in 1989 until 1993), and discusses its current status.

Appendix F describes analytical programs and the fitting procedure applied to determine electroweak parameters.

Appendix G lists all **L3** measurements used in the determination of electroweak parameters.

The system of units adopted to describe microscopic quantities is that of particle physics, where $\hbar = 1 = c$. Thus, energies are measured in units of electron volts $(1\,\text{eV} = 1.6 \cdot 10^{-19}\,\text{J})$, and cross sections in units of barns $(1\,\text{b} = 10^{-28}\,\text{m}^2)$. Otherwise, SI units are employed.

Chapter 2

The Standard Model of Particle Physics

This chapter describes the current theoretical understanding of the world of elementary particles. It describes the so-called Standard Model [1] (SM) of particle physics in its minimal realization (MSM). Special emphasis is put on implications for physics at high energy electron-positron (e^+e^-) colliders in order to prepare the theoretical basis for the measurements described in this work.

The important aspect of higher-order radiative corrections and the physics of the charged τ lepton are discussed in appendices A and B, respectively.

2.1 The Minimal Standard Model

The Minimal Standard Model (MSM) as the theory of elementary particles describes these particles and the various interactions between them. Over the last twenty years, many tests of the MSM have been carried out with increasing precision, but no lasting significant discrepancy has been established.

Mathematically speaking, the MSM (as well as its non-minimal extensions) belongs to the class of relativistic quantum field theories, applying the concepts of local symmetry and spontaneous symmetry breaking. The model describes spinless,

spin-1/2 and spin-1 fields interacting with one another. It incorporates all known interactions among the fundamental particles with the exception of gravity, a fully quantized version of which has yet to be developed. Experimentally, this point is not a drawback for the investigation of the fundamental electroweak and strong interactions, because the gravitational attraction of, e.g., an electron and a positron is about 40 orders of magnitude smaller than their electromagnetic attraction.

2.1.1   Local Symmetries

The **MSM** describes the electromagnetic, weak and strong interactions using local phase symmetries. Local phase symmetry requires the invariance of the underlying theory with respect to local phase transformations $U(x)$ of the fields $\Psi(x)$:

$$\Psi(x) \longrightarrow \Psi'(x) = U(x)\Psi(x) \quad , \tag{2.1}$$

where $U(x)$ is a symmetry operation depending continuously on the local space-time coordinate x. It can be expressed as an exponential using the generators A^i of the symmetry group:

$$U(x) = \exp\left[\alpha_i(x)A^i\right] \quad , \tag{2.2}$$

where in the exponent the index i is summed over, and $\alpha_i(x)$ are space-time coordinate dependent coefficients also regarded as fields. A first problem is the identification of the correct group of local symmetry operations, which can be Abelian or non-Abelian.

The strong-interaction theory of quarks is formulated in terms of so-called color quantum numbers. Quantum chromodynamics (QCD) is a Yang-Mills [2], i.e., a non-Abelian gauge theory, with local color $SU(3)_C$ symmetry, in which each quark flavor constitutes a three-dimensional color multiplet. The requirement of local phase invariance demands the existence of an octet of massless vector boson fields (G^a_μ, $a = 1, \ldots, 8$), the gluons, corresponding to the eight generators of $SU(3)$ symmetry transformations.

Electromagnetism is invariant under a local Abelian $U(1)_{EM}$ group, arising from gauge invariance of the electromagnetic potential. When electroweak unification was

proposed over twenty years ago, neutral weak interactions had not been discovered; only charged weak interactions were known. The smallest group that can describe these three interactions is SU(2). However, simple SU(2) leads to contradicting multiplet assignments of fermions. The reason for this is that the electromagnetic interaction does not distinguish between left- and right-handed fermions whereas only left-handed fermions participate in weak interactions. A simple way out is to add an additional U(1) interaction to the theory, which implies the existence of a neutral weak current. Its discovery [3] established that the local symmetry group of the electroweak sector has to be at least as large as $G_{EW} = \mathrm{SU(2)}_L \otimes \mathrm{U(1)}$, where the index L denotes left-handedness.

The group G_{EW} has four generators: the three generators T_1, T_2 and T_3 of $\mathrm{SU(2)}_L$ called weak isospin, and the generator Y of $\mathrm{U(1)}_Y$ group called weak hypercharge. The corresponding gauge fields consist of a massless vector triplet (W^i_μ, $i = 1, 2, 3$) and a massless vector singlet (B_μ). Independent linear combinations of the above four fields form four new bosons, three of which acquire mass as a result of spontaneous symmetry breaking, and one remains massless. The three massive bosons are the W$^\pm$ bosons mediating the charged weak current, and the Z$^\circ$ mediating the neutral weak current. The remaining massless boson can be identified with the photon. Hence, the electroweak symmetry group is broken down to the familiar $\mathrm{U(1)}_{EM}$ of electromagnetism, whose generator Q, the electromagnetic charge, is a linear combination of the generators of the unbroken group G_{EW}:[1]

$$Q = T_3 + Y \quad . \tag{2.3}$$

Summarizing, the underlying symmetry group G_{MSM} of the MSM of strong and electroweak interactions is given by:

$$G_{MSM} = \mathrm{SU(3)}_C \otimes G_{EW} \tag{2.4}$$

$$G_{EW} = \mathrm{SU(2)}_L \otimes \mathrm{U(1)}_Y \rightarrow \mathrm{U(1)}_{EM} \quad . \tag{2.5}$$

---

[1]The relation is often written as $Q = T_3 + Y/2$ due to historical reasons. The factor $1/2$ can be absorbed elsewhere.

Since G_{MSM} is a direct product of three independent groups, there are three independent coupling constants in the theory, g_1, g_2, g_3, for $U(1), SU(2), SU(3)$, respectively. The left- and right-handed parts of a fermion field Ψ are given by the following normalized orthogonal projections:

$$\Psi_L \equiv \frac{1-\gamma^5}{2}\Psi \qquad \Psi_R \equiv \frac{1+\gamma^5}{2}\Psi \quad . \tag{2.6}$$

The fermions (both leptons and quarks) come in three generations with increasing masses. The particle content of the MSM – spin-0 Higgs boson, spin-1/2 fermions and spin-1 gauge bosons – is listed in Table 2.1 together with the particle assignment to the various group multiplets and quantum numbers.

2.1.2   Lagrangian of the Minimal Standard Model

The framework used to derive the interactions among the matter fields is the language of Lagrangians. Lagrangians in field theory are just a generalization of the well known Lagrange formalism of classical mechanics. The complete Lagrangian [4] of the MSM can be expressed as a sum of four terms:

$$\mathcal{L}_{\text{MSM}} = \mathcal{L}_{\text{Yang-Mills}} + \mathcal{L}_{\text{Fermion}} + \mathcal{L}_{\text{Yukawa}} + \mathcal{L}_{\text{Higgs}} \quad . \tag{2.7}$$

The Yang-Mills Lagrangian contains the kinetic energy terms of the various gauge fields associated with the symmetry groups $U(1)$, $SU(2)$ and $SU(3)$. The Fermion Lagrangian describes the dynamics of the fermions, i.e., their kinetic energy and interactions with the gauge bosons, where the latter are introduced via the covariant derivative D_μ given below. The Yukawa Lagrangian implements mass terms for the fermions via couplings to the Higgs field [5].

2.1.3   Spontaneous Symmetry Breaking

The Lagrangian of the scalar Higgs field Φ can be written as:

$$\mathcal{L}_{\text{Higgs}} = (D^\mu\Phi)^\dagger(D_\mu\Phi) - V(\Phi^\dagger\Phi) \quad , \tag{2.8}$$

1.	2.	3.	$SU(3)_C$	$SU(2)_L$	T_3	Y	Q
$\begin{pmatrix} \nu_e \\ e^- \end{pmatrix}_L$	$\begin{pmatrix} \nu_\mu \\ \mu^- \end{pmatrix}_L$	$\begin{pmatrix} \nu_\tau \\ \tau^- \end{pmatrix}_L$	$\underline{1}$ $\underline{1}$	$\underline{2}$ $\underline{2}$	$+1/2$ $-1/2$	$-1/2$ $-1/2$	0 -1
e_R	μ_R	τ_R	$\underline{1}$	$\underline{1}$	0	-1	-1
$\begin{pmatrix} u \\ d' \end{pmatrix}_L$	$\begin{pmatrix} c \\ s' \end{pmatrix}_L$	$\begin{pmatrix} t \\ b' \end{pmatrix}_L$	$\underline{3}$ $\underline{3}$	$\underline{2}$ $\underline{2}$	$+1/2$ $-1/2$	$+1/6$ $+1/6$	$+2/3$ $-1/3$
u_R	c_R	t_R	$\underline{3}$	$\underline{1}$	0	$+2/3$	$+2/3$
d_R	s_R	b_R	$\underline{3}$	$\underline{1}$	0	$-1/3$	$-1/3$
			$SU(3)_C$	$SU(2)_L$	T_3	Y	Q
	G^a		$\underline{8}$	$\underline{1}$	0	0	0
	$\begin{pmatrix} W^+ \\ W^3 \\ W^- \end{pmatrix}$		$\underline{1}$ $\underline{1}$ $\underline{1}$	$\underline{3}$ $\underline{3}$ $\underline{3}$	$+1$ 0 -1	0 0 0	$+1$ 0 -1
	B		$\underline{1}$	$\underline{1}$	0	0	0
	$\begin{pmatrix} \phi^+ \\ \phi^0 \end{pmatrix}$		$\underline{1}$ $\underline{1}$	$\underline{2}$ $\underline{2}$	$+1/2$ $-1/2$	$+1/2$ $+1/2$	$+1$ 0

Table 2.1: Multiplet assignments and quantum numbers of leptons ν_ℓ, ℓ^- ($\ell = e, \mu, \tau$), quarks u, d' ($u = u, c, t$; $d = d, s, b$), gauge bosons (G's, W's and B), and Higgs boson (ϕ) in the MSM. The prime on the d-type quarks (d') denotes symmetry eigenstates, which arise from the mass eigenstates d by the unitary Cabibbo-Kobayashi-Maskawa quark mixing matrix. Indices L and R denote left-handed and right-handed fermions. The electromagnetic charge Q is given by $Q = T_3 + Y$.

with D_μ being the covariant derivative:

$$D_\mu = \partial_\mu + ig_1 Y B_\mu + ig_2 \frac{\tau_i}{2} W_\mu^i + ig_3 \frac{\lambda_a}{2} G_\mu^a \quad , \tag{2.9}$$

where the generators $\tau_i/2 \equiv T_i$ and $\lambda_a/2$ are those of the SU(2) and SU(3) groups. The matrix representations of τ_i's and λ_a's are known as Pauli and Gell-Mann matrices [6], respectively.

The MSM Higgs field transforms as a doublet under SU(2) and a singlet under SU(3). When expanding D_μ in the Higgs Lagrangian, the terms corresponding to

the $SU(3)_C$ symmetry can be dropped immediately. The Higgs potential V is:

$$V(\Phi^\dagger\Phi) \;=\; m^2(\Phi^\dagger\Phi) + \lambda(\Phi^\dagger\Phi)^2 \quad , \tag{2.10}$$

where for stability reasons at least λ must be larger than zero. However, the parameter m^2 may be less than zero, and in this case the potential has non-trivial minima at:

$$(\Phi^\dagger\Phi) \;=\; -\frac{m^2}{2\lambda} \;=\; \frac{1}{2}\Phi_0 \;>\; 0 \quad , \tag{2.11}$$

away from the origin, where the last equal sign defines the positive constant Φ_0. The symmetry of the Higgs potential V leads to a whole family of non-trivial potential minima. Choosing a specific one amounts to breaking of the symmetry. As Φ is a complex field, it has four real degrees of freedom. Thus, it can be cast in the form:

$$\Phi(x) \;=\; \exp\left[i\pi^i(x)\tau_i/2\Phi_0\right] \begin{pmatrix} 0 \\ \left[\rho(x) + \Phi_0\right]/\sqrt{2} \end{pmatrix} \quad . \tag{2.12}$$

The reason for writing the field in this special form is, that the first factor can now easily be removed by a local $SU(2)$ symmetry transformation:

$$\Phi'(x) \;=\; \exp\left[-i\pi^i(x)\tau_i/2\Phi_0\right]\Phi(x) \;=\; \begin{pmatrix} 0 \\ \left[\rho(x) + \Phi_0\right]/\sqrt{2} \end{pmatrix} \quad . \tag{2.13}$$

Hence there is effectively only one physical Higgs boson in the theory, called H^0.

2.1.4   Generation of Boson Masses

Using the above representation of the Higgs field Φ, and expanding the sum $\tau_i W^i$ in a spherical basis, $\tau_i W^i_\mu = \sqrt{2}(\tau^+ W^+_\mu + \tau^- W^-_\mu) + \tau_3 W^3_\mu$, the scalar Lagrangian becomes:

$$\begin{aligned}
\mathcal{L}_{\text{Higgs}} \;=\; & \frac{g_2^2}{4} W^\mu_- W^+_\mu (\rho + \Phi_0)^2 \\
& + \frac{1}{8}(g_2 W^\mu_3 - g_1 B^\mu)(g_2 W^3_\mu - g_1 B_\mu)(\rho + \Phi_0)^2 \\
& + \frac{1}{2}\partial^\mu\rho\,\partial_\mu\rho \;+\; \frac{m^2}{2}(\rho + \Phi_0)^2 \;+\; \frac{\lambda}{4}(\rho + \Phi_0)^4 \quad ,
\end{aligned} \tag{2.14}$$

containing mass terms for spin-1 bosons. The terms quadratic in the gauge fields determine that the $W^\pm$ fields describe particles $W^\pm$ having acquired a mass of $g_2\Phi_0/2$ and that the special combination $g_2 W_\mu^3 - g_1 B_\mu$ will also lead to a massive particle. Thus the fields B_μ and W_μ^3 may be rotated to new fields called $Z_\mu^0 \propto g_2 W_\mu^3 - g_1 B_\mu$ for a massive neutral boson, the Z°, and A_μ for a massless boson, the photon γ:

$$\begin{pmatrix} A_\mu \\ Z_\mu \end{pmatrix} = \begin{pmatrix} \cos\theta_W & \sin\theta_W \\ -\sin\theta_W & \cos\theta_W \end{pmatrix} \begin{pmatrix} B_\mu \\ W_\mu^3 \end{pmatrix} . \tag{2.15}$$

The rotation is defined in terms of the electroweak mixing angle θ_W given by the electroweak couplings g_1 and g_2:

$$\sin\theta_W \equiv \frac{g_1}{\sqrt{g_1^2 + g_2^2}} \qquad \cos\theta_W \equiv \frac{g_2}{\sqrt{g_1^2 + g_2^2}} . \tag{2.16}$$

Since the mass of the Z° is determined to be $\Phi_0\sqrt{g_1^2 + g_2^2}/2$, the ratio of the $W^\pm$ to the Z° mass also is given by θ_W:

$$\frac{m_W}{m_Z} = \cos\theta_W . \tag{2.17}$$

The remaining terms of the above Lagrangian govern the dynamics of the Higgs boson H^0, predicting cubic and quartic self-interactions.

2.1.5   Currents in Electroweak Theory

Matrix elements for electroweak interactions mediated by γ, Z° or $W^\pm$ can be written in terms of currents, i.e., terms bilinear in the fermion fields. With the help of Dirac's γ matrices, the most general term bilinear in fermion fields can be decomposed into a linear combination of 16 basic terms, which are defined by their transformation properties under Lorentz transformations. The 16 terms are: scalar S ($\overline{\Psi}1\Psi$), pseudoscalar P ($\overline{\Psi}\gamma^5\Psi$), vector V ($\overline{\Psi}\gamma^\mu\Psi$), axial-vector A ($\overline{\Psi}\gamma^\mu\gamma^5\Psi$), and tensor T ($\overline{\Psi}\sigma^{\mu\nu}\Psi$). Using the following natural definitions for certain currents:

$$J_\mu^\pm \equiv \overline{\Psi}_L \gamma_\mu \tau^\pm \Psi_L \tag{2.18}$$

$$J_\mu^3 \equiv \overline{\Psi}_L \gamma_\mu \frac{\tau^3}{2} \Psi_L \tag{2.19}$$

$$J_\mu^Y \equiv \overline{\Psi} \gamma_\mu Y \Psi , \tag{2.20}$$

and collecting the pieces which lead to fermion - gauge boson interactions:

$$\mathcal{L}_{\text{int}} = - \frac{g_1 g_2}{\sqrt{g_1^2 + g_2^2}} A_\mu J_{EM}^\mu - \sqrt{g_1^2 + g_2^2} Z_\mu^0 J_{NC}^\mu$$
$$- \frac{g_2}{\sqrt{2}} (W_\mu^+ J_+^\mu + W_\mu^- J_-^\mu) \quad , \tag{2.21}$$

one can derive the currents that couple to the physical boson fields A, Z and W:

$$J_{EM}^\mu = J_3^\mu + J_Y^\mu = Q \overline{\Psi} \gamma^\mu \Psi \tag{2.22}$$

$$J_{NC}^\mu = J_3^\mu - \sin^2 \theta_W J_{EM}^\mu = \overline{\Psi} \gamma^\mu \frac{\text{g}_V - \text{g}_A \gamma^5}{2} \Psi \tag{2.23}$$

$$J_\pm^\mu = \overline{\Psi} \gamma^\mu \frac{V - A \gamma^5}{2} \tau^\pm \Psi \quad , \tag{2.24}$$

respectively, where the relation between the electromagnetic charge q and the coupling constants g_1 and g_2 is given by:

$$\text{q} = \frac{g_1 g_2}{\sqrt{g_1^2 + g_2^2}} = g_1 \cos \theta_W = g_2 \sin \theta_W \quad . \tag{2.25}$$

The above equations define the customary vector and axial-vector coupling constants of the weak neutral current (depending on fermion species f):

$$\text{g}_A^f \equiv T_3^f \qquad\qquad \text{g}_V^f \equiv T_3^f - 2 Q_f \sin^2 \theta_W \quad , \tag{2.26}$$

and of the weak charged current (the same for all fermions):

$$A \equiv 1 \qquad\qquad V \equiv 1 \quad . \tag{2.27}$$

The relative sign of the vector and axial-vector part in the charged weak current is the reason for stating that the charged weak interaction has a (pure) $V - A$ structure (see below). The coupling constants and the electroweak mixing angle become effective quantities when including higher-order radiative corrections (see Appendix A).

Four-Fermion Theory

Fermi made a first attempt to formulate a theory of charged weak interactions in 1934 [7]. As an ansatz for the Lagrangian, he used a product of two currents, i.e.,
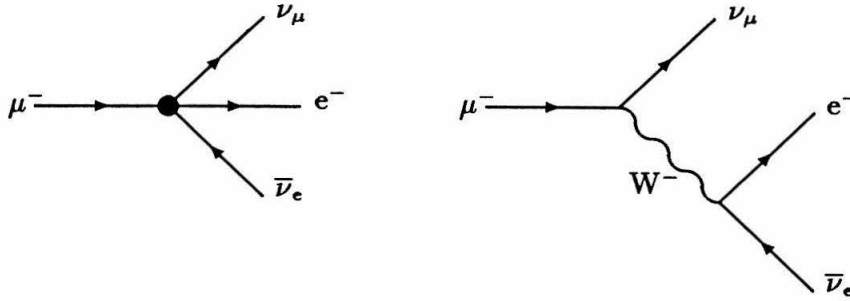
Figure 2.1: Muon decay in four-fermion theory (left) and the MSM (right), containing the two charged weak currents $\mu^-\nu_\mu$ and $e^-\nu_e$.

two terms bilinear in the fermion fields. All are evaluated at the same space-time point, therefore describing a vertex with four fermion lines. Experimental results collected in the following years let Feynman and Gell-Mann suggest in 1958 [8], that the interaction Lagrangian should be the product of two $V - A$ currents. The coupling constant connecting both currents is the Fermi constant G_F. Within the MSM, the weak charged current interaction is described by two currents coupled by the propagator of the charged intermediate vector boson $W^\pm$. Figure 2.1 shows a pictorial view of the two different interpretations.

The experiments at that time (1930–1960) measured processes, which take place at low energies and low momentum transfers $q^2 \to 0$ [9]. In this limit, the propagator term $G_V^{\mu\nu}(q^2)$ for a heavy spin-1 vector boson V becomes:

$$G_V^{\mu\nu}(q^2) \equiv \frac{-g^{\mu\nu} + q^\mu q^\nu/m_V^2}{q^2 - m_V^2} \xrightarrow{q^\lambda \to 0} \frac{g^{\mu\nu}}{m_V^2} \quad . \tag{2.28}$$

Thus the low energy limit of the MSM is obtained, which recovers precisely the old four-fermion theory, thereby connecting the Fermi constant G_F to the masses of the intermediate vector bosons m_W and m_Z:

$$\frac{G_F}{\sqrt{2}} = \frac{g_2^2}{8m_W^2} = \frac{\pi\alpha}{2\sin^2\theta_W m_W^2} = \frac{\pi\alpha}{2\sin^2\theta_W \cos^2\theta_W m_Z^2} \quad . \tag{2.29}$$

The two points of view are hence equivalent at low energies, but differ strongly in their

predictions at high energies: whereas the four-fermion theory violates the unitarity limit, the SM (after renormalization) leads to expressions that remain finite.

2.1.6   Status of the Minimal Standard Model

Besides the more philosophical question of why the SM is the way it is, there are a few other items in an unsatisfactory state. As already noted in the beginning, gravity is not part of the theory. Also, the MSM is not a completely predictive theory: for example, there are several parameters, e.g., all particle masses and coupling constants, which are not calculable within the MSM. Other physical observables, however, can be calculated in terms of these parameters. A comparison with experimental results then leads to a determination of these *a priori* free parameters. Consistency between all values derived from different measurements constitutes a test of the MSM.

Missing Particles

Not all particles listed in Table 2.1 have been directly observed experimentally so far. There is only indirect evidence for the existence of the τ neutrino ν_τ, the top quark t, and the Higgs boson H^0 [10]. Hence, only mass limits can be given [11, 12]:

$$m_{\nu_\tau} \; < \; 0.035 \text{ GeV} \tag{2.30}$$

$$m_t \; > \; 91 \text{ GeV} \tag{2.31}$$

$$m_H \; > \; 60 \text{ GeV} \; . \tag{2.32}$$

The existence of the two missing fermions is inferred from measurements of, e.g., decay properties relating to the weak isospin of the charged τ lepton and the b quark. These measurements confirm the assignment of both particles to weak doublets, which implies the existence of their isopartners, by definition the τ neutrino and the top quark, respectively.

Experimentally, the difficulty in observing and identifying the τ neutrino arises from the fact, that it interacts only weakly. The top quark, like the MSM Higgs

boson, has not been discovered simply due to kinematic effects: it must be so heavy, that it cannot be produced at current colliders, at a measurable rate.[2]

The existence of the Higgs boson is on less solid grounds. The only reason to believe in its existence is the fact that the SM needs a symmetry breaking, mass generating mechanism. The Higgs mechanism offers a solution, which requires the existence of one scalar particle, the Higgs boson, in its minimal realization. However, other mechanisms could be envisaged to replace the Higgs sector by something equivalent, but without the requirement of additional fundamental scalar particles.

Extended Higgs Sector

The MSM is "minimal" in the sense that its Higgs sector is the smallest one which can accommodate spontaneous symmetry breaking and mass generation. The Higgs sector might be more complicated, including additional doublets or consisting of larger multiplets, e.g., triplets of Higgses. In the case where there are several Higgs multiplets that couple to the gauge bosons, the gauge boson mass relation is modified as follows:

$$\frac{m_W^2}{m_Z^2} = \rho_{\text{tree}} \cos^2 \theta_W \quad . \tag{2.33}$$

Within the MSM, $\rho_{\text{tree}} = 1$, where "tree" denotes the use of lowest-order graphs and the lack of higher-order (loop) corrections. Any deviation from $\rho_{\text{tree}} = 1$ signals an extended Higgs sector, for example $\rho_{\text{tree}} = 1/2$ for a Higgs triplet.

2.2 Physics at Electron-Positron Colliders

2.2.1 Interactions

As the name electron-positron collider implies, the initial state at such accelerators consists of an electron and a positron. Since these particles are leptons, they interact

---

[2]Except possibly at the Fermilab Tevatron collider, where a "top candidate" event has recently been presented by the CDF collaboration at the 1992 APS/DPF meeting in Chicago [13].
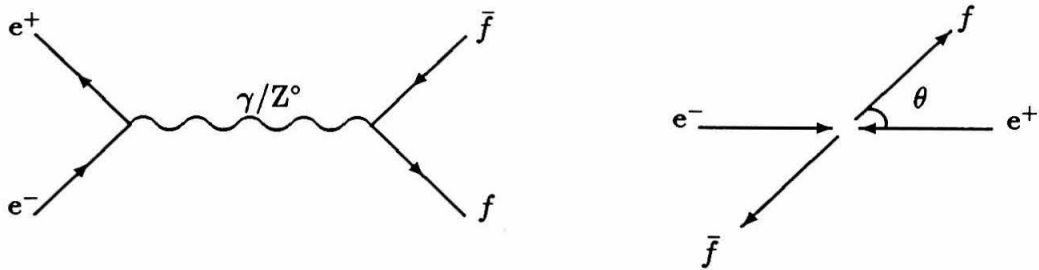
Figure 2.2: Scattering in s-channel leading to a pair of fermions in the final state, and definition of scattering angle θ.

only electroweakly. The Born term Feynman diagrams as derived from the MSM Lagrangian discussed above fall into two classes:

1. s-channel scattering via a (virtual) γ, Z° or H^0,

2. t-channel scattering via a (virtual) γ, $W^\pm$, Z°, e, ν_e or H^0.

In general, graphs involving the exchange of the Higgs boson H^0 lead to very small effects compared to others due to the fact, that the coupling of the Higgs to fermions is proportional to the fermion mass. These graphs will be neglected in the following discussion.

In the case of t-channel interactions, the initial-state particles and the t-channel-exchanged particle completely specify the final-state particle flavor. In the case they are fermions, they have to be e^+e^- (γ or Z° exchange) or $\nu_e\bar{\nu}_e$ ($W^\pm$ exchange). For e^+e^- final states, i.e., Bhabha scattering, the pure QED t-channel γ exchange dominates the cross section at small scattering angles. This process is used to monitor and measure the luminosity at e^+e^- colliders, and will be discussed in Chapter 5. The s-channel-produced (off-shell) vector bosons decay freely into any kinematically and dynamically allowed pair of fermions (Figure 2.2) or bosons.

2.2.2 The Z° Resonance

At center-of-mass energies $\sqrt{s}$ around the mass m_Z of the Z° boson, the s-channel Z° exchange dominates the total cross section. The differential cross section for $f\bar{f}$

production ($f \neq e, \nu_e$ for pure s-channel scattering) contains γ and Z° exchange and their interference. For unpolarized beams, the differential cross section for a certain fermion helicity $h_f = \pm 1$ reads (neglecting fermion masses for simplicity):

$$\frac{d\sigma_0(e^+e^- \to f\bar{f}; h_f)}{d\cos\theta} = \frac{3}{8}N_C^f \left[A(1+\cos^2\theta) + B\cos\theta - \right. \\ \left. h_f \left\{ C(1+\cos^2\theta) + D\cos\theta \right\} \right] \frac{\sigma_{QED}}{2} \quad , \qquad (2.34)$$

where N_C^f is the QCD color factor (1 for leptons, 3 for quarks). The (purely) QED point cross section is given by:

$$\sigma_{QED} = \frac{4\pi\alpha^2}{3s} \quad . \qquad (2.35)$$

The coefficients A to D contain various combinations of fermion coupling constants q_f, g_V^f, g_A^f:

$$A(s) = q_e^2 q_f^2 + 2q_e q_f g_V^e g_V^f \Re(\chi(s)) \\ + \left[(g_V^e)^2 + (g_A^e)^2 \right] \left[(g_V^f)^2 + (g_A^f)^2 \right] |\chi(s)|^2 \qquad (2.36)$$

$$B(s) = 4q_e q_f g_A^e g_A^f \Re(\chi(s)) + 8g_V^e g_A^e g_V^f g_A^f |\chi(s)|^2 \qquad (2.37)$$

$$C(s) = 2q_e q_f g_V^e g_A^f \Re(\chi(s)) + 2\left[(g_V^e)^2 + (g_A^e)^2 \right] g_V^f g_A^f |\chi(s)|^2 \qquad (2.38)$$

$$D(s) = 4q_e q_f g_A^e g_V^f \Re(\chi(s)) + 4g_V^e g_A^e \left[(g_V^f)^2 + (g_A^f)^2 \right] |\chi(s)|^2 \quad , \qquad (2.39)$$

where $\chi(s)$ is the ratio of the Z° and γ propagator:

$$\chi(s) = \frac{1}{4\sin^2\theta_W \cos^2\theta_W} \frac{s}{s - m_Z^2 + im_Z\Gamma_Z} \quad . \qquad (2.40)$$

In most cases, the helicity of the final-state fermion cannot be measured, so that the two possible helicity states $h_f = \pm 1$ are summed over:

$$\frac{d\sigma_0(e^+e^- \to f\bar{f})}{d\cos\theta} = \frac{3}{8}N_C^f \left[A(1+\cos^2\theta) + B\cos\theta \right] \sigma_{QED} \quad . \qquad (2.41)$$

Cross Sections

The total production cross section has the simple expression:

$$\sigma_0(e^+e^- \to f\bar{f}) = N_C^f A(s)\sigma_{QED}(s) \quad . \qquad (2.42)$$

Because of the Z° resonance, there is a large enhancement of the cross section with respect to pure QED γ exchange at center-of-mass energies near m_Z. This makes it possible to study the Z° boson with a high event rate. The cross section, neglecting γ exchange and γ/Z° interference, has the following simple form:

$$\sigma_Z \equiv \sigma_0(e^+e^- \to Z^\circ \to f\bar{f}) \tag{2.43}$$

$$= 12\pi N_C^f \frac{\alpha^2 \left[(g_V^e)^2 + (g_A^e)^2\right]\left[(g_V^f)^2 + (g_A^f)^2\right]}{(12\sin^2\theta_W\cos^2\theta_W)^2} \frac{s}{(s-m_Z^2)^2 + m_Z^2\Gamma_Z^2} \tag{2.44}$$

$$\equiv 12\pi\Gamma_e\Gamma_f \frac{s/m_Z^2}{(s-m_Z^2)^2 + m_Z^2\Gamma_Z^2} \quad, \tag{2.45}$$

where the last equation defines the partial widths Γ_f of the Z° boson in terms of a relativistic Breit-Wigner resonance, and where:

$$\Gamma_f = N_C^f \frac{\alpha m_Z}{12\sin^2\theta_W\cos^2\theta_W}\left[(g_V^f)^2 + (g_A^f)^2\right] \tag{2.46}$$

$$= N_C^f \frac{G_F m_Z^3}{6\sqrt{2}\pi}\left[(g_V^f)^2 + (g_A^f)^2\right] \quad . \tag{2.47}$$

Measurements of the production cross sections for various final states $f\bar{f}$ may be used to determine basic properties of the Z° boson. The mass m_Z, total width Γ_Z and partial decay widths Γ_f into fermions f can be determined from the position, width and height of the resonance curve describing the cross section as a function of $\sqrt{s}$.[3] On the peak ($\sqrt{s} = m_Z$), one measures directly the branching fractions $B_f \equiv \Gamma_f/\Gamma_Z$ of the Z° decay into fermion f:

$$\sigma_Z(s = m_Z^2) = \frac{12\pi}{m_Z^2}\frac{\Gamma_e}{\Gamma_Z}\frac{\Gamma_f}{\Gamma_Z} \equiv \frac{12\pi}{m_Z^2}B_e B_f \quad . \tag{2.48}$$

Interpreting the above formulae in terms of coupling constants of the weak neutral current, the production cross section determines these in the following combination:

$$\sigma_Z \propto \left[(g_V^e)^2 + (g_A^e)^2\right]\left[(g_V^f)^2 + (g_A^f)^2\right] \quad . \tag{2.49}$$

---

[3]Once radiative corrections are taken into account (see Appendix A).

Asymmetries

The following three asymmetries can be defined, which are simply given by the expectation values of the sign of the quantities $\cos\theta$, fermion helicity h_f, and $h_f\cos\theta$, respectively:

1. the forward-backward charge asymmetry A_{fb}:

$$A_{fb}(s) \equiv \frac{\sigma(\cos\theta > 0) - \sigma(\cos\theta < 0)}{\sigma(\cos\theta > 0) + \sigma(\cos\theta < 0)} = \frac{3}{8}\frac{B(s)}{A(s)} \quad , \tag{2.50}$$

2. the polarization asymmetry A_{pol}:

$$A_{pol}(s) \equiv \frac{\sigma(h_f = +1) - \sigma(h_f = -1)}{\sigma(h_f = +1) + \sigma(h_f = -1)} = -\frac{C(s)}{A(s)} \quad , \tag{2.51}$$

3. the forward-backward polarization asymmetry A_{pol}^{fb}:

$$A_{pol}^{fb}(s) \equiv \frac{\sigma(h_f\cos\theta > 0) - \sigma(h_f\cos\theta < 0)}{\sigma(h_f\cos\theta > 0) + \sigma(h_f\cos\theta < 0)} = -\frac{3}{8}\frac{D(s)}{A(s)} \quad . \tag{2.52}$$

On the peak of the Z° resonance, where the interference term vanishes and the pure photon exchange can be neglected, these asymmetries have a very simple expression in terms of the coupling constants g_A and g_V. Defining:

$$\mathcal{P}_f \equiv \frac{-2g_V^f g_A^f}{(g_V^f)^2 + (g_A^f)^2} \quad , \tag{2.53}$$

one finds:

$$A_{fb}(s = m_Z^2) = \frac{3}{4}\mathcal{P}_e\mathcal{P}_f \tag{2.54}$$

$$A_{pol}(s = m_Z^2) = \mathcal{P}_f \tag{2.55}$$

$$A_{pol}^{fb}(s = m_Z^2) = \frac{3}{4}\mathcal{P}_e \quad . \tag{2.56}$$

Note, that the polarization asymmetries are linear in $\mathcal{P}$, and that in this approximation $A_{fb} = A_{pol} \cdot A_{pol}^{fb}$.

2.2.3   Tests of the Standard Model at the Z° Resonance

The Z° resonance in e^+e^- annihilations offers a unique possibility for studying and testing the MSM, due the fact that it combines high center-of-mass energies with high cross sections, as can be seen in Figure 2.3.

A measurement of the Z° lineshape, i.e., the cross section as a function of the center-of-mass energy, leads to the determination of mass and decay widths of the Z° boson. Once the mass is determined, the lineshape and decay widths are predicted by the MSM. The comparison with the measured values constitutes a check of these predictions.

Production cross sections and asymmetries contain the neutral weak current coupling constants in different combinations. Making use of both the cross sections and the various asymmetries therefore allows the determination of the fundamental parameters of the theory, i.e., the coupling constants of the neutral weak current for each of the final-state fermions investigated, and especially the electroweak mixing angle. Further checks are then possible: Comparing the values of the electroweak mixing angle $\sin^2 \theta_W$ measured independently in different reaction serves as a consistency check of the MSM. Comparing the three different charged lepton species serves as a check of the predicted lepton universality of the neutral weak current.

In addition, information about the important two missing particles of the MSM, the top quark and the Higgs boson, can be obtained from precision measurements at the Z° resonance. This is due to the effect of higher-order radiative corrections (see Appendix A), which on the one hand modify expressions for cross sections and asymmetries with respect to the Born level discussed so far, and on the other hand depend on the masses of both particles.[4]

---

[4]Information on the top and Higgs masses obtained in this way cannot be disentangled from the possible existence of new fermion and boson families with large masses [14].

Tau-pair production
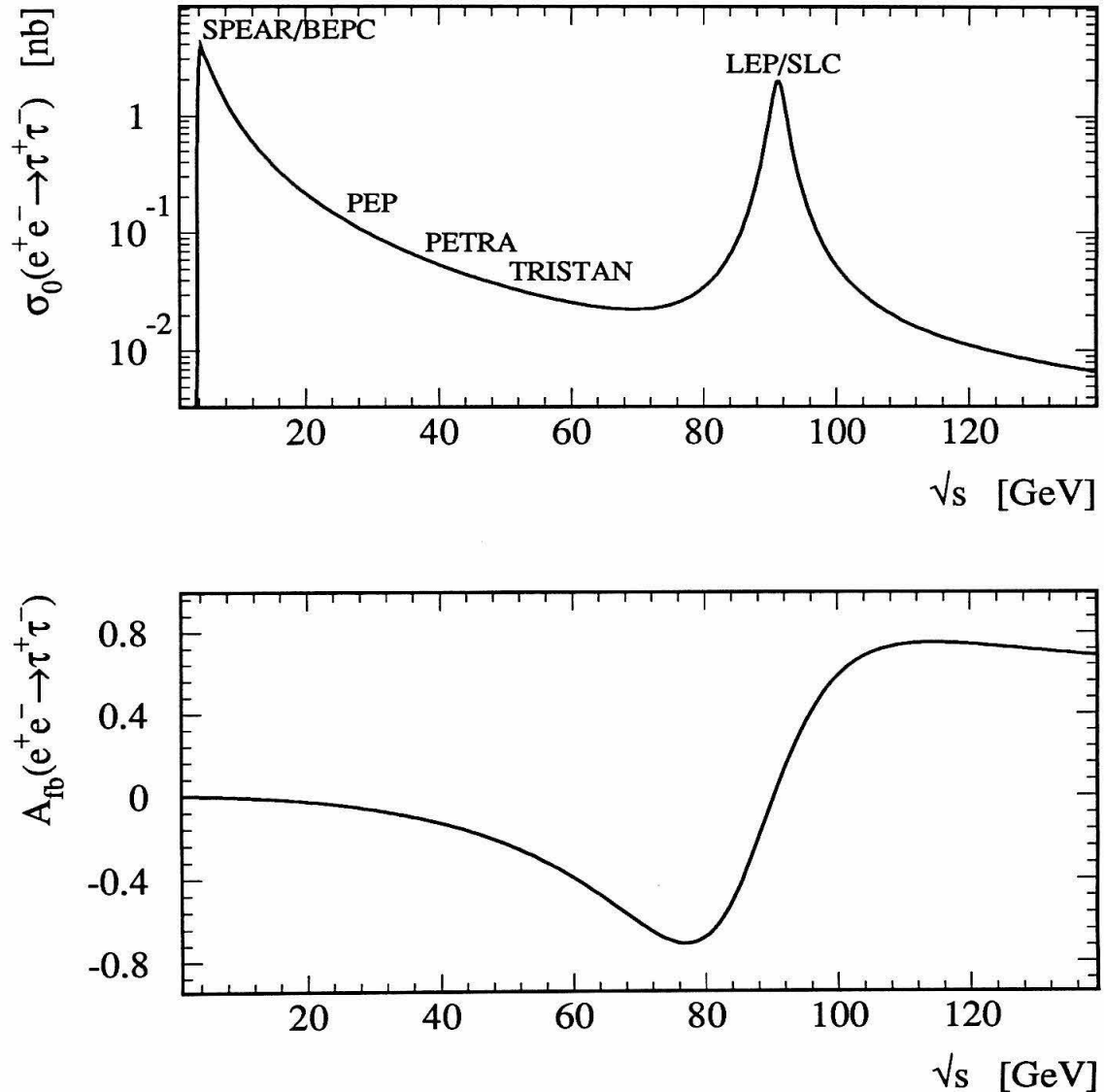
Figure 2.3: Born total cross section $\sigma_0(e^+e^- \to \tau^+\tau^-)$ and forward-backward charge asymmetry $A_{fb}(e^+e^- \to \tau^+\tau^-)$ as a function of the center-of-mass energy $\sqrt{s}$ between threshold and 140 GeV.

Chapter 3

The L$_3$ Experiment at LEP

The **L$_3$** detector [15, 16] is one of the six major detectors designed to operate at the new generation of electron-positron accelerators. These detectors, MARK II [17], SLD [18], ALEPH [19], DELPHI [20], OPAL [21] and **L$_3$** are especially built (in the case of MARK II upgraded) for the new high center-of-mass energy range opened up by the Stanford Linear Collider (SLC [22]) at SLAC, Stanford, and the Large Electron Positron (**LEP** [23]) machine at **CERN**, Geneva.

This chapter presents the **LEP** particle accelerator and describes in detail the **L$_3$** detector designed to study e^+e^- collisions at center-of-mass energies of up to 0.2 TeV. Future upgrades of **LEP** and **L$_3$** are summarized in Appendix D.

3.1 The LEP Storage Ring

The physics goals of the large electron-positron collider **LEP** are twofold. In its first stage, the machine is now producing the Z° boson copiously by operating with beam energies around 45 GeV. In a second stage, which will begin by 1994, the pair production of W$^\pm$ bosons is foreseen, which requires more than 80 GeV beam energy. These goals set the requirements on beam energy and luminosity, the two fundamental parameters constraining the design of any accelerator. Studies of the design started at **CERN** in 1976 with the first practical design published in 1978. The requirements on beam energy set the size of the machine: **LEP** has a circumference
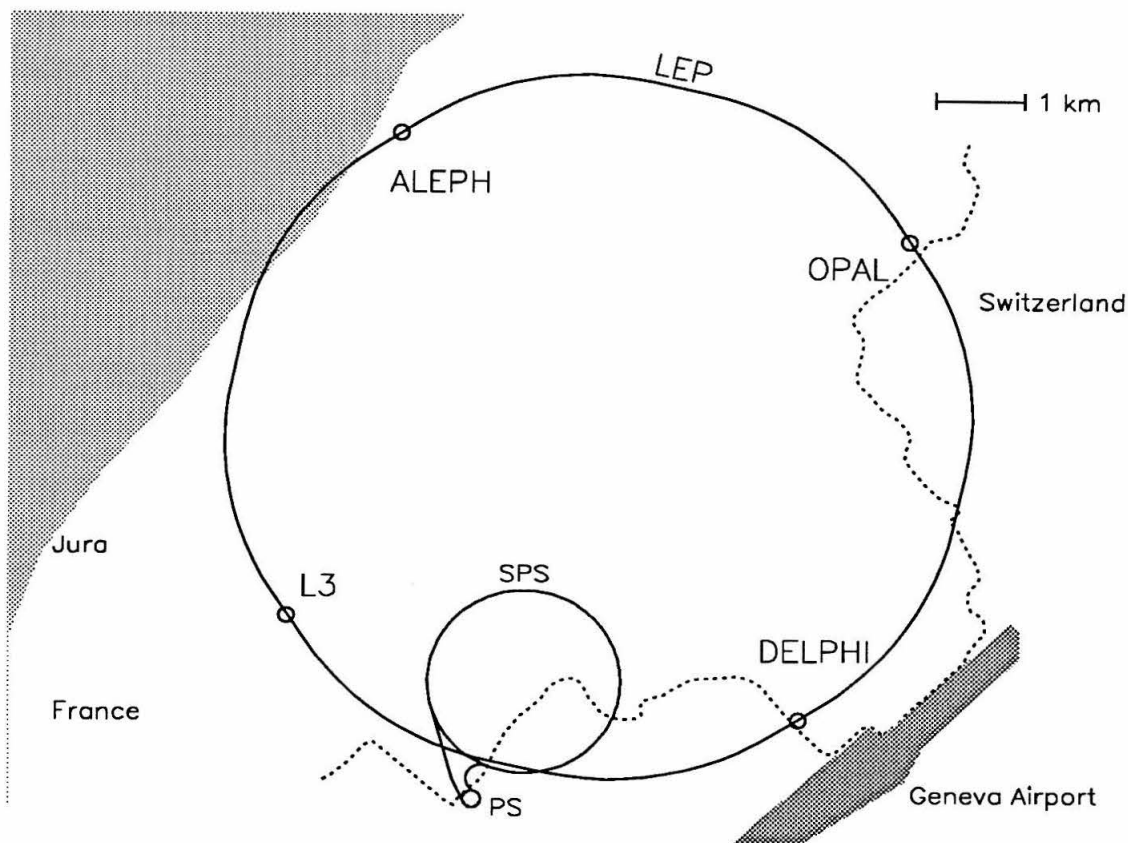
Figure 3.1: **LEP** site with four experiments.

of about 27 km, and is therefore located beneath the surface in a tunnel extending from the Jura mountains on the French side to the Geneva airport on the Swiss side, as shown in Figure 3.1.

The **LEP** storage ring is the last part in a whole chain of accelerators (Figure 3.2). The **LEP** injector system consists of two linacs (LIL) of 0.2 GeV and 0.6 GeV, followed by a 0.6 GeV electron-positron accumulator (EPA) to enhance electron and especially positron intensity. Accumulated particles are injected into the proton synchrotron (PS) operating as a 3.5 GeV e^+e^- synchrotron. The PS then injects into the super proton synchrotron (SPS). The SPS in turn operates as a 20 GeV
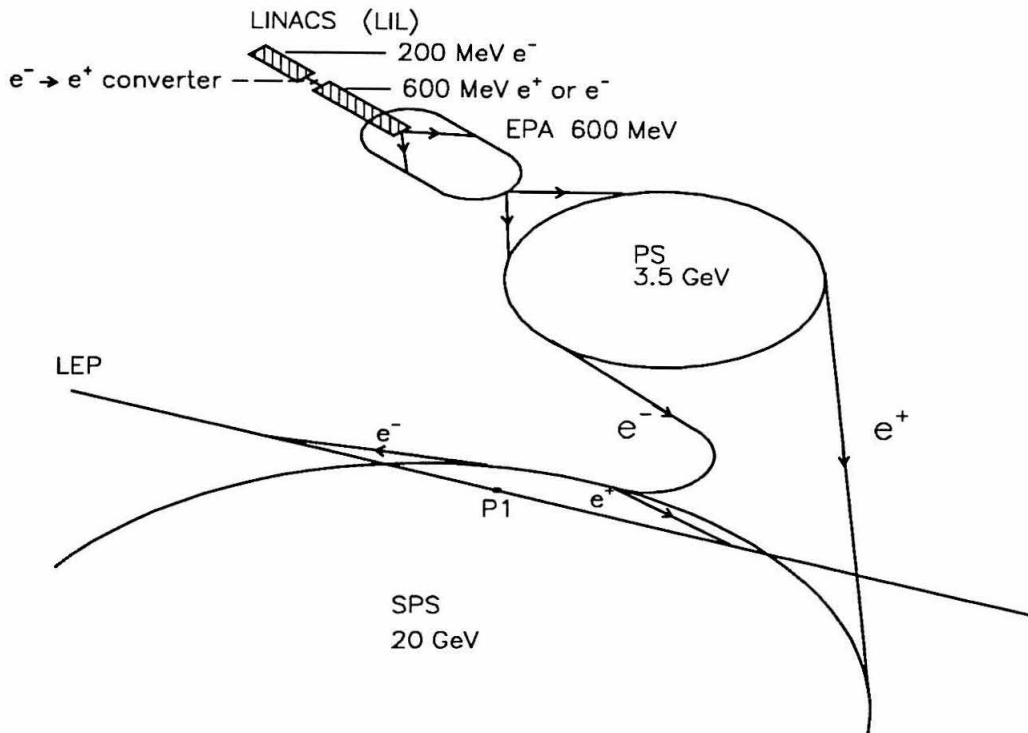
Figure 3.2: Injection scheme for **LEP**.

electron-positron injector for the **LEP** machine. **LEP** works as an accelerator to "ramp" from injection energy up to collision energies, and then as a storage ring to provide collisions.

Eight segments of a full circle, connected by eight straight sections, form the **LEP** machine. The bending sections have a length of 2840 m each, and are equipped with a total of 3304 dipole magnets. These magnets are able to produce a field of up to 0.134 T. To keep the circulating electrons and positrons on or near the ideal orbit through the lattice of **LEP** magnets, a field of 0.048 T is necessary at a beam energy of 45 GeV. Thus, from the point of view of magnetic bending power, **LEP** is capable of handling beam energies of up to 125 GeV.

All eight straight sections contain an interaction point (IP), numbered from 1 to 8. However, only the evenly numbered interaction regions have been equipped with large detectors, **L$_3$** (IP 2), ALEPH (IP 4), OPAL (IP 6) and DELPHI (IP 8). On both sides of each detector, superconducting quadrupole magnets focus the beams at the interaction point, thus increasing the luminosity of the experimental regions.

The electrons and positrons in the **LEP** beams are concentrated in a few short bunches, typically 1.6 cm long. The particle revolution time of 88 μs leads to a beam crossing rate of 45 kHz at the interaction regions when storing four bunches in either beam. At 45 GeV, the circulating electrons and positrons lose about 0.12 GeV per turn due to synchrotron radiation. This energy loss is compensated by RF cavities (352 MHz), placed left and right of the interaction points 2 (**L$_3$**) and 6 (OPAL). They provide a total power of up to 16 MW, both to accelerate the particles from their injection energy of 20 GeV up to the desired beam energy around 45 GeV, and to replace the energy lost by synchrotron radiation.

In 1991, the lifetime of the beams was of order of 10 hours and their total current 2 mA, after ramping to collision energies. During the 1991 data-taking period, the typical instantaneous luminosity delivered to **L$_3$** was $3 \cdot 10^{30} \mathrm{cm}^{-2} \mathrm{s}^{-1}$, with peak values reaching $5 \cdot 10^{30} \mathrm{cm}^{-2} \mathrm{s}^{-1}$, thus yielding on average 150 nb^{-1} of integrated luminosity per **LEP** machine fill. A peak luminosity of $10^{31} \mathrm{cm}^{-2} \mathrm{s}^{-1}$ was reached at the end of the 1991 **LEP** run, corresponding to 300 nb^{-1} per fill.

3.2   The L$_3$ Detector

The form of the **L$_3$** detector (symbolized in the **L$_3$** logo) depicts its most impressive component: the precise muon spectrometer, having an octagonal shape in the plane transverse to the beam axis. Together with the high precision electromagnetic crystal calorimeter, this emphasizes the design goal of **L$_3$**: the measurement of photons, electrons and muons ($\gamma e \mu$) with the highest resolution in energy and position.

Viewed from the interaction point, the **L$_3$** detector consists of the following active subdetector systems (see Figure 3.3):
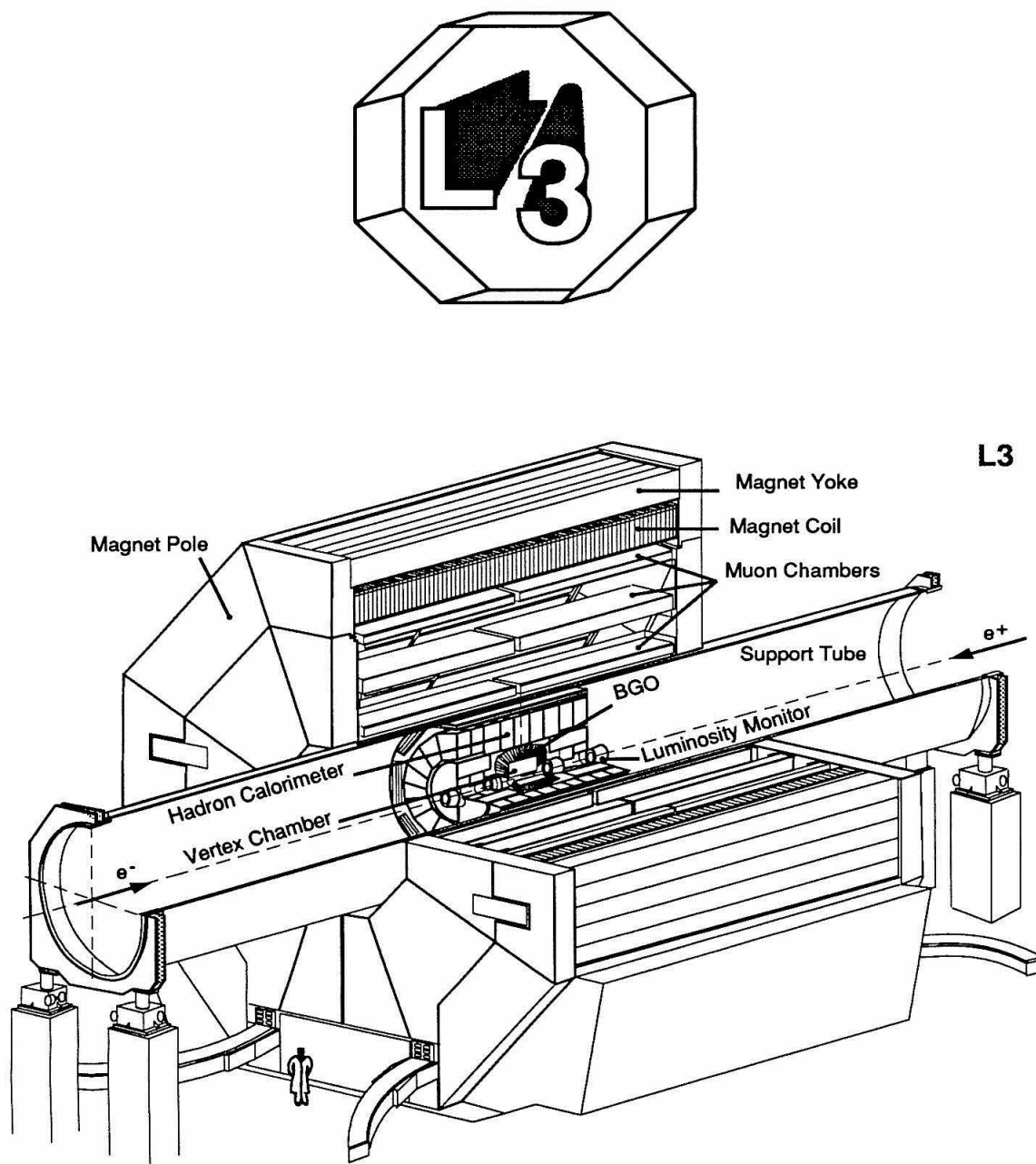
Figure 3.3: Perspective view of the **L3** detector.

- a time expansion chamber (TEC) for tracking charged particles,

- an electromagnetic calorimeter composed of bismuth germanium oxide (BGO) crystals,

- a luminosity monitor composed of BGO crystals,

- a cylindrical array of scintillation counters,

- a hadron calorimeter with depleted uranium as absorber and proportional wire chamber readout,

- a muon spectrometer made of multi-wire drift chambers.

The beam pipe, 5.3 cm in radius, is a composite structure made of beryllium in the central section (TEC), and carbon fiber up to the luminosity monitors. The inner detector elements TEC, calorimeters, scintillators and luminosity monitors are installed inside the central section of a 32 m long steel support tube of 4.5 m diameter (Figure 3.4). This central part of the tube is surrounded by three layers of muon chambers. All detector elements are installed in a 12 m inner diameter solenoidal magnet, which provides a uniform magnetic field of 0.5 T along the beam direction.

The right-handed coordinate system of the L$_3$ detector is specified as follows:

- The origin coincides with the geometrical center of the L$_3$ detector, which is also the nominal interaction vertex.

- The z direction coincides with the direction of the LEP e$^-$ beam.

- The y direction points vertically upwards.

- The x direction points to the center of the LEP ring.

The radius r denotes the distance to the origin. The polar angle θ is measured with respect to the z direction. The azimuthal angle ϕ is measured in the x/y plane with respect to the x direction.

In the following sections, the status of the L$_3$ detector during the 1991 running period is described.
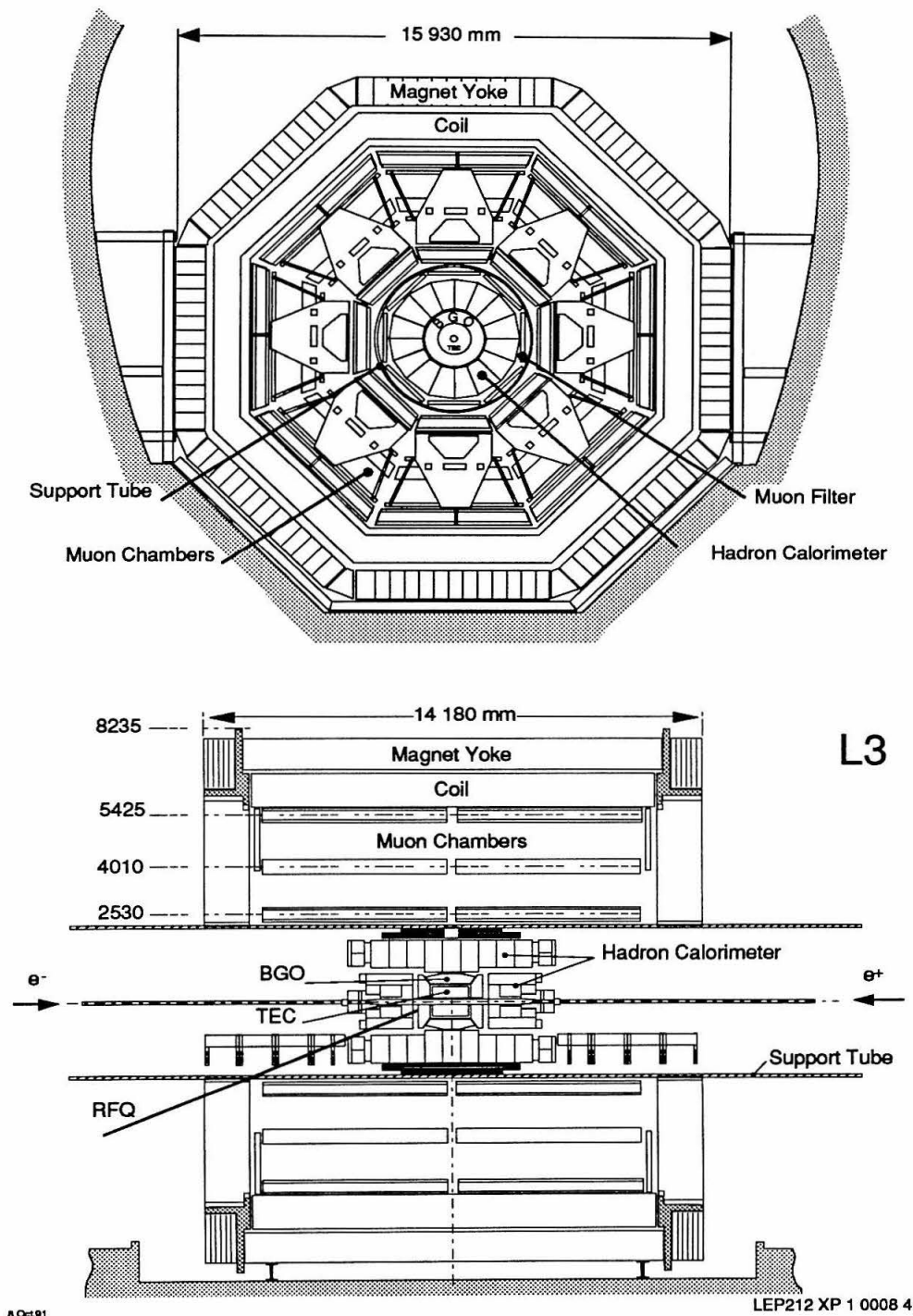
Figure 3.4: End and side view of the **L₃** detector.

3.2.1   Time Expansion Chamber

The inner central tracking chamber of the **L₃** detector has been designed to achieve the highest possible resolution in the limited volume available within the electromagnetic calorimeter. High spatial resolution is crucial to obtain precise information on charged particles emerging from the interaction region:

- location and direction of tracks,

- transverse momentum and charge,

- interaction point and secondary vertices,

- impact point and direction at the entrance of the electromagnetic calorimeter.

The main part of the central tracker consists of two concentric cylindrical drift chambers in a common volume, operated in the so-called "Time Expansion" mode. The detection principle of a Time Expansion Chamber (TEC) is schematically shown in Figure 3.5.

The TEC combines a large volume with a low, homogeneous drift field with a very small volume of high fields, where the gas amplification process takes place. The TEC operates with a gas mixture of 80% CO_2 and 20% *iso*-C_4H_{10}, which has low longitudinal diffusion and thus permits a low drift velocity of about 6 μm/ns. The two regions are separated by a grid plane, which, together with field shaping and cathode wires, ensures the homogeneity of the electric field within the drift region.

The total lever arm available for track measurement is 31.7 cm radially. The inner part of the TEC, divided into 12 sectors covering the full azimuthal angle, measures 8 coordinate points of an ionization track in the plane perpendicular to the beam direction. The outer TEC is composed of 24 sectors and a track is measured by up to 54 wires. Figure 3.6 shows the wire arrangement inside the TEC. The anode pulses are sampled by 100 MHz flash analog-to-digital converters (FADC) in order to obtain a precise drift-time measurement by a center-of-gravity method.

Because of the symmetry of the TEC sectors with respect to the anode plane, there arises a left-right ambiguity, i.e., an ambiguity on which side of the anode plane

Grid Wires Grid Wires Charged Particle Trajectory Cathode Wires

Focus Wire

Anode Wire

Electric Field Cluster

Amplification Region Drift Region
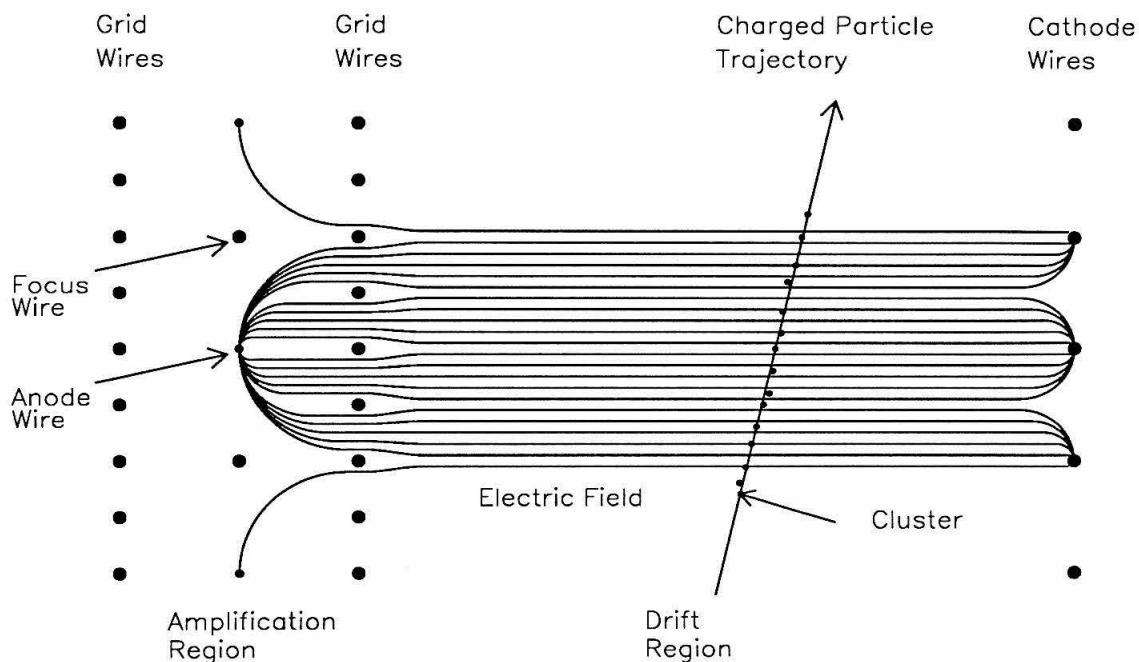
Figure 3.5: Principle of a time expansion chamber.

the track passed. This ambiguity problem is solved by matching those parts of the track measured in inner and outer TEC and by evaluating the response of pick-up wires within the grid plane of the outer TEC sectors.

To aid in the calibration of the TEC chamber, each outer TEC segment is equipped with a plastic scintillation fiber ribbon to monitor the drift velocity. The relationship between drift time and drift distance is obtained separately for every anode and half sector by averaging over the fitted tracks, and by imposing the interaction point and fiber position as constraints. A single wire resolution of 51 μm and a double-track resolution of better than 600 μm over the whole drift field region has been achieved. The transverse momentum resolution is given by $\sigma(1/p_\perp) = 0.022/\text{GeV}$. Track extrapolation to the face of the BGO calorimeter leads to a position resolution of 500 μm in the transverse plane.

+ = Charge Division Anode
· = Anode
• = Focus
● = Outer and Inner Focus, Cathode
═ = Grid
△ = Group of 5 Grid Wires for Solving
     Left–Right Ambiguity
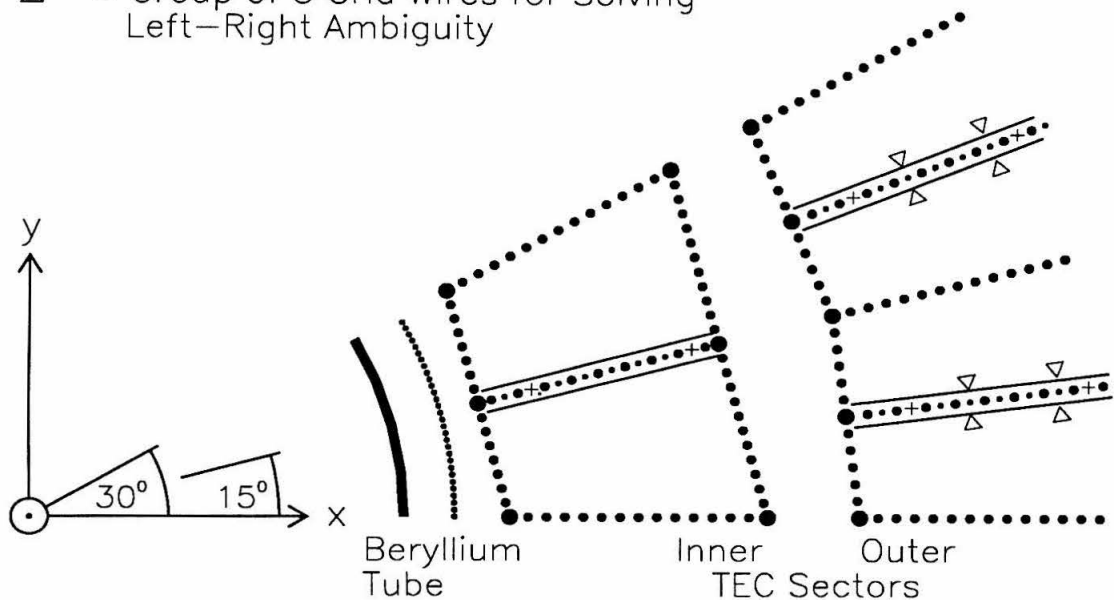
Figure 3.6: Wire layout of inner and outer TEC sectors. The innermost signal wire has a distance of 11 cm to the beam axis.

By construction, the coordinate measurement of a chamber with sense wires parallel to the z axis contains no information about the z coordinate (along the beam direction) of a track.[1] Measurement of the z coordinate is made by the charge division method. For this purpose, 11 out of the total of 62 sense wires along a radial track are read out at both ends with FADC's to obtain two pulse integrals, whose

---

[1]In principle, there is a z-dependent shift of the measured drift time due to the finite velocity of signal propagation along the sense wire. However, this shift is so small that in the case of the TEC the accuracy of a z determination from this effect is of the order of the z extent of the chamber itself [24]. On the other hand, this effect should be included for a precise $r/\phi/\theta$ calibration.
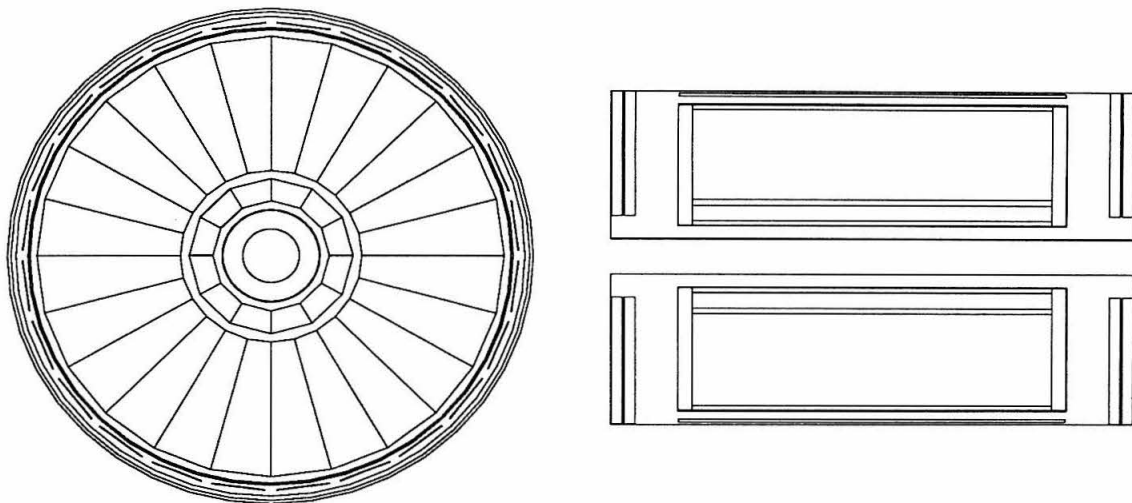
Figure 3.7: End and side view of the central tracking chamber TEC, having an outer diameter of 1 m.

ratio contains information about the z coordinate. However, this method alone is not precise enough, as the resolutions obtained are of the order of centimeters. Therefore, the outer surface of the TEC cylinder is equipped with a four-layer cylindrical proportional chamber, the Z-detector. This chamber measures four points of each track using cathode strip readout. The strips have a pitch of 4.45 mm and a gap of 0.65 mm and are inclined with respect to the chamber axis by angles of 69°, 90°, −69° and again 90°. The two 90° strip layers are offset from each other by half a pitch width. A position resolution of 320 μm in z has been obtained. The z information of the charge division wires in the TEC is used in the pattern-recognition phase of the track reconstruction: their prediction of a z range is used to search for hits in the Z-detector.

The θ determination for tracks outside the barrel region covered by the Z-detector is done by the forward tracking chamber (FTC), located between the TEC endflanges and the BGO endcap calorimeter. The FTC has a spatial resolution of better than 200 μm and an angular precision of better than 10 mrad.

3.2.2 Electromagnetic Calorimeter

The electromagnetic calorimeter has been designed to have the highest possible resolution in energy and position over a wide range of energies (from 100 MeV to 100 GeV). This requirement can only be met by a crystal calorimeter using the same medium for showering and detection, so that the complete shower is measured instead of only a sampled fraction of it.

Figure 3.8 shows the arrangement of the nearly 11000 crystals made of $Bi_4Ge_3O_{12}$ (BGO). The barrel part consists of 7860 crystals, arranged in two symmetrical half barrels with a total polar angular coverage of $42° < \theta < 138°$. The two endcaps, installed during the 1990/91 winter shutdown, contain 1527 crystals each, extending the angular coverage down to 12° from the beam line.

The crystals have the form of a truncated pyramid with a length of 24 cm (equivalent to 21 radiation lengths), a front face of $2 \cdot 2$ cm² and a rear face of $3 \cdot 3$ cm². All crystals are generally pointing to the vertex, with the exception of a small angular tilt in the azimuthal direction, which has been incorporated into the design to suppress the possibility of particles traversing solely the insensitive carbon-fiber support structure. Each crystal is viewed by two photodiodes glued to its rear face detecting the BGO scintillation light. In order to provide accurate measurements over the range of 100 MeV to 100 GeV, the digitizing range of the ADC's used is equivalent to 21 bits, with a resolution of at least 10 bits.

The barrel part of the BGO calorimeter was calibrated in **CERN** test beams with electrons at energies of 0.18, 2, 10 and 50 GeV. From these measurements, the energy resolution of the BGO calorimeter has been determined to be approximately 5% at 0.1 GeV, less than 2% above 2 GeV and about 1.2% at 45 GeV. The linearity is better than 1%. Above 2 GeV, the position resolution by the center-of-gravity method is less than 2 mm for electromagnetic showers.

In order to maintain the BGO calibration measured in the testbeam, continuous monitoring of the BGO calorimeter is necessary. For this purpose, a Xenon light monitoring system is installed, which measures the crystal transparency by injecting light pulses into the rear face of each crystal. Analysis of Bhabha ($e^+e^- \to e^+e^-$)
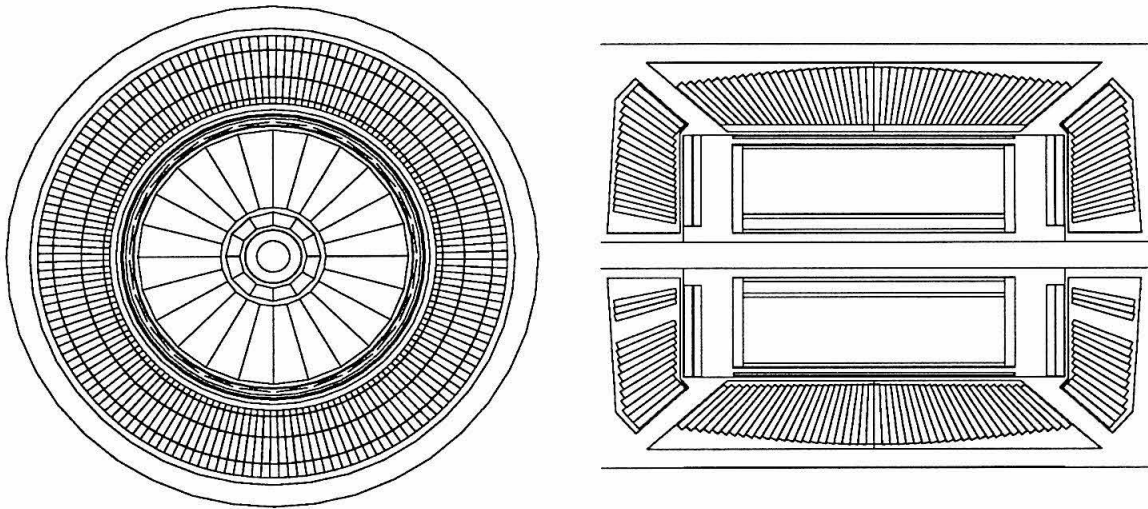
Figure 3.8: End and side view of the **L₃** BGO electromagnetic calorimeter, with a 1.5 m outer diameter, enclosing the TEC. The gap in the lower endcaps shown in the figure is only present in the vertical plane, to allow passage of the beam pipe for the RFQ calibration system developed at Caltech (see Appendix D).
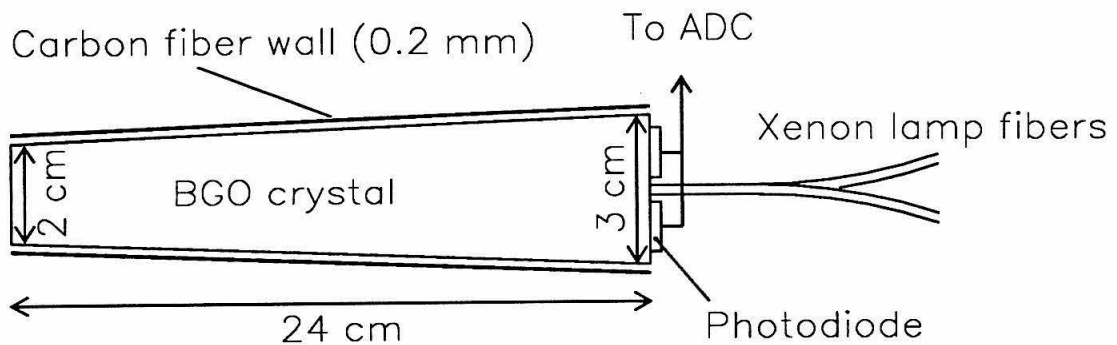
Figure 3.9: Mounting of a BGO crystal.

events allows for a global absolute energy calibration at the energy of the **LEP** beams. In addition, there are dedicated cosmic ray runs during shutdown periods. The minimum ionizing signal of cosmic muons provides an absolute energy scale calibration, at low energies.

Following initial tests completed in 1992, frequent *in situ* calibration using Caltech's RFQ system [25, 26] is foreseen starting in 1993 (see Appendix D).

3.2.3   Luminosity Monitor

The system to monitor and measure the luminosity at **L₃**'s interaction region consists of two dedicated BGO calorimeters and two sets of proportional wire chambers. The chambers are situated in front of the calorimeters, which are positioned symmetrically on either side of the interaction region at $z = \pm 2.7$ m. Each of the two calorimeters, split in the vertical plane to allow the retraction of the two halves from the beam during the filling of **LEP**, is otherwise an azimuthally symmetric and finely segmented array of 304 BGO crystals with improved radiation hardness (Figure 3.10).

The calorimeters cover the polar angular range of 25 mrad $< \theta\, (\pi - \theta) <$ 70 mrad, respectively. Every crystal is viewed by a photodiode and has a LED to monitor its transparency. The calorimeters have an energy resolution for electromagnetic showers of approximately 2% and an angular resolution of 0.4 mrad in θ and 0.5° in ϕ.

3.2.4   Scintillation Counters

An array of 30 scintillation counters is situated in the barrel region ($|\cos\theta| < 0.83$) between the electromagnetic and hadronic calorimeter, covering 93% of the azimuthal angular range. Discrimination of dimuon events from cosmic muons can easily be achieved using the accurate timing measurement from the scintillation counters associated with the muon tracks. The timing of cosmic muons is uncorrelated with the beam crossing; also, the time of flight difference between the opposite counters is zero for dimuon events, but about 5.8 ns for cosmics. For this reason the timing of the scintillation counters, with their resolution of 0.5 ns, is used for the trigger.
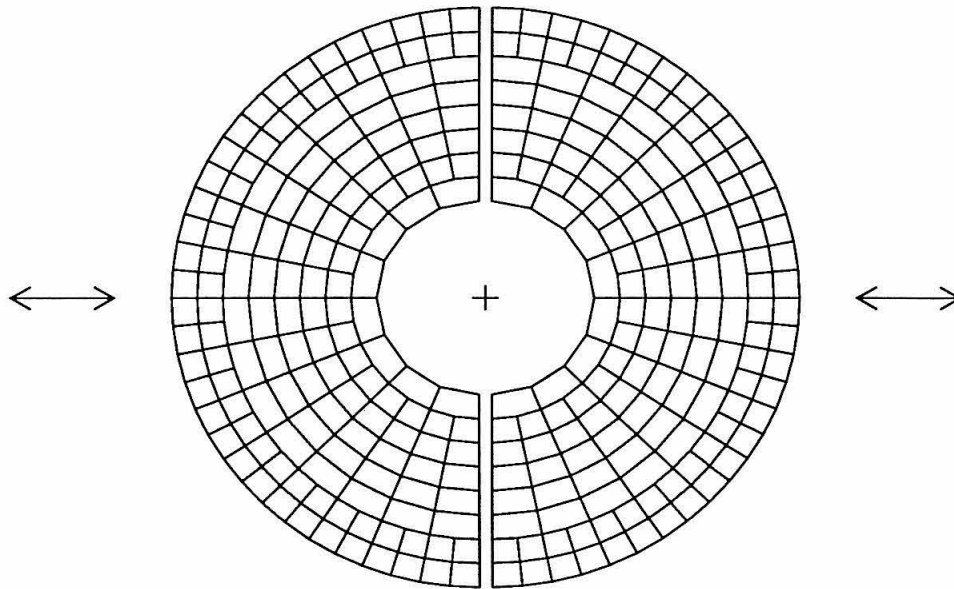
Figure 3.10: Crystal arrangement in the luminosity monitor, having an outer diameter of 38 cm. The arrows indicate the retraction of the calorimeters during filling of **LEP**.

3.2.5 Hadron Calorimeter

The **L₃** hadron calorimeter system is cylindrical in shape, enclosing the BGO calorimeter. It consists of three parts:

- the barrel hadron calorimeter covering the polar angular range of $35° < \theta < 135°$,

- the muon filter located between the barrel hadron calorimeter and the muon spectrometer,

- the endcap hadron calorimeter located behind the BGO endcaps ($5.5° < \theta < 35°$, $145° < \theta < 174.5°$).

Both barrel and endcap are fine sampling calorimeters made of uranium and brass absorber plates interleaved with proportional wire chambers.
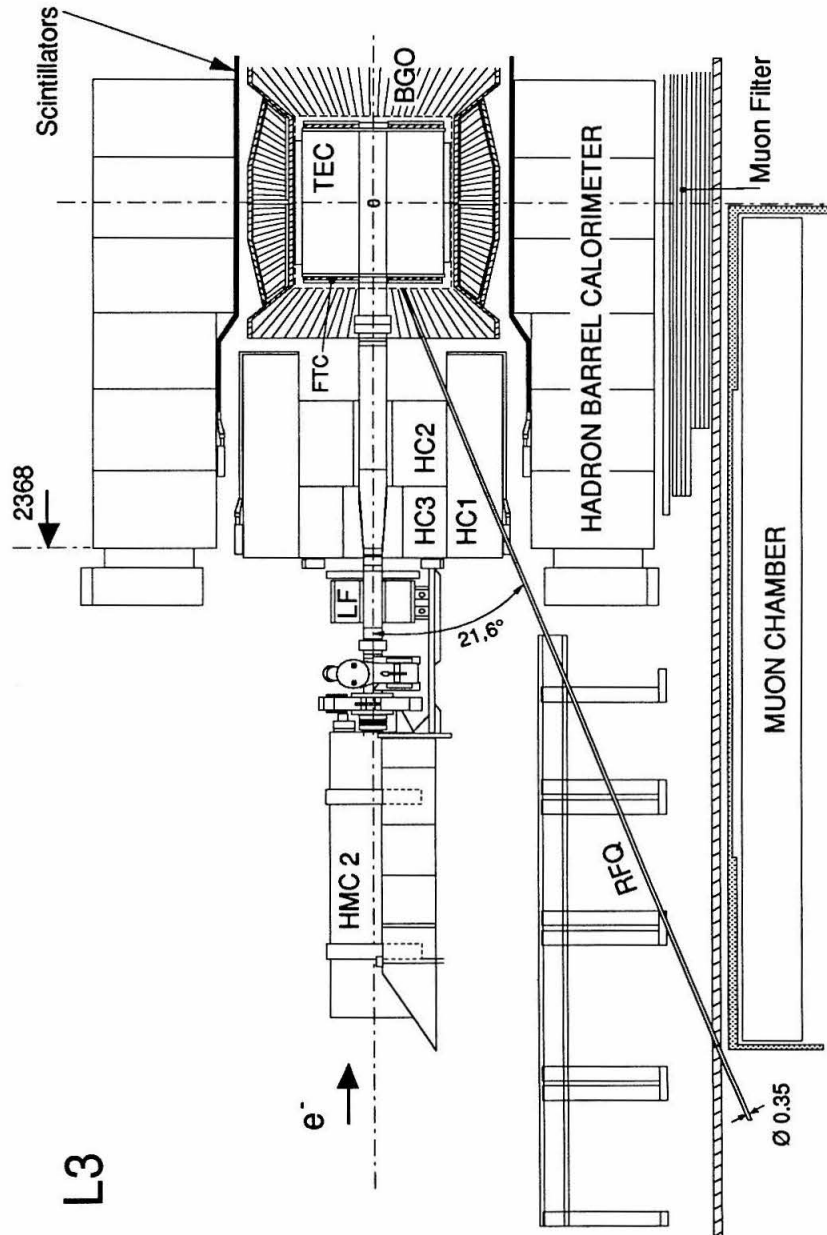
Figure 3.11: Central part of the **L₃** detector. The luminosity monitor is marked LF, the three rings of the hadron endcap calorimeter HC1, HC2 and HC3.
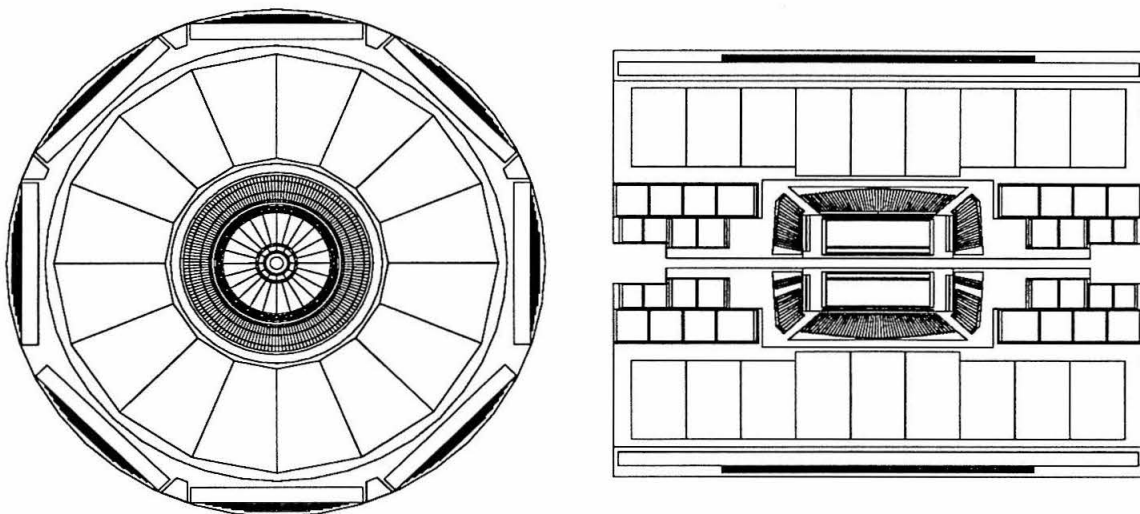
Figure 3.12: End and side view of the hadron calorimeter system (4.4 m outer diameter), enclosing TEC and BGO calorimeter.

The barrel calorimeter is composed of 9 rings along z. Each ring is symmetrically divided into 16 modules in the azimuthal direction ϕ. The modules of the three outer rings on both sides are 10 cm shorter than those of the three central rings to leave room for readout and supply cables. The fine sampling calorimeter contains 7968 proportional wire chambers, which are grouped in the readout to form 101088 projective towers pointing to the beam line. Each tower subtends an angle of 2.5° in θ and ϕ. Within a module, the segmentation is 9 in both transverse directions, and 8 (10) in the longitudinal direction for short (long) modules.

The endcap calorimeter extends the angular coverage of the hadronic calorimeter system to 99.5% of 4π. It consists of three rings on each side, one outer ring and two inner rings. Viewed from the interaction point, the amount of material varies between 6 and 7 nuclear absorption lengths. As for the barrel calorimeter, the wire signals are grouped to form 3960 towers. Combining the information from the BGO and hadron calorimeters, a resolution of 10% in total energy and 2° in direction of jets has been achieved for hadronic events.

The muon filter adds 1.0 nuclear absorption length to the 3.5 of the barrel hadron calorimeter. It consists of eight octants in the azimuthal direction. Each octant is made of six 1 cm thick brass (65% Cu, 35% Zn) absorber plates, interleaved with five layers of proportional tubes, followed by 1.5 cm thick absorber plates that match the circular shape of the supporting tube. The barrel calorimeter and muon filter act as particle filters, so that only non-showering particles, e.g., minimum ionizing muons, are able to to reach the precise muon spectrometer.

3.2.6   Muon Spectrometer

The muon detector has been designed for high-precision measurements of the momentum of muons. It consists of two "ferris wheels" ($+z$ and $-z$), each made up of eight octants supporting three layers of precision multi-wire drift chambers (P chambers), as shown in Figure 3.13.

Muons more energetic than 3 GeV will be confined to a single octant. Therefore, alignment is only critical between chambers in the same octant. To achieve the design resolution, systematic errors in the internal octant alignment have been kept below 30 μm. For this purpose, several alignment systems are used to monitor and correct the chamber positions, and to aid in the calibration procedure. These are:

1. an opto-mechanical system using LED's for vertical chamber alignment,

2. a laser beacon using a He-Ne laser for parallel chamber alignment,

3. a UV laser to simulate infinite momentum particles coming from the vertex through all three layers.

The inner (MI) and outer (MO) layer of P chambers contain 16 signal wires per cell, the middle layer (MM) has 24 wires per cell, which measure a given track in the bending plane (Figure 3.14). Both sides of the inner and outer P chambers are equipped with additional drift chambers (Z chambers), which measure the coordinate along the beam. They consist of two layers of drift cells offset by half a cell with respect to each other to resolve left-right ambiguities.
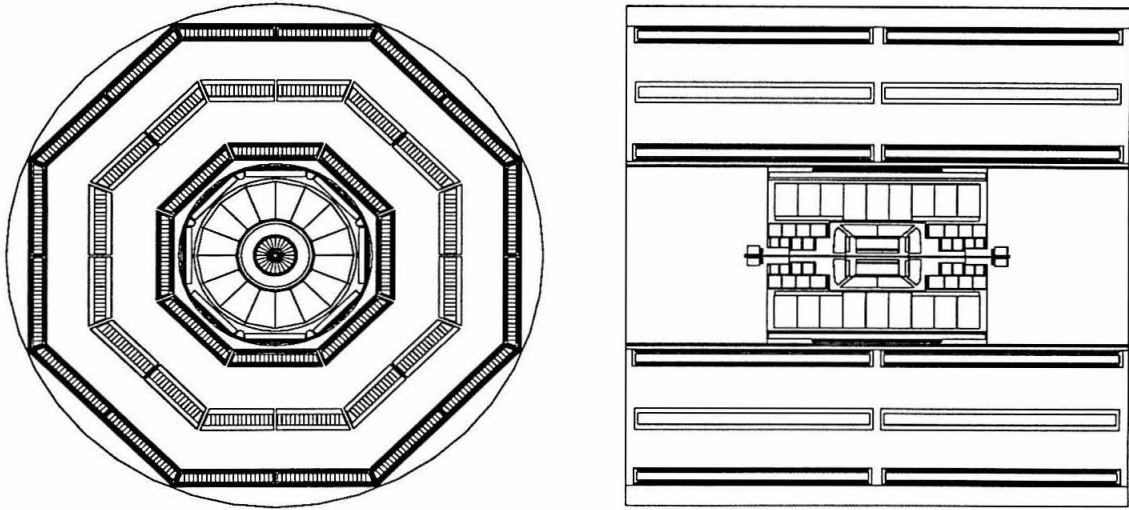
Figure 3.13: End and side view of the muon spectrometer, having an outer diameter of 12 m.
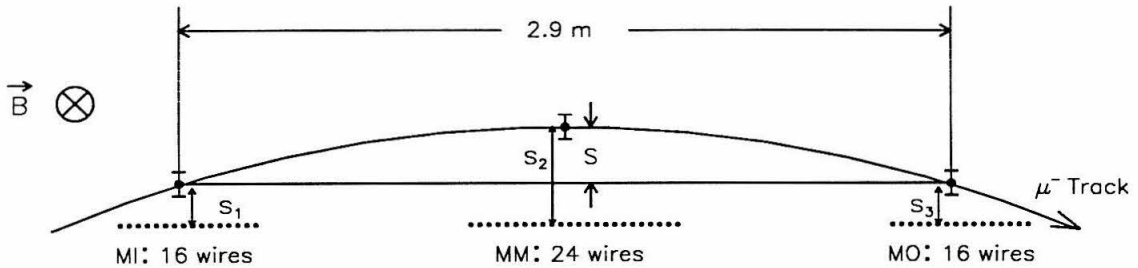
Figure 3.14: Muon chamber track measurement.

A single wire resolution of less than 200 μm for P chamber wires has been achieved. This is sufficient to reach the design momentum resolution of 2.5% at 45 GeV. For the Z chambers, a resolution of typically 500 μm has been achieved.

The **L₃** chambers not only measure the sagitta, i.e., the deviation of the position of the middle segment from the straight line connecting the inner with the outer segment (Figure 3.14), but also the local slope of the particle trajectory (slope of

track segment within a P chamber) to an accuracy of about 1 mrad. This allows a momentum determination even if there are only two P segments measured for a given track. The coverage of 76% of the solid angle will be enlarged by the forward-backward muon chambers to be installed by 1994 (see Appendix D).

3.2.7 Magnet

All detector systems are installed inside a large solenoid coil of 6 m inner radius and 12 m length, which is surrounded by an iron yoke. The ends are closed by two poles equipped with hinged doors. In order to create a magnetic field of 0.5 T on the beam axis, a current of 30 kA is driven through the 168 turns of the aluminum coil. Although a field of 0.5 T is relatively modest, the muon momentum resolution, which improves linearly with the field but quadratically with the track length, is cost-optimized due to the large magnetic volume.

Before installation of the detector, the magnetic field has been mapped in the complete volume. The support tube separates the magnetic volume into two parts. The field inside the support tube was measured with Hall plates. The outer volume is permanently monitored with about 1000 magnetoresistors installed on the muon chambers. Five NMR probes provide an absolute measurement of the field.

3.2.8 Trigger System

After each beam crossing, the trigger system has to decide whether an event should be recorded. This task is performed in a three-level process, with increased complexity at each level, reducing the event rate and thus leaving more time for more elaborate decisions at each stage. Thus, the beam crossing rate of 45 kHz in $4 + 4$ bunch mode is reduced to a few Hz of events finally written to tape.

Whereas the function of the level-1 trigger is to select interesting events, the task of the higher level-2 and level-3 triggers is to reject background events selected by level-1. During the 1990 data-taking period, the level-2 and level-3 triggers have been used in flagging mode only to check in detail their selection and rejection performance on hard- and software level. For the 1991 data-taking period, level-2 and level-3 have

been put into rejection mode. A prescaled fraction of events triggered by level-1 is passed through untouched to allow continuous monitoring of the level-2 and level-3 performance.

Level-1 Trigger

In the 22 μs before the next beam crossing, the level-1 trigger decides whether to initiate the digitization of the detector data or to drop the event. Thus, dead time occurs only in the case an event has been accepted by level-1. In the case of a positive decision, the detector data are digitized within 500 μs. The typical level-1 trigger rate is less than 8 Hz. Allowing for read-out time to store the data in multi-event buffers, this leads to a dead time of less than 5%.

The level-1 trigger consists of five subtriggers based on five mutually exclusive subdetector components of **L₃** (typical trigger rates are given in parenthesis):

1. Energy trigger (1 − 2 Hz):
   The level-1 calorimeter trigger selects events which deposit more than a few GeV in the electromagnetic or hadronic calorimeters. The calorimeters are divided into 896 cells, as shown in Figure 3.15. The analog sums of the energies deposited in each cell are digitized by fast ADCs. Trigger thresholds are set on total energy and BGO energy. For the complete detector, the thresholds are 25 GeV; in the restricted angular range of $18° < \theta < 162°$, they are 15 GeV and 8 GeV, respectively. Events with localized energy depositions (clusters) of more than 6 GeV (2.5 GeV in spatial coincidence with a TEC track) also are triggered. A special single-photon trigger searches for events which contain only a single electromagnetic energy deposition of at least 0.9 GeV.

2. Muon trigger (1 Hz):
   The level-1 muon trigger selects events with at least one muon reaching the muon spectrometer. Its raw trigger rate of 10 Hz is reduced by a factor of ten by requiring at least one good hit in a scintillator within a 30 ns gate to reject cosmic rays. Hits forming roads are required in either two out of three P chamber cells or three out of four Z chamber cells.
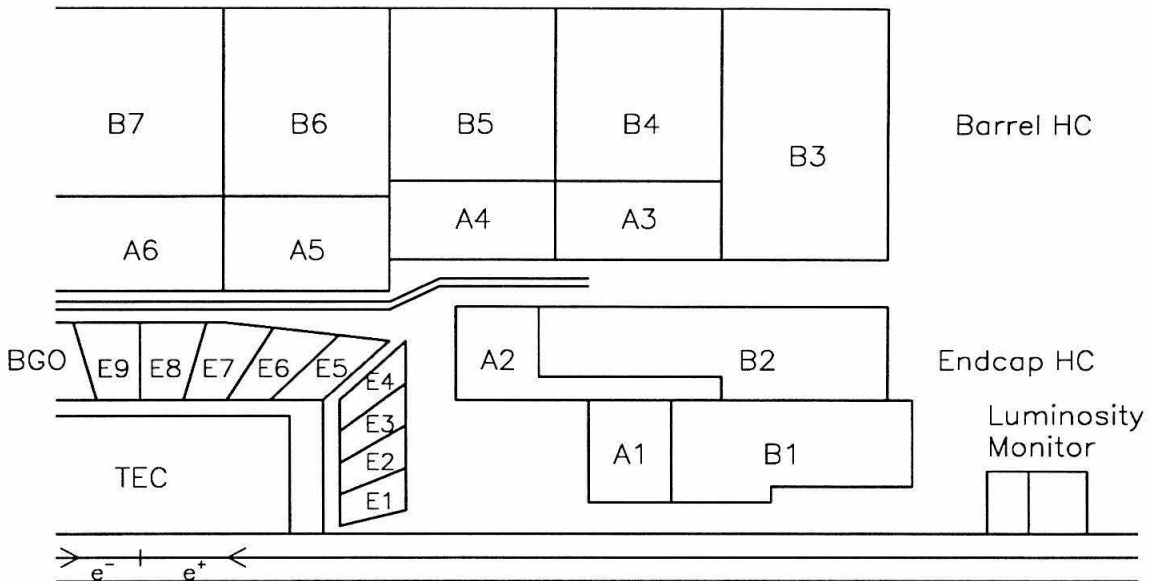
Figure 3.15: The segmentation of the calorimeters for the energy trigger. The BGO electromagnetic calorimeter has a segmentation of 32 in ϕ and 8 in θ for barrel and endcap. The hadron calorimeter has a segmentation of 16 in ϕ and 11 (layer A) or 13 (layer B) in θ. This yields 896 trigger channels in total.

3. TEC trigger (1 − 4 Hz):

The level-1 TEC trigger selects events having at least two TEC tracks of less than 60° acoplanarity. Signals of 14 anode wires of each outer TEC sector, binned into two bins of drift time, are used to search for correlated hits forming tracks. Thus, a track must have a transverse momentum of at least 150 MeV, and it cannot be closer than 25° in polar angle from the beam axis.

4. Scintillator trigger (0.1 Hz):

The level-1 scintillator trigger is used both to select high-multiplicity events and − together with the muon trigger − to reject cosmic rays. For the multiplicity trigger, two neighboring scintillators are ORed to yield 16 pairs in azimuth. Events must fire at least five of such pairs within a gate of 30 ns, and at least

two pairs must be separated by more than four pairs (90°) in azimuth.

5. Luminosity trigger (1.5 Hz):

The level-1 luminosity trigger specifically selects Bhabha events in the luminosity monitors. It uses the analog sums from the two BGO luminosity calorimeters, which are divided into 16 ϕ segments on each side, given by the angular coverage of the 16 innermost crystals (see Figure 3.10). Events are accepted if there are two clusters with more than 15 GeV in the calorimeters back-to-back within plus/minus one sector, or if the total energy is larger than 25 GeV on one side and 5 GeV on the other side, or if the total energy on either side is larger than 30 GeV.

Level-2 Trigger

In case of a positive level-1 trigger decision, the level-2 trigger, consisting of four special XOP programmable fast trigger processors designed at **CERN**, commences to work. It is designed to reject non-physical background events, arising from electronic noise, beam-gas and beam-wall interactions as well as synchrotron radiation. Events triggered by more than one level-1 subtrigger are never rejected. Information not available in time for a level-1 decision is now used, in particular charge and drift-time information from the charge division wires of the TEC, to perform three-dimensional track coordinate reconstruction. In particular, the following information is used:

- energy depositions in the BGO and hadron calorimeters, correlated in a coarse θ/ϕ map (the level-1 energy trigger data),

- longitudinal and transverse energy balance arising from this energy measurement,

- vertex along the beam axis using charge division information from the TEC.

Averaged over all level-1 triggers, the rejection rate is about 20% to 30%, such that the total rate after level-2 is typically less than 6 Hz. In case of a positive decision, the input to level-2 plus all level-2 results are forwarded to the level-3 trigger.

Level-3 Trigger

The level-3 trigger is based on three 3081/E emulators developed at SLAC and
CERN. Each 3081/E emulates a subset of the IBM 370 instruction set, and is
as powerful as an IBM 370/168 mainframe. Level-3 is the first point at which a
trigger decision can be made on the basis of the full detector readout. The accurate
digital data, with their finer granularity and higher resolution, allow thresholds to
be set tighter than in the lower level triggers. Events with multiple level-1 triggers
or luminosity trigger, are passed through untouched. The selection of good events is
based on:

- correlation of the energy deposited in the BGO and hadron calorimeters,

- reconstruction of muon tracks in the Z chambers,

- reconstruction of the vertex in the TEC chamber.

Level-3 trigger algorithms reject about 40% to 60% of all events, so that the final
output rate of the data acquisition system is about 2 Hz.

3.2.9 Data Taking in 1991

Two rather long development periods of the **LEP** machine, three weeks each, sepa-
rated the 1991 run into three data-taking periods called 91a, 91b and 91c.

Period 1991a

During the first period, 91a, which lasted from April until June 1991, **LEP** operated
exclusively at the energy corresponding to the Z° resonance peak, in order to let
the experiments collect as many Z°-decay events as possible with the initially small
luminosity. The start-up of **LEP** after the winter shut-down was rather slow in terms
of increasing luminosity and decreasing beam related background. Efforts to improve
luminosity and background conditions finally succeeded. The latter caused a lot of
problems in all four experiments during the first few weeks of running. For **L₃**, the
most important one was frequent trips of the TEC anode high voltage.

Period 1991b

The second period, 91b, lasted from July until September of 1991. In the middle of this period, the scan of the Z° lineshape in center-of-mass energy started. **LEP** was running smoothly and cleanly. Severe electronic noise in the BGO readout was created by servo motors correcting the temperature-induced motion of the support tube. Since the servos were operated only a few times a day for a few seconds, the loss of data was negligible. As soon as the reason was identified, the problem was cured.

Period 1991c

Period 91c lasted from October until the end of the run in November 1991. **LEP** continued the energy scan with much improved luminosity. Beam related background increased, because the carbon-fiber beam pipe developed minute cracks resulting in degraded vacuum in two interaction regions.

Chapter 4

Simulation and Reconstruction

Computer simulations of what is expected in an experiment are very valuable in order to perform the analysis of real data, i.e., to extract meaningful information about physical processes, and to perform precision measurements with small systematic errors. The analysis "chain" for high-energy physics experiments contains three different components:

1. Monte Carlo simulation,

2. event reconstruction,

3. physics analysis.

These steps within the overall framework of the experiment are illustrated in Figure 4.1.

This chapter illustrates the general processes of Monte Carlo simulation and event reconstruction, specializing on the needs of the L_3 experiment. Further technical comments on the simulation of the L_3 detector are given in Appendix E. The various levels of physics analysis which comprise the main work of this thesis are described in Chapters 5, 6, 7 and 8.

Event Generation
↓

Particles
↓

Detector Simulation

Accelerator
↓

Particles
↓

Detector

↘   ↙

Detector Event Data
↓   ↓

Event Reconstruction
↓   ↓

Hits, Tracks, Clusters, Jets, ...
↓   ↓
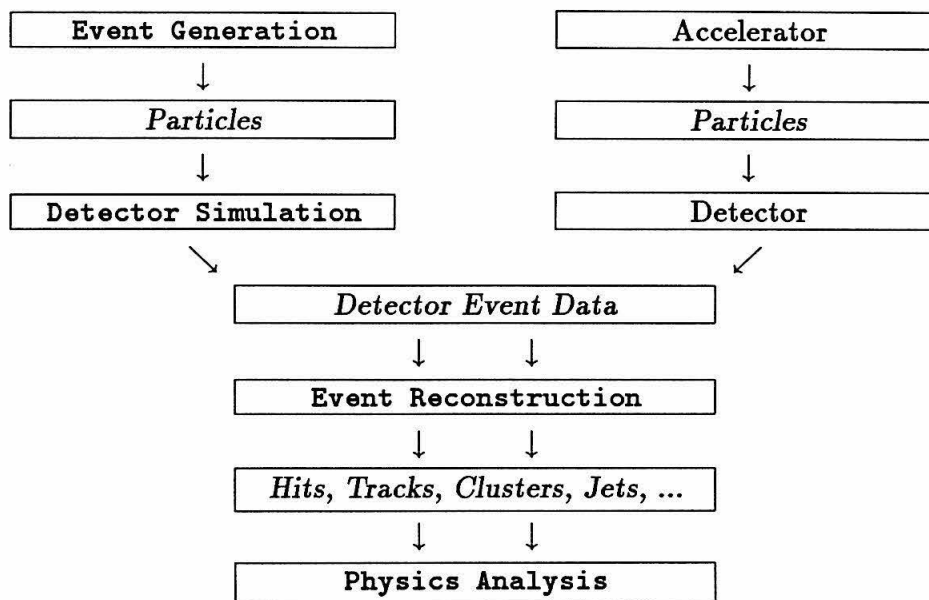
Physics Analysis

Figure 4.1: Analysis chain: both strings are needed for physics analysis resulting in precision measurements.

4.1   Monte Carlo Simulation

The process of Monte Carlo simulation in particle physics is usually split into two logically different tasks (Figure 4.1):

1. **event generation**, where the simulation of the interesting high-energy particle-physics processes which one aims at measuring is done, and

2. **detector simulation**, where the response of the detector to the interesting events is simulated.

In the world of simulation, event generators take the place of the accelerator, namely to produce events. Each simulated event contains the type, energy-momentum and space-time four-vectors of all particles in the final state. Subsequent detector simulation models the response of the specific measurement device to those particles

traversing the detector. The output of the detector simulation, the detector response, is identical in form to the readout of detector channels of a real event.

During the lifetime of an experiment, Monte Carlo simulation is used in many different ways:

- In the planning phase of a new detector, Monte Carlo simulations are used to find the optimal detector layout, and to set the performance requirements, so that the experiment can achieve the highest possible sensitivity to the physics of interest.

- Before and during data taking, Monte Carlo simulations give an estimate for the kind and number of events one may expect to find, in the context of both established, and candidate new theories.

- In all phases of the experiment, Monte Carlo simulations are one of the main sources of information to devise an analysis strategy, e.g., selection criteria, so that signal-to-background ratios are optimized.

- A necessary step in many analyses is the correction of the data for selection and detector effects, e.g., acceptance, efficiency and background contamination. These corrections, which only can be determined by Monte Carlo studies, have to be applied to the "raw" data in order to extract the physics signal.

- Comparison of the observed, uncorrected data with Monte Carlo predictions resulting from detector simulation is required: to assess the quality of the data, and to evaluate the performance and the level of understanding of the detector.

- Last but not least, Monte Carlo simulations provide a convenient framework to study and interpret the observed phenomena in terms of the fundamental underlying theory (MSM or other).

Added to this are analytical programs to calculate quantities of interest, such as cross sections and asymmetries. These programs do not allow one to implement arbitrary selection criteria, but are much faster than full Monte Carlo simulations

in calculating results of the same statistical precision. Programs to fit theoretical predictions to experimental data – corrected for detector effects by Monte Carlo – use these analytical programs to determine parameters of the theory. Analytical programs and fitting procedures used later in this thesis (Chapters 7 and 8) are described in detail in Appendix F.

4.1.1   Event Generation

Over the last six years, the 39 different event generators listed in Tables 4.1 and 4.2, have been collected to form an event-generator library [27] for $\mathbf{L_3}$ (EGL3). New generators are tested and evaluated for **LEP** physics and eventually interfaced to the $\mathbf{L_3}$ detector simulation program (see below). The EGL3 library contains generators for both **MSM** physics, as well as new physics beyond the Standard Model. The following describes briefly those generators relevant for Z° lineshape studies [28], and the interface between generators and the $\mathbf{L_3}$ detector simulation [27].

Generation of Hadronic Events

The generation of hadronic events (see Figure 4.2) is complicated by the fact that the fragmentation phase where the partons, quarks and gluons, are transformed into observable hadrons, cannot be described from first principles in QCD. Thus, different phenomenological models are used to describe the fragmentation. The two most popular schemes, called "string" and "cluster" fragmentation, are implemented in the JETSET [29] and HERWIG [30] generators, respectively.

The program JETSET 7.3 [29] is widely used to generate hadronic events in electron-positron annihilations. It contains the full $\gamma/Z°$ exchange together with first-order initial-state radiative corrections. The main part of the program, however, is less concerned with the electroweak part of the physics, and more with the further evolution of the $q\bar{q}$ pair once it is produced (Figure 4.2). The main ingredients here are (1) parton shower [28], which adds additional photons, gluons and light $q\bar{q}$ pairs to the original $q\bar{q}$ pair, and (2) string fragmentation [31], where the ensemble of partons produced in the shower is ordered with respect to the "color flow" to

MSM Physics Event Generators	
Channel	Generator
$e^+e^- \to e^+e^-(\gamma)$	BHABHA
	BABAMC
	BHLUMI
	EEG
	BHAGENE
$e^+e^- \to \mu^+\mu^-(\gamma)$	BHAGENE
	MUONMC
	DYMU3
	FPAIR
	KORALZ
$e^+e^- \to \tau^+\tau^-(\gamma)$	KORALZ + TAUOLA
$e^+e^- \to$ hadrons	ARIADNE
	JETSET
	PYTHIA
	NLLJET
	HERWIG
	COJETS
$e^+e^- \to \nu\bar{\nu}\gamma(\gamma)$	NNG
$e^+e^- \to \gamma\gamma(\gamma)$	GGG
	GGGSING
$e^+e^- \to f\bar{f}F\overline{F}$	DIAG36
	DIAG36ZN
	FERM4
$e^+e^- \to f\bar{f}F\overline{F}(\gamma)$	FERMISV
$e^+e^- \to e^+e^- +$ resonances	PC
$e^+e^- \to H^0 f\bar{f}(\gamma)$	HIGGSMOD
$e^+e^- \to W^+W^-(\gamma)$	GENTLE
$e^+e^- \to W^+W^-(\gamma), Z^\circ Z^\circ(\gamma)$	LEPWW

Table 4.1: MSM physics event generators used by the L_3 collaboration. Generators are grouped according to final states. See [27, 28] and references therein for detailed information on a specific event generator.

New Physics Event Generators		
Process		Generator
$e^+e^- \to ee^\star, e^\star e^\star$	Excited Electrons	ESTAR
$e^+e^- \to \mu\mu^\star, \mu^\star\mu^\star$	Excited Muons	MMSTR
$e^+e^- \to L_Q\overline{L}_Q$	Lepto-Quarks	LEPTOQUARK
$e^+e^- \to \tilde{q}\bar{\tilde{q}}(\gamma)$	SUSY Squarks	SQUARK
$e^+e^- \to h_0 A_0(\gamma)$	SUSY Higgs	SHIGGS
$e^+e^- \to \chi\chi^{(')}(\gamma)$	SUSY Neutralinos	STALINO
$e^+e^- \to L^+L^-, t\bar{t}, b'\bar{b}'$	New Seq. Fermions	TIPTOP
Special Purpose Generators		
Process		Generator
Heavy Flavor Decay		EURODEC
QED Decay Radiation		PHOTOS
Single Particle Production		SINGLEP
Cosmic Rays		COSMIC
Template		EGMC
Utilities		EGUTY

Table 4.2: New physics and special purpose event generators used by the L_3 collaboration. Generators are grouped according to final states. See [27, 28] and references therein for detailed information on a specific generator.

form a string, which subsequently fragments into hadrons. Most of the hadrons thus produced are unstable, so JETSET also is able to perform particle decays in great detail, optionally using EURODEC [32] to perform the decay of heavy flavors.

The HERWIG 5.6 [30] Monte Carlo offers an elaborate simulation of parton showers, and a simple model of hadronization phenomena. The parton shower algorithm accounts for correlations between the parton 4-momenta due to spin and and coherent emission of soft gluons, where the latter is based on the so-called coherent parton branching formalism [33]. The hadronization model employed is a cluster algorithm [34], which takes advantage of the preconfinement characteristic [35] of
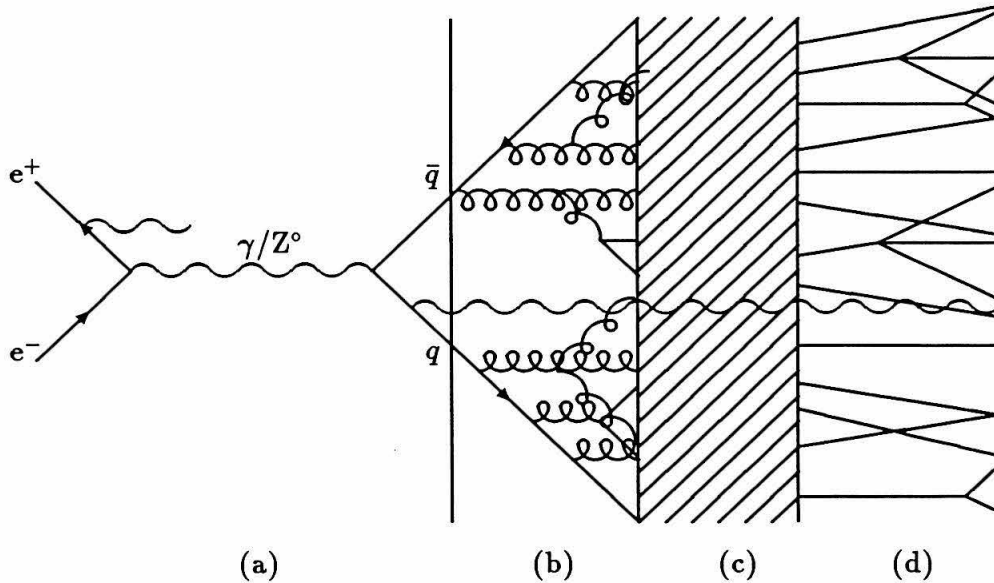
Figure 4.2: Generation of hadronic events: (a) electroweak part (photon radiation, e^+e^- annihilation to γ/Z°, $q\bar{q}$ production); (b) parton shower (quark and gluon emission); (c) fragmentation phase; (d) decay of unstable particles.

perturbative QCD. Preconfinement denotes the observation that a parton almost always finds itself nearby in phase space to a parton carrying the opposite color charge, whenever the partons have evolved from high to low virtuality, as in a parton shower. The two partons can therefore be collapsed into a low-mass colorless cluster, which has the properties of a hadronic resonance. Decays of unstable particles, optionally using EURODEC [32] for heavy flavor decays, are then performed, resulting in the final-state hadrons.

Generation of Four-Fermion Events

DIAG36 [36] is an event generator which simulates four-fermion final states in electron-positron annihilation, thus including the "classical" two-photon interactions $e^+e^- \rightarrow e^+e^-f\bar{f}$ (Figure 4.3).

Special care has been taken by L_3 in the case of hadronic two-photon interactions.
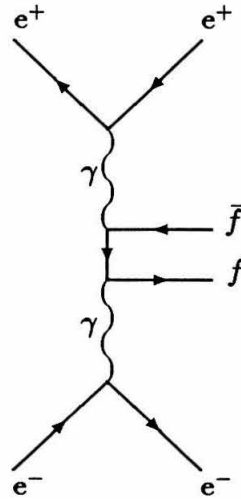
Figure 4.3: Two-photon process.

The matrix-element calculations are accurate for high-mass $q\bar{q}$-pair production, but due to the very low invariant mass of the additional fermion pair which occurs in most cases, hadrons rather than partons are produced. Form-factor effects thus come into play, which cannot be calculated from first principles. For this reason, a reweighting of the kinematic event distributions generated by DIAG36 in the $e^+e^- \rightarrow e^+e^-q\bar{q}$ mode is performed, in order to reproduce measurements at PETRA and PEP extrapolated to LEP energies.

FERMISV [37] is a recently written event generator for the four-fermion process $e^+e^- \rightarrow f\bar{f}F\overline{F}$, where f may also be equal to F in the case of electrons. It contains all the lowest-order diagrams involving γ and Z° propagators. Initial-state as well as final-state radiation has been included in a leading-log approach. Thus, the validity range of FERMISV ranges from 20 GeV to 200 GeV. The fact that this generator includes final-state radiation, which is important for four-lepton final states, makes FERMISV superior to any other four-fermion generator that is currently available.

Simulation of Lepton-Pair Production

During the last two years, a great deal of progress has been made in the theoretical understanding of small-angle Bhabha scattering ($e^+e^- \rightarrow e^+e^-(\gamma)$). The event generator BHLUMI 2.01 [38] was especially written for precision luminosity applications at **LEP** and **SLC**, at scattering angles of 10° and less. The quoted uncertainty of this generator due to missing higher-order terms is 0.25%. The generator uses $\mathcal{O}(\alpha)$ Yennie-Frautschi-Suura exponentiation [39] to sum up the contributions from soft virtual and real photons to all orders.

The program BABAMC [40] simulates radiative Bhabha scattering ($e^+e^- \rightarrow e^+e^-(\gamma)$) including first order radiative QED corrections, so that events contain up to one real bremsstrahlung photon. A complete lowest-order electroweak treatment is implemented. Therefore, the program can be used for both wide-angle Bhabha scattering, where the s-channel with Z° exchange dominates, and small-angle scattering, where the t-channel γ exchange dominates the total cross section.

The observation of events with a lepton pair and more than one hard photon prompted the need for a generator which is capable of simulating two hard photons. The event generator BHAGENE 3.0 [41] is able to simulate this kind of radiative scattering for $\mu^+\mu^-$ final states as well as for e^+e^- final states, where the t-channel has to be taken into account. This version of BHAGENE includes generation of up to three hard photons. Complete electroweak one-loop corrections and QED contributions with soft photon exponentiation are implemented. In principle, $\tau^+\tau^-(\gamma)$ final states could be simulated as well, but the implementation of τ decays depending on spin polarization is not available.

The event generator KORALZ 3.8 [42] is widely used to simulate the processes $e^+e^- \rightarrow f\bar{f}(\gamma)$, where f can by any fermion except an electron. For hadron production, JETSET (see above) may be used for further evolution of the $q\bar{q}$ pair. The main emphasis of KORALZ, however, is on production of $\mu^+\mu^-(\gamma)$ and especially $\tau^+\tau^-(\gamma)$ final states. In the latter case, a very elaborate library to decay τ's, TAUOLA is available (see below). KORALZ contains the YFS2 [43] multi-photon generator for initial-state radiation, and includes first-order QED corrections for final-state radia-

tion. A complete $\mathcal{O}(\alpha)$ electroweak treatment is implemented. Different electroweak libraries may be chosen, the **L₃** default being DIZET [44], which also is used within the analytical program ZFITTER [45].

The package TAUOLA 1.5 [46] performs the decay of τ leptons into the major final states of τ decay, namely: e, μ, π, ρ, a₁, K, K*, including the effect of the τ helicity on the decay kinematics. Also the decay of the vector resonances, ρ and a₁, to two and three pions, respectively, and of K* to Kπ is modeled according to the full matrix element. Hence, TAUOLA fully simulates the effect of τ polarization on the kinematics of the relevant decay chain, i.e., leading to only photons and scalar mesons in the final state. Decay modes of the τ lepton leading to 4, 5 or 6 pions are also simulated, but distributed according to (flat) phase space only (non-resonant decays). First-order QED radiative corrections in the leading-log approximation are implemented in all decay modes apart from the a₁ and the multi-pion mode. Table 4.3 lists all τ-decay modes simulated in TAUOLA.

Interface to the Detector Simulation

The events created by the generators described above consist of a list of particles with their identity code, energy-momentum vector, vertex of creation, and decay length for unstable particles. Special information is included, for example the helicity of charged τ leptons or the occurrence of $B^0 \leftrightarrow \bar{B}^0$ meson oscillation. For each particle, the pointer to its parent particle is recorded, so that it is possible to trace back the complete decay chain to the initial-state electron and positron. In addition, for all decaying particles, the decay length and pointers to the decay products are recorded.

Event generators such as JETSET contain elaborate libraries to decay unstable particles. Particles with an invariant lifetime of less than 10 mm/c have such a short lifetime that they can safely be decayed by the generator. However, particles with longer lifetimes (μ^-, π^-, K$^-$, K$_L^0$, K$_S^0$, n, Λ, Σ^-, Σ^+, Ξ^-, Ξ^0, Ω^-) and their antiparticles are left undecayed. Because these particles travel macroscopic distances before decaying, they must be treated within the specific detector set-up, i.e., during the detector simulation.

Tau-Decay Modes Simulated in TAUOLA			
Decay Mode of τ	Branching Fraction [%]	Matrix Element including Spin	Decay Radiation
$\tau^- \to e^- \bar{\nu}_e \nu_\tau$	18.5	yes	yes
$\tau^- \to \mu^- \bar{\nu}_\mu \nu_\tau$	18.0	yes	yes
$\tau^- \to \pi^- \nu_\tau$	11.2	yes	yes
$\tau^- \to \rho^- \nu_\tau$	23.0	yes	yes
$\tau^- \to a_1^- \nu_\tau$	15.6	yes	no
$\tau^- \to K^- \nu_\tau$	0.8	yes	yes
$\tau^- \to K^{*-} \nu_\tau$	1.5	yes	yes
$\tau^- \to \pi^- \pi^- \pi^+ \pi^0 \nu_\tau$	6.34	no	no
$\tau^- \to \pi^- \pi^0 \pi^0 \pi^0 \nu_\tau$	4.96	no	no
$\tau^- \to \pi^- \pi^- \pi^- \pi^+ \pi^+ \nu_\tau$	0.05	no	no
$\tau^- \to \pi^- \pi^- \pi^- \pi^+ \pi^+ \pi^0 \nu_\tau$	0.05	no	no

Table 4.3: Tau-decay modes simulated in TAUOLA. The first seven decay modes take into account the full matrix element including helicity. The four multi-pion modes are distributed according to (flat) phase space. The four multi-pion and the a_1 decay mode do not include radiative corrections in the decay.

All event information as described above is forwarded to the detector simulation, and subsequently to the event reconstruction program, in order to have this information available at the physics analysis stage [27].

4.1.2 Detector Simulation

The second step in the simulation chain consists of modeling the response of the measurement device, in this case the **L3** detector, to the final state particles produced by the event generators. The program package SIGEL3 written for this purpose is based on the general detector-simulation packages GEANT [47], GHEISHA [48] and on the detector-specific code describing the experimental setup and the detector response. This modular blocking makes it easy to incorporate improved knowledge

in the form of new code, e.g., new SIGEL3 versions, in one area without affecting any other part.

GEANT and GHEISHA

These packages perform the tracking of particles through a user-defined experimental setup, and simulate all relevant physical processes such as decay, energy loss, multiple scattering, showering and generation of secondaries. The results are dependent on the particle type being tracked and the detector materials encountered during each step of the tracking. GEANT, written at **CERN**, sets up the necessary framework, in which particle tracking and simulation of the detector response takes place. GHEISHA is a special program called by GEANT to simulate the complicated physics of hadronic interactions.

Experimental Set-up and Detector Response

The detector specific part of the simulation consists of the following two parts:

- XSL3 contains the code to describe the experimental setup L_3. This includes a description of the detector in terms of geometrical volumes filled with materials and embedded in magnetic fields. Whenever any detector component is changed or added, for example a new beam-pipe or a different position of the luminosity monitor, this description is updated accordingly.

- SIL3 contains the code to simulate the response of the L_3 detector, down to the level of the individual readout channels. The response of each channel is expressed in appropriate units, such as ADC or TDC counts, corresponding to the energy deposited by the final-state particles in the sensitive detector elements. Whenever new sensitive detector elements are added, for example the BGO endcap calorimeters, this description is updated accordingly.

Description of the Simulation Process

As the first step in simulating an event, the kinematic configuration of the event created by the generator is analyzed. The primary event vertex is smeared and shifted according to the observed size and offset of L_3's interaction region from the origin. Using the decay length of decaying particles, secondary vertices are determined taking into account the shifted position of the primary event vertex as well as bending of the path of decaying charged particles in the magnetic field of the detector. The event record is then analyzed for final-state particles within the overall detector volume, which are tracked one after the other, including the secondary particles generated during decay or showering, until they are either absorbed or leave the experimental setup.

For detector volumes declared sensitive by the user, information is stored, whenever particles or secondaries enter this volume during tracking. Usually, this information, called "hits" in the GEANT jargon, contains the particle type, coordinates, time of flight, energy deposited, etc. Hits are accumulated during the tracking phase for all sensitive volumes encountered by particles.

The simulation of the detector response takes place after the tracking of all particles has been completed. The accumulated hits of each sensitive detector element are retrieved in order to simulate the response in a realistic way, where the energies in a detector cell are summed, and the times corresponding to multiple hits in a *cell* are computed in a way that mimics the actual electronics. The output of this phase, called "digitization," resembles the actual raw data of an event recorded in the L_3 detector, i.e., the data after having applied basic calibrations.

Simulation of Detector Imperfections

For precision measurements with accuracies at and below the 1% level, the time dependence of the detector status and performance also must be taken into account. Although logically this is still part of Monte Carlo simulation, it is deferred to the very first step of event reconstruction, due to timing and practicality reasons. Detector simulation is a computing-time-intensive job, which can take a factor of 300 more

time than event reconstruction. Hence, in order to make multiple use of the simulated events possible, the Monte Carlo simulation adopts a perfect detector model. One is then free to impose various kinds of detector imperfections on the same set of events, in order to study their effect in detail.

During reconstruction, the Monte Carlo event is assigned a time and date such that all events are distributed over a certain data-taking period with the correct luminosity weighting. The actual detector status at that very moment is taken into account when calculating inefficiencies. For this purpose, the status of each subdetector, for example the high-voltage status of the TEC wires, dead or noisy BGO crystals, defective towers in the hadron calorimeter or disconnected drift cells in the muon chambers, is recorded in the corresponding subdetector database at the beginning of each data-taking period, and as soon as there is a change. Corresponding action such as "killing" of dead channels is taken accordingly, before starting the reconstruction of an event. Figure 4.4 shows the effect of this so-called "real" detector simulation on the distribution of the energy of the second most energetic bump in the BGO electromagnetic calorimeter and the second most energetic muon candidate.

For every lineshape analysis, this method of simulating the time dependent detector imperfections has been applied to the Monte Carlo simulations of both signal and background events. When it turns out that the degradation in detector performance leads to unrecoverable systematic biases, the corresponding real data and luminosity is declared bad ("bad runs"), and is dropped from the analysis.

4.2   Event Reconstruction

At this point, real data recorded by the detector and simulated data exist in the same format. From this stage of the analysis, they are treated alike: the same program, REGEL3, is used to reconstruct both simulated events and real events recorded with the L_3 detector. The process of event reconstruction transforms the digitized raw data read out from detector channels into fewer, higher-level objects, corresponding to particles or groups thereof, such as tracks, clusters, jets, etc. Physics analysis takes

Real / ideal detector
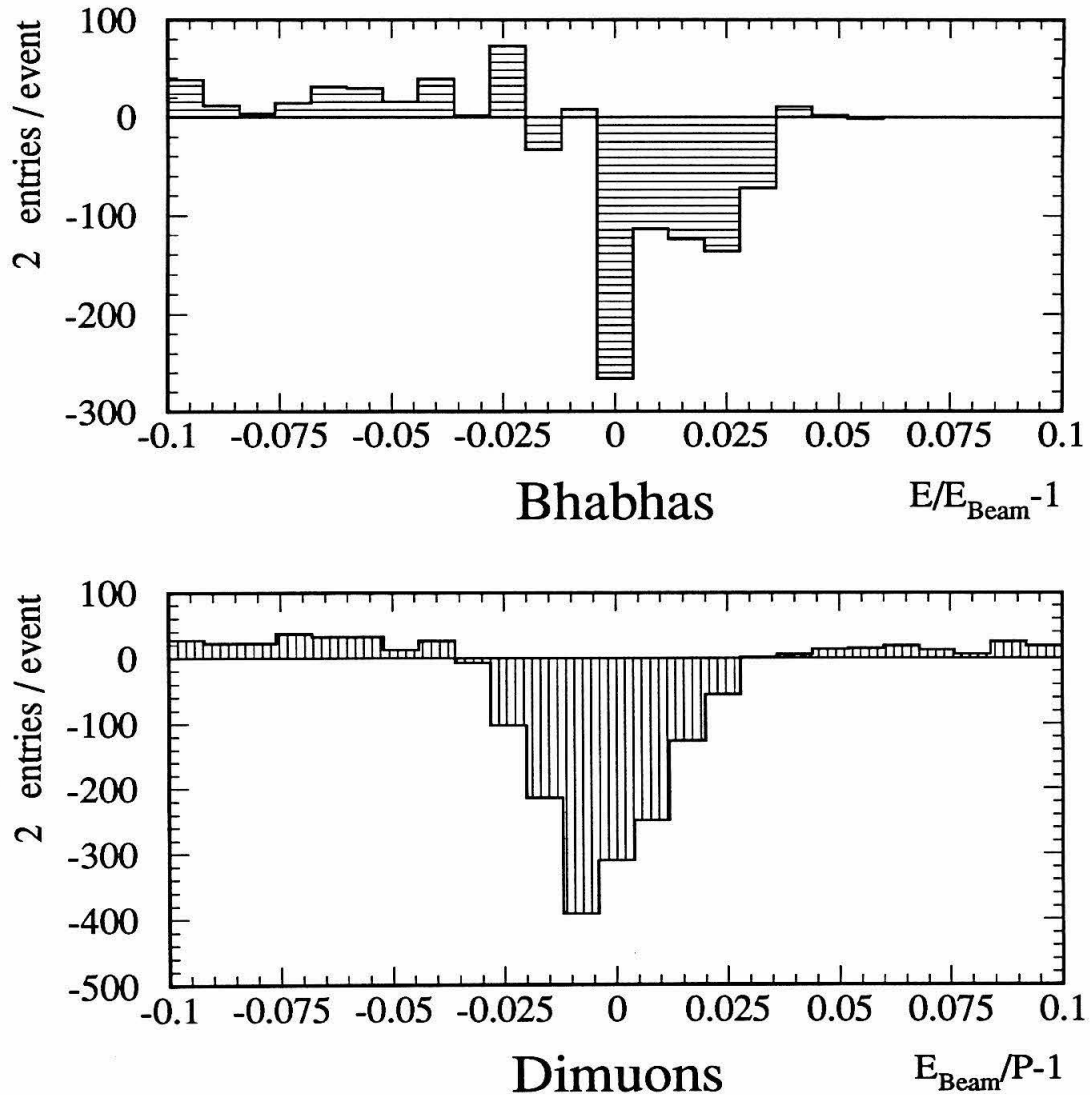
Figure 4.4: Effect of the "real" detector simulation on the distribution of energies of the two most energetic energy deposits in the BGO electromagnetic calorimeter (top) and the two most energetic muon candidates reconstructed in the muon spectrometer (bottom). The difference between real and perfect ideal detector simulation is shown, where the Monte Carlo luminosity used corresponds to the peak luminosity of 1991. Events have passed no cuts except an 0.25 rad acollinearity requirement.

place by comparing simulated and real events in terms of these high-level objects, in order to extract information about the underlying physics.

In the following, some standard quantities within the L_3 reconstruction context, which are used in this analysis, are listed. Specific criteria used in selecting or counting these quantities also are given.

- Tracks:

  Tracks are constructed out of hits in the central tracking chamber TEC. A fit is performed in order to extract from the coordinates of the hits the parameters of each track, including the curvature $1/R$ ($R \propto p_\perp$), distance of closest approach (DCA) of the track to the (fill) vertex, and angles ϕ and θ of the track at the vertex. The principal track parameters typically considered are:

  - number of hits on the track (total, outer or inner TEC),

  - length of the track,

  - DCA of the track,

  - momentum of the track (transverse or total),

  - χ^2 of the track fit.

  In the context of this analysis (Chapter 6), a TEC track must satisfy all the following special requirements in order to be counted: at least 20 hits on the track, track length (span) in radial direction at least 30 wires, at most a DCA of 20 mm, and a minimal transverse momentum of 50 MeV.

- Bumps:

  The map of crystals of the BGO calorimeter in θ and ϕ is searched for local maxima in energy depositions, which form the "seeds" for constructing bumps. In an iterative procedure, crystals with energy are assigned to the nearest bump, whenever they are geometrically connected to it and are not closer to any other bump. Typical quantities of interest of the bumps constructed in this way are:

    − number of crystals in the bump,

    − energy of bump, of central crystal, in n by n matrices around the central crystal (n odd),

    − ratio of the energies measured in the 3 by 3 and 5 by 5 crystal matrix around the central crystal,

    − χ^2 of the fit for electromagnetic shower shape,

    − second moments of the energy distribution.

- Clusters:

  Matching bumps with geometrically connected hits in the hadron calorimeter located behind BGO bumps leads to a formation of calorimetric clusters. Typical quantities to be considered are:

      − for the bump part: all of the bump quantities listed above,

      − energy (BGO, hadronic or total),

      − shower shape of the hadronic part.

  In the context of this analysis (Chapter 6), a cluster must satisfy at least one of the following three requirements in order to be counted: BGO energy larger than 0.1 GeV and hadron calorimeter energy larger than 0.9 GeV, or BGO energy larger than 0.1 GeV with more than one crystal inside the bump, or, in the case there is no BGO energy, at least 0.5 GeV hadron calorimeter energy.

- Muons:

  Tracks reconstructed in the muon chambers, having at least two P segments reconstructed in the precision chamber layers, so that a momentum measurement is possible, are called muon candidates, or muons for short (although there is some probability that these tracks might have been created by punch-through or sail-through). Relevant track parameters are:

      − number of segments on the track (P or Z chamber),

      − momentum of the track (transverse or total),

– DCA after back tracking,

– time of flight measured by the associated scintillator.

• Jets:

Jets are reconstructed from calorimetric clusters and muons. The standard algorithm used is based on geometrically close energy depositions within the L_3 detector. In an iterative procedure, the most energetic cluster not yet assigned to a jet is taken as a seed, and neighboring clusters are attached to it to form a jet. Characterizing quantities are:

– energy of the jet (total, calorimetric or muon),

– thrust [49] of the jet,

– invariant mass of the jet,

– multiplicity of the jet (cluster, track or muon).

The general reconstruction program calculates all these quantities and selectively many more, thus providing a flexible framework for data analysis.

Chapter 5

Measurement of Luminosity

Accurate measurement of the integrated luminosity $\mathcal{L}$ is crucial for precise cross section determinations. The measurement of a cross section within a fiducial volume a proceeds via the basic formula:

$$\sigma(a) = \frac{N}{\epsilon \mathcal{L}} \quad , \tag{5.1}$$

where N denotes the background-corrected number of selected data events within the fiducial volume. The overall efficiency to detect events within the fiducial volume, including detector and trigger efficiency as well as selection efficiency, is denoted by ϵ. The two quantities N and ϵ together with their errors are *discussed in detail in* Chapter 6 in the special circumstance of $\tau^+\tau^-(\gamma)$ production. This chapter describes the determination of the absolute integrated luminosity $\mathcal{L}$ [50, 51, 52].

5.1 Basic Principles

In principle, the integrated luminosity $\mathcal{L}$ can either be calculated from machine parameters or measured by an experimental setup. **LEP** machine parameters determine the instantaneous luminosity L:

$$L = \frac{\mathrm{d}\mathcal{L}}{\mathrm{d}t} = fn\frac{N_1 N_2}{A} \quad , \tag{5.2}$$

where f is the revolution frequency ($f = 11$ kHz), n is the number of bunches of either beam ($n = 4$), A is their cross-sectional area ($A \approx 4 \cdot 10^{-4}$ cm^2), assuming complete overlap, and N_i is the number of particles of a bunch ($N_i \approx 4 \cdot 10^{11}$). However, neither the beam cross-sectional area and overlap, nor the number of particles of a bunch is known with sufficient accuracy, i.e., on a sub-percent level.

A better determination of the luminosity arises from direct measurements. Although **LEP** beam orbit monitors exist and are used for machine tuning, their results do not take into account interaction-region-specific deviations and detector-specific dead times. Therefore, it turns out to be much more reliable and straightforward to let the detector itself measure the luminosity at its interaction region, so that both effects are automatically taken into account. Rewriting Formula 5.1 for a particular reaction e, the absolute luminosity $\mathcal{L}$ is given by:

$$\mathcal{L} = \frac{N_e}{\epsilon_e \sigma_e(a)} \quad , \tag{5.3}$$

where $\sigma_e(a)$ is the cross section of the reaction e within the fiducial volume a. Putting this expression back into Formula 5.1, one sees that the determination of an *unknown* cross section is nothing else but measuring it in units of a *known* cross section.

It is obviously advantageous to use a well known interaction with a high cross section $\sigma_e(a)$ to keep both the systematic error, e.g., the theoretical error on $\sigma_e(a)$, and the statistical error of N_e as small as possible. At e$^+$e$^-$ colliders, the reaction typically used is Bhabha scattering (e$^+$e$^- \to$ e$^+$e$^-(\gamma)$) measured at very small scattering angles θ, where the Bhabha cross section grows rapidly with decreasing θ:

$$\frac{\mathrm{d}\sigma_e(\theta)}{\mathrm{d}\theta} \propto \frac{1}{\theta^3} \quad . \tag{5.4}$$

This sharp rise is due to the t-channel exchange of a γ (Figure 5.1), which is a pure QED process. Thus, the measured luminosity is nearly completely independent of the Z$^\circ$, which is to be studied. On the peak of the Z$^\circ$ resonance, the effect of the Z$^\circ$ on the e$^+$e$^- \to$ e$^+$e$^-(\gamma)$ cross section measured in the **L$_3$** luminosity monitor is below 0.05%. It rises to 0.2% to 0.3% at energies 1 GeV to 2 GeV away from the peak (effect of the γ/Z$^\circ$ interference).
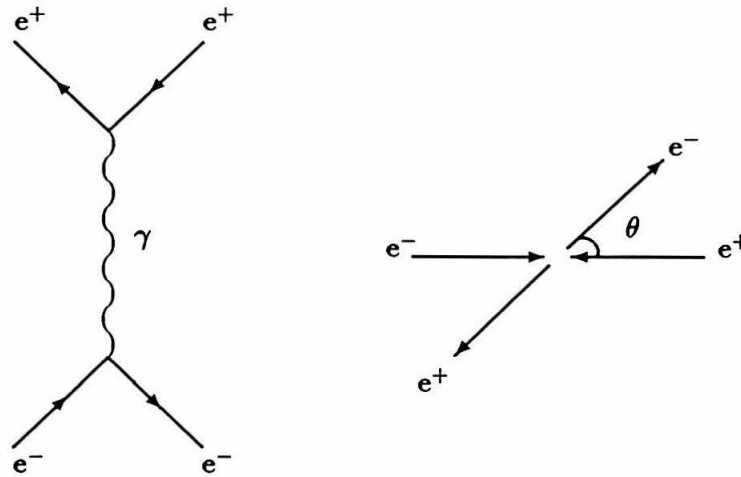
Figure 5.1: Bhabha t-channel scattering, and definition of scattering angle θ.

5.2 Event Selection

The selection of luminosity Bhabha events is based on energy depositions in the calorimetric part of the luminosity monitor described in section 3.2.3. Figure 5.2 shows a Bhabha event in the two BGO calorimeters of the luminosity monitor.

Most events accepted by the luminosity trigger (see section 3.2.8) contain just one bump in each of the two calorimeters. Additional bumps arise from spurious beam-gas interactions and genuine radiative events. To differentiate between the two cases, bumps are summed up vectorially in decreasing energy order. The summation is stopped when the difference between the energy of the resulting cluster and the beam energy is minimal. The event selection is based on the clusters constructed in this way. The criteria used for selection of luminosity events are:

1. The reconstructed impact point of the cluster on one side (see below) has to be at least one BGO crystal size away from the calorimeter edges:

$$84.4 \text{ mm} < R_{xy} < 176.2 \text{ mm} \tag{5.5}$$
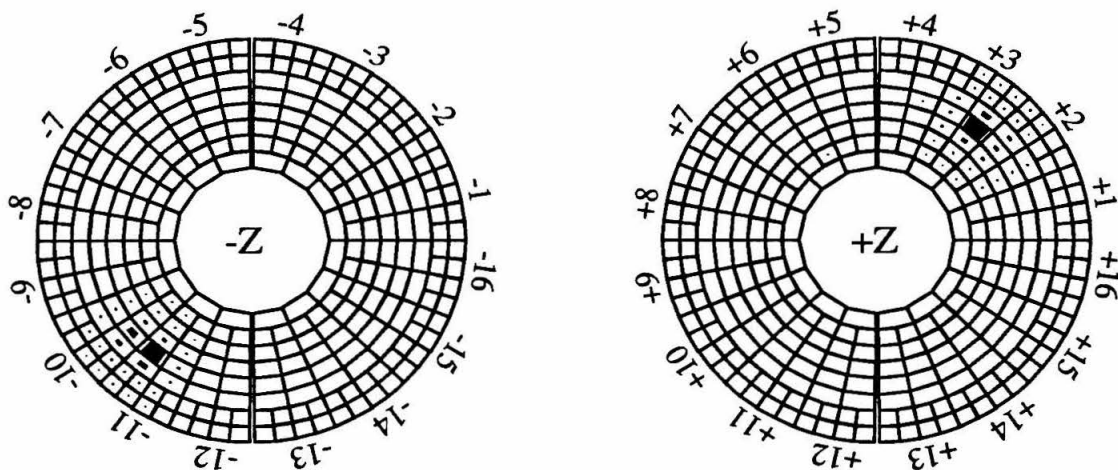
Figure 5.2: Bhabha event recorded in the calorimeters of the luminosity monitor. Only energy deposits exceeding 250 MeV are shown. The size of each dark box is proportional to the energy deposit in the corresponding crystal.

$$|\phi - 90°| > 11.25° \tag{5.6}$$

$$|\phi - 270°| > 11.25° \quad , \tag{5.7}$$

where R_{xy} is the reconstructed transverse distance of the shower maximum to the beam axis.

Precise knowledge of the fiducial volume is essential, because the cross section varies rapidly with the polar angle θ, as discussed above. Two samples of Bhabha events are selected, which differ by the application of the tight fiducial volume cut described above *either* to the cluster on the $+z$ side *or* to the one on the $-z$ side. The final luminosity is determined by averaging the values obtained from the two Bhabha samples. Effects of misalignments of the luminosity BGO calorimeters, with respect to each other and to the vertex, are largely canceled out in the average.

2. The reconstructed energy E_{max} of the most energetic cluster must be larger than 80% of the beam energy E_{Beam}; the energy E_{min} of the other cluster has

to be larger than 40% of the beam energy:

$$E_{max} > 0.8\ E_{Beam} \tag{5.8}$$

$$E_{min} > 0.4\ E_{Beam}\ . \tag{5.9}$$

The requirement of a high energy for the first cluster suppresses random beam-gas interactions, whereas the requirement of a low energy for the second cluster ensures that radiative events are retained. Energy losses due to dead crystals are recovered by a fit to the shower shape.

3. The acoplanarity angle of the two clusters must be less than 10°:

$$|\Delta\Phi - 180°| < 10°\ . \tag{5.10}$$

The requirement of coplanarity further suppresses beam-related background. Moreover, the sidebands of the coplanarity distribution for events having both energies E_{max} and E_{min} more than 5% different from the beam energy are used to subtract the remaining background ($< 0.1\%$) in the signal region on a fill-by-fill basis.

For example, two-photon events $e^+e^- \rightarrow e^+e^- f\bar{f}$ with a double tag in the luminosity monitor constitute a small background, which is generally uniform in $\Delta\Phi$ and therefore is accounted for by the background subtraction procedure using the $\Delta\Phi$ sidebands.

Figure 5.3 shows the distributions in the quantities used for selection, compared with Monte Carlo predictions.

Since the event selection is based on calorimetric quantities only, the contribution of the $e^+e^- \rightarrow \gamma\gamma(\gamma)$ process (0.02%) has to be added to the theoretical cross section. The visible cross section at the Z° resonance is about 88.5 nb, i.e., about three times the hadronic peak cross section. Hence the statistical error of the luminosity measurement is smaller than that of any Z° decay channel.

Luminosity selection variables
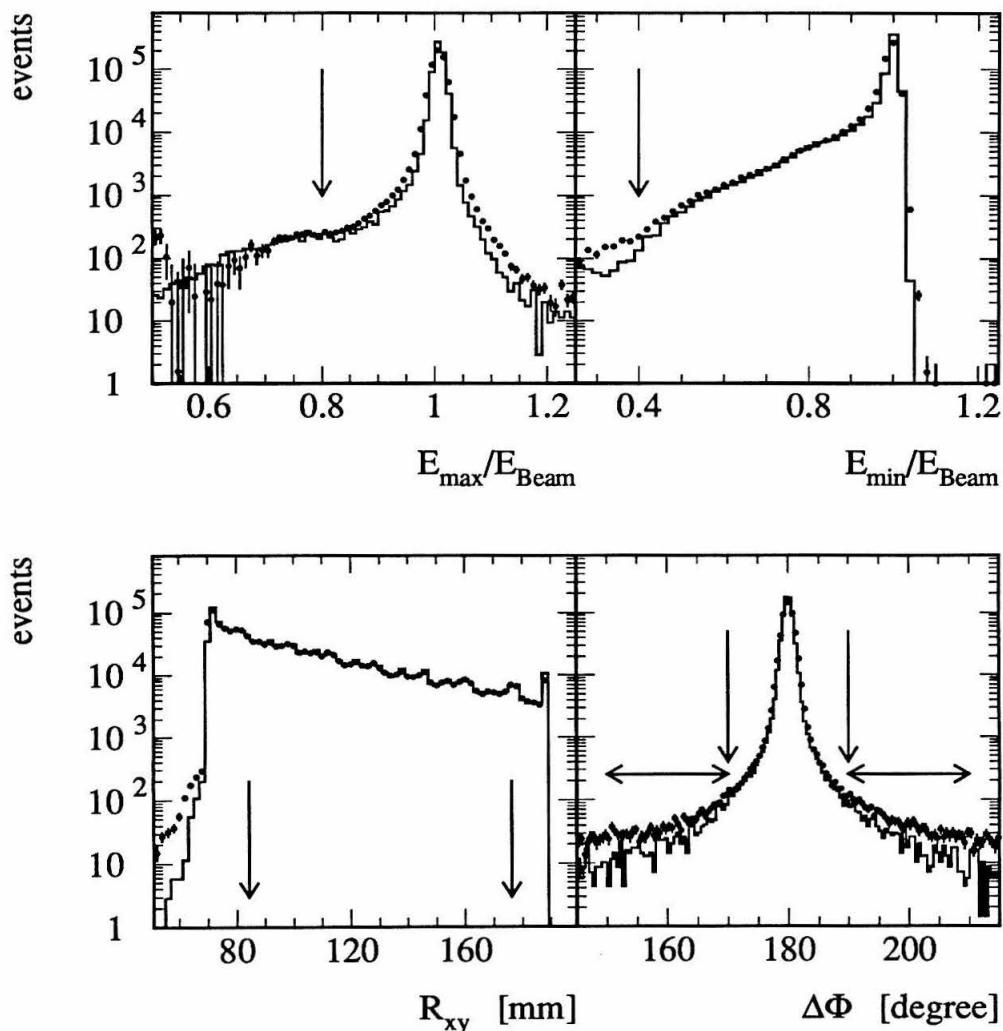
Figure 5.3: The energy of the most (E_{max}) and second most (E_{min}) energetic cluster, the transverse distance R_{xy} of the centroid of the energy cluster with respect to the beam axis, and the coplanarity ($\Delta\Phi$) are shown for Bhabha event candidates (dots with error bars) compared to the Monte Carlo simulation (solid line). All cuts have been applied except the cuts, shown as vertical arrows, in the variable plotted. The wiggles in the distribution of R_{xy} are due to the changing position resolution across the face of each crystal. Horizontal arrows indicate the sidebands of the coplanarity distribution used for background subtraction.

5.3 Systematic Errors

The total error of the luminosity enters in every cross section measurement, and therefore must be treated as a correlated systematic error when combining these measurements to extract the parameters of the Standard Model. It is therefore crucial to keep this error as small as possible. Table 5.1 provides a breakdown of all contributions to the total systematic error of 0.6% in the luminosity measurement.

Systematic Errors in Luminosity Measurement	
Source	Systematic Error $\delta\mathcal{L}/\mathcal{L}$ [%]
Luminosity Trigger	< 0.01
Geometry of the Calorimeters	0.4
Bhabha Event Selection Criteria	0.3
Background Subtraction	< 0.01
Monte Carlo Statistics	0.1
Total Experimental Systematic Uncertainty	0.5
Theoretical Systematic Uncertainty	0.3
Total Systematic Uncertainty	0.6

Table 5.1: Contributions to the systematic uncertainty in the luminosity measurement. The total systematic uncertainty is the quadratic sum of the contributions listed above.

Experimental Uncertainties

The effect of changes in the selection requirements on the integrated luminosity $\mathcal{L}$ is shown in Figure 5.4. The experimental uncertainties are dominated by the geometrical positioning accuracy of the calorimeters, and the accuracy in position reconstruction due to the steep variation of the Bhabha cross section with the scattering angle. First, the error on the absolute position of the calorimeters with respect to

Luminosity systematic errors
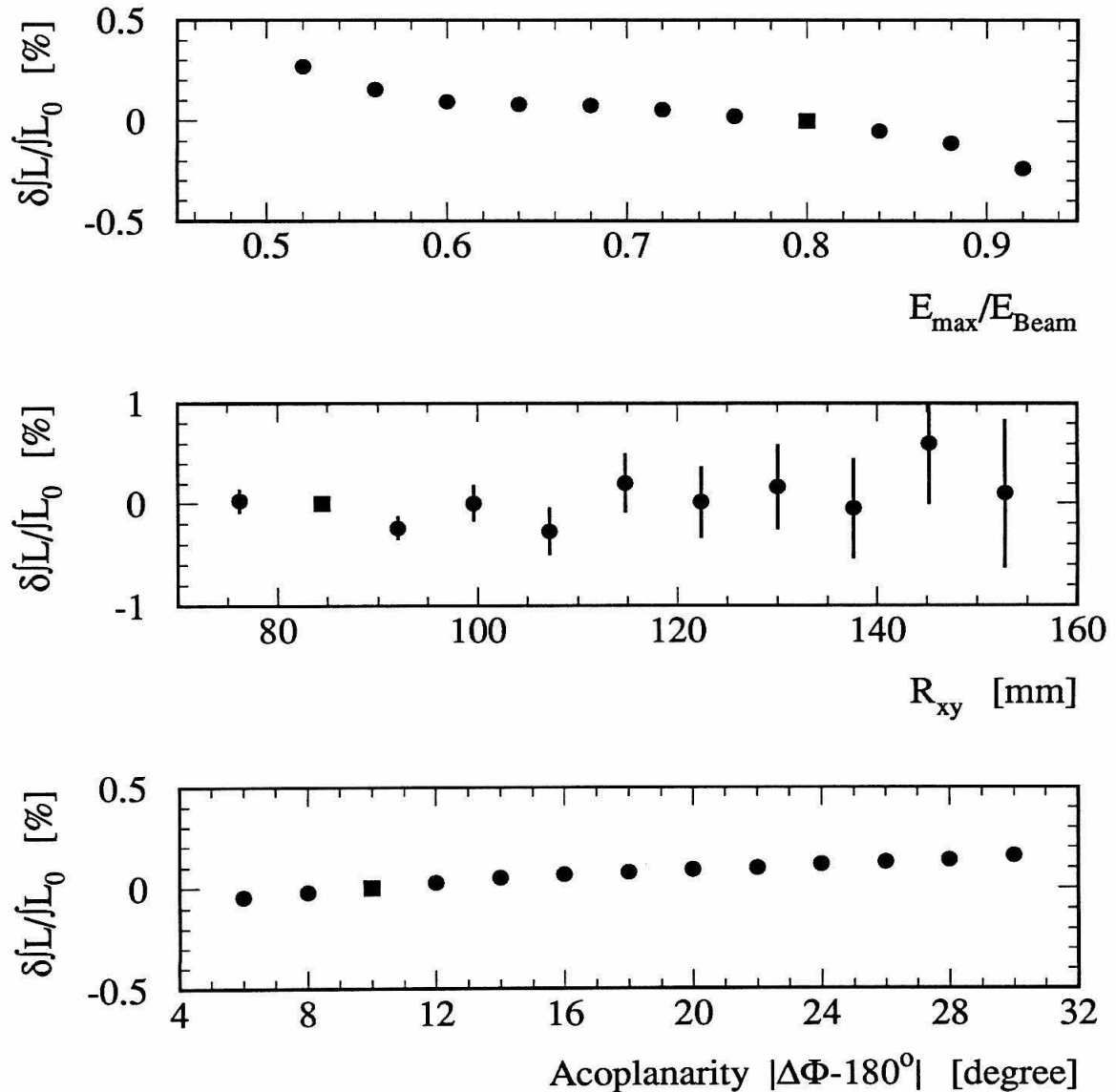
Figure 5.4: The relative change in integrated luminosity as a function of: the energy cut on E_{max}/E_{Beam}, the smaller fiducial volume cut on R_{xy}, and the acoplanarity cut on $|\Delta\Phi - 180°|$. Nominal cut values are indicated as squares.

the beam axis translates into an error on the luminosity of 0.4%. Second, systematic differences between the position reconstruction in data and Monte Carlo lead to a systematic error in the Bhabha event selection criteria of 0.3%.

The luminosity detector upgrade planned for 1993 **LEP** run (see Appendix D), with planes of silicon microstrips to define the acceptance more accurately, will reduce these two dominating contributions to the systematic error. The goal is to reach a total experimental uncertainty on the luminosity measurement of less than 0.2%.

Theoretical Uncertainties

The theoretical cross section is estimated by the two Monte Carlo programs **BABAMC** and **BHLUMI** (see Chapter 4). The theoretical uncertainty of 0.5% in 1990 has been reduced to 0.3% due to the availability of new calculations in Bhabha scattering, e.g., in the form of the new version of the **BHLUMI** event generator.

5.4 Experimental Results of the Luminosity Measurement

The 1990 and 1991 data-taking periods started out with **LEP** running at a center-of-mass energy corresponding to the peak of the Z° resonance. During the second half of each period, a scan of the Z° lineshape at seven energy points was performed, where each fill of the **LEP** machine at an off-peak energy was followed by a fill on the peak. The distribution of luminosity over the seven energy points in the 1990 and 1991 lineshape scan is shown in Table 5.2.

In total, L_3 collected about 19.2 pb^{-1} of integrated luminosity in 1990 and 1991, about 60% of it on the peak of the Z° resonance, and the rest roughly evenly distributed over the six off-peak energy points. Note, that only the nominal energies of the peak and the -1 point of both years coincide. The 1991 energies were chosen to optimize the probability to obtain polarized beams, which are used for a precise **LEP** energy calibration (see Appendix C).

Luminosity Collected by L_3 in 1990 and 1991				
Year	1990		1991	
Energy Point	Nominal Energy $\sqrt{s}$ [GeV]	Luminosity $\mathcal{L}$ [nb^{-1}]	Nominal Energy $\sqrt{s}$ [GeV]	Luminosity $\mathcal{L}$ [nb^{-1}]
-3	88.25	399	88.50	783
-2	89.25	551	89.50	862
-1	90.25	368	90.25	794
Peak	91.25	3056	91.25	8636
$+1$	92.25	400	92.00	737
$+2$	93.25	525	93.00	759
$+3$	94.25	490	93.75	833
Sum		5790		13403

Table 5.2: Luminosity collected by L_3 in 1990 and 1991, at each of the seven center-of-mass energy points. The total systematic error is estimated to be 0.6%.

Chapter 6

Data Analysis

In the first part of this chapter, the selection of $e^+e^- \to \tau^+\tau^-(\gamma)$ events using the $\mathbf{L_3}$ detector is described. The aim of the selection is to obtain a clean sample of events, with high acceptance for the signal and with background contamination from other processes as small as possible. Using this clean sample of $e^+e^- \to \tau^+\tau^-(\gamma)$ events, one can then proceed to determine the production cross section and forward-backward charge asymmetry, and the corresponding statistical and systematic errors. This is presented in the second and third part of this chapter.

6.1   Selection of $\tau^+\tau^-(\gamma)$ Events

Since the charged τ lepton is a short lived unstable particle (lifetime $\tau_\tau = 0.3$ ps resulting in $\beta\gamma\tau_\tau = 2.3$ mm/c at 45 GeV), it decays before it can leave the beam pipe surrounding the interaction region, where it has been produced. As can be seen from Table 6.1, which lists the main τ-decay modes and branching fractions, τ's manifest themselves in vastly different ways in the detector. They appear as minimum-ionizing muons, single electrons, single charged hadrons or few light charged and neutral hadrons, possibly accompanied by radiative photons. Figures 6.1 and 6.2 show two examples of $e^+e^- \to \tau^+\tau^-(\gamma)$ events in the various subdetectors of $\mathbf{L_3}$, where one τ decays to a μ, which is measured in the muon chambers, and the other to three charged hadrons measured in the calorimeters.
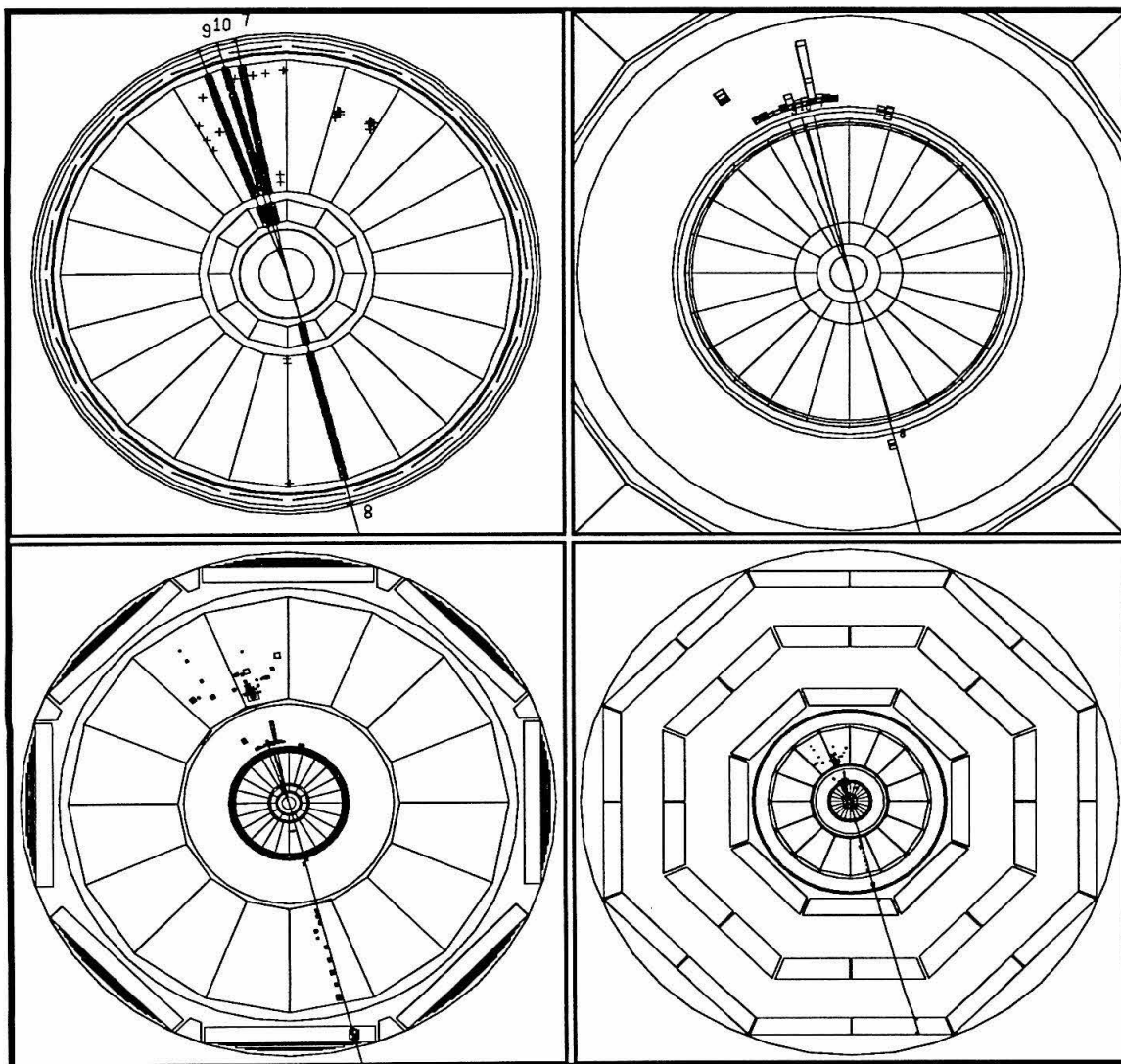
Figure 6.1: End view of a $\tau^+\tau^-(\gamma)$ event seen in the various subdetectors of L_3: central tracking chamber TEC, BGO electromagnetic calorimeter, hadron calorimeter, and muon spectrometer.
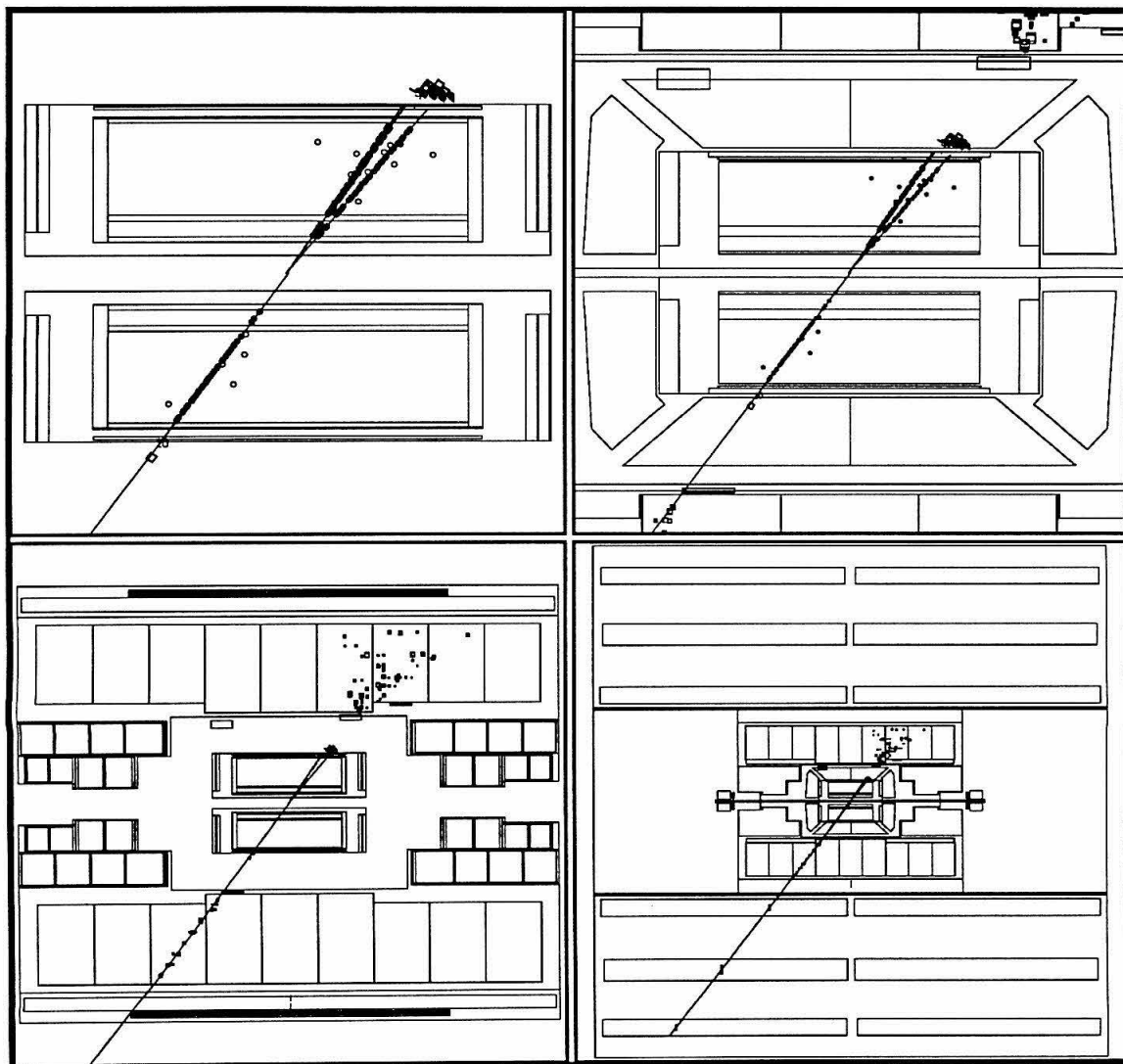
Figure 6.2: Side view of another $\tau^+\tau^-(\gamma)$ event seen in the various subdetectors of $\mathbf{L_3}$: central tracking chamber TEC, BGO electromagnetic calorimeter, hadron calorimeter, and muon spectrometer.

Branching Fractions of τ Decays	
Decay Mode of τ	Branching Fraction [%]
$\tau \to e\bar{\nu}_e\nu_\tau$	17.93 ± 0.26
$\tau \to \mu\bar{\nu}_\mu\nu_\tau$	17.58 ± 0.27
$\tau \to \pi\nu_\tau$	11.6 ± 0.4
$\tau \to \rho\nu_\tau$	24.0 ± 0.6
$\tau \to a_1\nu_\tau$	15.9 ± 1.6
$\tau \to \omega\pi\nu_\tau$	1.6 ± 0.5
$\tau \to K^*\nu_\tau$	1.42 ± 0.18
$\tau \to K\nu_\tau$	0.67 ± 0.23
$\tau \to K\pi\pi\nu_\tau$	$0.22^{+0.16}_{-0.13}$
$\tau \to KK\pi\nu_\tau$	$0.22^{+0.17}_{-0.11}$

Table 6.1: Branching fractions of main τ-decay modes [11].

Nevertheless, the aim is to select $e^+e^- \to \tau^+\tau^-(\gamma)$ events using all possible decay modes of the τ lepton. Since τ decays are always accompanied by one or two neutrinos, which are invisible in the detector, the measured energy in $e^+e^- \to \tau^+\tau^-(\gamma)$ events can take on any value down to zero. All these aspects make an efficient selection of $e^+e^- \to \tau^+\tau^-(\gamma)$ events with a low background level challenging, compared to other charged lepton channels and to hadronic events at the same center-of-mass energy.

For center-of-mass energies around 91 GeV, the pair-produced τ leptons are highly boosted ($E_{\text{Beam}} \gg m_\tau$), so that their decay products are rather tightly collimated within a cone of a few degrees. This is in contrast to τ-pair production at lower energies, especially near production threshold. In addition, whereas the multiplicity of τ events stays constant, that of hadron events rises with increasing center-of-mass energy. Hence, a discrimination of τ events from hadron events using multiplicity becomes more efficient at high center-of-mass energies.

6.1.1 Summary of Selection Criteria

The selection criteria used are based on information obtained from all subdetector components of **L$_3$**: central tracking chamber (TEC), electromagnetic (BGO) and hadronic calorimeters, scintillation counters and muon chambers. The strategy to select $e^+e^- \rightarrow \tau^+\tau^-(\gamma)$ events follows roughly a three step approach. First, a geometrical fiducial volume is identified, which for this selection is the barrel region of the **L$_3$** detector. Second, certain minimal quality requirements are imposed on a candidate event, which assure that the event arises from a Z° decay. In a third step, the actual $e^+e^- \rightarrow \tau^+\tau^-(\gamma)$ events are selected by exclusion of unwanted Z° decays, the idea of which is shown in Figure 6.3. The aim is to achieve as high a selection efficiency as possible, while keeping the background low.

In general, the selection criteria are formulated in such a way as to reduce the sensitivity of their efficiency to the actual **LEP** center-of-mass energy, whenever possible. This is achieved by formulating the selection criteria, which concern the energies deposited by primary Z° decay products, as fractions of the actual beam energy E_{Beam}.

The selection criteria are summarized below, followed by a detailed discussion of each criterion in the subsequent sections.

- Fiducial volume:

  - The polar angle Θ_{thrust} of the event axis (thrust axis) has to lie in the barrel region:

$$|\cos \Theta_{\text{thrust}}| < 0.73 \quad . \tag{6.1}$$

- Minimal requirements:

  - The total energy of the two most energetic jets must be larger than 7 GeV and 3 GeV, respectively:

$$E_{\text{Jet 1}} > 7 \text{ GeV} \tag{6.2}$$

$$E_{\text{Jet 2}} > 3 \text{ GeV} \quad . \tag{6.3}$$

Distribution of Z decays
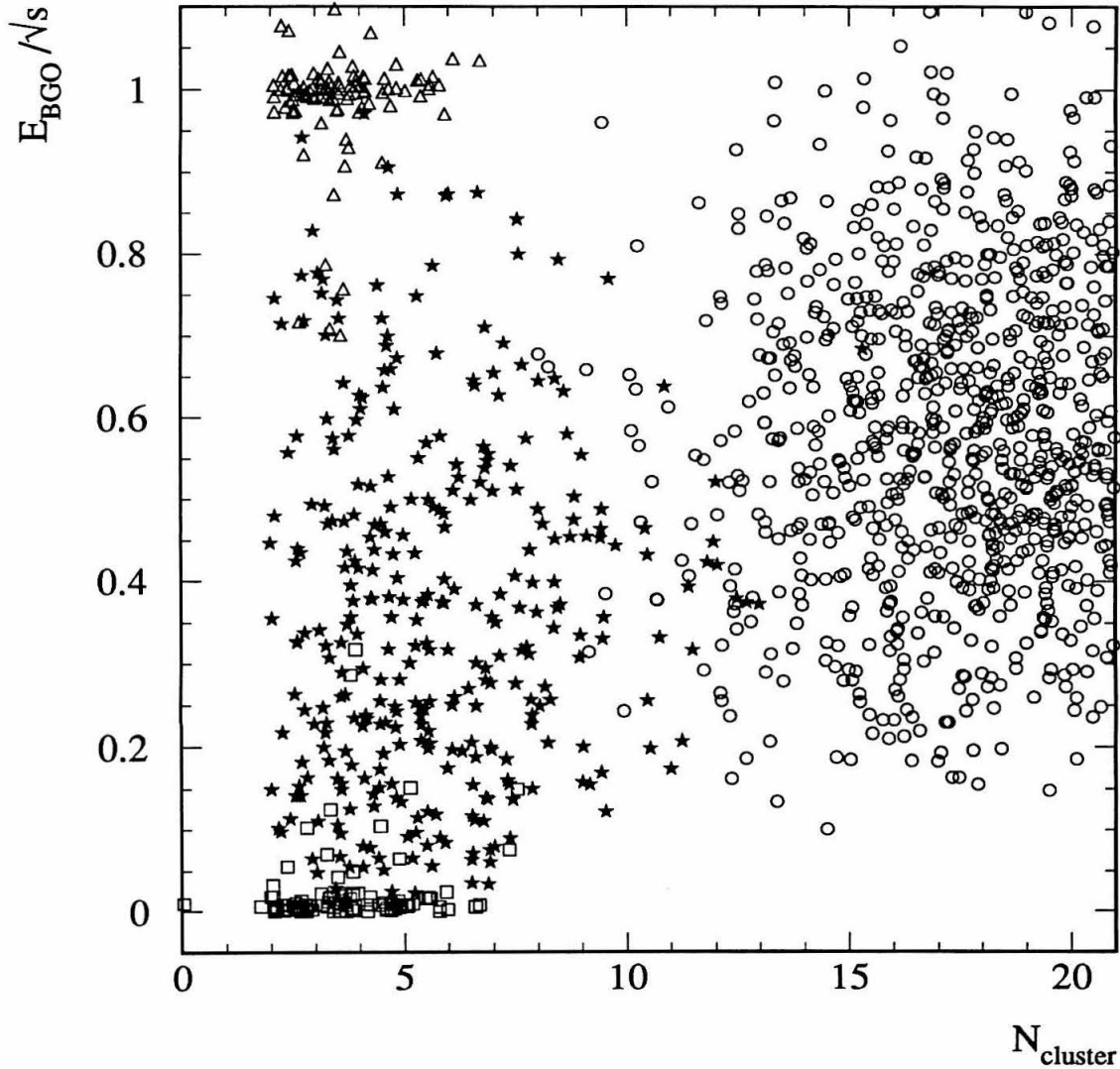
Figure 6.3: Scatter plot visualizing the third step in the $e^+e^- \to \tau^+\tau^-(\gamma)$ selection, the rejection of unwanted Z° decays. The correlation between total electromagnetic energy (E_{BGO}) and number of calorimetric clusters ($N_{cluster}$) for hadrons (open circles), Bhabhas (open triangles), dimuons (open squares), and τ pairs (solid stars) shows a good separation between all channels.

— The acollinearity between the two most energetic jets, i.e., their deviation from being back-to-back, must be smaller than 0.25 rad (14.3°) :

$$\zeta_{12} \equiv \pi - \angle(\text{Jet 1, Jet 2})$$
$$< 0.25 \text{ rad} . \tag{6.4}$$

— The total energy deposited in the BGO electromagnetic barrel calorimeter has to be larger than 2 GeV:

$$E_{\text{BGO}} > 2 \text{ GeV} . \tag{6.5}$$

— The best scintillator time, i.e., the time measured by a scintillator (corrected for time of flight), which is closest to the beam crossing (defined as t = 0), must lie within 2.5 ns of the beam crossing:

$$|t_{\text{best}}| < 2.5 \text{ ns} . \tag{6.6}$$

• Rejection of other Z° decays:

— Electromagnetic energy depositions must be smaller than that of $e^+e^- \rightarrow e^+e^-(\gamma)$ events, by requiring limits on the most and second most energetic bump in the BGO:

$$E_1 < 0.9 \, E_{\text{Beam}} \tag{6.7}$$
$$E_2 < 0.65 \, E_{\text{Beam}} . \tag{6.8}$$

— The energy of reconstructed muons must be smaller than that in $e^+e^- \rightarrow \mu^+\mu^-(\gamma)$ events, by requiring limits on the most and second most energetic muon reconstructed in the muon chambers of the detector:

$$P_1 < 0.9 \, E_{\text{Beam}} \tag{6.9}$$
$$P_2 < 0.4 \, E_{\text{Beam}} . \tag{6.10}$$

— In order to reject broad, high multiplicity hadronic events, there are two quantities considered. These are the number N_{cluster} of clusters reconstructed in the calorimeters, and the maximum angle Φ_{TEC} of a track to

the nearest jet, in the plane perpendicular to the beam direction.

$$N_{\text{cluster}} \quad < \quad 13 \tag{6.11}$$

$$\Phi_{\text{TEC}} \quad < \quad 0.25 \text{ rad} \quad . \tag{6.12}$$

Systematic Errors of Selection Criteria

Having defined the selection criteria, one can now estimate both overall acceptance and background contamination in the accepted sample of data events, using Monte Carlo simulations of signal and background channels. The remaining small amount of background will be subtracted from the number of selected data events, i.e., corrected for on a statistical basis. Dividing the corrected number of events by acceptance and luminosity yields the cross section of the reaction $e^+e^- \to \tau^+\tau^-(\gamma)$.

The instability of this measured cross section with respect to variations in the actual value of a selection cut, gives a first hint of the presence of systematic errors. The mathematical procedure to quantify this is as follows: Let the subscript $i = 0$ denote variables obtained at the standard settings of all cuts, and the subscript $i = 1, 2, \ldots$ denote variables evaluated with a different cut setting, usually, a single cut moved to a different value. Then one has different measurements of the cross section: $(i = 0, 1, 2, \ldots)$:

$$\sigma_i \;=\; \frac{N_i}{a_i \mathcal{L}} \quad , \tag{6.13}$$

where a_i incorporates both acceptance and background corrections (for each i determined by Monte Carlo). N_i is the number of selected data events, and $\mathcal{L}$ is the integrated luminosity. A measure of the systematic error is given by the relative change in cross section:

$$\frac{\Delta\sigma_i}{\sigma_0} \pm \delta\left(\frac{\Delta\sigma_i}{\sigma_0}\right) \;\equiv\; \frac{\sigma_i - \sigma_0}{\sigma_0} \pm \delta\left(\frac{\sigma_i}{\sigma_0}\right) \quad , \tag{6.14}$$

which should be zero within its error δ. It can be assumed that the Monte Carlo statistical error entering via a_i is negligible, compared to the statistical error in the number N_i of selected data events, because the number of Monte Carlo events is

large compared to N_i. Then the absolute error in the relative change of cross section can be computed using binomial statistics:

$$\delta\left(\frac{\Delta\sigma_i}{\sigma_0}\right) \;=\; \delta\left(\frac{\sigma_i}{\sigma_0}\right) \;=\; \sqrt{\frac{|\,N_0 - N_i\,|}{N_0 N_i}} \quad . \tag{6.15}$$

If the relative change in the cross section deviates significantly from zero, a systematic difference between data and Monte Carlo is present, which leads to a non-vanishing systematic error.

In a fit to the data to determine electroweak parameters (Chapters 7 and 8), the statistical and systematic errors are treated as one-sigma errors (Appendix F). Thus, all errors quoted in the following sections correspond to one-sigma estimates.

The selection criteria and their associated systematic errors will be discussed in detail in the following paragraphs. For this purpose, the distribution of data and Monte Carlo events in the cut variables will be shown, after having applied most or all of the other selection criteria. The different symbols and hatch styles used to denote data and various Monte Carlo event types are explained in Figure 6.4. Also, the change in cross section including its error when moving the cut position will be shown.

6.1.2   Fiducial Volume

The status of the **L₃** detector during 1991, as discussed in Chapter 3, shows that only the barrel region is covered by all the major subdetector components (TEC chamber, BGO calorimeter, scintillation counters, hadron calorimeter and muon spectrometer). Because of the complicated signature of $\tau^+\tau^-(\gamma)$ events, the selection has to be restricted to the geometrical fiducial volume of the barrel, in order to have the maximal amount of information available for classifying an event as signal or background.

Only quite recently has the understanding and calibration of the forward tracking chamber (FTC) and the BGO endcap calorimeter reached the level necessary to start the data analysis for events in the endcap region. For example, the $e^+e^- \rightarrow e^+e^-(\gamma)$ analysis for the endcap region is in a preliminary state. Thus, only a future analysis of $e^+e^- \rightarrow \tau^+\tau^-(\gamma)$ events will extend the fiducial volume to the endcap region.
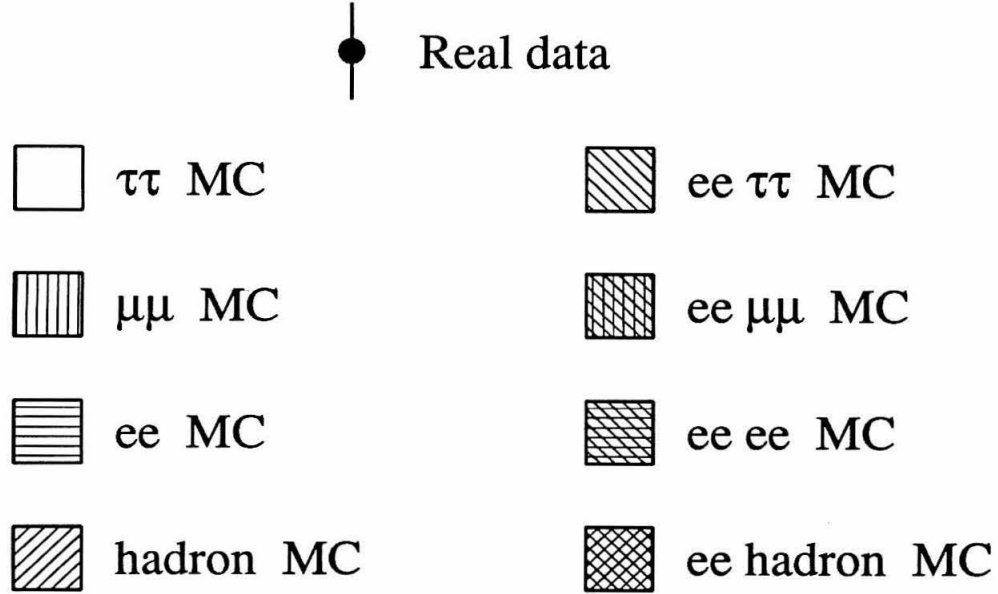
Figure 6.4: Explanation of different symbols and hatch styles used in the following histograms to denote real data and various Monte Carlo (MC) channels: fermion-pair production (left) and two-photon processes (right). The corresponding Monte Carlo event generators are discussed in Chapter 4.

The thrust axis is used as an event axis, to decide whether an event lies inside the barrel region or not. This axis is implicitly defined in the definition of the thrust [49] value T itself:

$$T \equiv \max_{\vec{n}_t} \frac{\sum_i E_i \, |\vec{n}_i \cdot \vec{n}_t|}{\sum_i E_i} \quad , \tag{6.16}$$

where the summation runs over all calorimetric clusters i with energy E_i in direction $\vec{n}_i$ ($|\vec{n}_i| = 1$). The maximization procedure runs over all unit vectors $\vec{n}_t$; the one corresponding to the the maximum T value, $\vec{n}_T$, is called the event's thrust axis. This axis maximizes the longitudinal projection of the energy vectors of all clusters. The definition of T fixes only the thrust *axis*, the *direction* remains undefined due to the sign ambiguity in $\vec{n}_T$ in the definition of T. The convention chosen is to let

the thrust vector point into the hemisphere containing the most energetic jet. Using the thrust axis as the event axis and expressing it in the $\mathbf{L_3}$ coordinate system, the restriction to the barrel region can be written as:

$$|\cos\Theta_{\text{thrust}}| \equiv |n_z| < 0.73 \quad . \tag{6.17}$$

As an additional advantage, restriction to the wide-angle barrel region largely suppresses effects due to **LEP**-machine-related background problems, as well as all channels of the two-photon reactions $e^+e^- \to e^+e^- f\bar{f}$. Figure 6.5 shows the distribution in $|\cos\Theta_{\text{thrust}}|$ of real and simulated events in the region of the cut value, and the variation of the measured cross section when changing the value of the cut. The gap between the BGO barrel and endcap calorimeter manifests itself by the large background of Bhabha events at angles around 40° and 140° degrees. This is due to the fact, that the rejection of Bhabha events is based on the identification of high energy electromagnetic showers in the BGO calorimeter.

In this region, there is also some disagreement between data and Monte Carlo. There are two reasons for this effect: First, there is a trigger inefficiency for low energy events, whose particles do not pass through the BGO calorimeter. Although the hadron calorimeter trigger channels should still pick up the event, inefficiencies occur due to a large amount of insensitive material at the positions of the mechanical supports inside the hadron calorimeter barrel. This leads to a loss in the measured shower energy, and hence to a slightly reduced trigger efficiency. A second reason is the approximate treatment of the material in the gap within the detector simulation: the inhomogeneous material inside the gap is represented by an azimuthally averaged medium in the Monte Carlo description of the $\mathbf{L_3}$ detector (see Appendix E).

6.1.3 Minimal Requirements

In order to ensure that selected events do indeed arise from $Z^\circ \to f\bar{f}$ decays, basic requirements have been set on the energy, event topology and event timing with respect to the beam crossing.
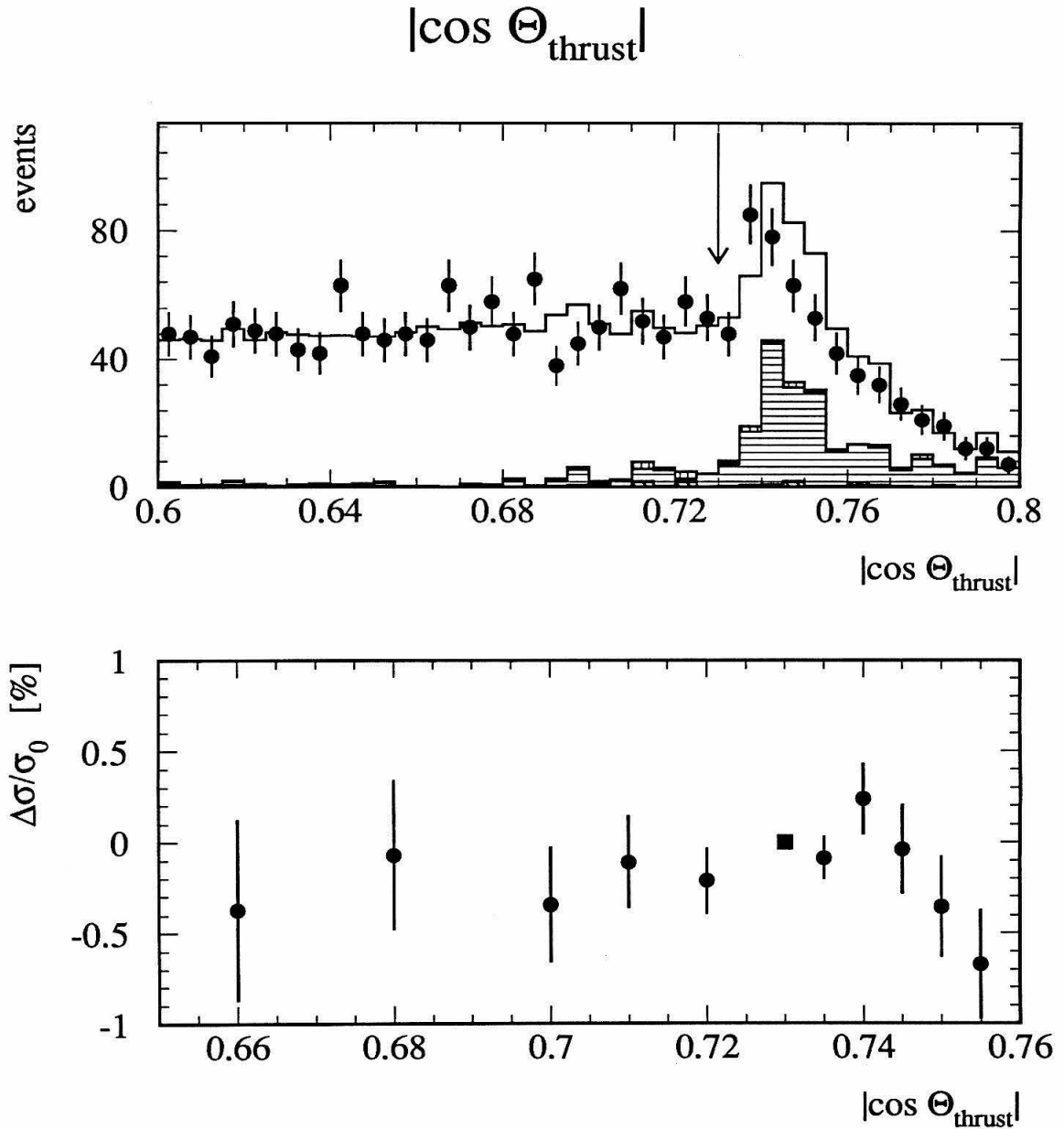
$$|\cos\Theta_{\text{thrust}}|$$

Figure 6.5: Distribution of $|\cos\Theta_{\text{thrust}}|$ in the region of the cut value, after having applied all other selection cuts; and influence on the cross section when moving the cut. See text for a definition of the quantity $|\cos\Theta_{\text{thrust}}|$. The arrow indicates the nominal cut value. The main background (hatched area) arises from Bhabha events.

Jet Energies and Acollinearity

Events are required to have at least two jets: the most energetic must have an energy above 7 GeV, and the second most energetic must have at least 3 GeV. This requirement mirrors the expected two-jet event topology of $Z^\circ \to f\bar{f}$ decays, where each fermion other than neutrino causes at least one jet in the detector. The asymmetric minimal jet energy requirements ensure that:

- background from two photon $e^+e^-e^+e^-$ final-state events ($E_{\text{Jet }1} > 7$ GeV, Figure 6.6) is suppressed down to the level of 0.1%;

- at the trigger level, the cluster trigger (part of the energy trigger) is fully efficient. $E_{\text{Jet }1} > 7$ GeV is well above the energy threshold of 6 GeV for the cluster trigger without an associated TEC track, and $E_{\text{Jet }2} > 3$ GeV is above the energy threshold of 2.5 GeV for the cluster trigger with an associated TEC track;

- at the reconstruction level, the jet finding algorithm has reached full efficiency ($E_{\text{Jet }2} > 3$ GeV).

Figures 6.6 and 6.7 show the distribution of jet energies for the most and second most energetic jet, respectively. The background from two-photon $e^+e^- \to e^+e^-e^+e^-$ events at low jet energies of the first jet is clearly visible. In the distribution of the energy of the second jet, the background in the cut region arises from muons, which are not measured in the muon chambers. Hence, the energy of the associated jet is given purely by the energy loss deposited in the calorimeters.

The additional requirement of the two most energetic jets being back-to-back within 0.25 rad ensures the geometrical balance of the events, which is expected from $Z^\circ \to f\bar{f}$ decays measured in a laboratory frame that coincides with the rest frame of the Z°. This is in contrast to the event signature of all channels of (untagged) two-photon events ($e^+e^- \to e^+e^- f\bar{f}$), cosmic rays or beam-gas or beam-wall interactions. This requirement leads to slightly lower selection efficiencies at the off-peak center-of-mass energies, which will be discussed later. Figure 6.8 illustrates the comparison

Energy of most energetic jet
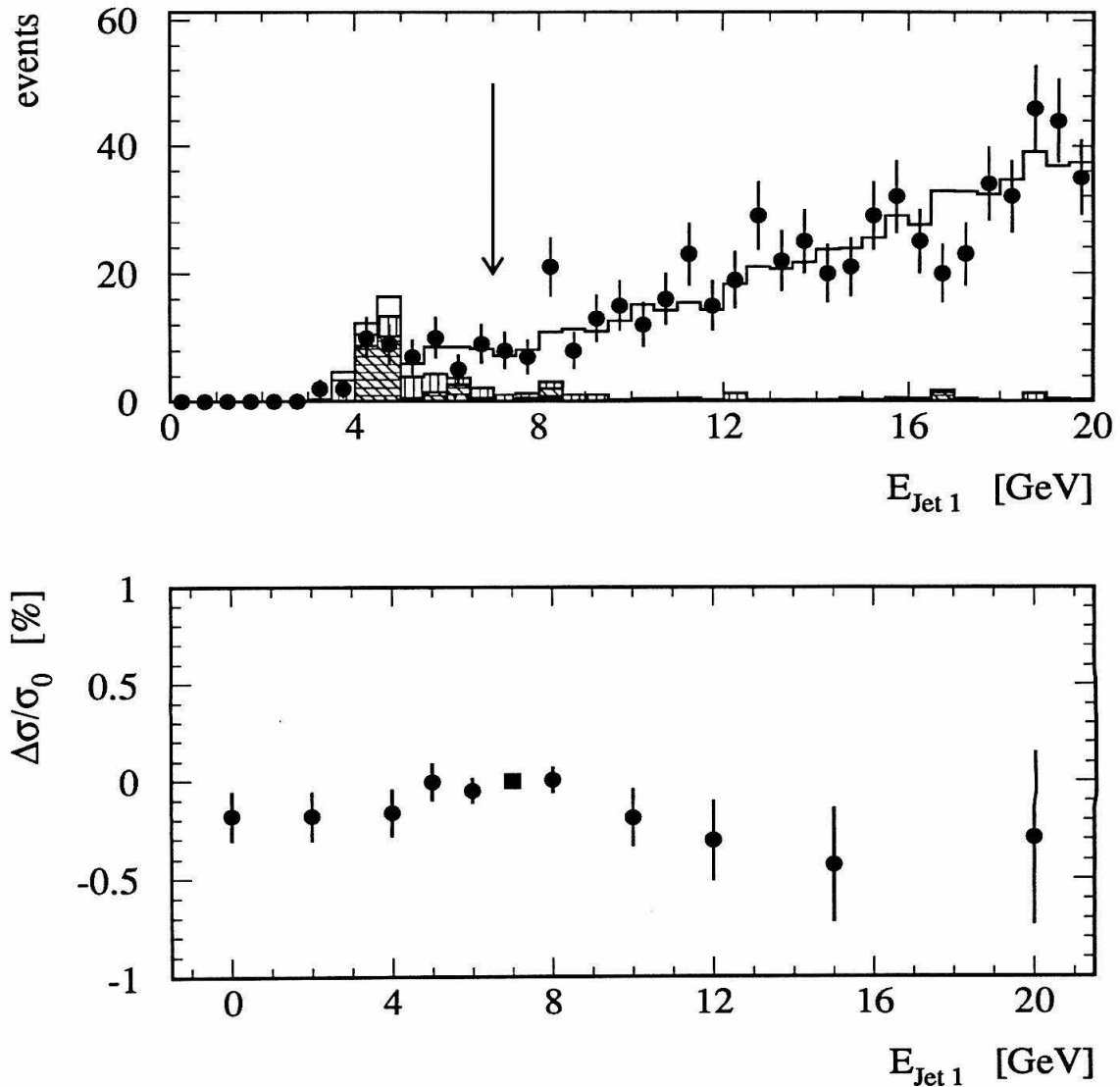
Figure 6.6: Distribution of energy of the most energetic jet ($E_{Jet\ 1}$) in the region of the final cut value, after having applied all other selection cuts; and influence on the cross section when moving the cut. The arrow indicates the nominal cut value. The main background (hatched area) arises from two-photon four-electron and dimuon events.

Energy of second most energetic jet
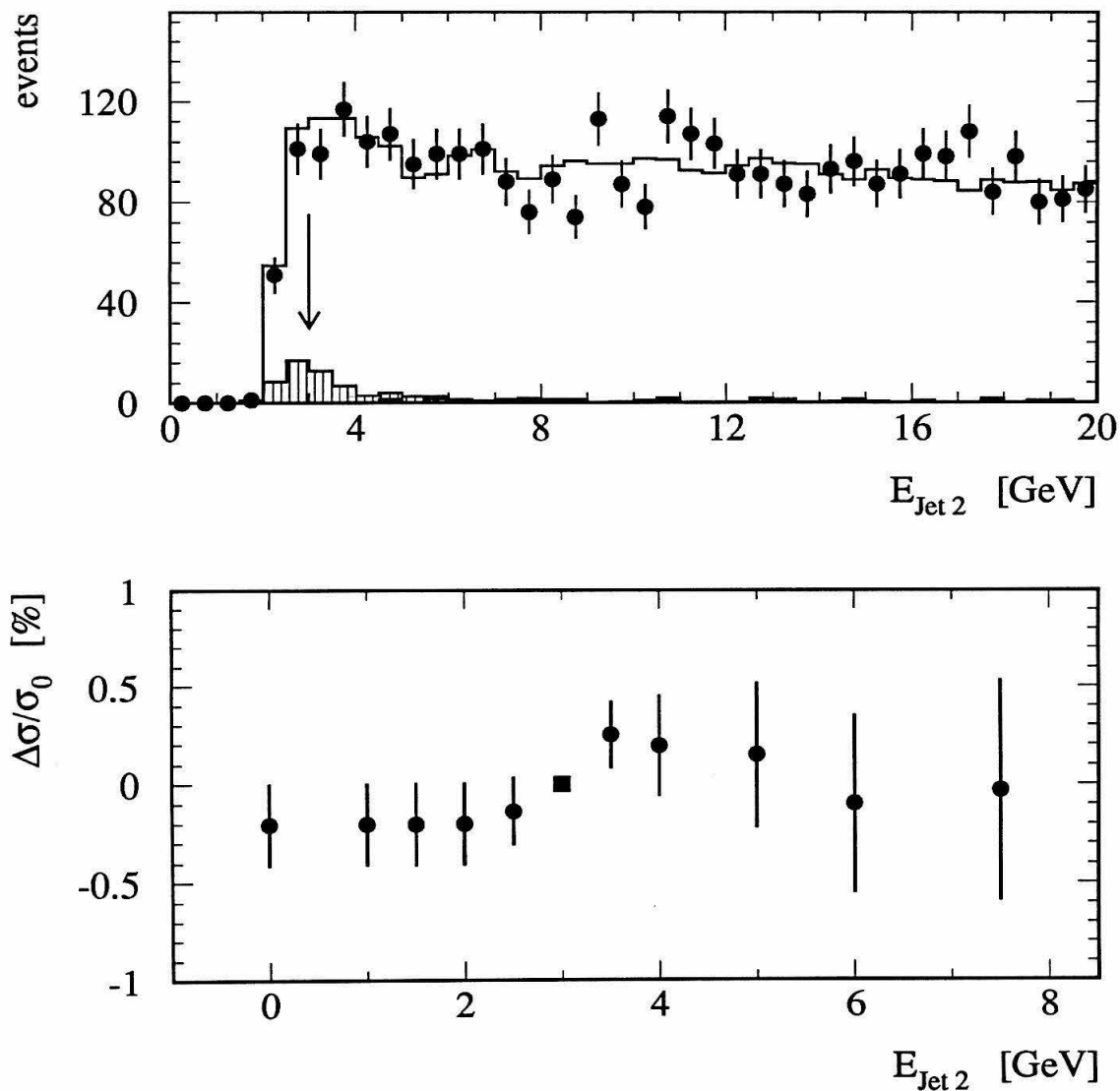
Figure 6.7: Distribution of energy of second most energetic jet ($E_{Jet\ 2}$) in the region of the final cut value, after having applied all other selection cuts; and influence on the cross section when moving the cut. The arrow indicates the nominal cut value. The main background (hatched area) arises from dimuon events.

Acollinearity ζ of jets
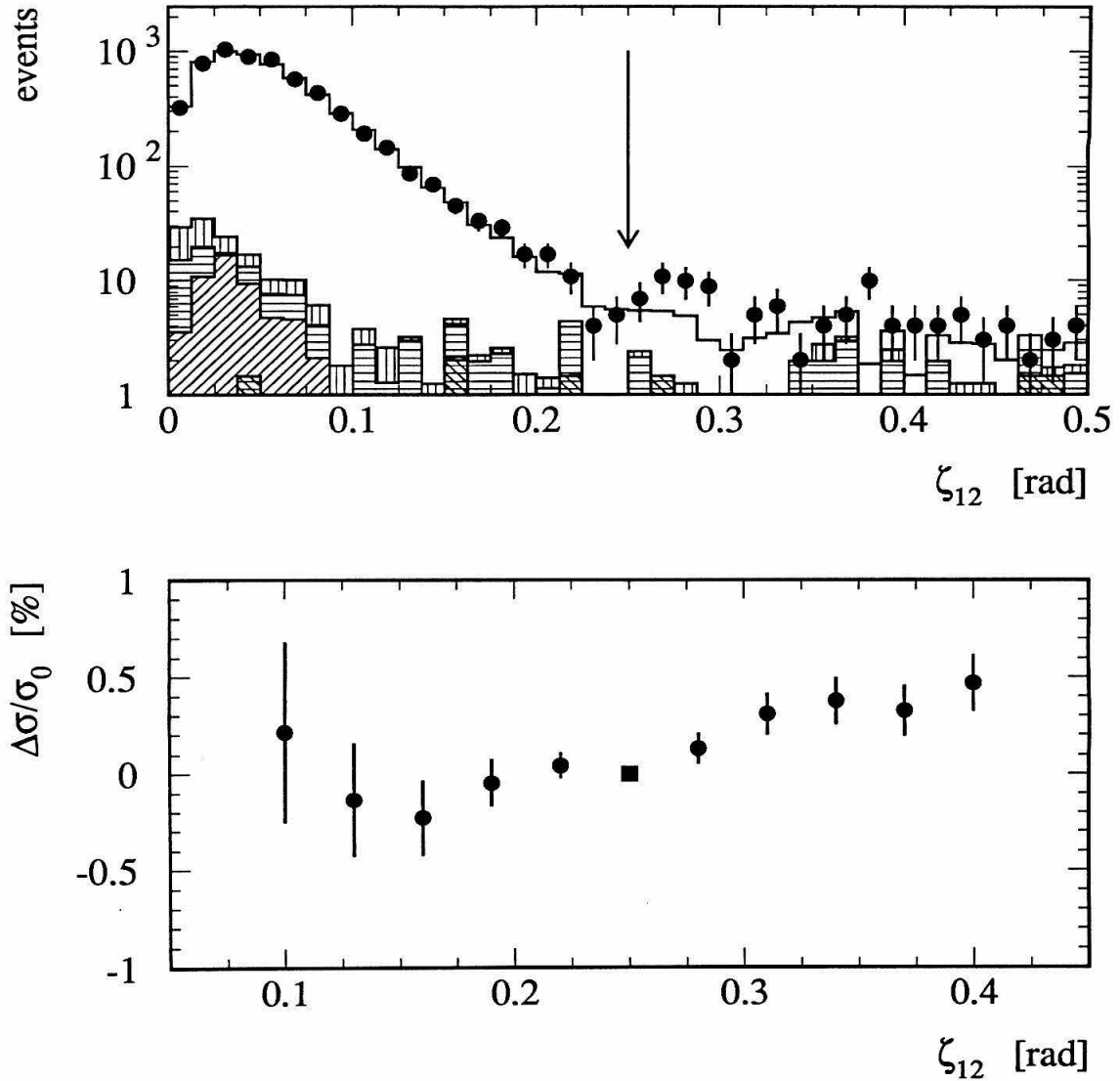
Figure 6.8: Distribution of accollinearity between two most energetic jets (ζ_{12}) in the region of the final cut value, after having applied all other selection cuts; and influence on the cross section when moving the cut. The arrow indicates the nominal cut value. The main background (hatched area) at large acollinearities arises from Bhabha events.

between data and Monte Carlo in the jet acollinearity. The excess of data with respect to Monte Carlo at large acollinearity angles is attributed to a mixture of cosmic ray events and beam related background.

Electromagnetic Energy

The requirement of at least 2 GeV deposited in the electromagnetic barrel calorimeter greatly helps to reduce the background from cosmics and from dimuon events. This is due to the fact that this kind of background manifests itself mostly as a single minimum ionizing track traversing the detector. Therefore, a cut well above twice the average signal of a minimum ionizing particle (to allow for the Landau tail) in the BGO calorimeter removes all of the non-radiative events of these types, and also, due to the 1/E spectrum of QED radiation, some of the radiative ones. In the case of $\tau^+\tau^-$ events, this cut effectively removes those events where both τ decays are only minimum ionizing inside the BGO, i.e., events of the type $\tau^+\tau^- \rightarrow \mu^+\mu^-, \pi^+\pi^-, \mu^\pm\pi^\mp$ with the pions noninteracting in the BGO. This leads to a τ-decay-mode-dependent selection efficiency, the effect of which will be discussed later in the context of systematic errors. Figure 6.9 shows the distribution of data events and the prediction from Monte Carlo, for the energy deposited in the BGO barrel calorimeter. The minimum-ionizing peak stands out clearly. Only part of its height is predicted by physics events such as dimuon events or τ pairs. The rest of the entries are caused by cosmic ray events which triggered the detector.

Scintillator Time

The timing of cosmic rays is clearly uncorrelated with the crossing of the **LEP** beams at the interaction region. Therefore, the event time measured by the scintillation counters (corrected for time of flight of a particle originating at the interaction region) is required to lie within 2.5 ns of the beam crossing time. This removes out-of-time cosmic ray events very effectively. The distribution of the time measured by the scintillators is shown in Figure 6.10. Events with large scintillator time, $| t_{best} | >$ 3.0 ns, have been identified as being mostly cosmic ray events by scanning.

Barrel BGO energy
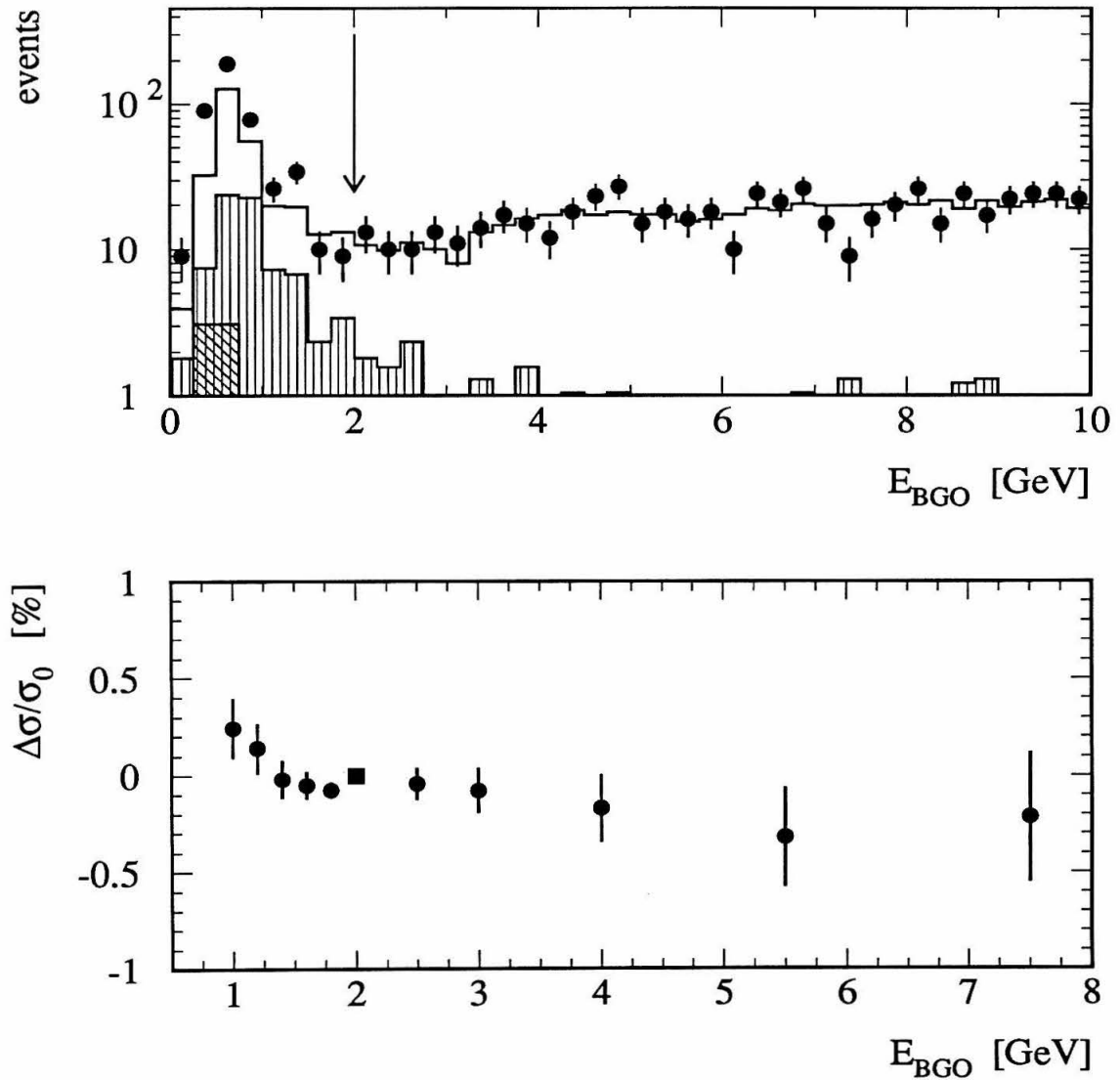
Figure 6.9: Distribution of electromagnetic energy (E_{BGO}) in the region of the final cut value, after having applied all other selection cuts; and influence on the cross section when moving the cut. The arrow indicates the nominal cut value. The main background (hatched area) arises from dimuon and two-photon $e^+e^-\mu^+\mu^-$ events.

Best scintillator time
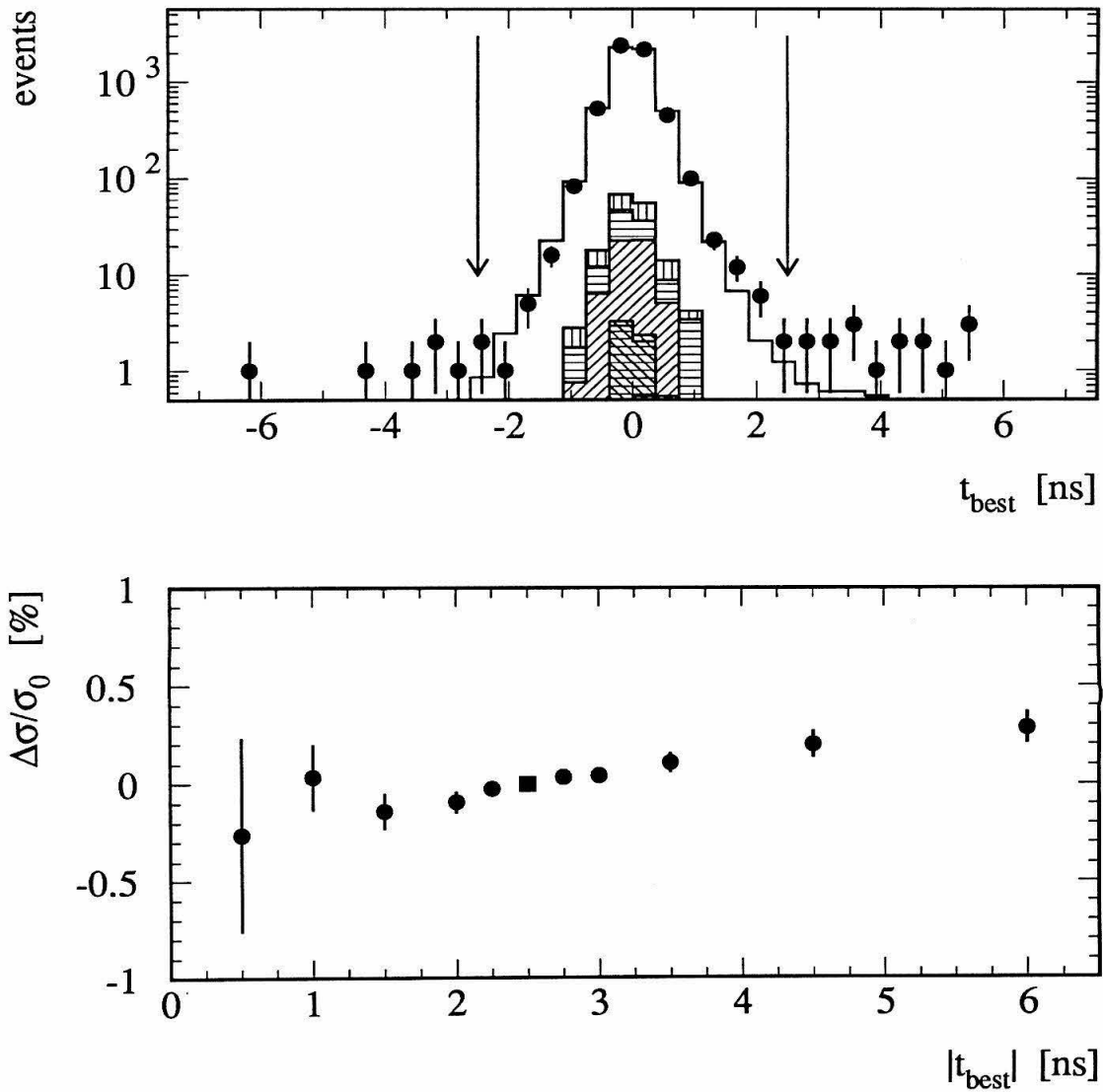
Figure 6.10: Distribution of scintillator time (t_{best}) in the region of the final cut value, after having applied all other selection cuts; and influence on the cross section when moving the cut. The arrows indicate the nominal cut values.

Treatment of Non-Simulated Background

As is clearly visible in the acollinearity, BGO energy and scintillator time distributions used to select genuine Z° decays, there exist background events for which no Monte Carlo simulation is available. These events are either cosmic muon events, or machine-related background events such as beam-wall and beam-gas interactions. Because they are not simulated, they clearly shift the calculated cross section when moving the corresponding cut value. There are now two ways to proceed:

1. The change in cross section is taken at face value, and a corresponding systematic error is worked out and assigned. This method can always be applied, but leads to rather large systematic errors.

2. The amount of remaining background inside the selected region is subtracted on a statistical basis. In this case, some assumptions have to be made on the shape of the background "buried" under the signal events, and there is an additional systematic error due to this shape uncertainty.

In the case of cosmic rays, which are evenly distributed in time, a flat distribution in the measured scintillator time is assumed, whose height is determined by the sidebands of the time distribution (outside of the selected region). The amount of cosmics thus determined, $(0.25 \pm 0.08)\%$, is subtracted, and a remaining systematic error of 0.1% is assigned to the scintillator timing cut.

The non-simulated minimum-ionizing peak in the BGO energy distribution is simply cut out. The stability of the measured cross section with respect to an increase in cut value indicates, that there is no further non-simulated background.

In the case of the acollinearity distribution, the background arising from cosmics has already been taken care of by the above cosmic ray subtraction procedure. Some beam-related background remains. A variation of 0.3% is conservatively assigned as a systematic error, based on the variation of the cross section with cut position.

6.1.4 Rejection of other Z° Decays

At this stage of the selection, the remaining background arises from Z° decays to $e^+e^-(\gamma)$, $\mu^+\mu^-(\gamma)$ or hadrons. The rejection of this background is discussed below.

Rejection of Bhabha Events

The rejection of $e^+e^- \to e^+e^-(\gamma)$ events naturally relies on the high-resolution BGO electromagnetic calorimeter. Figure 6.11 shows the resolution of the BGO electromagnetic calorimeter for bumps around 45 GeV. The Bhabha peak is clearly visible. The resolution of 1.4% is slightly worse than the 1.2% quoted in Chapter 3, due to the fact that *no* Bhabha selection has been applied.

The typical Bhabha event configuration shows two (or more) highly energetic bumps of BGO crystals. The cut values are chosen to be $0.9E_{Beam}$ and $0.6E_{Beam}$ for the first (E_1) and second (E_2) bump (energy ordered). Figure 6.12 shows the distribution in the energy of the most energetic bump.

Because of the energy ordering, the effect of QED radiation and of "killed" crystals is more pronounced in the distribution of E_2. Using the "real" detector simulation as described in Chapter 4, noisy crystals recognized in the data as well as dead crystals are killed in both data and Monte Carlo in order to have a consistent treatment of the BGO calorimeter imperfections.[1] Killing crystals (about 0.6% in the barrel and 2.5% in the endcap calorimeter) obviously leads to a loss of observed energy in E_2, as does final-state radiation. Both effects contribute to the tail running from the Bhabha peak down towards lower energies (as can be seen in the distribution of E_2 shown in Figure 6.13), although final-state QED radiation is predominant in causing the tail.

---

[1] Bumps containing killed crystals are still reconstructed, unless the bump consisted only of the killed crystal. For electromagnetic energy depositions above 0.5 GeV, the energy deposited in the remaining crystals after having killed any crystal (even the central one), is still larger than the 40 MeV required to form a bump.

Energy resolution for Bhabhas

χ^2		1.081	
Constant	763.0 $\pm$		8.877
Mean	0.1995E-02 $\pm$		0.1715E-03
Sigma	0.1403E-01 $\pm$		0.1548E-03
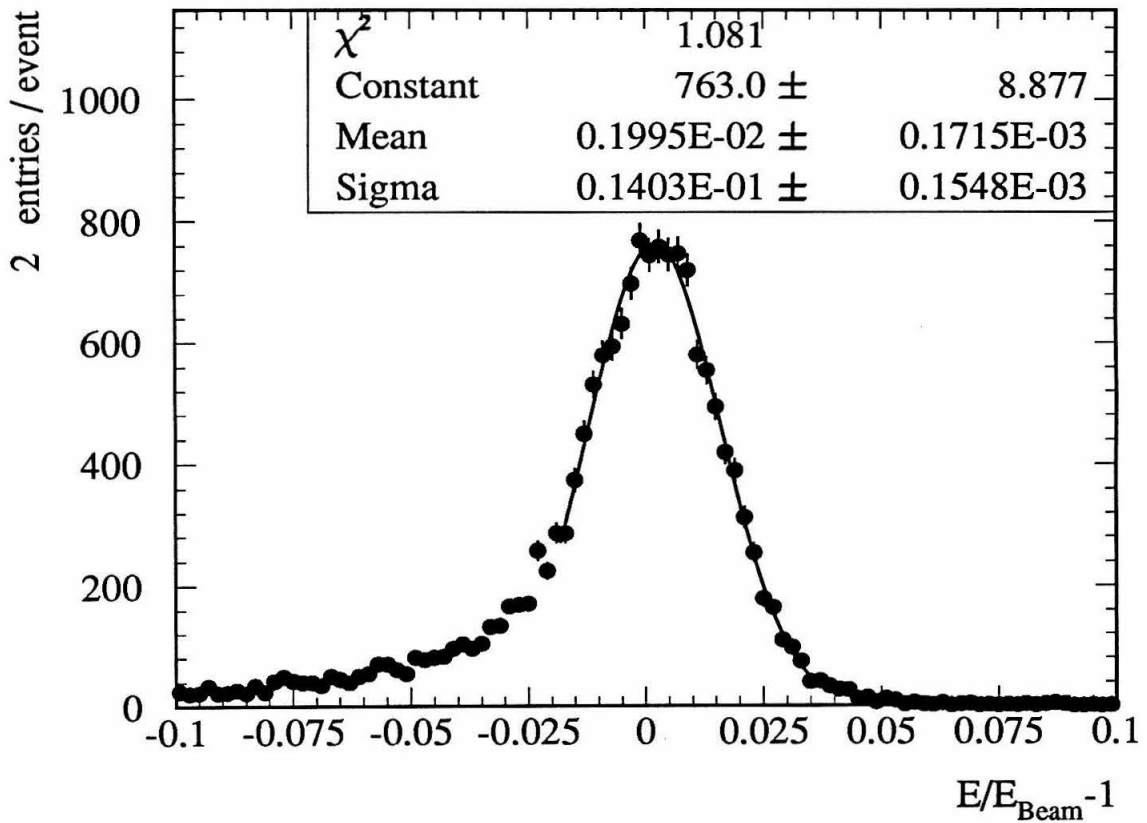
Figure 6.11: BGO energy resolution in the region of 45 GeV for data. Events have passed *no* cut except 0.25 rad acollinearity. The curve shows the result of a Gaussian fit to the Bhabha peak.

Energy of most energetic bump
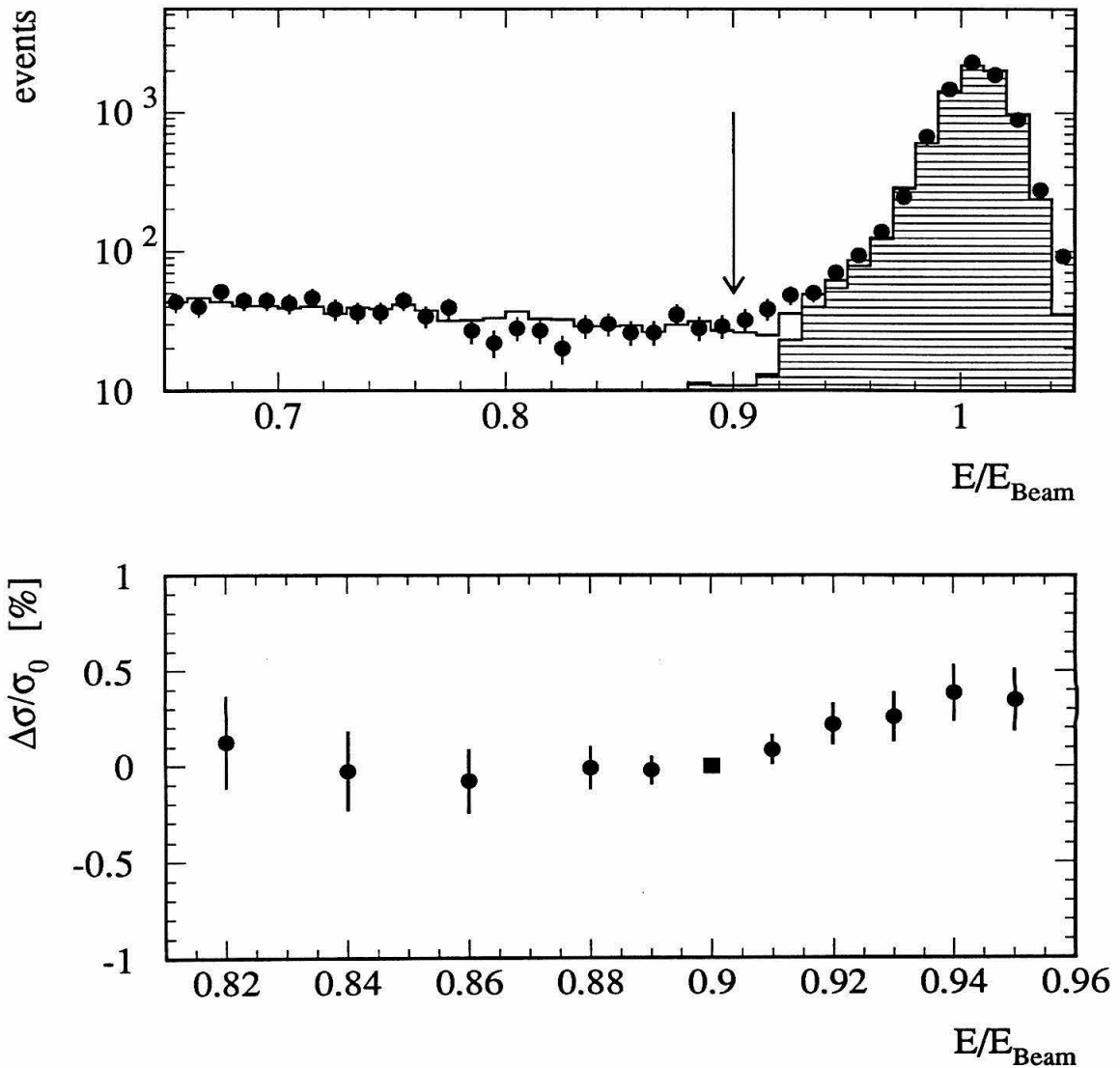
Figure 6.12: Distribution of energy of most energetic BGO bump in the region of the final cut value, after having applied all selection cuts except the two to reject Bhabha events; and influence on the cross section when moving the cut. The arrow indicates the nominal cut value. The main background (hatched area) arises from Bhabha events.

Energy of second most energetic bump
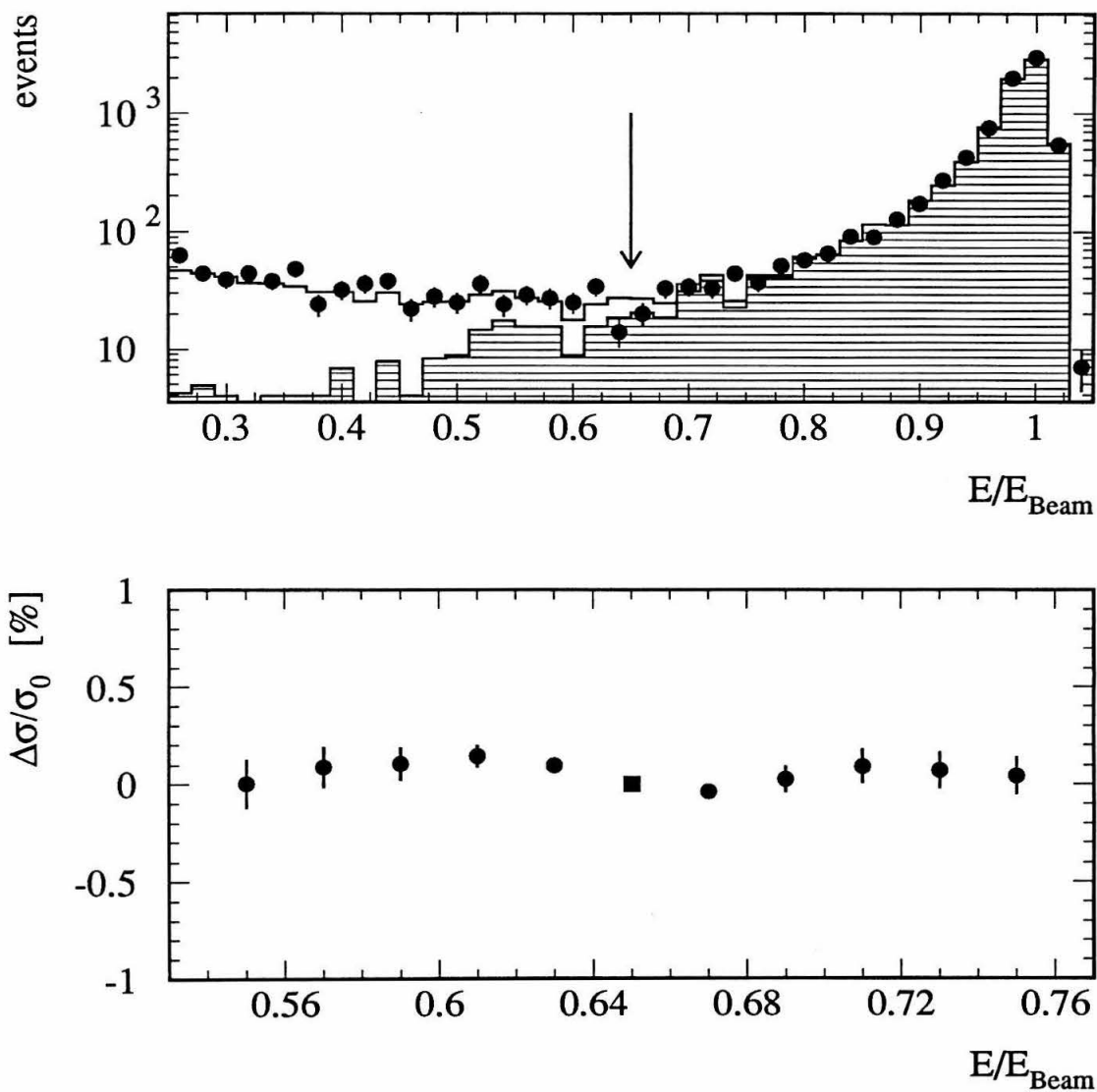
Figure 6.13: Distribution of energy of second most energetic BGO bump in the region of the final cut value, after having applied all selection cuts except the two to reject Bhabha events; and influence on the cross section when moving the cut. The arrow indicates the nominal cut value. The main background (hatched area) arises from Bhabha events.

Rejection of Dimuon Events

The rejection of $e^+e^- \rightarrow \mu^+\mu^-(\gamma)$ events relies on the precise muon chambers, besides the requirement of at least 2 GeV BGO energy to remove purely minimum-ionizing events. Figure 6.14 shows the resolution of the muon spectrometer for reconstructed muons around 45 GeV. The dimuon peak is clearly visible. The resolution of 2.7% is slightly worse than the 2.5% quoted in Chapter 3, due to the fact that *no* dimuon selection has been applied.

Non-radiative dimuon events have already been removed at this stage of the analysis, by the requirement of at least 2 GeV BGO energy. Still remaining are the radiative events, which are further rejected by a momentum cut on the first and second reconstructed muon (again energy ordered) of $0.9E_{Beam}$ and $0.4E_{Beam}$. The muon momentum distribution of the most energetic muon is shown in Figure 6.15.

In the case a muon passes through a disconnected P chamber cell in one of the three layers of the muon spectrometer, only a doublet of segments is available for momentum determination instead of a triplet. This leads to degraded momentum resolution (22% instead of 2.7%). On average, about 9% of all P chamber cells must be killed in the "real" detector Monte Carlo (see Chapter 4). If only a singlet is available, no momentum determination, and thus no rejection of dimuon events based on momentum is possible. However, the event is still rejected due to the measurement of the second muon. In the case where both muons are not reconstructed in the muon chambers, the requirements of 2 GeV BGO energy and of two jets of 7 GeV and 3 GeV (where these energies are now given purely by the calorimeters), still remove this type of dimuon event.

QED radiative effects explain the long tail towards low energies in the distribution of the energy of the second most energetic muon candidate, shown in Figure 6.16.

Momentum resolution for Dimuons
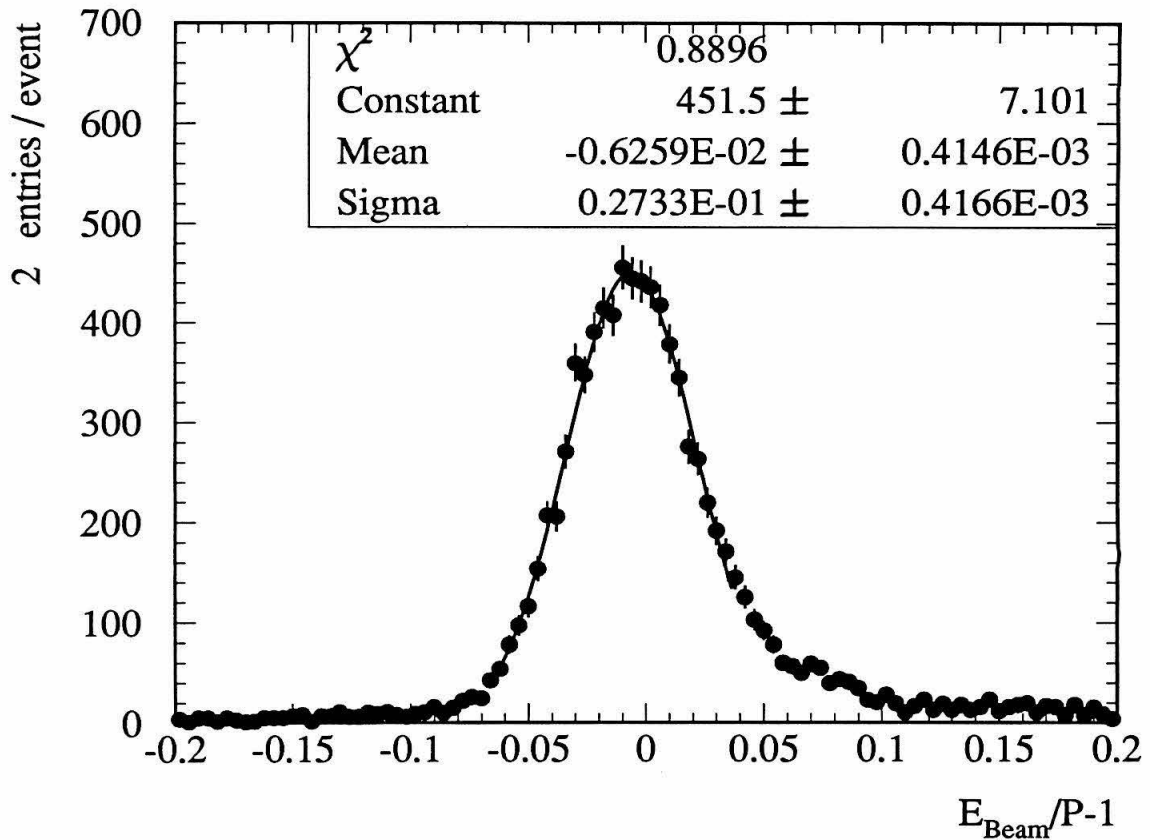
Figure 6.14: Muon chamber momentum resolution in the region of 45 GeV for data. Events have passed *no* cut except 0.25 rad acollinearity. The curve shows the result of a Gaussian fit to the dimuon peak. Note, that for tracking devices, the resolution is Gaussian in curvature, which is proportional to the inverse of the momentum P.

Energy of most energetic muon
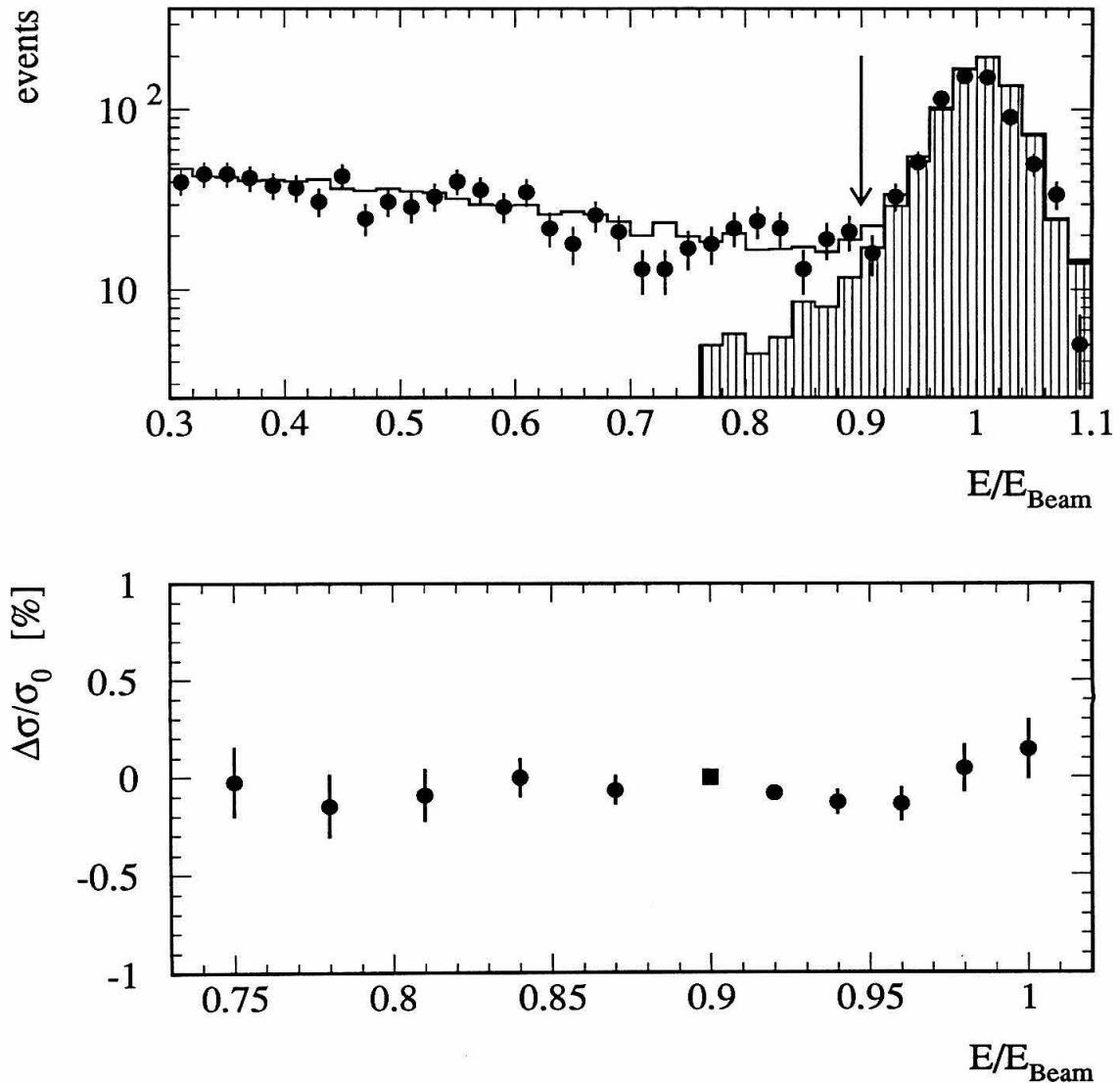
Figure 6.15: Distribution of energy of most energetic muon candidate in the region of the final cut value, after having applied all selection cuts except the two to reject dimuon events; and influence on the cross section when moving the cut. The arrow indicates the nominal cut value. The main background (hatched area) arises from dimuon events.

Energy of second most energetic muon
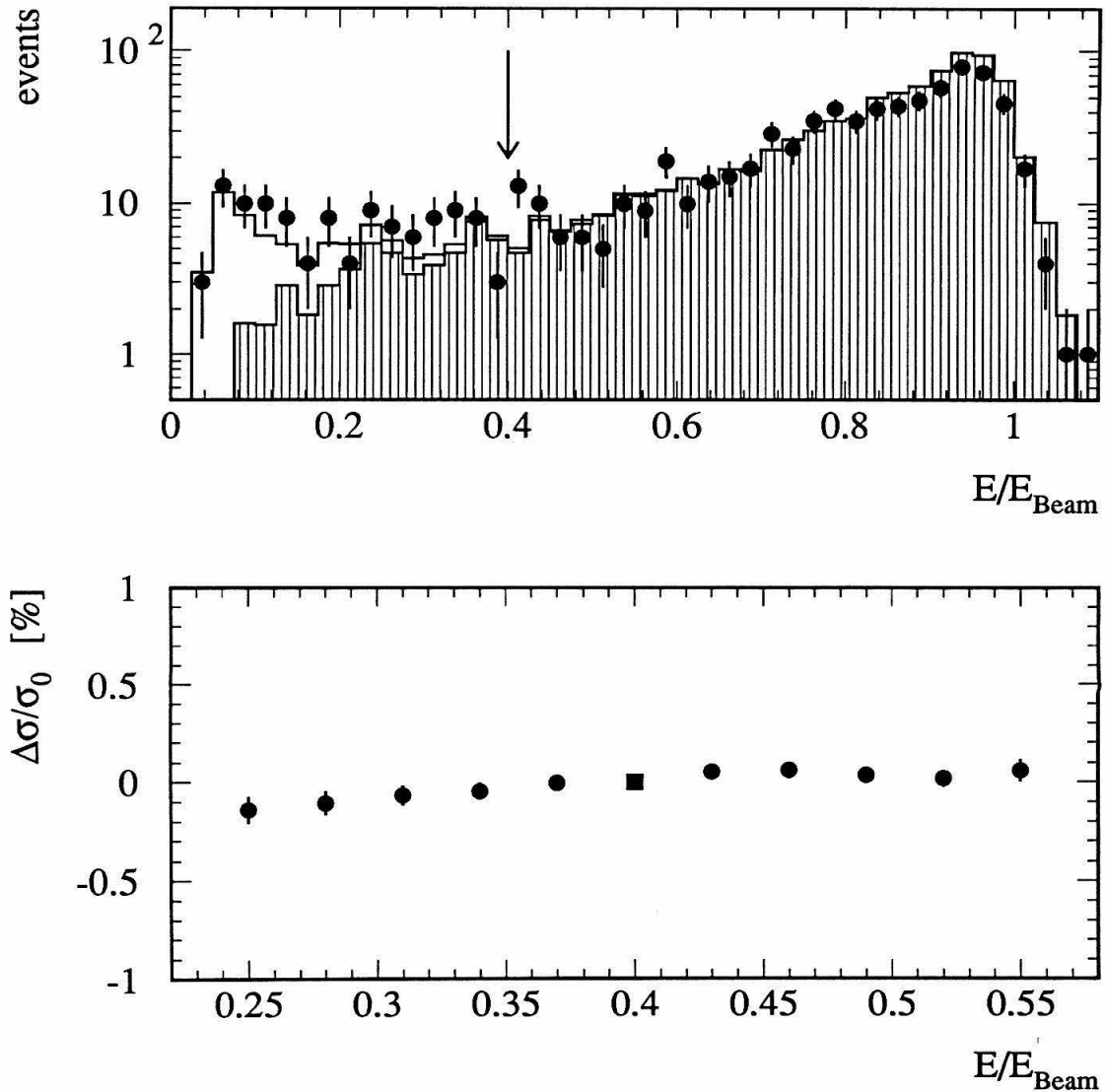
Figure 6.16: Distribution of energy of second most energetic muon candidate in the region of the final cut value, after having applied all selection cuts except the two to reject dimuon events; and influence on the cross section when moving the cut. The arrow indicates the nominal cut value. The main background (hatched area) arises from dimuon events.

Rejection of Hadron Events

Whereas the leptonic final states $e^+e^-(\gamma)$ and $\mu^+\mu^-(\gamma)$ occur with a rate comparable to that of $\tau^+\tau^-(\gamma)$ final states (for $e^+e^- \to e^+e^-(\gamma)$ this holds in the large-angle barrel region), hadronic events are a factor of ≈ 21 more abundant.

An effective cut to reject hadronic Z° decays exploits the different jet structure of hadronic jets and jets from τ decays. The latter are low-multiplicity, highly boosted slim jets, whereas the former are high-multiplicity broad jets. A quantity used to distinguish the two types of Z° decays on an event-by-event basis is the largest angle that any TEC track in the event has with respect to its nearest jet, called Φ_{TEC}, because it is measured in the x/y plane. The cut is placed at $\Phi_{\mathrm{TEC}} < 0.25$ rad. Figure 6.17 shows the distribution of this quantity in the region of the cut value.

Hadron events also are distinguished from the signal by a higher multiplicity of particles in the final state, which translates into a higher multiplicity of reconstructed clusters in the calorimeters. In fact, the multiplicity distribution (Figure 6.18) shows a striking separation between the signal of $\tau^+\tau^-(\gamma)$ events with a small number of clusters, and hadronic events with a large number of clusters. However, the region of the signal does not show a good agreement between the Monte Carlo prediction and the distribution of the data events. The transition region, where the cut is placed ($N_{\mathrm{cluster}} \leq 12$) and the background region are described better. The rather obvious discrepancy points to a deficiency in the simulation program (see Appendix E).

The Monte Carlo multiplicities of both the signal and the hadronic background, in the region of the cut position, are shifted to the left. Since the cut is placed in the transition region between signal and background, the curve for the variation in cross section takes on a parabolic shape. The competing systematic differences change the slope from positive on the signal side to negative on the background side. This compensating effect makes it difficult to assess the systematic error based on the observed change in cross section alone. Also, it introduces a systematic shift in the central value of the measured cross section towards lower values.

For this reason, another method is used to evaluate the systematic error including the shift in the central value. Using a selection of $\tau^+\tau^-(\gamma)$ events based on tracks, a

$$\Phi_{TEC}$$
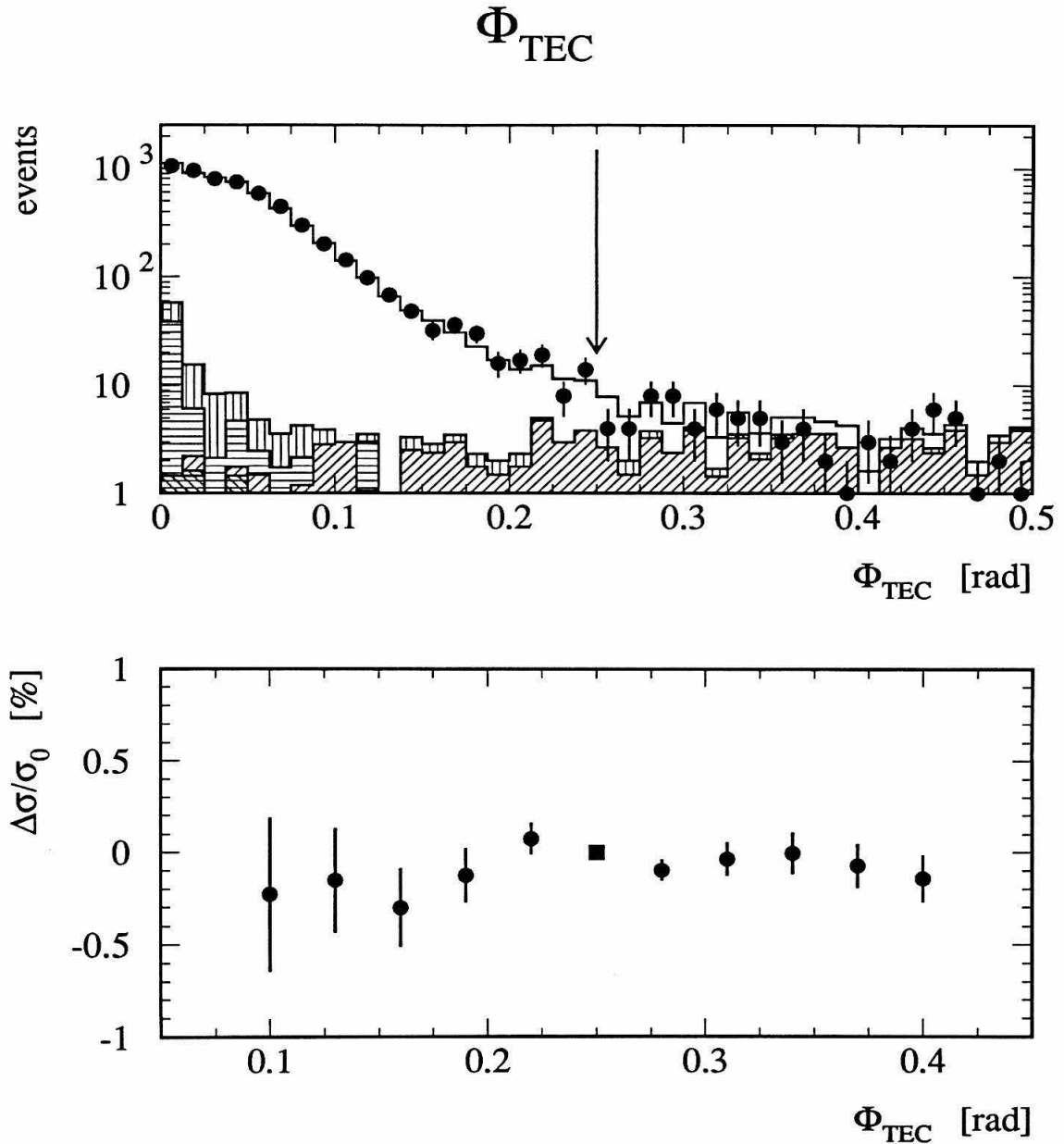
Figure 6.17: Distribution of Φ_{TEC} in the region of the final cut value, after having applied all other selection cuts; and influence on the cross section when moving the cut. See text for the definition of the quantity Φ_{TEC}. The arrow indicates the nominal cut value. The main background (hatched area) at large values of Φ_{TEC} arises from hadronic events.

Cluster multiplicity
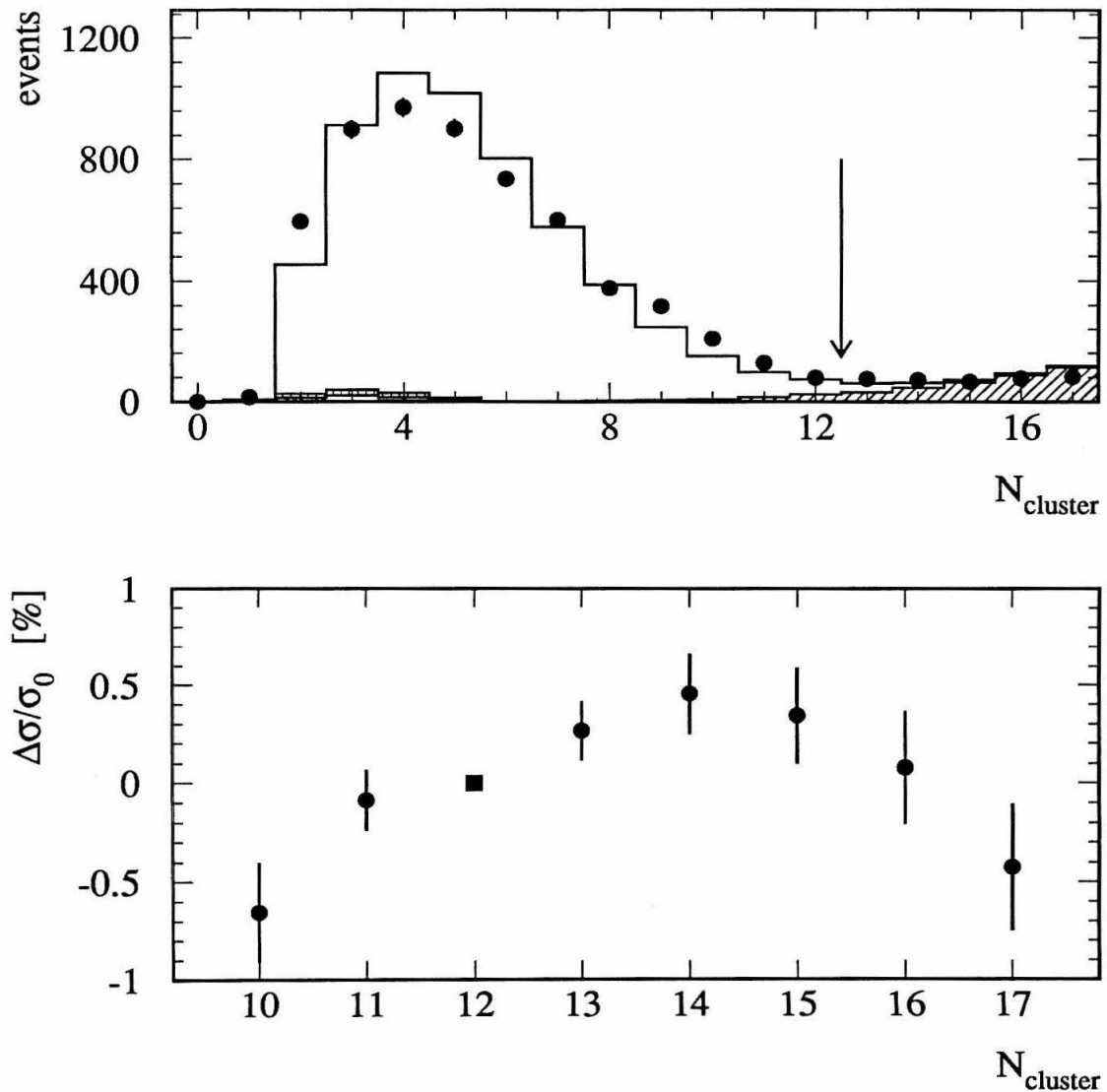
Figure 6.18: Distribution of number of clusters ($N_{cluster}$) in the region of the final cut value, after having applied all other selection cuts; and influence on the cross section when moving the cut. The arrow indicates the nominal cut value. The main background (hatched area) at large values of $N_{cluster}$ arises from hadronic events.

sample of signal events can be obtained without any bias in the cluster-multiplicity distribution, and correspondingly higher hadronic background. The efficiency of the cut on the number of clusters can now be evaluated from the data directly. Since the data distribution has an extended tail, the efficiency determined in this way is decreased with respect to the efficiency evaluated by Monte Carlo, because more events are above threshold. The cross section based on the Monte Carlo predictions must therefore be corrected by multiplying it with the ratio of the two efficiencies.

The treatment described above yields a relative increase in cross section with respect to the one derived from pure Monte Carlo of $+(0.6 \pm 0.2 \pm 0.2)\%$, where the first error corresponds to the statistical accuracy with which the total correction can be estimated, and the second corresponds to the scatter of values obtained from samples of $\tau^+\tau^-(\gamma)$ events selected by different means. The same procedure is applied to hadronic events, to estimate the effect on the cross section due to the correction of the hadronic background, with the result of $+(0.2 \pm 0.1 \pm 0.2)\%$. A simple rescaling of the hadronic background to get agreement yields the same result.

Summarizing, the cross section which results from the use of Monte Carlo predictions for the signal efficiency and for the background has to be corrected by $+0.8\%$. The total systematic error assigned to this number, which includes the systematic error associated with the N_{cluster} cut after applying the correction, is given by 0.4%, i.e., half the total correction, when adding the errors in quadrature.

At this point, there are two possible ways to finalize the rejection of hadron events and thus the selection of τ events. The first method is to use the cut on the number of clusters, and to make the appropriate corrections as described above. The second method uses a rejection of hadron events based on the number of TEC tracks instead. In the latter case, the rejection of hadron events relies completely on TEC tracks. The consequence of this is that all data must be dropped where the TEC high voltage was not at nominal value. The second method thus suffers from a loss in statistics, an increase in the hadronic background, and an additional systematic error in the number of TEC tracks. The first method therefore has been used to extract the final sample of τ events.

6.2 Production Cross Section

After having applied the above selection criteria, approximately 7.4 K events survive in the 1991 data sample, corresponding to an integrated luminosity of 12.5 pb^{-1}. The loss of luminosity due to "bad runs" is small, about 7% in total.

Most of the events (5.8 K) in the data sample are at the peak energy. There are two reasons for this: first, the cross section is maximal on the peak; second, about a factor of ten more luminosity was collected on the peak than at each of the off-peak energy points.

Table 6.2 lists the luminosity used for the analysis at each energy point, the corresponding number of selected events, and the measured cross section extrapolated to the full solid angle. Selection efficiencies and backgrounds are discussed in detail below. The cross section on the peak of the Z° resonance is given by:

$$\sigma(e^+e^- \rightarrow \tau^+\tau^-(\gamma)) \; = \; 1.481 \pm 0.019 \pm 0.013 \text{ nb} \quad , \tag{6.18}$$

where the first error is statistical, and the second systematic. The systematic error of 0.9% (1.4% for the off-peak energies), which includes the error of the luminosity measurement of 0.6%, also is discussed in detail below.

6.2.1 Systematic Errors

There are several contributions to the systematic error in the cross section measurement of the process $e^+e^- \rightarrow \tau^+\tau^-(\gamma)$:

- selection criteria,

- acceptance corrections,

- background subtractions,

- modeling of τ decays in the event generator,

- trigger efficiency,

- luminosity.

Cross Section of $e^+e^- \to \tau^+\tau^-(\gamma)$				
Energy Point	Energy $\sqrt{s}$ [GeV]	Luminosity $\mathcal{L}(s)$ [nb^{-1}]	N_{Data}	Cross Section $\sigma_\tau(s)$ [nb]
-3	88.480	780.4	95	$0.236 \pm 0.024 \pm 0.003$
-2	89.469	851.1	229	$0.531 \pm 0.035 \pm 0.007$
-1	90.228	794.3	359	$0.885 \pm 0.047 \pm 0.012$
Peak	91.242	7795.2	5822	$1.481 \pm 0.019 \pm 0.013$
$+1$	91.967	690.2	425	$1.224 \pm 0.059 \pm 0.017$
$+2$	92.966	759.2	248	$0.641 \pm 0.041 \pm 0.009$
$+3$	93.716	831.9	225	$0.535 \pm 0.036 \pm 0.007$
Sum		12501.3	7403	

Table 6.2: Number of selected data events, luminosity and cross section, where the latter is corrected for acceptance and background, for the process $e^+e^- \to \tau^+\tau^-(\gamma)$. Energies are the luminosity weighted energies of all fills belonging to the energy point. The first errors are statistical, the second systematic.

The measurement of the luminosity is discussed in detail in Chapter 5. The quoted error of the luminosity measurement is 0.6%. The remaining contributions to the systematic error will be discussed in the following paragraphs.

Selection Criteria

There are two cuts which show a clear systematic difference between data and Monte Carlo: the acollinearity and the cluster-multiplicity distributions. The systematic errors associated with these two selection cuts is estimated to be 0.3% and 0.4% respectively, which results into a lower limit of the total systematic error due to event selection of 0.5%.

For each selection criterion, an estimate for the associated systematic error can be derived from the maximal deviations of the cross section when moving the cut position. Table 6.3 lists these systematic error estimates.

Systematic Error due to Selection Criteria		
Selection Criterion	Variation of Cut from ... to	Error $\delta\sigma_\tau/\sigma_\tau$ [%]
$\lvert\cos\Theta_{\text{thrust}}\rvert < 0.73$	0.66 ... 0.75	0.3
$E_{\text{Jet 1}} > 7$ GeV	0 ... 20 GeV	0.3
$E_{\text{Jet 2}} > 3$ GeV	0 ... 7.5 GeV	0.2
$\zeta_{12} < 0.25$ rad	0.10 ... 0.35 rad	0.3
$E_{\text{BGO}} > 2$ GeV	1 ... 7.5 GeV	0.2
$\lvert t_{\text{best}}\rvert < 2.5$ ns	0.5 ... 6.0 ns	0.1
$E_1 < 0.9\,E_{\text{Beam}}$	0.82 ... 0.95 E_{Beam}	0.2
$E_2 < 0.6\,E_{\text{Beam}}$	0.55 ... 0.75 E_{Beam}	0.1
$P_1 < 0.9\,E_{\text{Beam}}$	0.75 ... 1.00 E_{Beam}	0.1
$P_2 < 0.4\,E_{\text{Beam}}$	0.25 ... 0.55 E_{Beam}	0.1
$\Phi_{\text{TEC}} < 0.25$ rad	0.1 ... 0.4 rad	0.2
$N_{\text{cluster}} < 13$	10 ... 17	0.4
Total Estimate		0.8
Estimated Statistical Part		0.5
Total Systematic Error		0.6

Table 6.3: Contribution to systematic error of event selection due to selection criteria. The total error is the quadratic sum of the individual contributions.

However, due to the method used, the estimated errors contain not only a systematic part, but also a statistical part due to the limited amount of data events available for the analysis. This means that the computed cross sections would vary as a function of the cut values, even if the signal and background were perfectly represented by Monte Carlo, due to the statistical fluctuations arising from the finite number of data events. To estimate the statistical part, two methods are employed:

1. The sample of real data events is replaced by a Monte Carlo sample of the same size. These Monte Carlo events are subjected to the same selection pro-

cess and the same procedure to obtain a systematic error. Since in this case by definition the systematic error has to be zero, the estimated values and their variation between different Monte Carlo batches gives a measure of the statistical component of a systematic error.

Several different Monte Carlo samples have been subjected to this procedure. On average, the computed systematic error is of the order of 0.5%. A subtraction in quadrature of this statistical part from the estimated 0.8% (which contains both systematic and statistical effects) yields the purely systematic part, 0.6%.

2. The statistical part of the estimate of the systematic error can be taken into account directly, since the number of data events is known. This amounts to an analysis which determines if the deviations seen in the series of $\Delta\sigma_i/\sigma_0$ points for a given cut are significant or not. The procedure adopted is as follows: For each cut in question, a constant, line, and parabola are successively fitted to the $\Delta\sigma_i/\sigma_0$ points, properly taking into account the correlations between the input points. The polynomial, where the step to the next higher order polynomial gains less than a factor of two in χ^2 per degree of freedom, is taken to determine the systematic error. This is done for each selection criterion by evaluating the mean absolute value of the fitted curve, calculated over the cut range shown in Table 6.3. This procedure results in an estimate of the purely systematic error of 0.55%.

To summarize, the different methods to obtain a systematic error by varying cuts arrive at values between 0.5% and 0.6%. Thus, a total of 0.6% is assigned as the systematic error arising from selection criteria.

Acceptance Correction

A detailed Monte Carlo study of $e^+e^- \rightarrow \tau^+\tau^-(\gamma)$ events including full detector simulation (see Chapter 4) was performed in order to determine the geometrical acceptance and event selection efficiency. The statistical error in the determination

Efficiency and Acceptance of $e^+e^- \to \tau^+\tau^-(\gamma)$ Selection				
Energy Point	Energy $\sqrt{s}$ [GeV]	N_{MC}	Efficiency [%]	4π Acceptance [%]
-3	88.50	10K	77.9 ± 0.5	48.4 ± 0.5
-2	89.50	10K	78.1 ± 0.5	48.6 ± 0.5
-1	90.25	10K	78.3 ± 0.5	49.6 ± 0.5
Peak	91.25	208K	78.05 ± 0.12	49.30 ± 0.12
$+1$	92.00	10K	78.1 ± 0.5	49.1 ± 0.5
$+2$	93.00	10K	77.9 ± 0.5	49.5 ± 0.5
$+3$	93.75	10K	79.0 ± 0.5	48.9 ± 0.5

Table 6.4: Efficiency within the fiducial volume $|\cos\Theta_{thrust}| < 0.73$, and the overall selection efficiency relative to 4π for $e^+e^- \to \tau^+\tau^-(\gamma)$ events for each of the seven energy points. The number N_{MC} of Monte Carlo events used in the analysis also is given.

of these numbers, due to the finite amount of Monte Carlo events available, translates directly into a systematic error on the acceptance correction. In order to keep this error well below the statistical error of the data, a Monte-Carlo sample 16 times as large as the data sample has been used. Table 6.4 lists the values of the selection efficiency determined for each of the seven energy points: within the fiducial volume and within the full 4π acceptance.

It can be seen that the selection efficiency shows a slight variation with center-of-mass energy $\sqrt{s}$. This comes from the one cut, on the acollinearity, which is indirectly $\sqrt{s}$ dependent. The acollinearity between the two most energetic jets of the events, ζ_{12}, must be smaller than 0.25 rad for all energy points. However, the acollinearity distribution becomes wider with increasing center-of-mass energy. In addition, time dependent detector effects imposed on the Monte Carlo events lead to varying efficiencies.

Background Subtraction

The event selection still selects a few background events together with the signal events. However, this remaining background can be subtracted on a statistical basis in order to obtain a precise value for the number of signal events. The amount of background in the accepted sample is determined by using Monte-Carlo event samples for each of the background channels.

The statistical error on the background contamination then leads to a systematic error on the number of selected signal events, after background correction. Since the amount of background in each channel is below the 1% level, its error is not as crucial as the error on the selection efficiency for the signal. Nevertheless, simulated event samples are needed which are at least three to four times as large as the real data sample for each background process.

Table 6.5 lists the background contamination within the accepted sample of events, as estimated by the Monte Carlo study for all possible background reactions. The events are simulated at the Z° peak. The corresponding values for the off-peak $\sqrt{s}$ points are calculated by scaling the number of events for each background process, according to the expected variation of the cross section as a function of $\sqrt{s}$.

Modeling of τ Decays in the Event Generator

In contrast to other leptonic channels, the event generator simulating $e^+e^- \rightarrow \tau^+\tau^-(\gamma)$ events also has to model the decay of the τ's produced, taking into account spin polarizations and their non-trivial influence on the momentum spectra of the τ decay products. Whereas this full dependency can be calculated and implemented in exclusive decays, there still remains one systematic incompleteness. The event generator has implemented only some of the known τ decay channels, and the corresponding branching fractions are neither theoretically nor experimentally known with infinite precision. Because each τ lepton is decayed, the generator implicitly renormalizes the branching fractions of the built-in decay channels to add up to one. Thus the approach of selecting $\tau^+\tau^-(\gamma)$ events by excluding the easier-to-identify

Background in Selected Event Sample		
Channel	N_{MC}	Contamination [%]
Cosmics	—	0.25 ± 0.08
$e^+e^- \to$ hadrons	896K	0.89 ± 0.07
$e^+e^- \to e^+e^-(\gamma)$	60K	0.91 ± 0.12
$e^+e^- \to \mu^+\mu^-(\gamma)$	50K	0.90 ± 0.06
$e^+e^- \to e^+e^- q\bar{q}$	30K	0.02 ± 0.02
$e^+e^- \to e^+e^- e^+e^-$	10K	0.08 ± 0.04
$e^+e^- \to e^+e^- \mu^+\mu^-$	10K	< 0.02
$e^+e^- \to e^+e^- \tau^+\tau^-$	15K	0.02 ± 0.02
Sum	1071K	3.07 ± 0.18

Table 6.5: Background contamination of the selected $\tau^+\tau^-(\gamma)$ sample on the Z° peak. The number N_{MC} of Monte Carlo events used in the analysis also is given.

other Z° decays is well justified.

The most complete event generator available for the simulation of $e^+e^- \to \tau^+\tau^-(\gamma)$ events was used, taking into account electroweak radiative corrections at each stage as well as carrying through helicity amplitudes from the beginning to the τ decays. This generator consists of KORALZ for the electroweak part, combined with TAUOLA to perform the decays of polarized τ leptons (see Chapter 4).

As already indicated during the discussion of the event selection criteria above, the efficiency to select a certain $\tau^+\tau^-(\gamma)$ event will depend on the decay mode of both τ leptons. This is most visible in the case of events where one τ decays into a μ. Figure 6.19 shows the result of a Monte Carlo study to estimate the efficiency for selecting $\tau^+\tau^-(\gamma)$ events, containing muons or not, as a function of $\cos\Theta_{\mathrm{thrust}}$.

Because of the fact that the selection efficiency depends on the τ decay modes, the overall (decay mode averaged) efficiency is dependent on the composition of the event sample, i.e., on the values of the assumed branching fractions of τ decay. An

Efficiency (MC Tag)
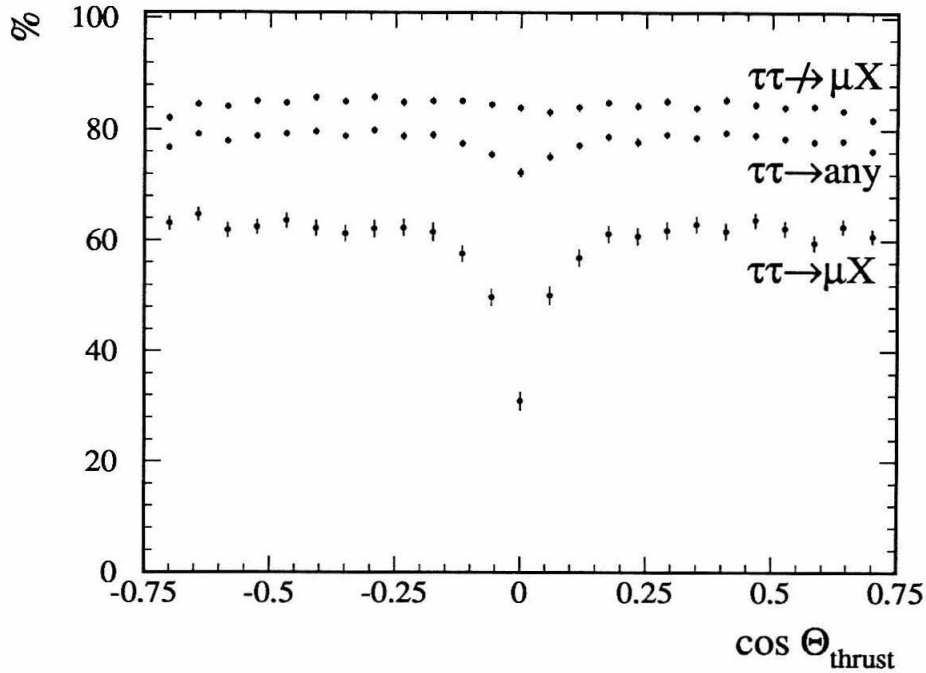
Figure 6.19: Monte Carlo study of efficiency to select $e^+e^- \rightarrow \tau^+\tau^-(\gamma)$ events, where either no τ or at least one τ decays to a μ. The average also is given. The loss in efficiency at $\cos\theta = 0$ for inclusive muon events is due to the crack between the $+z$ and $-z$ chambers of the muon spectrometer. The width of the gap shown here is enlarged, because the angle of the thrust axis is plotted and not the angle of the μ.

error in the branching fractions translates directly into an error in the determination of the branching-fraction-weighted selection efficiency.

In order to estimate the effect, one has to study the selection efficiency as a function of both τ decays in an event, since $e^+e^- \rightarrow \tau^+\tau^-(\gamma)$ events are selected, and not single τ leptons. Let i denote a specific τ decay. One can define efficiencies m_{ij} to select $\tau^+\tau^-(\gamma)$ events, where the $\tau^+(\tau^-)$ decays via channel i (j).

First, one may check whether the efficiency matrix $M = (m_{ij})$ is symmetric, i.e., whether the efficiency depends on the τ charge. Within the statistical accuracy, the

Efficiency matrix   Efficiency matrix (folded)

	e	μ	π	ρ	a₁	K	K*	nπ	
nπ								92	nπ
K*							92	92	K*
K						66	78	90	K
a₁					93	85	92	91	a₁
ρ				95	94	89	93	94	ρ
π			54	80	80	66	72	79	π
μ		4	42	75	74	43	72	73	μ
e	65	66	72	85	87	80	90	86	e
	e	μ	π	ρ	a₁	K	K*	nπ	
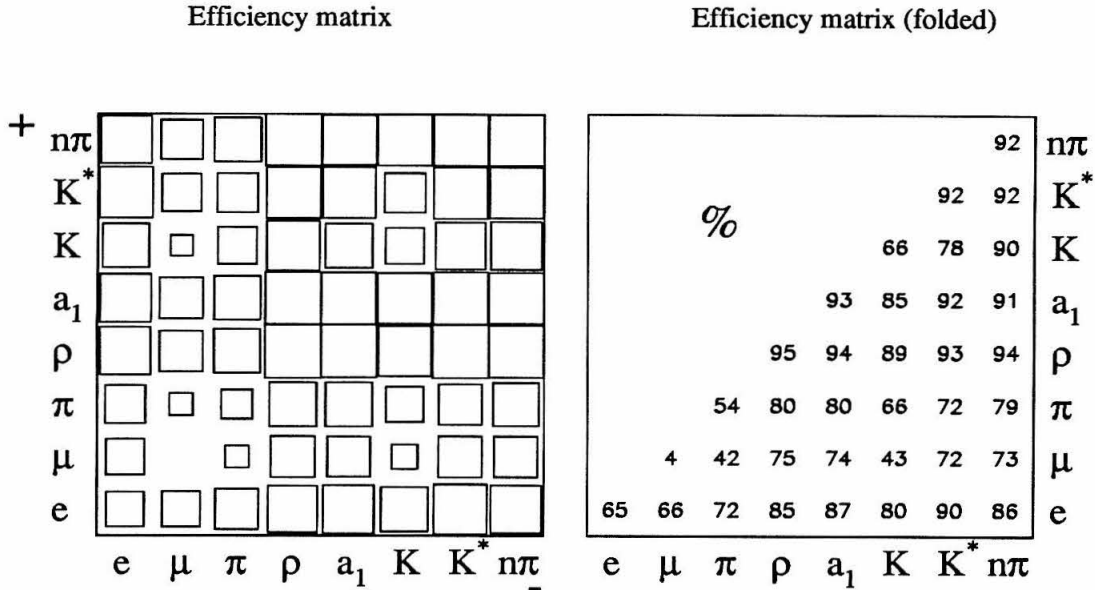
Figure 6.20: Monte Carlo study of efficiency to select $e^+e^- \to \tau^+\tau^-(\gamma)$ events for each combination of the simulated decay modes. The 4 non-resonant decay modes are combined into a generic mult-pion mode denoted $n\pi$. The size of each square is proportional to the selection efficiency. The matrix on the right is calculated from the matrix on the left by averaging over the charge of the decaying τ lepton.

matrix is indeed symmetric, as can be seen graphically in Figure 6.20. The symmetry is expected for the leptonic decay modes (muons of both charges are minimum ionizing, and both electrons and positrons lead to electromagnetic showers with the same average properties). Since the **L₃** detector is approximately an isoscalar target, one expects this to hold also for strongly interacting hadrons (mostly charged pions). After having established that the efficiency is independent of a charge flip, one can fold over the efficiency "square" along its diagonal in order to obtain the efficiency "triangle" (Figure 6.20). The lower than average efficiencies for events containing a μ or single charged π are clearly visible in the figure.

The following consideration will quantify the implications of this effect on the efficiency determination in more detail. Let d_i be the branching fraction of the τ decay mode i. The d_i's can be arranged to form a vector $\vec{d}$, whose actual value is

known only up to a certain accuracy:

$$\vec{d} = \vec{d_0} \pm \delta\vec{d_0} \quad , \tag{6.19}$$

where the index 0 denotes world averages and their errors [11]. Using the symmetry of the matrix M, the efficiency and its uncertainty can be calculated:

$$\begin{aligned} \epsilon \ \equiv \ \vec{d}M\vec{d} \ &= \ \left(\vec{d_0} \pm \delta\vec{d_0}\right) M \left(\vec{d_0} \pm \delta\vec{d_0}\right) \\ &= \ \vec{d_0}M\vec{d_0} \pm \left(\delta\vec{d_0}M\vec{d_0} + \vec{d_0}M\delta\vec{d_0}\right) + \mathcal{O}(\delta^2) \\ &\approx \ \vec{d_0}M\vec{d_0} \pm 2\delta\vec{d_0}M\vec{d_0} \ \equiv \ \epsilon_0 \pm \delta\epsilon_0 \quad . \end{aligned} \tag{6.20}$$

The matrix M listed in Figure 6.20 and the errors on the world-average branching fractions [11] cause an uncertainty in the selection efficiency of $\delta\epsilon_0/\epsilon_0 = 0.25\%$. The dominant contribution to this uncertainty (80% of it) arises from the uncertainty in the muonic branching fraction of $\delta d_\mu = 0.27\%$.

Trigger Efficiency

As described in Chapter 3, the trigger system of the **L3** detector consists of three levels, and each level contains several categories or subtriggers. The selection criteria described above have been designed to lie within the acceptance of the trigger system. Because of the redundancy built into the trigger system, this statement also holds in cases of not too severe subdetector malfunction. To ensure the latter, the time dependent status of each subdetector component, including the trigger, is recorded in the corresponding status database. Detector and/or trigger malfunctioning, which would lead to trigger inefficiencies and loss of events, are thus recognized. The data collected during such periods are declared as bad and not used in the analysis.

In order to check the above statements, one has to make an *a posteriori* analysis of the trigger efficiency using the sample of selected $\tau^+\tau^-(\gamma)$ events. At the basic trigger level, level-1, $e^+e^- \rightarrow \tau^+\tau^-(\gamma)$ events are mainly triggered by the energy and charged track (TEC) subtriggers. The single muon and the scintillator multiplicity subtrigger are of secondary importance. Figure 6.21 shows the trigger efficiencies

Level-1 trigger efficiency   Level-1 Trigger correlation

	Muon	TEC	Scint.	Energy	
Energy				99.07 ± 0.13	
Scint.			27.24 ± 0.58	27.21 ± 0.58	
TEC		87.77 ± 0.43	24.08 ± 0.56	86.95 ± 0.44	
Muon	25.95 ± 0.57	23.45 ± 0.56	2.80 ± 0.22	25.20 ± 0.57	

(%)

Histogram (Level-1 trigger efficiency, %): Muon ≈ 26, TEC ≈ 88, Scint. ≈ 27, Energy ≈ 99.
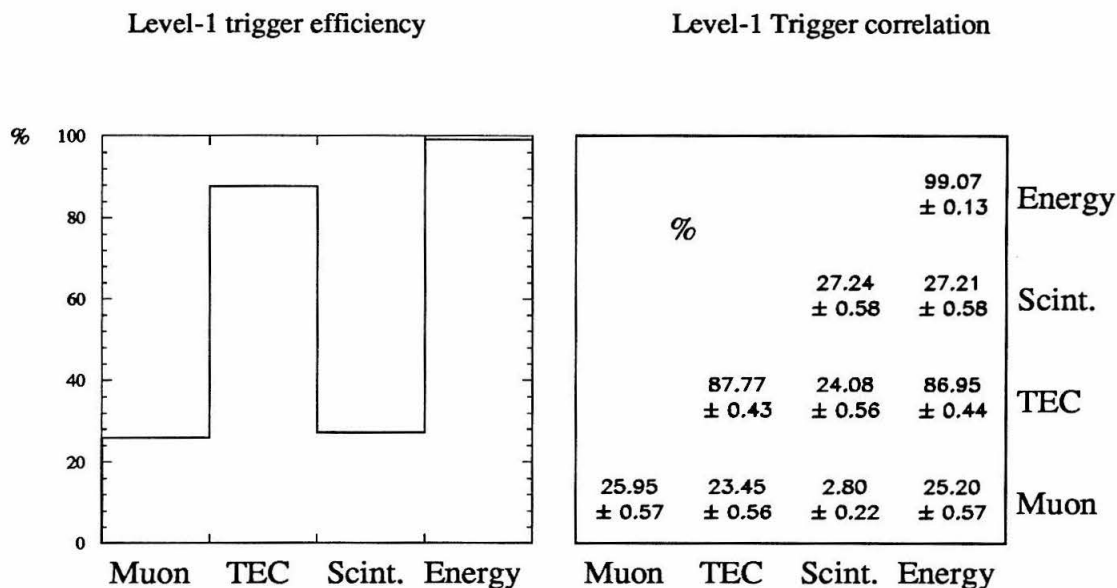
Figure 6.21: Trigger efficiencies and correlations for selected real data $e^+e^- \rightarrow \tau^+\tau^-(\gamma)$ events: The histogram on the right shows the trigger efficiency of the four level-1 trigger categories relevant for $e^+e^- \rightarrow \tau^+\tau^-(\gamma)$ events. The table on the left shows the corresponding numerical values on its diagonal. The percentage of events triggered by at least two triggers is given as the off-diagonal numbers for all possible combinations.

and correlations for all four triggers: muon trigger, TEC trigger, scintillator multiplicity trigger and energy trigger. Since these level-1 triggers make use of mutually exclusive detector components of the $\mathbf{L_3}$ detector, they can safely be assumed to be uncorrelated at the first trigger level. In order to reduce the number of events eventually written to tape further, a level-2 and a level-3 trigger system act on those events which have been triggered by only one of the basic level-1 trigger categories.

Hence there are two categories of events, for which different methods must be used to evaluate the trigger (in)efficiencies:

- Selected $\tau^+\tau^-(\gamma)$ events triggered by more than one level-1 trigger:
  In this case, level-2 and level-3 do not act and therefore need not be considered. Decisions of the level-1 trigger categories are correlated only by the physics

channel under investigation.

- Selected $\tau^+\tau^-(\gamma)$ events triggered by only one level-1 trigger:
  In this case, the level-2 and level-3 triggers must be included in the study of
  the overall trigger efficiency. Decisions of the level-1 trigger categories can
  no longer be assumed to be uncorrelated, since the higher-level triggers make
  extensive use of lower level trigger data.

In total, the analysis of the selected event sample in terms of trigger efficiency leads
to the result, that the combined trigger efficiency is in excess of 99.9% for selected
$\tau^+\tau^-(\gamma)$ events. A correction for trigger inefficiencies is therefore negligible, and the
systematic error arising from it is less than 0.1%.

Summary of Systematic Errors

The total systematic error due to event selection is now calculated as the quadratic
sum of the individual contributions summarized in Table 6.6. Whereas the on-peak
acceptance is known to an accuracy of 0.23%, the off-peak acceptance has an error
of 1% due to a factor of 21 smaller Monte Carlo statistics for these energy points.
This is acceptable, because the statistical error of the off-peak data is appreciably
larger.

The total systematic error of the cross section measurement is thus given by the
systematic error due to event selection, 0.7% (1.2% off-peak), and the error in the
luminosity measurement, 0.6% (Chapter 5). Adding both contributions in quadra-
ture, the total systematic error of the $e^+e^- \rightarrow \tau^+\tau^-(\gamma)$ cross section measurement
amounts to 0.9% for the peak center-of-mass energy, and 1.4% for the off-peak energy
points.

6.2.2 Quality of Data

In order to assess further the quality of the $\tau^+\tau^-(\gamma)$ data in terms of signal and
background, a comparison of the data with Monte Carlo predictions for many vari-

Systematic Error of Cross Section Measurement	
Source	Systematic Error $\delta\sigma_\tau/\sigma_\tau$ [%]
Selection Criteria	0.6
Acceptance Correction (on/off peak)	0.23 / 1.0
Background Subtraction	0.18
Event Generator	0.25
Trigger Efficiency	0.10
Event Selection Total (on/off peak)	0.7 / 1.2
Luminosity	0.6
Total Systematic Error (on/off peak)	0.9 / 1.4

Table 6.6: Contributions to the systematic error of the cross section measurement. The total systematic error is the quadratic sum of the individual contributions.

ables, including some not used in the selection is useful. Some example distributions, shown in Figure 6.22, are discussed below:

- Distribution of $\cos\Theta_{\text{thrust}}$:

  The $\cos\Theta_{\text{thrust}}$ distribution should follow a $1+\cos^2\theta$ form *without* an asymmetry term $A_{\text{fb}}\cos\theta$, since the directional assignment of the thrust axis is given by the energy flow of the event and not by its charge flow. The increase in $e^+e^-(\gamma)$ background towards the boundary of the geometrical fiducial volume, which is close to the physical boundary of the BGO barrel calorimeter, is clearly visible. At these angles, the Bhabha rejection, which is based on high-energy clusters in the BGO with electromagnetic shower shape, becomes less efficient due to edge effects.

- Distribution of Φ_{thrust}:

  The distribution of Φ_{thrust} is expected to be flat, since there is no transverse polarization during physics running at **LEP**. Note that transverse polarization,
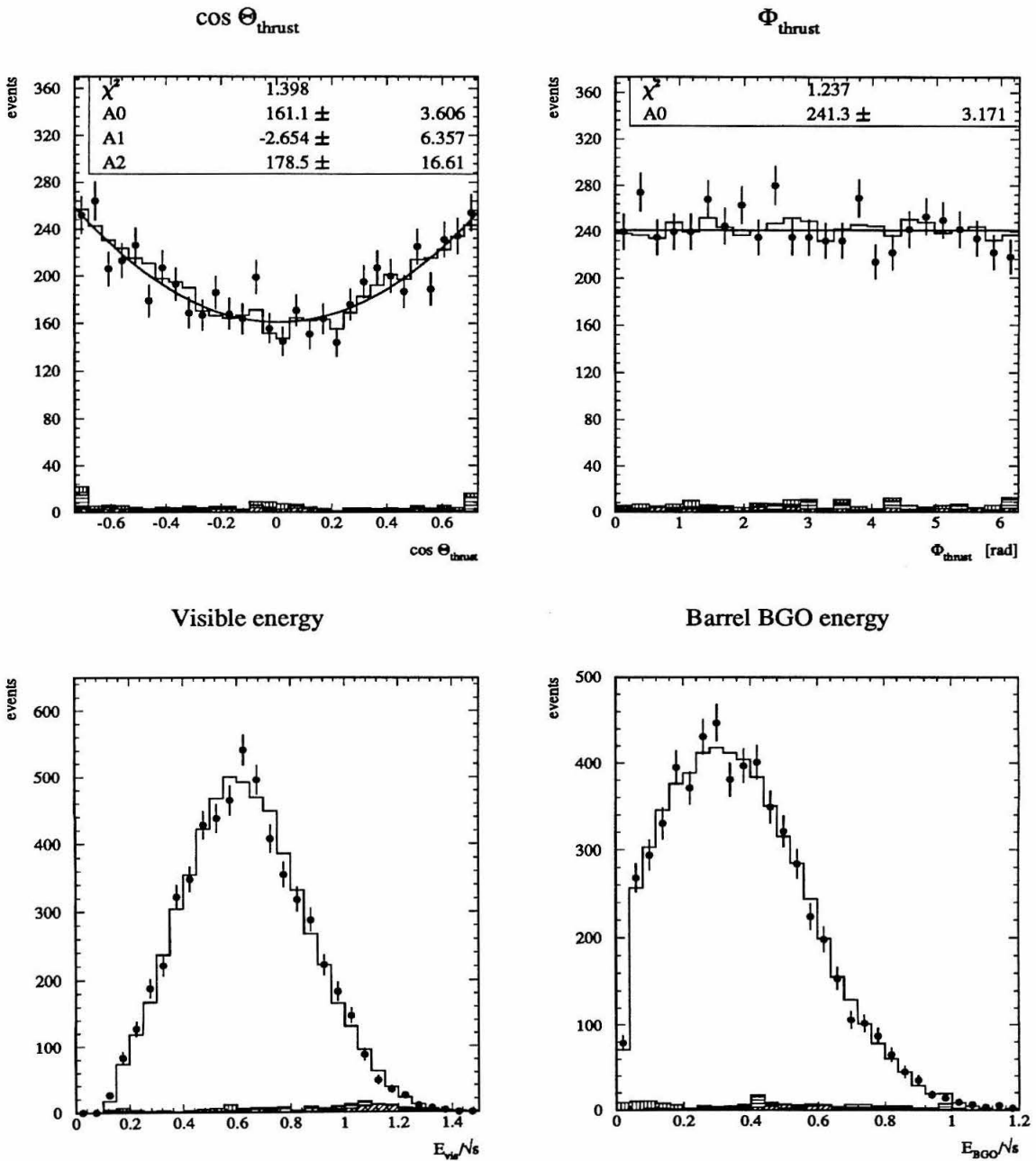
Figure 6.22: Distribution of $\cos\Theta_{\text{thrust}}$, Φ_{thrust}, visible and BGO electromagnetic energy. Also shown are the results of a χ^2 fit of a polynomial of second and zeroth degree to the distributions of $\cos\Theta_{\text{thrust}}$ and Φ_{thrust}, respectively.

used for example to obtain the energy calibration of the **LEP** beams, requires special running conditions of the **LEP** machine.

- Distribution of the total visible energy:
  The distribution of the total visible energy provides a check on backgrounds, especially at low energies (e.g., two-photon events) and at the nominal center-of-mass energy ($e^+e^-(\gamma)$, $\mu^+\mu^-(\gamma)$, and hadron events). No excess with respect to the Monte Carlo prediction is seen in the data.

- Distribution of the total BGO barrel energy:
  The distribution of the total BGO energy checks the rejection of $e^+e^-(\gamma)$ events, which relies on the measurement of high-energy electromagnetic showers in the BGO calorimeter. Again, no excess is visible.

Summarizing, within the statistical accuracy of the data events, no detector malfunctioning or other unexpected physics related effect can be found, either in the variables presented or in any others.

Consistency of 1991 Data

For the peak energy, where the cross section is high, it is possible to measure the production cross section for each fill of the **LEP** machine with a statistical accuracy which is useful for a check of any unexpected time-dependence. Figure 6.23 shows the measured cross section σ_{fill} with statistical error bars $\delta\sigma_{\text{fill}}$. The figure also shows the distribution of $(\sigma_{\text{fill}} - \sigma_0)/\delta\sigma_{\text{fill}}$, which, if truly time-independent, should be Gaussian distributed with a mean of zero and a sigma of one. Within the errors, a Gaussian fit yields the expected values. In order to check for time-dependent effects, a fit is performed to the cross section as a function of fill number, using a straight line as the fitting function. No significant slope is observed.

A coarser binning of the data is obtained by looking at the production cross section on the peak, for each of the three data-taking periods a, b, and c in 1991 separately, as done in Table 6.7. The results are fully statistically compatible, although the **LEP** machine and detector status were quite different during the three periods.

Z-peak cross section per fill
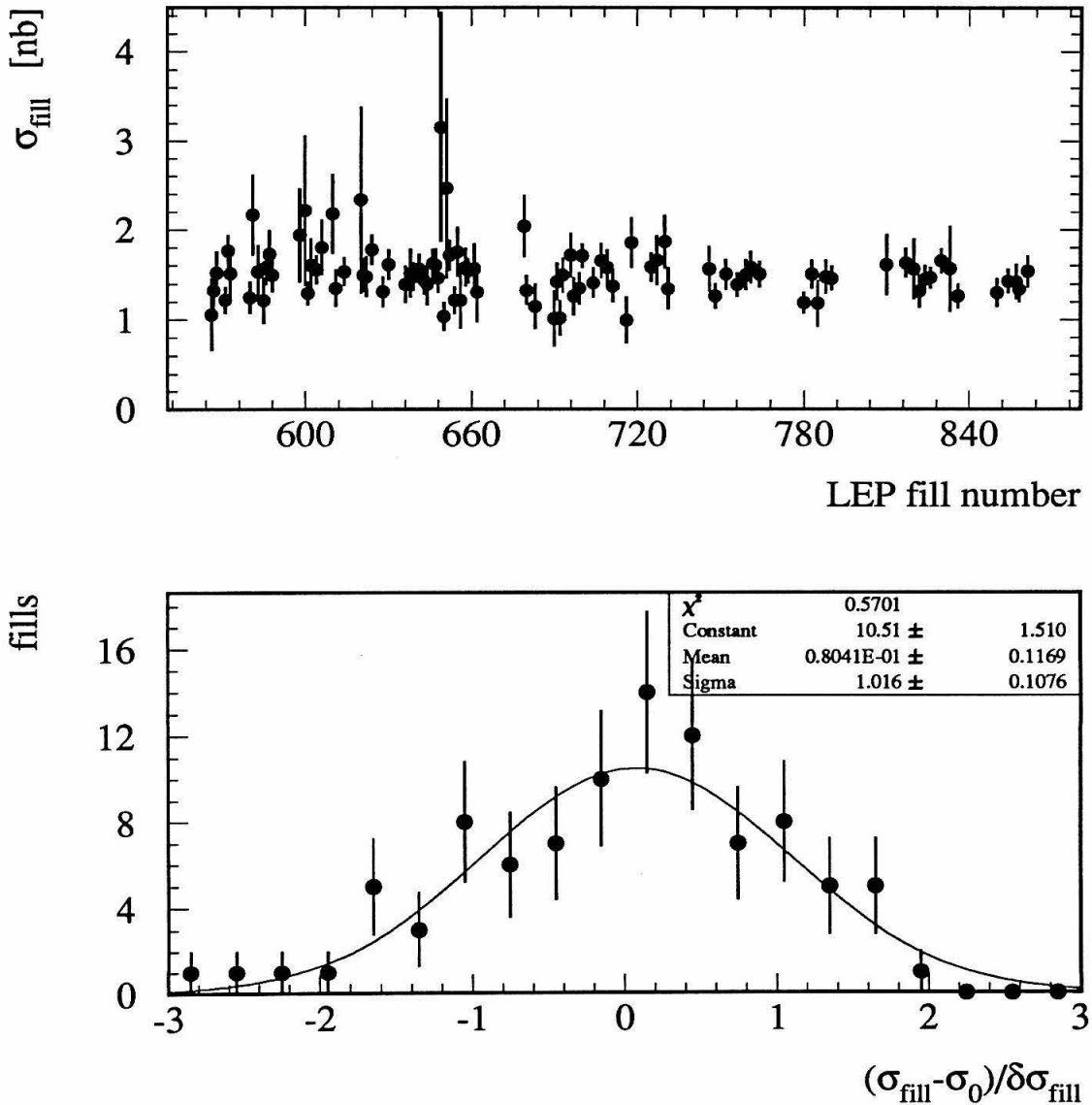
Figure 6.23: Cross section of $e^+e^- \rightarrow \tau^+\tau^-(\gamma)$ for each fill of the **LEP** machine on the Z° peak; and distribution of the deviation of this cross section from the overall result in units of Sigma $= \delta\sigma_{fill}$.

Cross Section Measurement with L_3 in 1991		
Data-Taking Period	Cross Section $\sigma_\tau(m_Z)$ [nb]	1.4 1.5 1.6
1991 a	1.508 ± 0.030	
1991 b	1.461 ± 0.031	
1991 c	1.463 ± 0.044	
L_3 1991	$1.481 \pm 0.019 \pm 0.013$	

Table 6.7: Measurements of the $e^+e^- \to \tau^+\tau^-(\gamma)$ cross section on the peak for the three data-taking periods of 1991, and the combined L_3 result. The first error is statistical. The second is systematic, and includes the error on the luminosity measurement.

6.2.3   Comparison of Cross-Section Measurements

Measurements of L_3

The above measurements using data collected in 1991 can be compared to the results obtained from the 1990 data. For the 1990 analysis [50], different selection criteria were used. Because of less luminosity in 1990, the statistical error in the cross section measurement is clearly larger. The systematic error could be reduced from 2.1% in 1990 to 0.7% for the 1991 data sample (in both cases excluding the uncertainty in luminosity measurement). The main reasons for this reduction are:

- Improved understanding of the L_3 detector:

  - better treatment of time-dependent detector inefficiencies,

  - improved quality of event reconstruction.

- Improved Monte Carlo simulation of the L_3 detector (see Appendix E):

  - switch to a superior GEANT version,

  - more accurate description of the detector within the simulation.

The measurements for 90.25 and 91.25 GeV center-of-mass energy are in good agreement with each other (Table 6.8). The measurements at the other energy points can not be compared directly between the two years, because the two sets of remaining off-peak center-of-mass energies are exclusive.

Cross Section Measurement with L_3 in 1990/91		
Year	Cross Section $\sigma_\tau(s)$ [nb]	
1990	0.921 ± 0.077	1.461 ± 0.033
1991	0.885 ± 0.047	1.481 ± 0.019
Energy	$\sqrt{s} = 90.25$ GeV	$\sqrt{s} = 91.25$ GeV

Table 6.8: Measurements of the $e^+e^- \rightarrow \tau^+\tau^-(\gamma)$ cross section at the two coinciding center-of-mass energies of 1990 and 1991. The error is statistical only.

Measurements of Other LEP Experiments

All **LEP** experiments have performed a measurement of the production cross section of the reaction $e^+e^- \rightarrow \tau^+\tau^-(\gamma)$. Thus, the results from L_3 described above can be compared with the results from ALEPH [53, 54], DELPHI [55, 56] and OPAL [57, 58]. Table 6.9 summarizes the measurements of $\sigma(e^+e^- \rightarrow \tau^+\tau^-(\gamma))$ at the Z° peak obtained by all four **LEP** experiments.

6.2.4 Future Improvements and Final Limitations

Statistical Error

For a given integrated luminosity, the statistical error on the cross section measurement can be reduced in two ways:

1. **Extension of fiducial volume:**
   The current selection is restricted to the barrel region. An extension to the endcap region will enlarge the size of the data sample by approximately 30%.

Cross Section Measurement at **LEP**					
Experiment at LEP	Data of	Cross Section $\sigma_\tau(m_Z)$ [nb]	1.4	1.5	1.6
ALEPH	90	$1.494 \pm 0.024 \pm 0.017$			
DELPHI	90	$1.481 \pm 0.036 \pm 0.022$			
L$_3$	90	$1.461 \pm 0.033 \pm 0.033$			
OPAL	90	$1.443 \pm 0.024 \pm 0.022$			
LEP	90	$1.471 \pm 0.014 \pm 0.011$			
ALEPH	91	$1.481 \pm 0.017 \pm 0.012$			
DELPHI	91	$1.470 \pm 0.020 \pm 0.013$			
L$_3$	91	$1.481 \pm 0.019 \pm 0.013$			
OPAL	91	$1.438 \pm 0.015 \pm 0.011$			
LEP	91	$1.465 \pm 0.009 \pm 0.006$			

Table 6.9: Measurements of the $e^+e^- \rightarrow \tau^+\tau^-(\gamma)$ cross section on the peak of all four **LEP** experiments in 1990 and 1991 and the combined **LEP** result. The first error is statistical, the second systematic.

However, due to lower detector performance in the endcap region (coarser granularity within the hadron calorimeter endcap, no muon chamber and scintillator coverage), larger backgrounds and systematic effects must be expected.

2. Increase of selection efficiency:

Currently, the selection is based mainly on calorimetric quantities. A side effect of this is a low selection efficiency for $\tau^+\tau^-(\gamma)$ events depositing a small amount of energy in the detector. In this respect, a selection also based on tracks can recover events that would be lost otherwise. This is expected to increase the event sample by approximately 8%.

Systematic Error

The systematic error of the cross section measurement is currently dominated by event selection and luminosity. This is unlikely to change. Prospects for an improved luminosity measurement have been discussed in Chapter 5. The error arising from event selection is dominated by the cluster-multiplicity cut used to reject hadron events. Thus the error can easily be reduced if this problem can be solved, either by an improved Monte Carlo simulation or by a (partial) replacement of the $N_{cluster}$ cut by a cut on another variable. Both directions are currently under investigation. Especially due to the excellent HV stability of the TEC during the 1992 data-taking period (less than one momentary HV trip per fill), it may now be possible to perform both a hadron rejection and $\tau^+\tau^-(\gamma)$ event selection on the basis of TEC tracks. The evaluation of different hadronic shower generators within the detector simulation, combined with an ongoing analysis of test beam data, may solve the Monte Carlo discrepancy.

Final Limitations

Final limitations in the $e^+e^- \rightarrow \tau^+\tau^-(\gamma)$ cross section arise from various sources:

- **Event generator – modeling of τ decay channels and kinematics:**
  The hadronic decay modes of the charged τ lepton cannot be calculated from first principles. Thus measurements on τ decays are used as input for event generators to simulate τ decays. In this sense, their simulation will always be slightly worse than the quality of the best available measurements. A way to circumvent this problem is to have a selection which has – as much as possible – the same efficiency for any possible τ decay mode.

- **Selection – complicated $\tau^+\tau^-(\gamma)$ event signature:**
  Since τ decay channels look vastly different in a detector, the above requirement is hard to meet. On the contrary, for a given selection, one wants to use a perfect decay simulation to evaluate efficiencies.

- **Two-photon background − normalization problems:**
  As soon as the fiducial volume is extended to the region of small scattering angles, a problem to worry about is four-fermion processes, especially two-photon hadronic events. They are copiously produced, and no accurate cross section determination is possible using event generators up to now.

- **Luminosity measurement − total error:**
  Independent of the τ analysis, the measurement of luminosity used for normalization introduces an error in each and every cross section measurement.

6.3 Forward-Backward Charge Asymmetry

The forward-backward charge asymmetry, which involves ratios of cross sections:

$$A_{fb} = \frac{\sigma(\cos\theta > 0) - \sigma(\cos\theta < 0)}{\sigma(\cos\theta > 0) + \sigma(\cos\theta < 0)} , \qquad (6.21)$$

has the advantage of being free of normalization uncertainties. In addition to the selection of $\tau^+\tau^-(\gamma)$ events, an asymmetry measurement requires the determination of the scattering angle θ, i.e., the angle of the outgoing fermion (τ^-) with respect to the direction of the beam fermion (e^-), on an event-by-event basis. Its measurement is discussed below.

6.3.1 Determination of Scattering Angle

In order to extract the scattering angle θ_i for event i experimentally, both a geometrical angle of the event, θ_{event} (this yields $\cos\theta_i$ up to a sign), and a charge q (which fixes the sign) has to be measured.

Measurement of Angle

Many different conventions for the geometrical angle θ_{event} are possible, five of which are listed below. They are the polar angle of:

1. the thrust axis,

2. the most energetic charged jet,

3. the second most energetic charged jet,

4. the negatively charged jet,

5. the positively charged jet.

However, all of these choices are equivalent for the kinematically constrained selection used in this analysis, as discussed below. In this analysis, the polar angle Θ_{thrust} of the thrust axis will be used.

Measurement of Charge

Additional requirements must be met by the selected events in order to ensure a correct charge measurement. The charge of the τ lepton is determined from the charge of the decay products, as measured by the curvature of the corresponding tracks in the inner tracking chamber (TEC), in the muon spectrometer as well in the case of muons from τ decay. The sum of the charges of all tracks assigned to a τ jet gives the charge of the jet.

6.3.2   Determination of Asymmetry

Fitting Procedure

The sample of events selected for the measurement of the cross section for $e^+e^- \rightarrow \tau^+\tau^-(\gamma)$ also is used to determine the forward-backward charge asymmetry. This event sample contains no events with hard bremsstrahlung photons due to the cut in acollinearity, and is restricted to large scattering angles due to the fiducial volume cut. Thus it is possible to use an approximate form for the angular dependent part of the differential cross section, which is derived from the lowest-order Born-term formula:

$$\frac{1}{\sigma_{\text{tot}}(s)} \frac{d\sigma(s)}{d\cos\theta} \; = \; \frac{3}{8}\left(1 + \cos^2\theta\right) + A_{\text{fb}}(s)\cos\theta \quad , \tag{6.22}$$

where $A_{\text{fb}}(s)$ is the asymmetry to be measured. A comparison of this ansatz with the full electroweak corrected calculation using the analytical program ZFITTER[2] shows that this approximation gives rise to a systematic error of less than 0.003 in the determination of the asymmetry A_{fb} [50], which is negligible compared to the current statistical errors.

For each center-of-mass energy point, the determination of the asymmetry is carried out using a maximum likelihood fit, where the likelihood function L is defined as the product over the selected events i weighted by the differential cross section

---

[2]The analytical program ZFITTER [45] is discussed in Appendix F.

evaluated at their direction $\cos\theta_i$:

$$L \equiv \prod_i \left[\frac{3}{8} \left(1 + \cos^2\theta_i \right) + A_{fb} \cos\theta_i \right] \quad . \tag{6.23}$$

As a general feature of likelihood fits, a multiplication of the weights with any function symmetric in $\cos\theta_i$ does not change the fitted value of the asymmetry. Since $\cos\theta_i$ is a product of the cosine of a geometrical angle θ_{event} and a charge q, *this* aspect may also be interpreted in the following two ways:

- The acceptance as a function of the geometrical polar angle $\cos\theta$ is not needed, provided that the acceptance is independent of the charge.

- The acceptance as a function of charge is not needed, provided that the acceptance is symmetric in $\cos\theta$.

However, only the first interpretation leads to a useful insight: for an acceptance independent of charge, the advantage of this method to extract A_{fb} is that one does not have to perform a geometrical acceptance correction in order to extract the asymmetry from the data.

As can be seen from the distribution of the thrust axis of selected $\tau^+\tau^-(\gamma)$ events (Figure 6.22), the background of Bhabha events is concentrated at the edges of the fiducial volume, $0.70 < |\cos\Theta_{thrust}| < 0.73$. It is essential to remove this background in order to ensure correct fitting with the ansatz presented above, and to avoid a bias. This is especially true for Bhabha events, which have a much different charge asymmetry due to t-channel effects. Thus, only events whose thrust axis lies within the restricted region of $|\cos\Theta_{thrust}| < 0.70$ are used for the asymmetry measurement.

Correction for Charge Confusion

If N_f and N_b are the number of forward and backward events, measured with an ideal detector, the asymmetry is simply given by:

$$A_{fb}^{true} = \frac{N_f - N_b}{N_f + N_b} \quad . \tag{6.24}$$

However, charge confusion, i.e., the probability P to measure the charge of a given τ jet with the opposite sign, is non-zero for a real detector. Hence the observed asymmetry will be different from the true asymmetry of the event sample. The correction for this effect depends on which requirements are imposed on the charge balance of the event, i.e., whether the charge measurements of both charged jets of an event are combined or not:

1. Looking at the charge of one jet only, the observed number N_f of forward and N_b of backward events is modified to:

$$N_f^{\text{observed},1} = (1-P)N_f + PN_b \tag{6.25}$$

$$N_b^{\text{observed},1} = (1-P)N_b + PN_f \quad , \tag{6.26}$$

which leads to an observed asymmetry of:

$$
\begin{aligned}
A_{\text{fb}}^{\text{observed},1} &= \frac{N_f^{\text{observed},1} - N_b^{\text{observed},1}}{N_f^{\text{observed},1} + N_b^{\text{observed},1}} \\
&= \frac{N_f(1-P) + N_b P - [N_b(1-P) + N_f P]}{N_f + N_b} \\
&= (1-2P)\frac{N_f - N_b}{N_f + N_b} = (1-2P)A_{\text{fb}}^{\text{true}} \quad .
\end{aligned}
\tag{6.27}
$$

Hence the correction to the observed asymmetry is given by:

$$A_{\text{fb}}^{\text{true}} = \frac{A_{\text{fb}}^{\text{observed},1}}{1-2P} \quad . \tag{6.28}$$

An additional relative error of $2\delta P/(1-2P)$ occurs due to the error in the charge confusion, δP. Since one does not exploit the charge correlation of the two charged jets, the correction is linear in P, i.e., large.

2. Deriving the charge of the event from the measurement of the charge of both jets requires the jets to have opposite charge. In this case, the number of forward and backward events becomes:

$$N_f^{\text{observed},2} = (1-P)^2 N_f + P^2 N_b \tag{6.29}$$

$$N_b^{\text{observed},2} = (1-P)^2 N_b + P^2 N_f \quad , \tag{6.30}$$

which leads to an observed asymmetry of:

$$
\begin{aligned}
A_{\text{fb}}^{\text{observed},2} &= \frac{N_f^{\text{observed},2} - N_b^{\text{observed},2}}{N_f^{\text{observed},2} + N_b^{\text{observed},2}} \\
&= \frac{N_f(1 - 2P + P^2) + N_b P^2 - [N_b(1 - 2P + P^2) + N_f P^2]}{(N_f + N_b)(1 - 2P + 2P^2)} \\
&= \frac{1 - 2P}{1 - 2P + 2P^2} \frac{N_f - N_b}{N_f + N_b} \approx \frac{1}{1 + 2P^2} A_{\text{fb}}^{\text{true}} \quad , \tag{6.31}
\end{aligned}
$$

where in the approximation terms of order P^3 have been neglected. Hence the correction to the observed asymmetry is given by:

$$A_{\text{fb}}^{\text{true}} \approx (1 + 2P^2) A_{\text{fb}}^{\text{observed},2} \quad . \tag{6.32}$$

The relative error introduced by δP, using this technique is $4P\delta P/(1 + 2P^2)$. This method is preferable, because the correction factor is much closer to unity. In addition, for a given charge confusion $P \pm \delta P$, the associated error in the correction is smaller by a factor of order $2P$. However, the number of events used in the asymmetry determination has been reduced by $2P(1 - P)(N_f + N_b)$.

The two possible ways to determine the charge confusion from the data are discussed in detail below, along with the corresponding systematic errors. The correction of the observed asymmetry for charge confusion uses method 2 for the reasons given above.

Results

The strict requirement on charge conservation, i.e., that the two charged jets of the event have opposite charge, are fulfilled by 5.7 K events, including 4.5 K on the peak. The main loss of events arises from the charge requirements on the jets, when particles pass through the low resolution regions of the TEC close to the cathode and anode wire planes, and from the reduced fiducial volume of $|\cos \Theta_{\text{thrust}}| < 0.70$.

Forward-Backward Charge Asymmetry of $e^+e^- \rightarrow \tau^+\tau^-(\gamma)$			
Energy Point	Energy $\sqrt{s}$ [GeV]	N_{Data}	Charge Asymmetry $A_{\text{fb}}^\tau(s)$
-3	88.480	80	$-0.106 \pm 0.127 \pm 0.006$
-2	89.469	168	$-0.152 \pm 0.083 \pm 0.006$
-1	90.228	278	$-0.137 \pm 0.070 \pm 0.006$
Peak	91.242	4496	$+0.014 \pm 0.017 \pm 0.006$
$+1$	91.967	328	$+0.042 \pm 0.063 \pm 0.006$
$+2$	92.966	186	$+0.161 \pm 0.079 \pm 0.006$
$+3$	93.716	175	$+0.058 \pm 0.082 \pm 0.006$
Sum		5711	

Table 6.10: Forward-backward charge asymmetry for $e^+e^- \rightarrow \tau^+\tau^-(\gamma)$ measured with **L3** in 1991, corrected for background and charge confusion. The first errors are statistical, the second systematic.

The results for the forward-backward charge asymmetry, after correcting for background and charge confusion, are summarized in Table 6.10 for the seven different center-of-mass energies. Note, that the quoted asymmetries are not corrected for the 0.25 rad acollinearity cut. This modification, which is approximately a tenth of the statistical error, is taken into account in the fitting procedure discussed in Appendix F. The forward-backward charge asymmetry on the peak of the Z° resonance is given by:

$$A_{\text{fb}}(e^+e^- \rightarrow \tau^+\tau^-(\gamma)) = +0.014 \pm 0.017 \pm 0.006 \quad , \tag{6.33}$$

where the first error is statistical, and the second systematic. The systematic error is discussed in detail below.

The distributions of the scattering angle $\cos\theta$ for the on-peak and off-peak event samples are shown in Figures 6.24 and 6.25, respectively. The charge asymmetry changes from negative to positive values as a function of $\sqrt{s}$, when crossing the point $\sqrt{s} = m_Z$.

Distribution of cos Θ   (on peak)
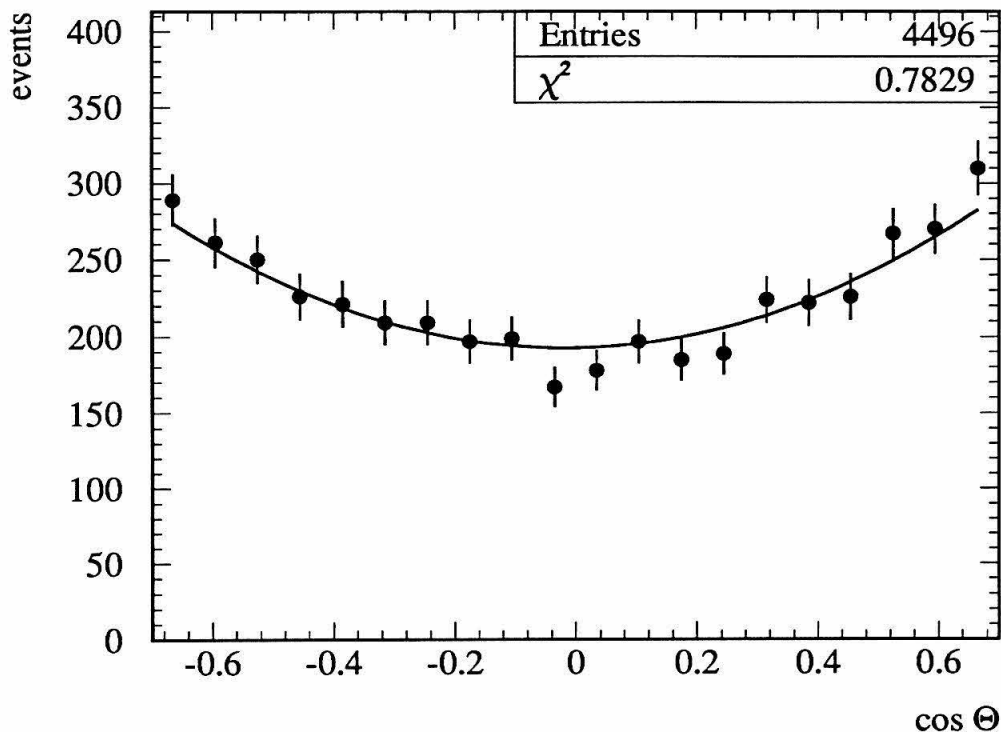
Figure 6.24: Distribution of the scattering angle $\cos\theta$, for events on the Z° peak. The solid line shows the result of a χ^2 fit.

6.3.3   Systematic Errors

The charge confusion, and the way the asymmetry is corrected for it, are possible sources of significant systematic errors. This is discussed in more detail below.

Measurement of Charge Confusion

Charge confusion, the probability P to measure the charge of a τ jet with the wrong sign, results from the finite momentum resolution of the chambers used to measure the track. The space points which are reconstructed from the coordinates measured

Distribution of cos Θ   (off peak)
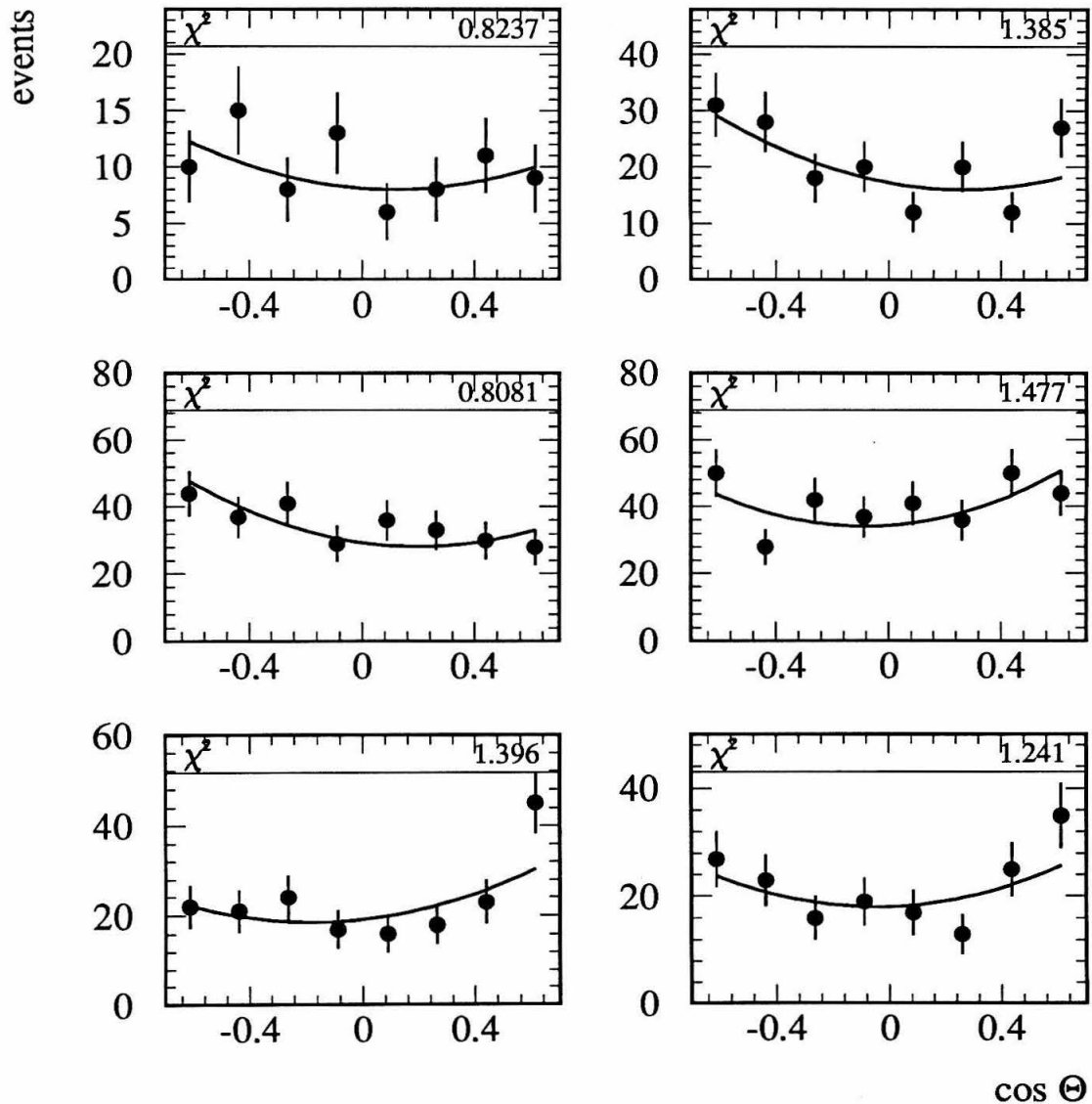
Figure 6.25: Distribution of the scattering angle $\cos\theta$ for events at off-peak center-of-mass energies (energy points $-3, -2$; $-1, +1$; $+2, +3$). The solid line shows the result of a χ^2 fit.

in each chamber are subsequently fitted to a helix, i.e., the trajectory of a particle moving in a homogeneous magnetic field. One of the parameters describing a helix is the curvature of the track, which is directly proportional to q/p, where p is the momentum transverse to the magnetic field, and q is the charge of the particle under consideration ($|q| \equiv 1$ for all particles which it is possible to measure in this way). The intrinsic position resolution of the chamber (Gaussian in coordinates) translates into an error on the fitted quantity q/p, and sometimes leads to a sign flip in this quantity. It is possible to determine the charge confusion of a given event sample from the two-dimensional distribution of the charge of one jet versus the charge of the other jet, as shown in Figure 6.26.

For τ events containing a muon, the charge of the τ lepton decaying to a muon also can be determined by the precise muon chambers. Since the large muon spectrometer has a much better momentum resolution than the compact TEC, this measurement has a negligible charge confusion compared to the charge measurement with the TEC alone. Additionally, using these tagged events, one can estimate the charge confusion of the TEC for τ jets in an unbiased way, by looking at the charge measured in the TEC on the side *opposite* to the muon.

Both methods agree within errors. The value of the charge confusion probability P determined in this way, $P = (10.23 \pm 0.28)\%$, is used to correct the observed charge asymmetry according to method 2.

Momentum Bias of Charge Confusion

The simple recipe presented above, for correcting the observed asymmetry, holds only in the case of an equal and constant charge confusion for each event in the sample. Unfortunately, this is not the case for the τ data. Since the charge confusion arises from momentum resolution, which is itself dependent on the momentum, a momentum dependent charge confusion correction might be needed before integrating over the momentum spectra of the τ decay products. For the two cases discussed above,

Charge versus charge
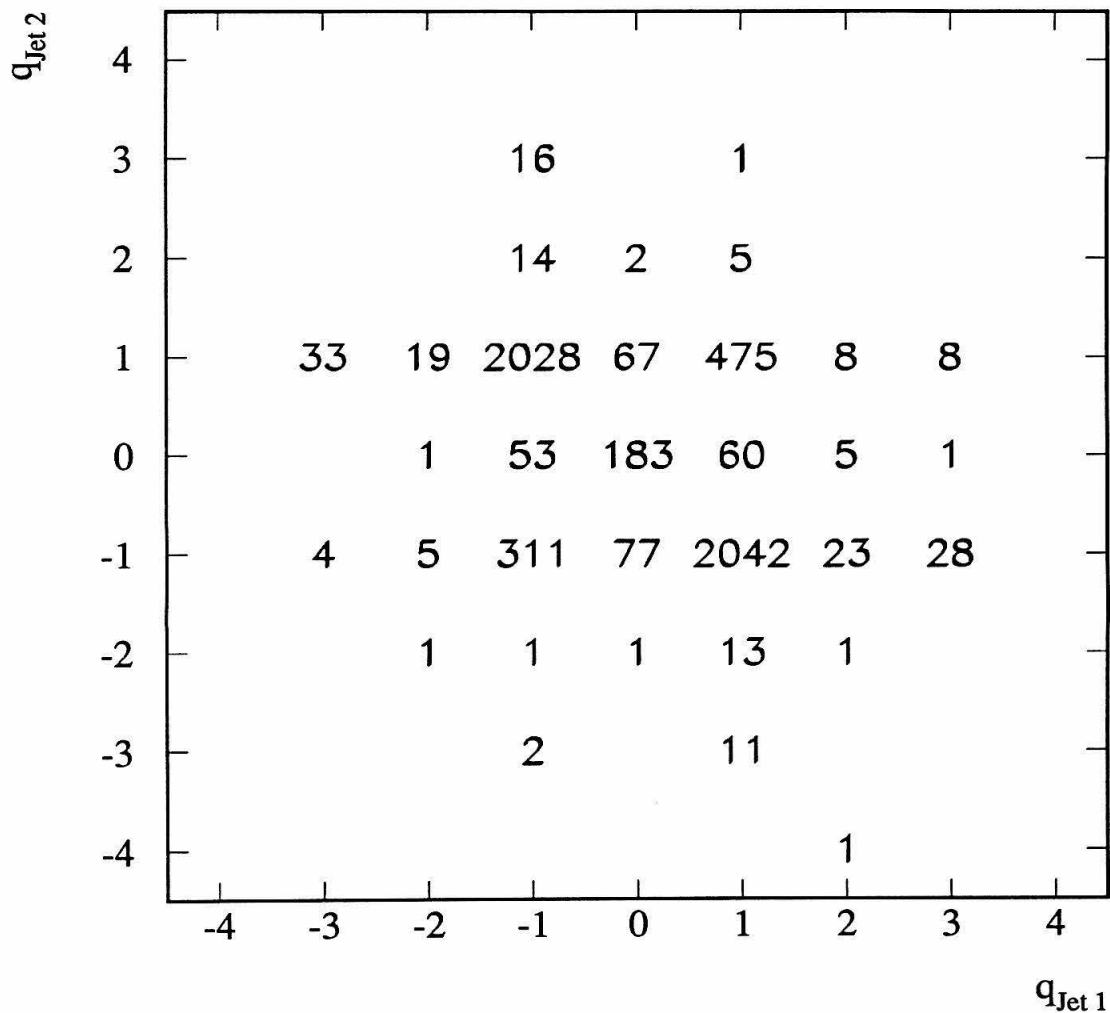
Figure 6.26: Distribution of the charge of jet 1 versus the charge of jet 2 for selected $\tau^+\tau^-(\gamma)$ events on the peak. Of all events, 75% belong to the class where the two jets have opposite unit charges: $q_{Jet\ 1} = \pm 1$, $q_{Jet\ 2} = \mp 1$.

A_{fb}^{true} was computed as follows:

$$A_{fb}^{true} = \int_0^1 dx \int_0^1 dy \sum_{i,j} \frac{n_{i,j}(x,y)}{\epsilon_{i,j}(x,y)} \frac{A_{fb}^{observed,i}(x)}{1 - 2P(x)} \tag{6.34}$$

$$A_{fb}^{true} = \int_0^1 dx \int_0^1 dy \sum_{i,j} \frac{n_{i,j}(x,y)}{\epsilon_{i,j}(x,y)} \frac{A_{fb}^{observed,i,j}(x,y)}{1 - 2P(x)P(y)} \quad , \tag{6.35}$$

where $n_{i,j}(x,y)dxdy$ is the fraction of $\tau^+\tau^-(\gamma)$ events with decay mode i (j) for the $\tau^+(\tau^-)$, $\epsilon_{i,j}(x,y)$ is the selection efficiency for this type of event, and x (y) is the energy fraction carried by the visible decay products.

Equations 6.34 and 6.35 therefore represent an averaging over the various τ decays, where the branching fractions and the efficiencies for each mode are used as energy dependent weights.[3]

A Monte Carlo simulation was then performed, in order to study the importance of using the precise forms for A_{fb}^{true} (Equations 6.34 and 6.35). The result of this study is, that a correction based on a constant charge confusion P (Equations 6.28 and 6.32), is sufficiently accurate. This is because the statistical errors on A_{fb} due to the finite τ sample size are dominant (see Table 6.10).

Because the Monte Carlo simulation of the L_3 detector does not exactly reproduce the behavior of the TEC (see Appendix E) in the non-Gaussian part of the momentum resolution, which is mainly responsible for any charge confusion, the data itself was used to check the above assertion. The asymmetry was determined for different data samples with different intrinsic charge confusion:

1. sample with charge balance $\text{sign}(q_1) \neq \text{sign}(q_2)$,

2. sample with charge balance $q_1 * q_2 = -1$,

3. sample with charge determined by the muon chambers,

4. samples for specific τ decay channels: e, μ, π, ρ.

---

[3]Note, that the efficiencies $\epsilon_{i,j}(x,y)$ for a $\tau^+\tau^-(\gamma)$ event, where one τ decays into mode i and the other into mode j are not simply a product of individual efficiencies $\epsilon_i(x)$ and $\epsilon_j(y)$.

Within the statistical errors, no bias was be found. This leads to the result that at the current level of statistical significance, the use of the energy dependent weighting of the charge confusion to correct A_{fb} is not required.

Forward-Backward Bias of Charge Confusion

The measurement of the forward-backward charge asymmetry also could be biased, if the charge confusion for forward events, P_f, were different from that of backward events, P_b. Using the average charge confusion P for the total event sample:

$$P \equiv \frac{N_f P_f + N_b P_b}{N_f + N_b} \quad , \tag{6.36}$$

the observed asymmetry would then deviate from the true asymmetry according to:

$$A_{fb}^{\text{observed},1} = (1 - 2P)A_{fb}^{\text{true}} - \left(1 - A_{fb}^{\text{true}} \cdot A_{fb}^{\text{true}}\right)(P_f - P_b) \tag{6.37}$$

$$A_{fb}^{\text{observed},2} \approx \frac{A_{fb}^{\text{true}}}{1 + 2P^2} - \left(1 - A_{fb}^{\text{true}} \cdot A_{fb}^{\text{true}}\right)\frac{P_f - P_b}{1 - 2P} \quad . \tag{6.38}$$

The only possible source for a θ dependence of the charge confusion is a rotation of the two endflanges of the central tracking chamber TEC with respect to each other. This would add an additional amount of curvature $(1/R)$ which has a different sign for forward and backward tracks to the true curvature of a track. After the construction of the TEC had been completed, the rotation of one endflange with respect to the other was measured and found to be (1.55 ± 0.22) μrad, i.e., less than 1μm on the outer radius of the TEC. For 45 GeV tracks in the angular range $45° < \theta < 135°$ (maximal effect), the relative change in sagitta is maximal 0.6%. For charge asymmetries of less than 10%, this leads to a bias of less than 0.1% in the forward-backward charge asymmetry [59]. Since the rotation adds a constant increment to the curvature measured for each track, the relative size of the effect is smaller for tracks of less than 45 GeV momentum, as is the case for τ decay products. The bias of the forward-backward charge asymmetry is thus completely negligible.

An independent check was made to determine $P_f - P_b$, by using the the measurement of the charge in the muon chambers for $\tau^+\tau^-(\gamma)$ events, where one of the

τ's decays to a muon. The charge of the muon is determined with negligible error with the precise muon spectrometer, so that the scattering angle of the event is known, and the event sample can be separated into forward and backward events. To determine the charge confusion P for τ jets in an unbiased way, the charge of the *opposite* τ jet as measured by the TEC is considered. Hence, the charge confusion was determined separately for forward and backward events, with the result:

$$P_f = (11.9 \pm 1.8)\% \tag{6.39}$$

$$P_b = (10.8 \pm 1.7)\% \quad , \tag{6.40}$$

so that:

$$P_f - P_b = (1.1 \pm 2.5)\% \quad , \tag{6.41}$$

which is compatible with zero. Because of the limited sample of data events used for the measurement of the charge confusion for forward and backward events, the accuracy of the quantity $P_f - P_b$ inferred from data is not competitive with that obtained from the geometrical arguments described above.

Summary of Systematic Errors

The correction for the TEC charge confusion introduces a systematic error of $0.001 A_{fb}$. The uncertainty of the asymmetry measurement due to cosmic rays is negligible (less than 0.001). The forward backward asymmetry is corrected for the remaining Bhabha background, which introduces an uncertainty of less than 0.005. The total systematic error on the asymmetry is therefore 0.006.

6.3.4   Quality of Data

The selection of $\tau^+\tau^-(\gamma)$ events for a measurement of the $e^+e^- \rightarrow \tau^+\tau^-(\gamma)$ cross section makes only indirect use of the inner tracking chamber, i.e., in the rejection of high multiplicity hadron events. However, the determination of the forward-backward charge asymmetry fully relies on the track measurement and charge determination given by the TEC. The charge confusion for reconstructed tracks has

Systematic Error of Charge Asymmetry Measurement	
Source	Systematic Error δA_{fb}^{τ}
Fitting Method	0.003
TEC Charge Confusion	$0.001 \cdot A_{fb}^{\tau}$
Background Subtraction	0.005
Cosmic Contamination	0.001
Total Systematic Error	0.006

Table 6.11: Contributions to the systematic error of the forward-backward charge asymmetry measurement. The total systematic error is the quadratic sum of the individual contributions.

already been discussed. A more basic requirement is given by the capability of the TEC to measure tracks. The distribution of the number of TEC tracks for selected events (Figure 6.27) shows good agreement between the data and the Monte Carlo prediction.

Consistency of 1991 Data

As in the case of the cross section measurement, the amount of data allows separate asymmetry measurements for each of the three data-taking periods of 1991. The measured asymmetries on the peak of the Z° resonance, corrected for charge confusion and background, are given in Table 6.12. The values are in agreement with each other, within statistics.

6.3.5   Comparison of Asymmetry Measurements

Measurements of L$_3$

The above measurements using data collected in 1991 can be compared with the results obtained from the 1990 data. Because of less luminosity in 1990, the statis-

Number of TEC tracks   Number of TEC tracks
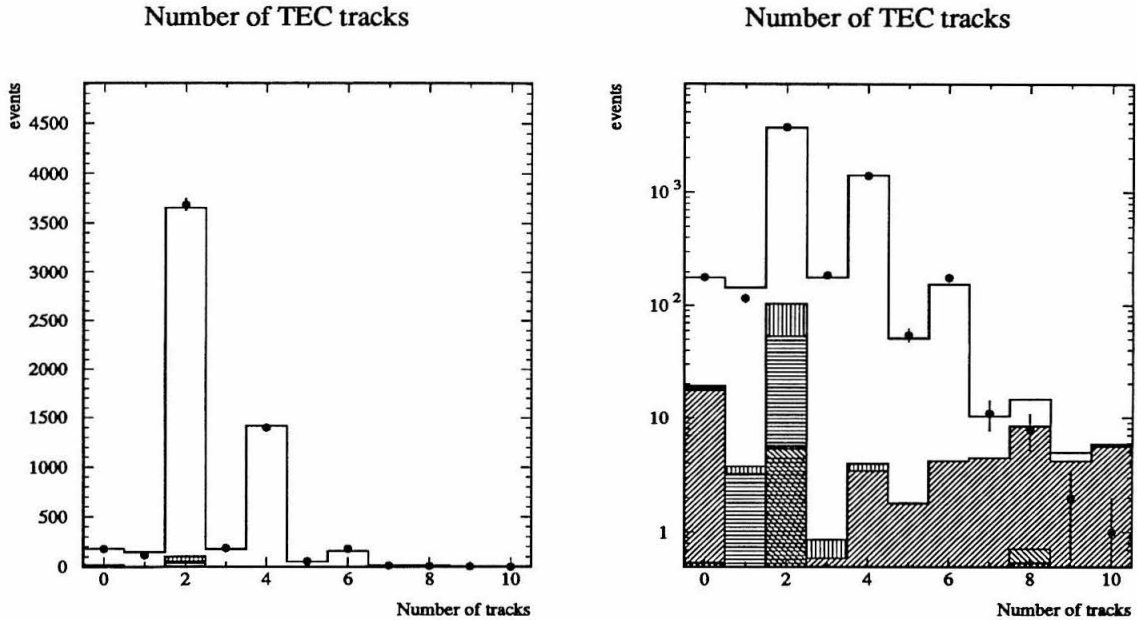
Figure 6.27: Distribution of number of tracks reconstructed in the inner tracking chamber (TEC) for selected $\tau^+\tau^-(\gamma)$ events in linear and logarithmic scale. The background at high number of TEC tracks is given by hadronic events. Bhabha and dimuon background enter in the bin of two (and one) tracks. The entries in the first bin (zero tracks) arise from data taken when the TEC high voltage was off. Hadronic events are thus the dominant background in this bin.

Charge Asymmetry Measurement with **L$_3$** in 1991		
Data-Taking Period	Charge Asymmetry $A_{fb}^\tau(m_Z)$	-0.1 0 $+0.1$
1991 a	$+0.040 \pm 0.025$	
1991 b	$+0.017 \pm 0.027$	
1991 c	-0.061 ± 0.040	
L$_3$ 1991	$+0.014 \pm 0.017 \pm 0.006$	

Table 6.12: Measurements of the $e^+e^- \to \tau^+\tau^-(\gamma)$ charge asymmetry on the peak for the three data-taking periods of 1991, and the combined **L$_3$** result. The first error is statistical, and the second is systematic.

tical error in the asymmetry measurement is larger. The systematic error could be reduced from 0.010 in 1990 to 0.006 for the 1991 data sample. The measurements for 90.25 GeV and 91.25 GeV center-of-mass energy are in agreement (Table 6.13). The measurements at the other energy points cannot be compared directly, because the remaining off-peak energy values do not coincide.

Charge Asymmetry Measurement with $\mathbf{L_3}$ in 1990/91	
Year	Charge Asymmetry $A_{fb}^{\tau}(s)$	
1990	-0.18 ± 0.11	$+0.073 \pm 0.032$
1991	-0.14 ± 0.07	$+0.014 \pm 0.017$
Energy	$\sqrt{s} = 90.25$ GeV	$\sqrt{s} = 91.25$ GeV

Table 6.13: Measurements of the $e^+e^- \to \tau^+\tau^-(\gamma)$ charge asymmetry at the two coinciding center-of-mass energies of 1990 and 1991. The error is statistical only.

Measurements of Other LEP Experiments

All **LEP** experiments have performed a measurement of the forward-backward charge asymmetry of the reaction $e^+e^- \to \tau^+\tau^-(\gamma)$. Thus, the results from $\mathbf{L_3}$ described above can be compared with the results from ALEPH [53, 54], DELPHI [55, 56] and OPAL [57, 58]. Table 6.14 summarizes the measurements on $A_{fb}(e^+e^- \to \tau^+\tau^-(\gamma))$ for the peak energy from all four **LEP** experiments.

6.3.6   Future Improvements and Final Limitations

Statistical Error

As for the cross section measurement, a gain in statistical accuracy is obtained by a higher selection efficiency within the fiducial volume, and/or by a selection using an enlarged fiducial volume. In the case of the forward-backward asymmetry, a selection of endcap events is more important, because such events carry a higher weight in the

Charge Asymmetry Measurement at **LEP**			
Experiment at **LEP**	Data of	Charge Asymmetry $A_{fb}^{\tau}(m_Z)$	$-0.1 \qquad 0 \qquad +0.1$
ALEPH	90	$+0.021 \pm 0.016 \pm$ negl.	
DELPHI	90	$-0.014 \pm 0.026 \pm 0.005$	
L$_3$	90	$+0.073 \pm 0.032 \pm 0.010$	
OPAL	90	$-0.007 \pm 0.015 \pm 0.003$	
LEP	90	$+0.009 \pm 0.010$	
ALEPH	91	$+0.003 \pm 0.012 \pm$ negl.	
DELPHI	91	$+0.024 \pm 0.012 \pm 0.003$	
L$_3$	91	$+0.014 \pm 0.017 \pm 0.006$	
OPAL	91	$+0.011 \pm 0.010 \pm 0.003$	
LEP	91	$+0.013 \pm 0.006$	

Table 6.14: Measurements of the $e^+e^- \to \tau^+\tau^-(\gamma)$ charge asymmetry on the peak of all four **LEP** experiments in 1990 and 1991 and the combined **LEP** result. The first error is statistical, the second systematic.

asymmetry determination. However, the amount of charge confusion increases due to shorter TEC tracks at low scattering angles, which reduces the sensitivity.

Systematic Error

Currently, the systematic errors are dominated by the fitting method, i.e., how one extracts the asymmetry from the data, and the background correction.

The fitting method adopted forces the differential cross section into a second-order polynomial in order to extract the asymmetry. This is correct at Born level, but not after inclusion of all corrections. With enough statistics, however, one can revert to the simple counting method, thus avoiding this source of systematic error.

On the experimental side, an improved TEC calibration will result in reduced charge confusion. The improved calibration thus will lead to a reduction in both the

statistical error (because of less events with like-sign jets) and the systematic error (due to a smaller correction for charge confusion).

Final Limitations

Final limitations in the measurement of the $e^+e^- \rightarrow \tau^+\tau^-(\gamma)$ forward-backward charge asymmetry arise from charge confusion and background corrections. The correction for the momentum bias introduced by charge confusion requires accurate event generation, modeling of τ decays, and simulation of the tracking chamber TEC. With increased statistics and improved Monte Carlo simulation of the TEC, careful studies of the momentum and forward-backward bias discussed above will need to be carried out. Accurate event generation also will be required, i.e., only those decay channels will be used for which the full matrix element including spin is available.

Chapter 7

Summary of τ Results from L_3

The first part of this chapter summarizes other measurements of τ leptons performed by the L_3 collaboration [60, 61, 52]. In the second part of this chapter, the measurements are analyzed in the context of the MSM, assuming lepton universality where indicated. The global analysis of the L_3 measurements of Z° decays in terms of both electroweak parameters and new physics is presented in Chapter 8.

7.1   Other L_3 Measurements of Charged τ Leptons

7.1.1   Polarization

The kinematics of τ decay products contain information about the longitudinal polarization $\mathcal{P}_\tau$ of the produced charged τ leptons (Appendix B). L_3 has performed a polarization analysis in all five relevant decay channels [61]. The polarization $\mathcal{P}_\tau$ of the charged τ lepton is measured by determining the linear combination of the helicity $h_\tau = +1$ and $h_\tau = -1$ Monte Carlo distributions which best fit the distribution of data events. For e, μ and π(K) decay modes, the energy distribution of the charged decay product is used. The sensitivity of the decay energy spectrum to $\mathcal{P}_\tau$ in the case of hadronic spin-1 decay products x ($x = \rho, a_1$), is suppressed by a factor
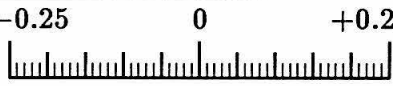
Polarization $\mathcal{P}_\tau$ of the Charged τ Lepton		
Decay Mode of τ	Polarization $\mathcal{P}_\tau$	-0.25 $\qquad$ 0 $\qquad$ $+0.25$
$\tau \to e\nu_e\nu_\tau$	$-0.127 \pm 0.097 \pm 0.062$	
$\tau \to \mu\nu_\mu\nu_\tau$	$-0.020 \pm 0.101 \pm 0.055$	
$\tau \to \pi(\mathrm{K})\nu_\tau$	$-0.148 \pm 0.046 \pm 0.033$	
$\tau \to \rho\nu_\tau$	$-0.152 \pm 0.035 \pm 0.029$	
$\tau \to \mathrm{a}_1\nu_\tau$	$+0.105 \pm 0.164 \pm 0.093$	
L3 $\mathcal{P}_\tau$	$-0.132 \pm 0.026 \pm 0.021$	

Table 7.1: Summary of $\mathcal{P}_\tau$ measurements for all analyzed τ decay channels. The first error is statistical, the second systematic. Also given is the combined value.

$\alpha_x = (m_\tau^2 - 2m_x^2)/(m_\tau^2 + 2m_x^2) < 1$, and is recovered by further analysis of the decays of these particles, i.e., $\rho \to \pi\pi^0$ and $\mathrm{a}_1 \to \rho^0\pi \to \pi\pi\pi$, respectively.

In the polarization fit, the overall normalization has been left free, so that the branching fractions of τ decays are not determined. The τ polarization results for the 1991 data, including 1990 data except for the a_1, are summarized in Table 7.1.

In each decay channel, the statistical error is larger than the systematic error. This will continue to be so even with a much increased number of data events, because the dominant systematic error, due to the limited amount of Monte Carlo events used in the fit, can easily be reduced. The most important systematic errors for each channel are summarized in Table 7.2.

When combining the results of the individual channels, correlations have to be taken into account. For the hadronic decay modes, the common calibration of the calorimetric energy scale for charged pions introduces a correlation of the systematic errors in these channels. The statistical errors are correlated by the fact that the helicities of the two τ decays of each event are completely correlated. The weighted mean from all five analyzed decay modes, taking correlations into account, is:

$$\mathcal{P}_\tau = -0.132 \pm 0.026 \pm 0.021 \quad , \tag{7.1}$$

Systematic Errors of τ Polarization				
Decay Mode of τ	Selection	Background	Calibration	Radiative Corrections	Monte Carlo Statistics
$\tau \to e\nu_e\nu_\tau$	0.027	0.020	0.020	0.020	0.046
$\tau \to \mu\nu_\mu\nu_\tau$	0.020	0.020	0.020	0.010	0.046
$\tau \to \pi(K)\nu_\tau$	0.017	0.009	0.013	0.005	0.021
$\tau \to \rho\nu_\tau$	0.013	0.005	0.020	negl.	0.016
$\tau \to a_1\nu_\tau$	0.045	0.010	0.033	negl.	0.073

Table 7.2: Summary of systematic errors in $\mathcal{P}_\tau$ measurement for all channels.

where the first error is statistical and the second systematic.

This result implies that parity is violated in the neutral weak current process of $\tau^+\tau^-$ production at the Z° resonance, assuming a V − A structure of the charged weak current.

7.1.2 Branching Fractions

Topological Decays

Topological branching fractions are of an inclusive nature. Decays of the charged τ lepton are distinguished solely by the number of charged particles among the decay products. Topological decays are labeled n-prong decays, meaning τ decays to n charged particles plus any number of neutral particles.

The observed multiplicity distribution is corrected for detector effects and for backgrounds, which allows one to determine the τ branching fractions into 1 and 3 charged particles. The branching fraction into 5 or more charged particles cannot be determined directly because the limited size of the data sample (1990 data only), but it is obtained from the normalization condition that all branching fractions sum up to 100%. The results of the measurement are:

$$B(\tau \to 1\text{–prong}) = (85.6 \pm 0.6 \pm 0.3) \,\% \qquad (7.2)$$

$$B(\tau \rightarrow 3\text{–prong}) = (14.4 \pm 0.6 \pm 0.3) \ \% \qquad (7.3)$$

$$B(\tau \rightarrow \geq 5\text{–prong}) < 0.34 \ \% \quad (95\% \ \text{Confidence Level}) \ , \qquad (7.4)$$

where the first error is statistical and the second systematic. The results are in good agreement with current world averages [11].

Exclusive Decays

The measurement of τ polarization results in clean samples of various identified τ decay modes, which are used to determine the branching fractions of the corresponding exclusive τ decay modes. The samples are normalized by using the corresponding integrated luminosity. The preliminary results of an analysis of the leptonic branching fractions of the τ, using the 1991 data are:

$$B(\tau \rightarrow e\nu_e\nu_\tau) = (17.9 \pm 0.4 \pm 0.4) \ \% \qquad (7.5)$$

$$B(\tau \rightarrow \mu\nu_\mu\nu_\tau) = (17.6 \pm 0.4 \pm 0.4) \ \% \ , \qquad (7.6)$$

where the first error is statistical and the second systematic. The results are in good agreement with current world averages [11].

7.1.3   Lifetime

There are two possible methods to determine the lifetime of unstable particles in colliding beam experiments:

1. the decay-length method, which is appropriate when the decay vertex can be reconstructed due to the presence of more than one charged decay product, for example 3-prong τ decays,

2. the impact-parameter method, which is used when there is only one charged particle among the decay products or identified in the detector, for example 1-prong τ decays.

Both methods require the extrapolation of tracks measured in the detector to the region of the interaction point. A reduced error in the track fit can be obtained by

using an external measurement of the energy as a constraint. $\mathbf{L_3}$ is most suited for this procedure in the leptonic decay modes of the τ, due to precise measurements of electron energies in the BGO calorimeter, and muon momenta in the muon chambers.

The lifetime τ_τ of the τ lepton is thus measured with three mutually exclusive event samples (Table 7.3). Since the three event samples are exclusive, the results can be combined. However, the part of the systematic error due to TEC calibration, e.g., drift velocities and time-zero offsets, is correlated. Taking this correlation into account, the combined value for the lifetime of the charged τ lepton is given by:

$$\tau_\tau = (293 \pm 9 \pm 12) \text{ fs} \quad , \tag{7.7}$$

where the first error is statistical and the second systematic.

Obviously, the current τ lifetime measurement of $\mathbf{L_3}$, using solely the inner drift chamber (TEC) for track measurement, will not profit from increased statistics. However, this will change dramatically with the inclusion of the silicon microvertex detector (SMD), which will increase the sensitivity and reduce the systematic error due to track extrapolation towards the vertex.

Lifetime τ_τ of the Charged τ Lepton		
Decay Mode of τ	Lifetime τ_τ [fs]	250 300 350
leptonic	287 ± 17	
1-prong hadronic	289 ± 12	
3-prong hadronic	316 ± 22	
$\mathbf{L_3}\ \tau_\tau$	$293 \pm 9 \pm 12$	

Table 7.3:   Summary of τ lifetime measurements for leptonic decays (impact-parameter method with energy constraint), 1-prong hadronic decays (impact-parameter method), and 3-prong hadronic decays (decay-length method), including statistical errors. Also given is the combined value, where the second error is systematic.

7.2   Standard Model Parameters from τ Data

7.2.1   Lifetime and Branching Fractions

There exists a linear relationship between the lifetime τ_τ and the leptonic branching fractions B_ℓ^τ of charged τ leptons:

$$\tau_\tau = \frac{1}{\Gamma_\ell^\tau} B_\ell^\tau \quad , \tag{7.8}$$

where the leptonic decay width Γ_ℓ^τ of the charged τ lepton can be very accurately calculated within the framework of the MSM (Appendix B).

Previous measurements show an inconsistency between the measured values and their ratio predicted by the MSM, which is often referred to as the consistency problem in the τ sector. Figure 7.1 shows this relationship, displaying L$_3$ measurements, world averages [11] and the MSM relation using the new measurements of the mass of the charged τ lepton (Appendix B).

7.2.2   Strong Coupling Constant

As explained in Appendix B, the ratio of the hadronic to the leptonic decay width of the charged τ lepton is sensitive to the strong coupling constant α_s. Following initial studies [62, 63], L$_3$ was the first LEP experiment to measure $\alpha_s(m_\tau)$ [60]. These initial results are now updated using more precise lifetime and branching fraction measurements [64, 52].

The value for R$_\tau$ obtained by the leptonic branching fractions and by the lifetime of the charged τ lepton are:

$$R_\tau^{\text{branching fractions}} = 3.61 \pm 0.15 \tag{7.9}$$

$$R_\tau^{\text{lifetime}} = 3.60 \pm 0.29 \quad , \tag{7.10}$$

using the leptonic branching fractions and τ_τ as measured by the L$_3$ collaboration and presented above. From the weighted average:

$$R_\tau = 3.61 \pm 0.13 \quad , \tag{7.11}$$

Consistency in τ decays
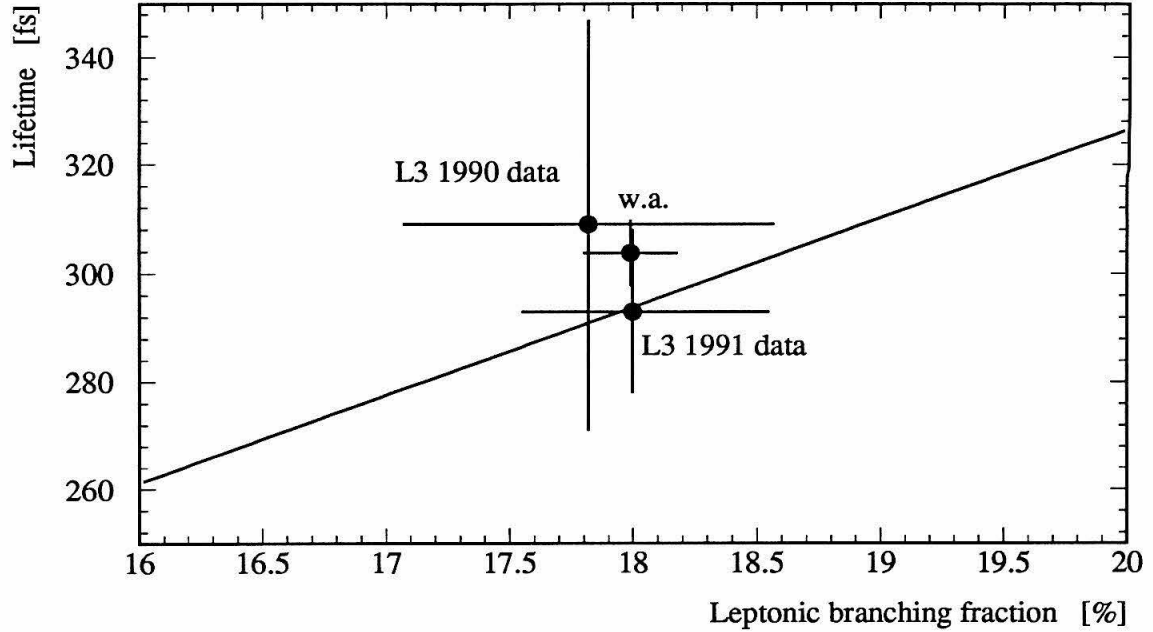
Figure 7.1: Consistency of τ lifetime and leptonic branching fractions of τ decays, comparing **L₃** measurements of 1990 [60], 1991 [52] and world averages [11] (w.a.) with the MSM relation shown as a line.

the value of the strong coupling constant at the scale m_τ is calculated to be:

$$\alpha_s(m_\tau) \;=\; 0.35 \pm 0.06 \pm 0.03 \quad , \tag{7.12}$$

where the first error is experimental, and the second contains the theoretical uncertainty due to missing higher order terms. The latter is estimated as the difference between the results obtained using two different perturbative calculations [65, 66]. The uncertainty due to non-perturbative effects is negligible.

Using the renormalization group equation, this value of the strong coupling constant α_s at the scale of the τ mass can be extrapolated to the scale of the Z° mass, with the result:

$$\alpha_s(m_Z) \;=\; 0.121 \pm 0.006 \pm 0.003 \quad , \tag{7.13}$$

where the first error is from the experimental measurement, and the second is from the theoretical error in $\alpha_s(m_\tau)$. The error of the extrapolation process itself is small. Chapter 8 gives a comparison with other $\alpha_s(m_Z)$ measurements.

7.2.3   Electroweak Parameters

From the cross section measurement for $e^+e^- \rightarrow \tau^+\tau^-(\gamma)$, some basic properties of the Z° boson – the mass, width and the partial decay width into τ pairs – have been extracted. By combining these measurements with the measured asymmetries, the forward-backward charge asymmetry and the polarization asymmetry of τ's, the effective weak neutral current coupling constants of the charged τ lepton under the assumption of e/τ universality also have been determined.

A discussion of the general fitting procedure is given in Appendix F. The current measurement errors in the τ sector allow one to neglect any effects arising from the non-zero **LEP** beam energy spread. The results of the three model independent fits to the τ data alone are listed in Table 7.4.

Electroweak Parameters		
Parameter	Fit Result	Standard Model
m_Z [MeV]	91191 ± 35	—
Γ_Z [MeV]	2502 ± 64	2489
Γ_τ [MeV]	84.1 ± 2.0	83.6
$\chi^2_a/$dof	$6.9/(14\text{-}3)$	—
m_Z [MeV]	91190 ± 37	—
Γ_Z [MeV]	2506 ± 64	2489
g_A^τ	-0.5010 ± 0.0059	-0.501
g_V^τ	$-0.049^{+0.014}_{-0.011}$	-0.035
$\chi^2_b/$dof	$18.7/(28\text{-}4)$	—
m_Z [MeV]	91184 ± 36	—
Γ_Z [MeV]	2505 ± 64	2488
g_A^τ	-0.5017 ± 0.0058	-0.501
g_V^τ	-0.039 ± 0.008	-0.035
$\chi^2_c/$dof	$19.5/(29\text{-}4)$	—

Table 7.4: Results from fits to the $e^+e^- \rightarrow \tau^+\tau^-(\gamma)$ data of **L$_3$** assuming e/τ universality: a) cross section data only; b) cross section and charge asymmetry data; c) cross section, charge asymmetry and τ polarization data. MSM expectations are presented for the fitted Z° mass, $m_t = 150$ GeV, $m_H = 100$ GeV, $\alpha_s = 0.125$.

Tau-pair production
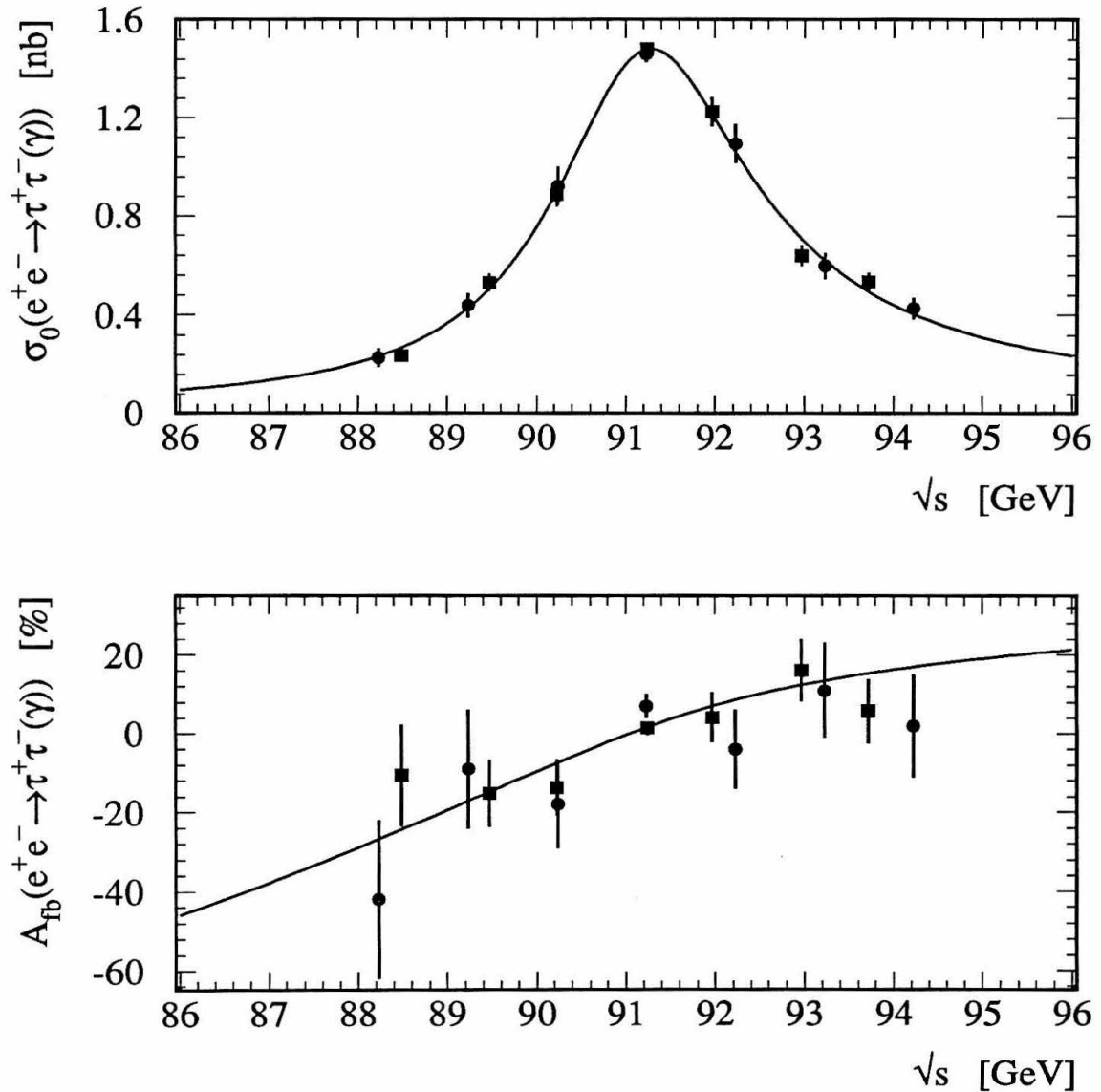
Figure 7.2: The cross section and charge asymmetry for the process $e^+e^- \to \tau^+\tau^-(\gamma)$ as a function of the center-of-mass energy $\sqrt{s}$. Points with error bars are the measured values (circles for 1990 data, squares for 1991 data). The solid curve is the result of the fit to the τ cross section and charge asymmetry data, assuming e/τ universality.

Chapter 8

Standard Model Parameters and New Physics

The first part of this chapter introduces other measurements of Z° bosons relevant for electroweak studies performed by the **L₃** collaboration [50, 67, 68, 52]. In the second part, all these measurements are used to evaluate parameters of the MSM [69, 52]. Evaluation of the same data with respect to possible new physics effects [52] is presented in the last part of this chapter.

8.1   Other **L₃** Measurements of Z° Bosons

The **L₃** collaboration has measured all MSM Z° decay channels, split into the following five different groups:

1. $e^+e^- \rightarrow \tau^+\tau^-(\gamma)$,

2. $e^+e^- \rightarrow \mu^+\mu^-(\gamma)$,

3. $e^+e^- \rightarrow e^+e^-(\gamma)$,

4. $e^+e^- \rightarrow$ hadrons,

5. $e^+e^- \rightarrow \nu\bar{\nu}(\gamma)$.

Because of the hadronization of $q\bar{q}$ pairs from Z° decays, yielding on average about 30 hadrons in the final state, the identification of the flavor of the initial $q\bar{q}$ pair on an event-by-event basis is often impossible. Therefore, all quark flavors are summed over to yield the generic Z° decay to hadrons. Semileptonic decays of b quarks (and to a lesser extend of c quarks) can be used to distinguish $b\bar{b}$ ($c\bar{c}$) from light quarks.

The Z° decays to $\nu\bar{\nu}(\gamma)$ are often referred to as *invisible* decays, because neutrinos are not detected. Therefore, the final state is summed over all existing light neutrino species, i.e., those kinematically accessible in Z° decays. Invisible decay events are tagged by the sole presence of radiative photons from the initial state, i.e., it is purely a measurement of the higher order corrections ($e^+e^- \rightarrow \nu\bar{\nu}\gamma(\gamma)$ events) to the process of neutrino production.

Appendix G contains all the measurements of $\mathbf{L_3}$ used in the following analysis in tabular form. For all fits to the data presented below, the analytical program **ZFITTER** [45] has been used. The types of fits performed, i.e., model independent fit for mass and (partial) widths of the Z° boson, model independent fit for effective coupling constants, and MSM fit, are described in Appendix F.

8.2   Minimal Standard Model Results

8.2.1   Properties of the Z° Boson

Cross section data alone already constrain the basic properties of the Z° boson, including mass, total width and partial widths into the fermion species. A fit of these parameters within a model independent framework is performed, yielding the results presented in Table 8.1. The main results are the measurement of the mass and total width of the Z° boson:

$$m_{\rm Z} = 91.195 \pm 0.006 \pm 0.007 \text{ GeV} \tag{8.1}$$

$$\Gamma_{\rm Z} = 2.490 \pm 0.010 \pm 0.005 \text{ GeV} \quad , \tag{8.2}$$

where the first error is experimental, and the second due to the uncertainties in the **LEP** energy calibration (see Appendix C).

The agreement among the leptonic partial widths, shown in Figure 8.1, confirms lepton universality of the weak neutral current, which is required by the **MSM**. The partial decay width into charged leptons thus is given by:

$$\Gamma_\ell \;=\; 83.1 \pm 0.5 \pm 0.2 \, (LEP) \; \text{MeV} \quad . \tag{8.3}$$

In general, very good agreement with **MSM** predictions is observed.

Number of Light Neutrino Species

The determination of the total and partial widths of the Z boson into charged fermions also constrains the invisible width Γ_{inv}, i.e., the partial width of the Z° decaying into light neutrinos ($m_\nu < m_Z/2$), summed over all species:

$$\Gamma_{\text{inv}} \;\equiv\; \sum_{\ell=e,\mu,\tau} \Gamma_{\nu_\ell} \;=\; \Gamma_Z - \Gamma_{\text{had}} - 3\Gamma_\ell \;=\; 494.0 \pm 9.6 \; \text{MeV} \quad . \tag{8.4}$$

The invisible width is used to determine the number N_ν of light neutrino species. In order to obtain a result independent of the unknown parameters of the **MSM**, such as top and Higgs masses, the following relation is used to evaluate N_ν:

$$N_\nu \;=\; \frac{\Gamma_{\text{inv}}}{\Gamma_\ell} \left(\frac{\Gamma_\ell}{\Gamma_\nu} \right)_{\text{MSM}} \quad . \tag{8.5}$$

Most higher order corrections involving m_t and m_H cancel in the ratio:

$$\left(\frac{\Gamma_\ell}{\Gamma_\nu} \right)_{\text{MSM}} \;=\; 0.5015 \pm 0.0007 \quad , \tag{8.6}$$

where the error is due to residual m_t and m_H dependence estimated by varying m_t between 100 and 200 GeV and m_H between 60 and 1000 GeV. The value of N_ν is thus determined to be:

$$N_\nu \;=\; 2.98 \pm 0.06 \quad , \tag{8.7}$$

where the error, dominated by the error in the luminosity measurement, includes statistical and systematic uncertainties.

Properties of the Z° Boson			
Parameter [MeV]	Results of the Fit with		Standard Model
	six Parameters	four Parameters	
m_Z	$91195 \pm 6 \pm 7$		—
Γ_Z	$2490 \pm 10 \pm 5$		2491^{+13}_{-11}
Γ_{had}	1750 ± 13	1747 ± 11	1740^{+10}_{-8}
Γ_e	83.0 ± 0.6	—	83.8
Γ_μ	82.8 ± 1.0	—	83.8
Γ_τ	84.6 ± 1.2	—	83.6
Γ_ℓ	—	83.1 ± 0.5	$83.7^{+0.5}_{-0.4}$
χ^2/dof	$51/(60\text{-}6)$	$53/(60\text{-}4)$	—

Table 8.1: Properties of the Z° boson obtained from fits to cross section data of L_3. The four parameter fit assumes lepton universality, while the six parameter fit does not. The second error on mass and total width of the Z° boson is due to the uncertainties in the LEP energy calibration (see Appendix C). MSM expectations are listed for the fitted Z° mass (91.195 ± 0.009 GeV), $m_t = 150 \pm 50$ GeV, $m_H = 300^{+700}_{-240}$ GeV, $\alpha_s = 0.124 \pm 0.006$.
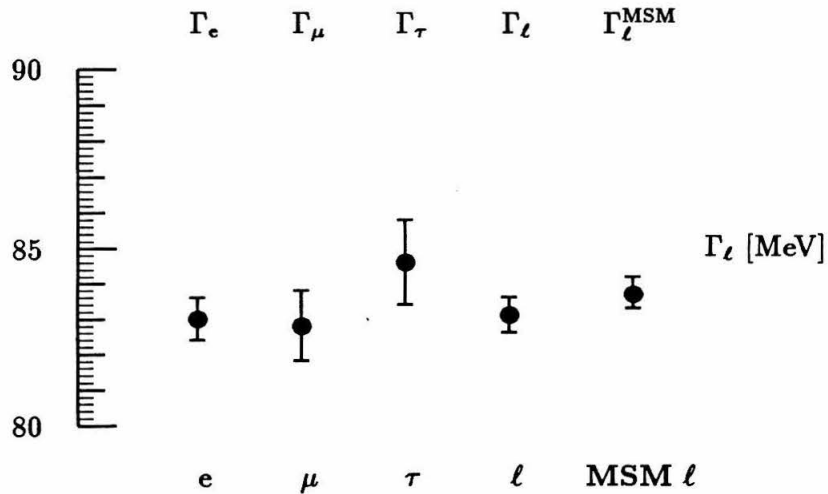
Figure 8.1: Partial widths into charged lepton species.

The above results are verified by the analysis of single photon ($\nu\bar{\nu}\gamma$) events [68], which leads to the following values:

$$\Gamma_{\mathrm{inv}} = 524 \pm 40 \pm 20 \text{ MeV} \tag{8.8}$$

$$N_\nu = 3.14 \pm 0.24 \pm 0.12 \quad , \tag{8.9}$$

where the first errors are statistical, and the second systematic.

8.2.2 Coupling Constants

Strong Coupling Constant

The ratio of the hadronic to the leptonic decay width of the Z° boson is sensitive to the value of the strong coupling constant α_s at the scale of the Z° boson mass. Since most top and Higgs mass dependent corrections are common to both the leptonic and hadronic width, they cancel in the ratio, thus making R_Z, like R_τ, a sensitive tool to determine α_s. The data from $\mathbf{L_3}$ determine:

$$R_Z \equiv \frac{\Gamma_{\mathrm{had}}^Z}{\Gamma_\ell^Z} = 21.00 \pm 0.15 \quad , \tag{8.10}$$

which yields the following value for the strong coupling constant α_s:

$$\alpha_s(m_Z) = 0.156 \pm 0.022 \quad . \tag{8.11}$$

This value has to be compared with the values of α_s obtained from τ decays (Chapter 7) and QCD event shape variables [70]. The numerical results are summarized in Table 8.2. There is good agreement between the results shown in the table.

Weak Neutral Current Coupling Constants

The combination of the forward-backward charge asymmetries for $e^+e^- \to \ell^+\ell^-(\gamma)$, ($\ell = e, \mu, \tau$) can be used to determine the effective weak neutral current coupling constants for charged leptons. Forward-backward charge asymmetries are quadratic in vector and axial-vector couplings:

$$A_{\mathrm{fb}} = \frac{3}{4} \frac{-2g_A^e g_V^e}{(g_A^e)^2 + (g_V^e)^2} \frac{-2g_A^f g_V^f}{(g_A^f)^2 + (g_V^f)^2} \quad , \tag{8.12}$$

Strong Coupling Constant α_s		
Method	$\alpha_s(m_Z)$	0.10 0.15 0.20
Topology	$0.125 \pm 0.003 \pm 0.008$	
R_Z	$0.156 \pm 0.022 \pm 0.005$	
R_τ	$0.121 \pm 0.006 \pm 0.003$	
L3 $\alpha_s(m_Z)$	0.124 ± 0.005	

Table 8.2: Measurements of the strong coupling constant α_s from event shape variables, Z° hadronic width and τ hadronic width; and their weighted mean. The first error is experimental, the second theoretical.

on the peak of the Z° resonance, while the τ polarization is linear in g_A and g_V:

$$\mathcal{P}_\tau = \frac{-2g_A^\tau g_V^\tau}{(g_A^\tau)^2 + (g_V^\tau)^2} \quad . \tag{8.13}$$

Thus, the inclusion of τ polarization in the analysis improves the precision of these constants substantially, and it yields the relative sign between g_A and g_V directly. The absolute sign is inferred from the results of neutrino experiments [71].

A model-independent fit to the combined cross section and lepton charge asymmetry data under the assumption of lepton universality has been performed. Figures 8.2, 8.3, 8.4 and 8.5 show the measured cross sections compared to the result of the fit, as well as the ratio between measured and fitted cross sections. Likewise, Figures 8.6, 8.7 and 8.8 show the measured forward-backward charge asymmetries compared to the result of the fit, as well as the difference between the measured and fitted asymmetries.

In order to determine the effective coupling constants of the weak neutral current for charged leptons as precisely as possible, the τ polarization is included as a constraint in the fit. Table 8.3 summarizes the results of two model-independent fits to the data, which either assume or do not assume lepton universality. In case of the non-universality fit, the values of the fitted parameters again support the hypothesis of lepton universality of the neutral weak current.

Hadron cross section
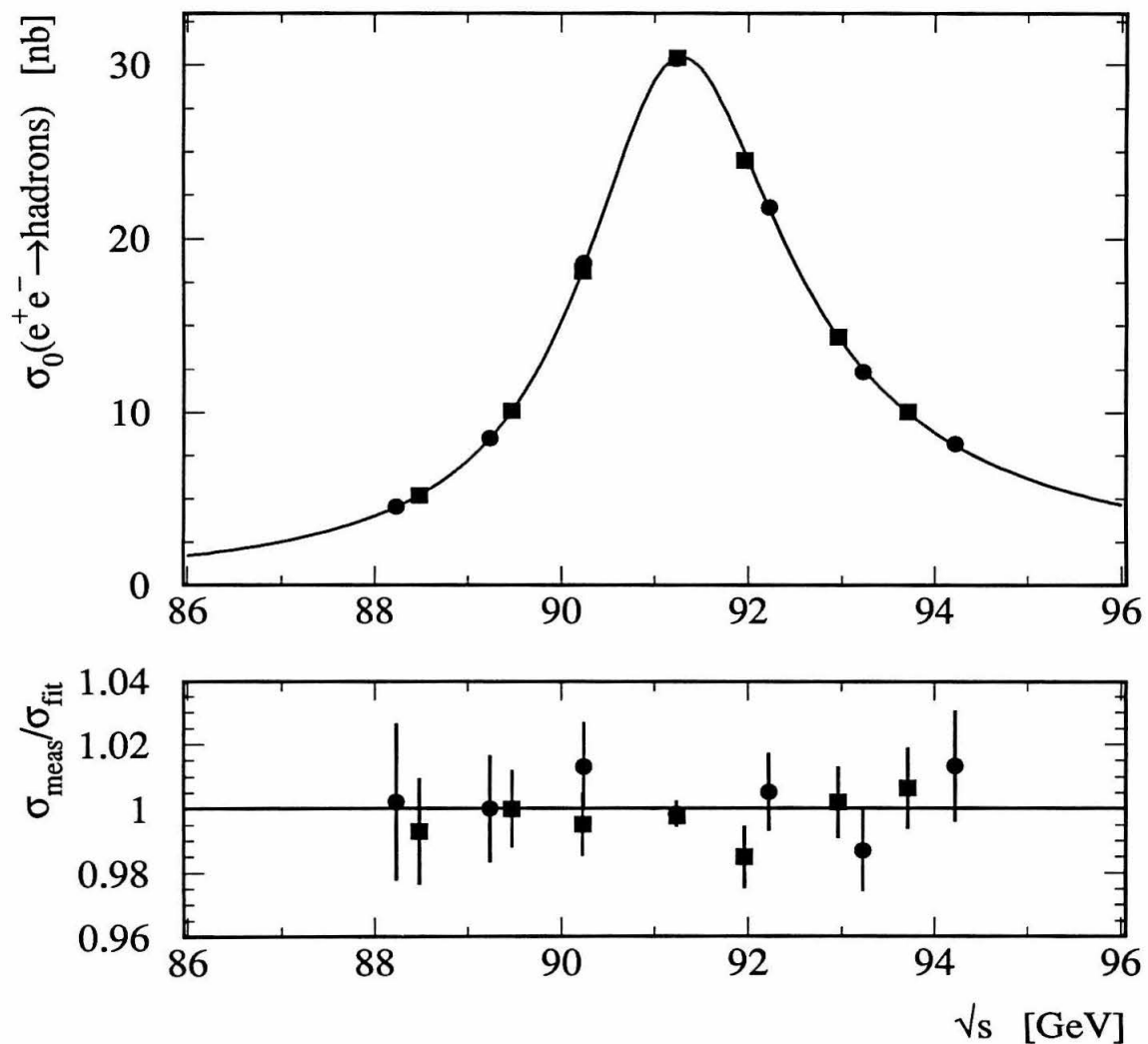
Figure 8.2: Cross section $\sigma_{had}(s)$ for the process $e^+e^- \rightarrow$ hadrons as a function of $\sqrt{s}$. Points with error bars are the measured values (circles for 1990 data, squares for 1991 data). The solid curve is the result of the fit to the combined cross section and lepton charge asymmetry data, assuming lepton universality. Also shown is the ratio of the measured cross section to the fitted cross section for all center-of-mass energy points.

Electron cross section
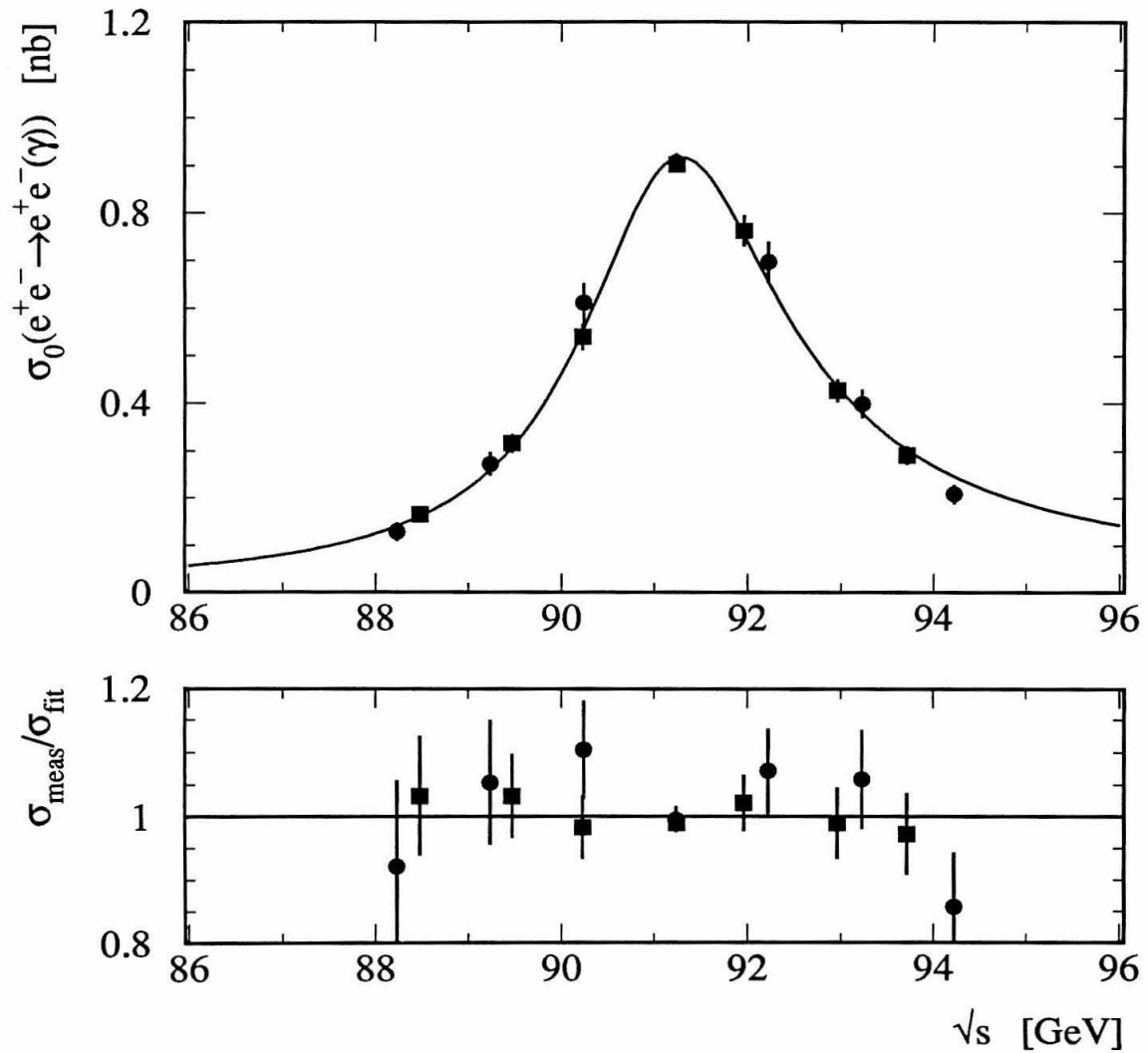
Figure 8.3: Cross section $\sigma_e(s)$ for the process $e^+e^- \to e^+e^-(\gamma)$ as a function of $\sqrt{s}$. Points with error bars are the measured values (circles for 1990 data, squares for 1991 data). The solid curve is the result of the fit to the combined cross section and lepton charge asymmetry data, assuming lepton universality. Also shown is the ratio of the measured cross section to the fitted cross section for all center-of-mass energy points.

Muon cross section
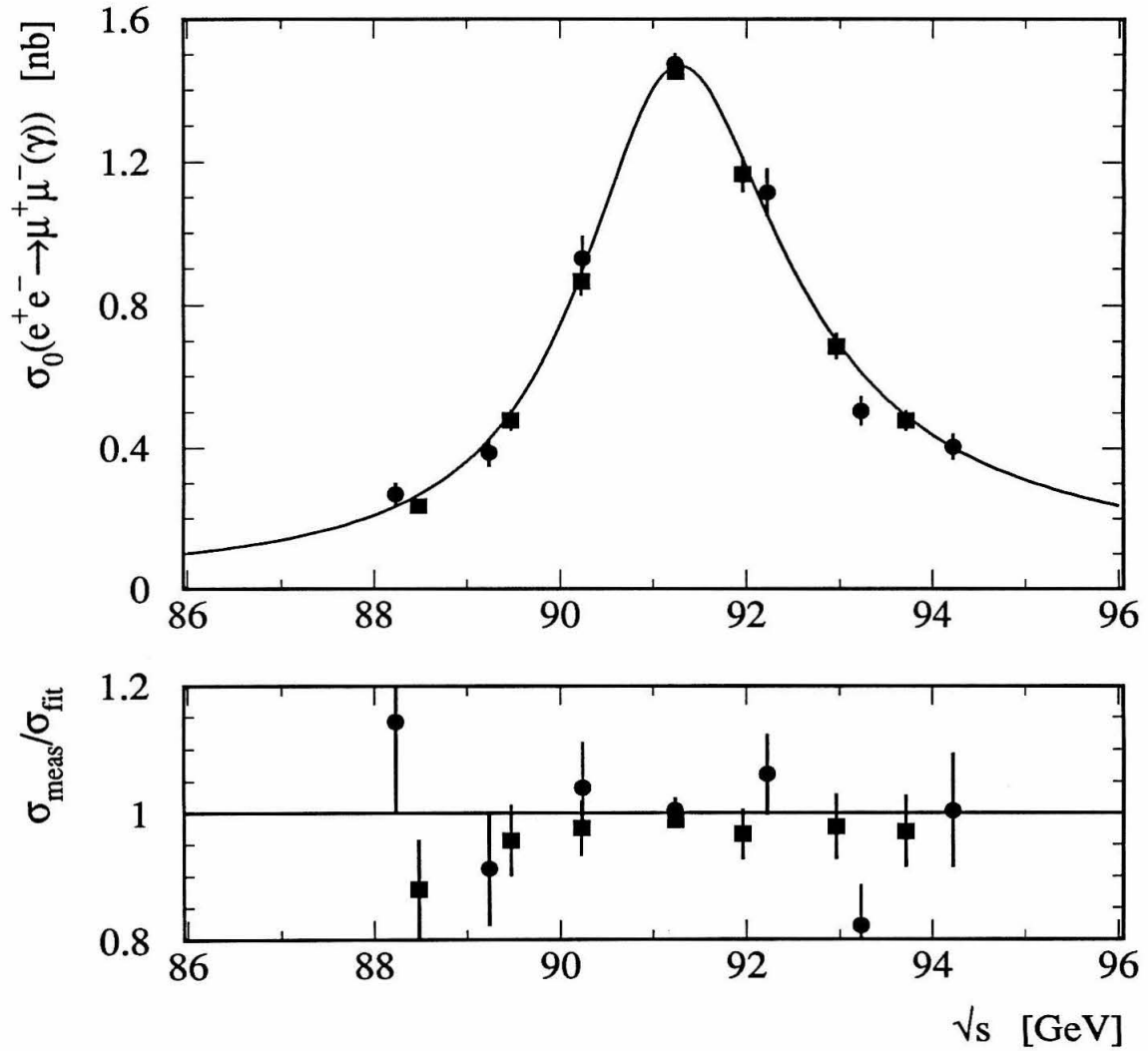
Figure 8.4: Cross section $\sigma_\mu(s)$ for the process $e^+e^- \to \mu^+\mu^-(\gamma)$ as a function of $\sqrt{s}$. Points with error bars are the measured values (circles for 1990 data, squares for 1991 data). The solid curve is the result of the fit to the combined cross section and lepton charge asymmetry data, assuming lepton universality. Also shown is the ratio of the measured cross section to the fitted cross section for all center-of-mass energy points.

Tau cross section
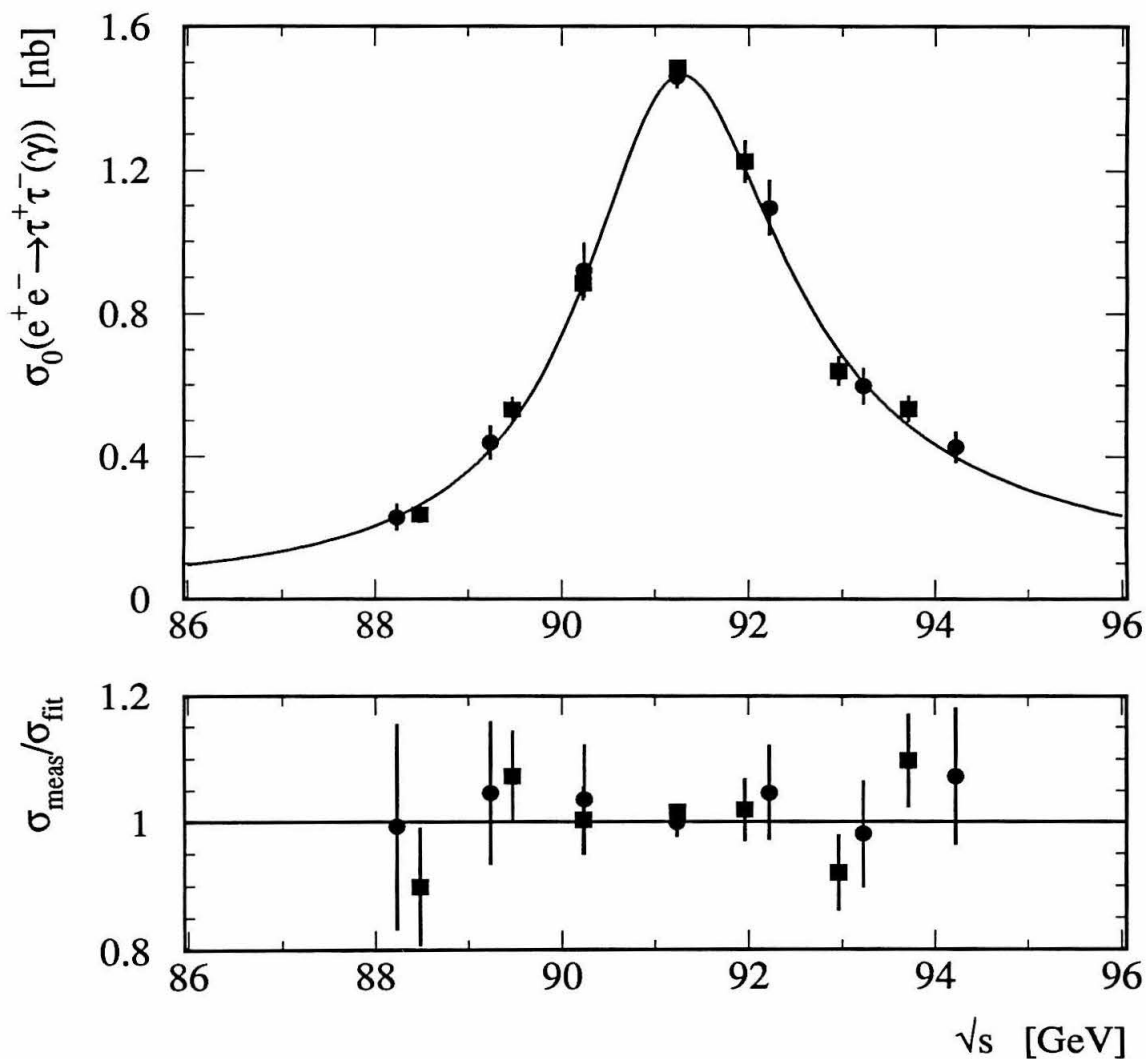
Figure 8.5: Cross section $\sigma_\tau(s)$ for the process $e^+e^- \to \tau^+\tau^-(\gamma)$ as a function of $\sqrt{s}$. Points with error bars are the measured values (circles for 1990 data, squares for 1991 data). The solid curve is the result of the fit to the combined cross section and lepton charge asymmetry data, assuming lepton universality. Also shown is the ratio of the measured cross section to the fitted cross section for all center-of-mass energy points.

Electron charge asymmetry
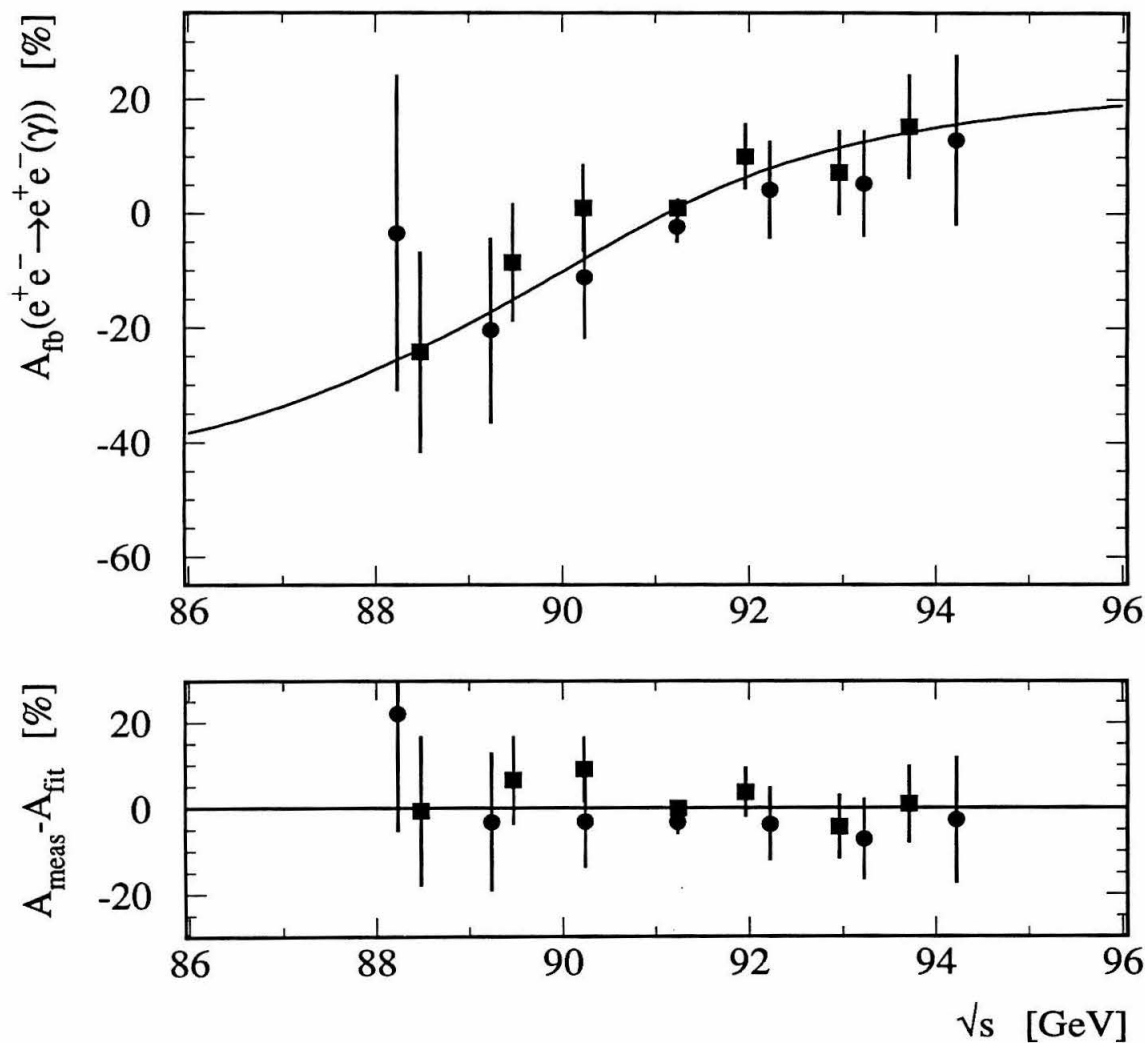
Figure 8.6: Forward-backward charge asymmetry $A_{fb}^e(s)$ for the process $e^+e^- \rightarrow e^+e^-(\gamma)$ as a function of $\sqrt{s}$. Points with error bars are the measured values (circles for 1990 data, squares for 1991 data). The solid curve is the result of the fit to the combined cross section and lepton charge asymmetry data, assuming lepton universality. Also shown is the difference between the measured asymmetry and the fitted asymmetry for all center-of-mass energy points.

Muon charge asymmetry
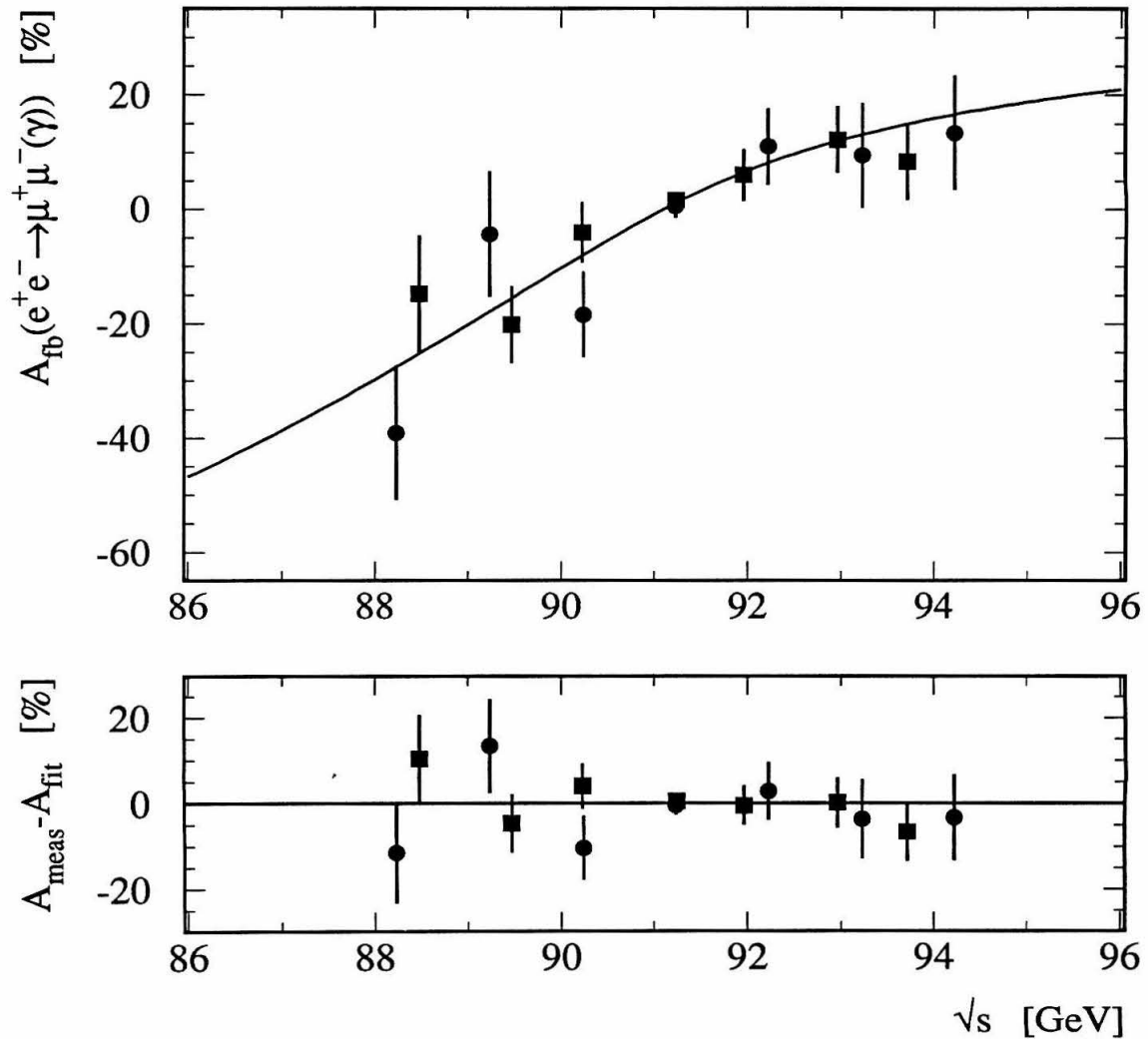
Figure 8.7:   Forward-backward   charge   asymmetry $A_{fb}^{\mu}(s)$ for   the   process $e^{+}e^{-} \rightarrow \mu^{+}\mu^{-}(\gamma)$ as a function of $\sqrt{s}$. Points with error bars are the measured values (circles for 1990 data, squares for 1991 data). The solid curve is the result of the fit to the combined cross section and lepton charge asymmetry data, assuming lepton universality. Also shown is the difference between the measured asymmetry and the fitted asymmetry for all center-of-mass energy points.

Tau charge asymmetry
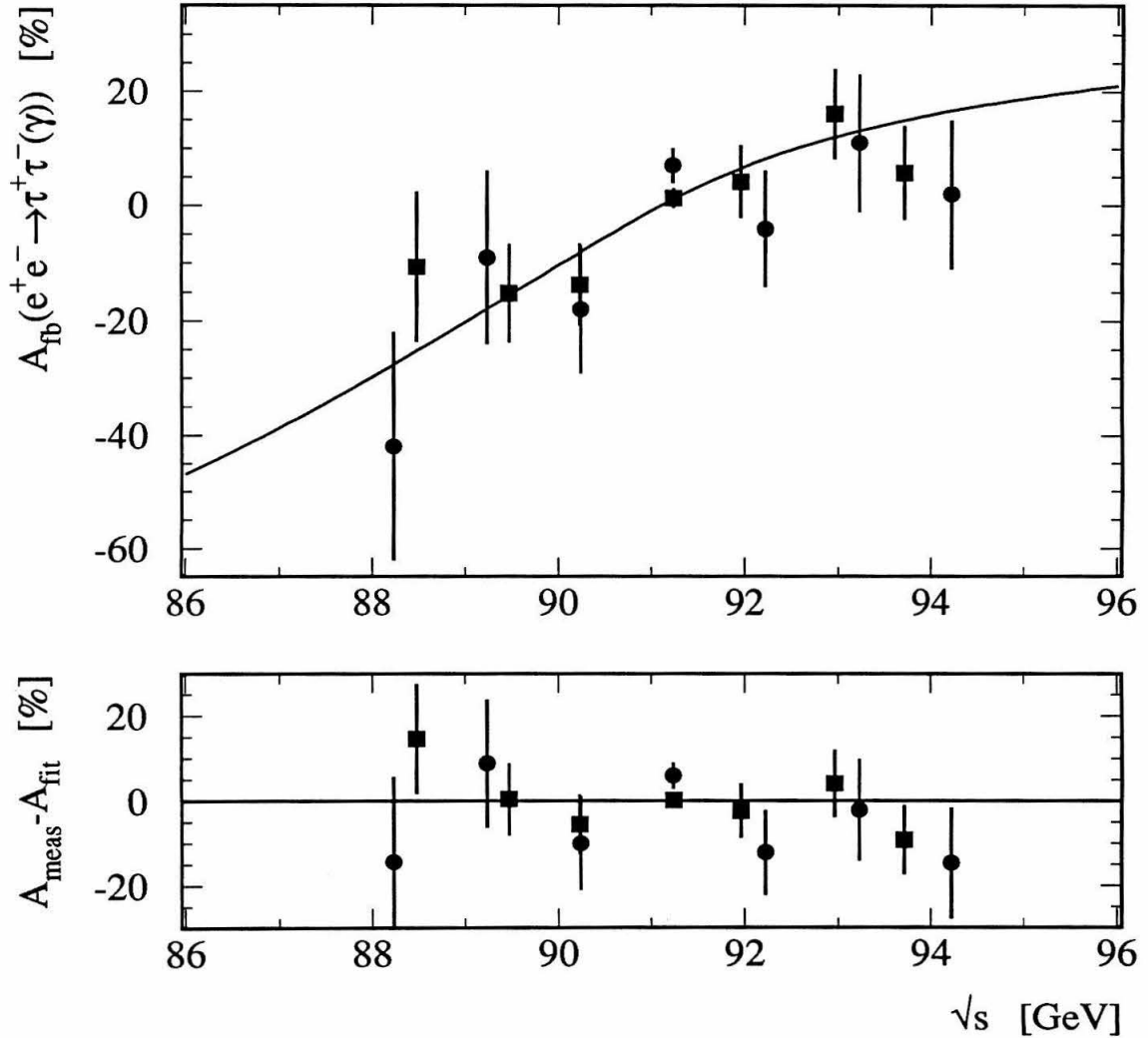
Figure 8.8: Forward-backward charge asymmetry $A_{fb}^{\tau}(s)$ for the process $e^+e^- \rightarrow \tau^+\tau^-(\gamma)$ as a function of $\sqrt{s}$. Points with error bars are the measured values (circles for 1990 data, squares for 1991 data). The solid curve is the result of the fit to the combined cross section and lepton charge asymmetry data, assuming lepton universality. Also shown is the difference between the measured asymmetry and the fitted asymmetry for all center-of-mass energy points.

Electroweak Parameters			
Parameter	Results of the Fit with		Standard
	nine Parameters	five Parameters	Model
m_Z [MeV]	$91195 \pm 6 \pm 7$		—
Γ_Z [MeV]	$2490 \pm 10 \pm 5$		2491^{+13}_{-11}
Γ_{had} [MeV]	1750 ± 13	1747 ± 11	1740^{+10}_{-8}
g_A^e	-0.4980 ± 0.0021	—	-0.501
g_A^μ	$-0.4968^{+0.0050}_{-0.0037}$	—	-0.501
g_A^τ	-0.5032 ± 0.0037	—	-0.501
g_A^ℓ	—	-0.4986 ± 0.0015	-0.501 ± 0.001
g_V^e	$-0.040^{+0.013}_{-0.011}$	—	-0.034
g_V^μ	$-0.048^{+0.021}_{-0.033}$	—	-0.034
g_V^τ	-0.037 ± 0.008	—	-0.034
g_V^ℓ	—	$-0.040^{+0.006}_{-0.005}$	$-0.034^{+0.004}_{-0.003}$
χ^2/dof	$81/(106\text{-}9)$	$83/(106\text{-}5)$	—

Table 8.3: Electroweak parameters obtained from fits to the cross section and lepton charge asymmetry data including τ polarization, of **L3**. The five parameter fit assumes lepton universality, while the nine parameter fit does not. The second error on mass and total width of the Z° boson is due to the uncertainties in the **LEP** energy calibration (see Appendix C). MSM expectations are listed for the fitted Z° mass (91.195 ± 0.009 GeV), $m_t = 150 \pm 50$ GeV, $m_H = 300^{+700}_{-240}$ GeV, $\alpha_s = 0.124 \pm 0.006$.
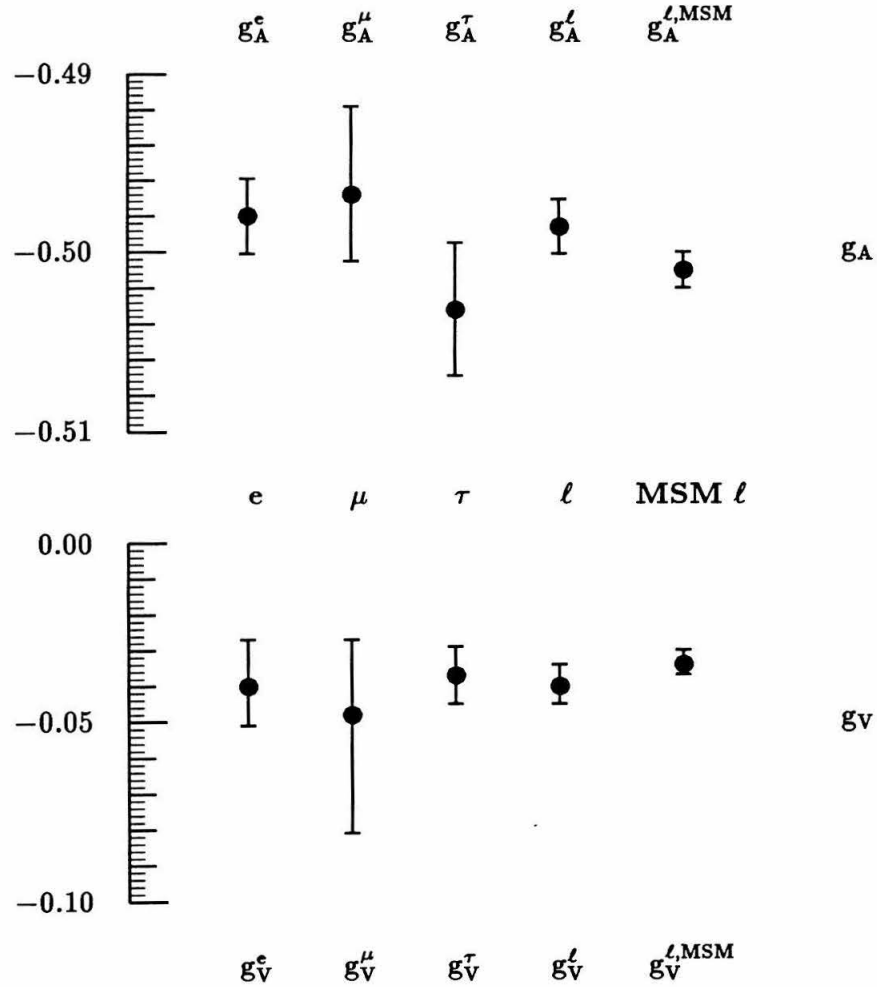
Figure 8.9: Effective axial-vector (g_A, top) and vector (g_V, bottom) coupling constants of the charged lepton species. MSM expectations are given for the fitted Z° mass (91.195 ± 0.009 GeV), $m_t = 150 \pm 50$ GeV, $m_H = 300^{+700}_{-240}$ GeV, $\alpha_s = 0.124 \pm 0.006$.

The effective coupling constants for charged leptons are thus determined to be:

$$g_A^\ell = -0.4986 \pm 0.0015 \qquad (8.14)$$

$$g_V^\ell = -0.040^{+0.006}_{-0.005} \quad . \qquad (8.15)$$

Figure 8.10 shows their correlation 68% confidence level contours together with MSM predictions.

Effective couplings: g_A and g_V
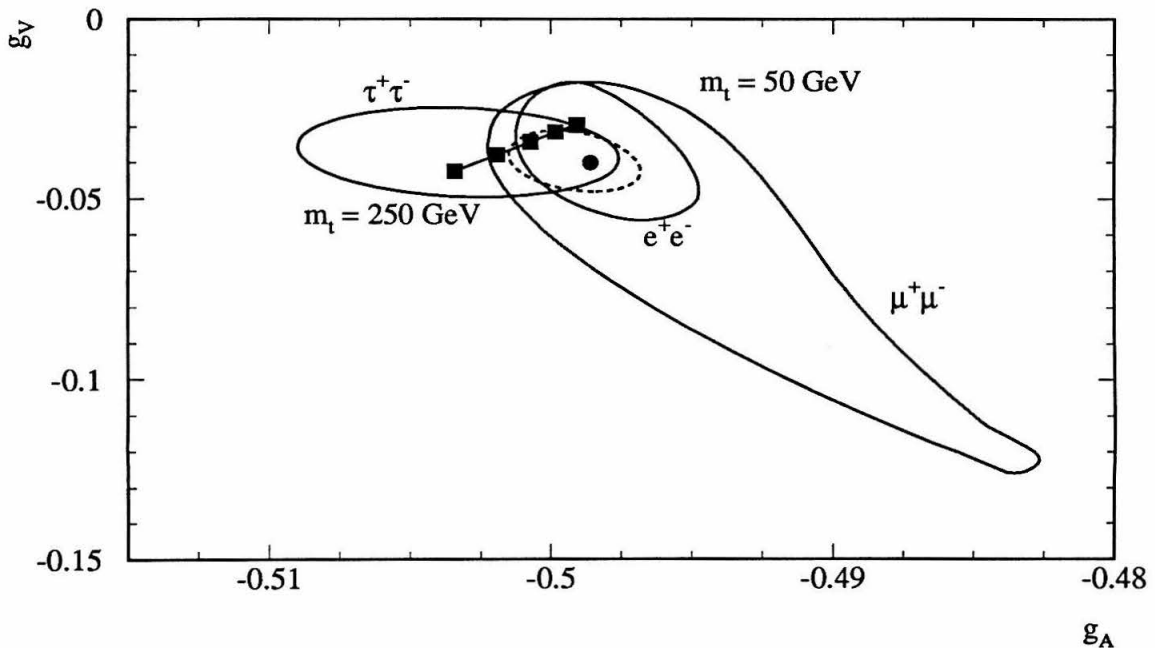
Figure 8.10: Correlation between effective vector (g_V) and axial-vector (g_A) coupling constants of charged leptons obtained from a fit to the combined cross section and asymmetry data including τ polarization. The central value and the 68% confidence level contours are shown: solid lines for each lepton species, dashed line for lepton universality. The squares indicate MSM predictions for top masses of 50, 100, 150, 200 and 250 GeV.

Weak Mixing Angle

A comparison between the values of the effective weak mixing angle obtained by different measurements constitutes a precision test of the MSM. A value for $\sin^2 \overline{\theta}_W$ can be determined from a fit to ρ_{eff} and $\sin^2 \overline{\theta}_W$ by replacing g_V and g_A in the framework of the improved Born approximation (see Appendix A). The following input data have been used by **L₃** to determine $\sin^2 \overline{\theta}_W$:

1. The partial width Γ_ℓ of the Z° decaying to charged leptons ℓ:

   Equation 2.47 can be used, written in the improved Born approximation and corrected for final state QED effects:

$$\Gamma_\ell = \frac{\alpha(m_Z) m_Z K_{TH}}{48 \sin^2 \overline{\theta}_W \cos^2 \overline{\theta}_W} \left[1 + (1 - 4\sin^2 \overline{\theta}_W)^2 \right] \left(1 + \frac{3\alpha}{4\pi} \right) \quad . \tag{8.16}$$

   The theoretical factor K_{TH} contains top and Higgs effects, and is evaluated for $m_t = 150 \pm 50$ GeV and $m_H = 300^{+700}_{-240}$ GeV. The result obtained from the above fit is:

$$\sin^2 \overline{\theta}_W = 0.2347 \pm 0.0017 \quad . \tag{8.17}$$

2. The forward-backward charge asymmetry A_{fb}^ℓ of charged leptons ℓ:

   Using Equation 2.50 for charged leptons, the value of $\sin^2 \overline{\theta}_W$ is determined to be:

$$\sin^2 \overline{\theta}_W = 0.2283 \pm 0.0032 \quad . \tag{8.18}$$

3. The longitudinal polarization $\mathcal{P}_\tau$ of charged τ leptons:

   Using Equation 2.51 for τ leptons, the measured τ polarization $\mathcal{P}_\tau$ constraints $\sin^2 \overline{\theta}_W$ to:

$$\sin^2 \overline{\theta}_W = 0.2326 \pm 0.0043 \quad . \tag{8.19}$$

4. The forward-backward charge asymmetry A_{fb}^b of b quarks:

   Using Equation 2.50 for b quarks yields an effective weak mixing angle of:

$$\sin^2 \overline{\theta}_W = 0.2336 \pm 0.0029 \quad . \tag{8.20}$$
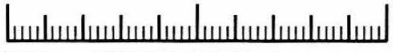
Effective Weak Mixing Angle $\overline{\theta}_W$		
Method	$\sin^2 \overline{\theta}_W$	0.22 0.23 0.24
m_Z, Γ_ℓ	0.2347 ± 0.0017	
A_{fb}^ℓ	0.2283 ± 0.0032	
$\mathcal{P}_\tau$	0.2326 ± 0.0043	
A_{fb}^b	0.2336 ± 0.0029	
$\mathbf{L_3} \, \sin^2 \overline{\theta}_W$	0.2328 ± 0.0013	

Table 8.4: Values of $\sin^2 \overline{\theta}_W$ determined from partial Z° widths, leptonic forward-backward charge asymmetry, τ polarization and forward-backward charge asymmetry of b quarks, and their weighted average.

All values of $\sin^2 \overline{\theta}_W$ are in good agreement with each other (Table 8.4). A weighted average adjusted for common input data and correlations yields the same result as a fit to the complete data set within the framework of the MSM:

$$\sin^2 \overline{\theta}_W = 0.2328 \pm 0.0013 \quad . \tag{8.21}$$

Electromagnetic Coupling Constant

Within the improved Born approximation, the QED electromagnetic coupling constant α is energy dependent (Appendix A):

$$\alpha(s) = \frac{\alpha}{1 - \Delta\alpha(s)} \quad . \tag{8.22}$$

The non-vanishing value of $\Delta\alpha$ arises from the photonic vacuum polarization (a correction to the photon propagator due to the insertion of particle loops). The total width of the Z° boson can be used to determine $\alpha(s)$ in a model independent way, which is also independent of the luminosity normalization. In determining $\alpha(s)$, use of a variable such as Γ_Z which is independent of the luminosity is important, because the luminosity determination implicitly involves $\alpha(s)$, through the event generator

used for acceptance corrections. The total width Γ_Z is simply expressed as a sum of partial widths:

$$\Gamma_Z = \sum_{\ell=e,\mu,\tau} (\Gamma_\ell + \Gamma_{\nu_\ell}) + \sum_{q=u,d,s,c,b} \Gamma_q \quad , \tag{8.23}$$

which in turn are given in the improved Born approximation by:

$$\Gamma_f = N_C^f \frac{\alpha_{\text{eff}}(m_Z) m_Z}{48 \sin^2 \overline{\theta}_W \cos^2 \overline{\theta}_W} \left[1 + (1 - 4 |q_f| \sin^2 \overline{\theta}_W)^2 \right] (1 + \frac{3}{4} q_f^2 \frac{\alpha}{\pi}) \tag{8.24}$$

$$N_C^f = \begin{cases} 1 & \text{for leptons} \\ 3(1 + \delta_{QCD}) & \text{for quarks} \end{cases} , \tag{8.25}$$

where δ_{QCD} is a QCD correction which vanishes for leptons (Equation A.6), and where the factor K in Equation 8.16 has been absorbed in $\alpha(m_Z)$ yielding $\alpha_{\text{eff}}(m_Z)$. Thus, the effective electromagnetic coupling constant $\alpha_{\text{eff}}(m_Z)$ at the scale of the Z° boson can be extracted [72]. Knowing m_Z, Γ_Z and $\sin^2 \overline{\theta}_W$ from a fit to the combined cross section and asymmetry data, the result is:

$$\alpha_{\text{eff}}^{-1}(m_Z) = 128.6 \pm 1.2^{+0.1}_{-0.2} \quad , \tag{8.26}$$

where the first error is experimental, and the second is due to the unknown top mass varied from 100 GeV to 200 GeV. This value is in good agreement with the prediction of the MSM of $128.0^{+0.2}_{-0.4}$.

8.2.3 Top Quark and Higgs Boson

Because of higher order corrections depending on the masses of the Higgs boson and the top quark, the data – cross sections, charged lepton asymmetries, b quark charge asymmetry, and τ polarization – contain information about these quantities (Appendix A). For example, the sensitivity of the cross section data to the top mass is large a few GeV away from the peak [73]. Strictly within the framework of the MSM, parameters not constrained are m_Z, m_t, m_H and α_s. LEP I data alone are not yet very sensitive to reasonable values of the Higgs mass m_H. Therefore, m_H has been fixed to a central value of 300 GeV, and the fit has been repeated with 50 GeV

and 1000 GeV Higgs masses. The results for m_t and α_s are:

$$m_t = 132^{+44}_{-63} \pm 18 \ (Higgs) \ \text{GeV} \tag{8.27}$$

$$\alpha_s = 0.140 \pm 0.016 \quad . \tag{8.28}$$

The correlation between the strong coupling constant α_s and the mass m_t of the top quark is shown in the Figure 8.11. This correlation can be exploited, to arrive at an improved determination of the top quark mass. The strong coupling constant also has been measured elsewhere at $\mathbf{L_3}$ (see Section 8.2.2 for a summary). Constraining α_s to the result $\alpha_s = 0.124 \pm 0.006$ presented above, the mass of the top quark has been determined by $\mathbf{L_3}$ to be:

$$m_t = 152^{+36}_{-46} \pm 20 \ \text{GeV} \quad . \tag{8.29}$$

The second error on m_t shown above arises from the unknown Higgs mass, which has been varied around the central value of 300 GeV from 50 GeV to 1000 GeV.

The following quantities which are discussed in Chapter 2 and Appendix A can now be derived:

$$\sin^2 \theta_{\mathrm{W}} = 0.227 \pm 0.005 \tag{8.30}$$

$$\sin^2 \overline{\theta}_{\mathrm{W}} = 0.2328 \pm 0.0013 \tag{8.31}$$

$$\Delta r = 0.047 \pm 0.014 \tag{8.32}$$

$$m_{\mathrm{W}} = 80.2 \pm 0.3 \ \text{GeV} \quad . \tag{8.33}$$

8.2.4   Other Quantities

For the purpose of averaging the results of the four **LEP** experiments, it is useful to provide a set of parameters, which are least correlated among themselves. Under the assumption of lepton universality, the parameters and their values determined from $\mathbf{L_3}$ data are:

$$m_{\mathrm{Z}} = 91.195 \pm 0.009 \ \text{GeV} \tag{8.34}$$

$$\Gamma_{\mathrm{Z}} = 2.490 \pm 0.011 \ \text{GeV} \tag{8.35}$$

Standard Model: m_t and α_s
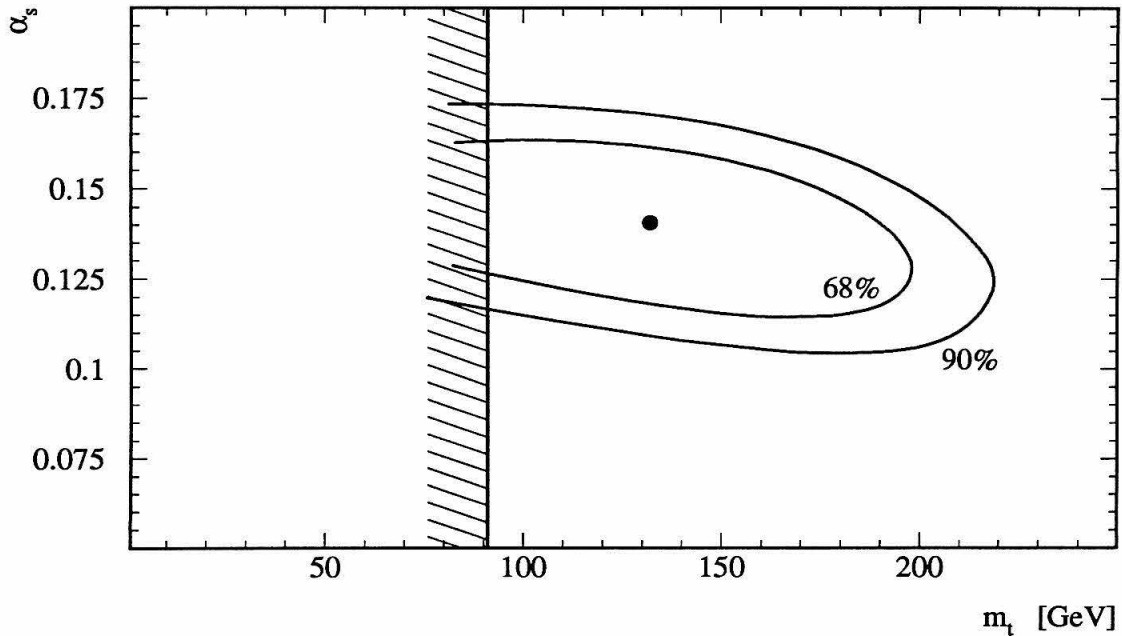
Figure 8.11: Correlation between α_s and m_t obtained from a fit to the combined cross section and asymmetry data assuming lepton universality. The central value and the 68% and 90% confidence level contours are shown. Using a direct search, the CDF collaboration has set a lower limit of 91 GeV for the mass of the top quark [74].

$$R_Z = 21.00 \pm 0.15 \tag{8.36}$$

$$\sigma^0_{\text{had}} = 41.34 \pm 0.28 \text{ nb} \tag{8.37}$$

$$A^0_{\text{fb}} = 0.0187 \pm 0.0048 \quad , \tag{8.38}$$

where the cross section and asymmetry is given on the peak and the superscript 0 indicates, that the corresponding variables have been unfolded for QED corrections. In the case of non-universality, values for R_Z and A^0_{fb} are given for each of the three charged lepton species.

8.3   Limits from Electroweak Data on New Physics

8.3.1   Additional $Z°$ Decay Modes

A new $Z°$ decay mode will manifest itself by enlarging the total width Γ_Z of the $Z°$ boson, and the appropriate partial width Γ_ℓ, Γ_{had}, or Γ_{inv}. The upper limit on an additional width contribution is estimated using a one-sided 95% confidence limit on the difference between the fitted $Z°$ width and the corresponding MSM prediction, where for the latter, a variation of m_t between 91 and 300 GeV and m_H between 50 and 1000 GeV has been allowed. This yields 2472 MeV and 498 MeV as low bounds for the total and invisible width of the $Z°$ boson. In this way the following upper limits for additional contributions to the total and invisible width of the $Z°$ boson have been derived (95% confidence level):

$$\Delta\Gamma_Z = 35.1 \text{ MeV} \tag{8.39}$$

$$\Delta\Gamma_{inv} = 16.2 \text{ MeV} \quad . \tag{8.40}$$

Limits on the mass of new sequential quarks and leptons, and supersymmetric particles, obtained using these results, are listed in Table 8.5.

For the special case of additional sequential leptons and quarks, standard quantum numbers can be assumed and mass limits can be evaluated directly. In the case of supersymmetric particles, the influence of the new decay mode on radiative corrections has been neglected. Thus, the limits listed may be considerably weaker, if some conspiracy between different channels exists.

The mass limits for many new particles are close to the kinematic limit of 45 GeV accessible at **LEP I**. Thus, only **LEP 200** data will allow one to set improved limits.

8.3.2   Additional Heavy Gauge Bosons

In extended versions of the MSM, additional gauge bosons exist with higher masses, such as an additional neutral heavy boson Z'. The addition of a heavy Z' modifies the expressions for cross sections and asymmetries predicted by the MSM due to

Mass Limits [GeV]	From Γ_Z $\Delta\Gamma_Z < 31.5$ MeV	From Γ_{inv} $\Delta\Gamma_{inv} < 16.2$ MeV
Limits on Additional Sequential Fermions		
m_t	41.8	—
m_B	44.7	—
m_L	30.2	—
m_N	—	45.2
Limits on Supersymmetric Particles		
$m_{\tilde{\nu}}$	—	37.1
$m_{\tilde{U}}$	35.3	—
$m_{\tilde{D}}$	36.8	—
$m_{\tilde{H}^\pm}$	44.0	—
$m_{\tilde{W}}$	45.5	—

Table 8.5: 95% confidence level limits on the mass of new particles obtained from the Z° widths limits. The particles are assumed to be sequential up- and down-type quarks (top t and B), neutral and charged leptons (N and L) with standard weak isospin assignment. The limits on the masses of their supersymmetric partners, including those of the Higgs and W boson, also are given.

the additional exchange of a (virtual) Z′ in e⁺e⁻ annihilations:

$$e^+e^- \longrightarrow \gamma/Z/Z' \longrightarrow f\bar{f}(\gamma) \quad . \tag{8.41}$$

In general [75], the mass eigenstates Z_1 and Z_2 arise from the symmetry eigenstates Z and Z′ via mixing:

$$\begin{pmatrix} Z_1 \\ Z_2 \end{pmatrix} = \begin{pmatrix} \cos\theta_M & \sin\theta_M \\ -\sin\theta_M & \cos\theta_M \end{pmatrix} \begin{pmatrix} Z \\ Z' \end{pmatrix} \quad . \tag{8.42}$$

The mixing angle θ_M relates the masses of the two massive gauge bosons:

$$\tan\theta_M^2 = \frac{m_Z^2 - m_1^2}{m_2^2 - m_Z^2} \quad , \tag{8.43}$$

where the parameter m_Z, fixed by θ_M, has been introduced. The resonance observed at **LEP I** has mass m_1 $(= m_Z$ in the absence of mixing) and width Γ_1.

Two models which are often considered are either based on the superstring-inspired broken E_6 group as a gauge group, or on left-right symmetric extensions of the **MSM**. In both models, there is one additional parameter, θ_6 and α_{LR}, respectively, on which the couplings of the additional Z' to the fermions depend.

Compared to the **MSM**, the principal effects of a Z' are threefold:

1. virtual Z' exchange (always present),

2. shift of the mass of the standard Z boson seen at **LEP I** (for non-vanishing ZZ' mixing),

3. modification of the couplings of the standard Z boson (for non-vanishing ZZ' mixing).

The analysis of the combined cross section and asymmetry data is performed using the supplemental package ZEFIT of ZFITTER (see Appendix F). No indication for additional heavy neutral gauge bosons is seen and 95% confidence level limits are established. The lower limit for the mass varies between 100 GeV and 130 GeV depending on the specific model chosen. The lower limit for θ_M ranges from -0.029 rad to -0.002 rad, and the upper limit ranges from $+0.010$ rad to $+0.020$ rad, again depending on the model parameters. Thus θ_M is always compatible with the **MSM** value of zero. All limits take into account the uncertainty of the top mass.

8.3.3   Extended Higgs Sector

An extended Higgs sector within the **SM** can manifest itself by a deviation of the ρ_{tree} parameter from unity. In Chapter 2, the definition of ρ_{tree} is given, which yields:

$$\rho_{\text{tree}} = \frac{m_W^2}{m_Z^2 \cos^2 \theta_W} \quad . \tag{8.44}$$

The quantity ρ_{tree} modifies **MSM** expressions in the following way:

$$m_Z \longrightarrow \frac{1}{\sqrt{\rho_{tree}}} \cdot m_Z^{\text{MSM}} \tag{8.45}$$

$$\Gamma_Z \longrightarrow \rho_{tree} \cdot \Gamma_Z^{MSM} \tag{8.46}$$

$$\Gamma_f \longrightarrow \rho_{tree} \cdot \Gamma_f^{MSM} \quad . \tag{8.47}$$

A fit of ρ_{tree} to the combined cross section and asymmetry data is performed (following the recipe given in [76]) by fixing the mass of the top quark to 150 GeV and constraining α_s to 0.124 ± 0.006. The result is:

$$\rho_{tree} = 1.0001 \pm 0.0015 \pm 0.0020 \quad . \tag{8.48}$$

The first error is experimental. The second error arises from m_t, using a central value of 150 GeV and a variation from 90 GeV to 200 GeV. The effect of varying the mass of the Higgs boson from 50 GeV to 1000 GeV is negligible.

8.3.4 Parametrization of New Physics

It has been studied how one can disentangle new physics from the possibly large, unknown top quark corrections of leading order $G_F m_t^2$. For this purpose, three new parameters ϵ_1, ϵ_2, ϵ_3, are introduced [77, 78]. In the MSM, they take on the form [79]:

$$\epsilon_1 = \Delta\rho = \frac{3G_F m_t^2}{8\pi\sqrt{2}} - \frac{3G_F m_W^2}{4\pi^2\sqrt{2}}\tan^2\theta_W \ln\left(\frac{m_H}{m_Z}\right) + \ldots \tag{8.49}$$

$$\epsilon_2 = -\frac{G_F m_W^2}{2\pi^2\sqrt{2}}\ln\left(\frac{m_t}{m_Z}\right) + \ldots \tag{8.50}$$

$$\epsilon_3 = \frac{G_F m_W^2}{12\pi^2\sqrt{2}}\ln\left(\frac{m_H}{m_Z}\right) - \frac{G_F m_W^2}{6\pi^2\sqrt{2}}\ln\left(\frac{m_t}{m_Z}\right) + \ldots \quad . \tag{8.51}$$

While these new parameters are merely rearrangements of corrections arising from higher order diagrams, their merit lies in separating out the m_t dependent effects in ϵ_1 and other (m_H) effects in ϵ_3.

The **LEP I** data constrains ϵ_1 and ϵ_3, whereas ϵ_2 will be measured at **LEP 200** (measurement of the W mass). Thus, for an analysis of **LEP I** data alone, the ϵ_2 parameter can be ignored. Any new physics signal can manifest itself in deviations of the ϵ parameters from the MSM predictions presented above.

The result of the analysis of the L_3 data in terms of the parameters ϵ_1 and ϵ_3 is:

$$\epsilon_1 = -0.0044 \pm 0.0060 \tag{8.52}$$

$$\epsilon_3 = -0.0028 \pm 0.0071 \quad . \tag{8.53}$$

The central values and the 68% and 90% confidence level contours are shown in Figure 8.12. No significant deviation from MSM predictions is seen. Low top and Higgs masses are preferred by the L_3 data.

Parametrization of new physics: ϵ_1 and ϵ_3
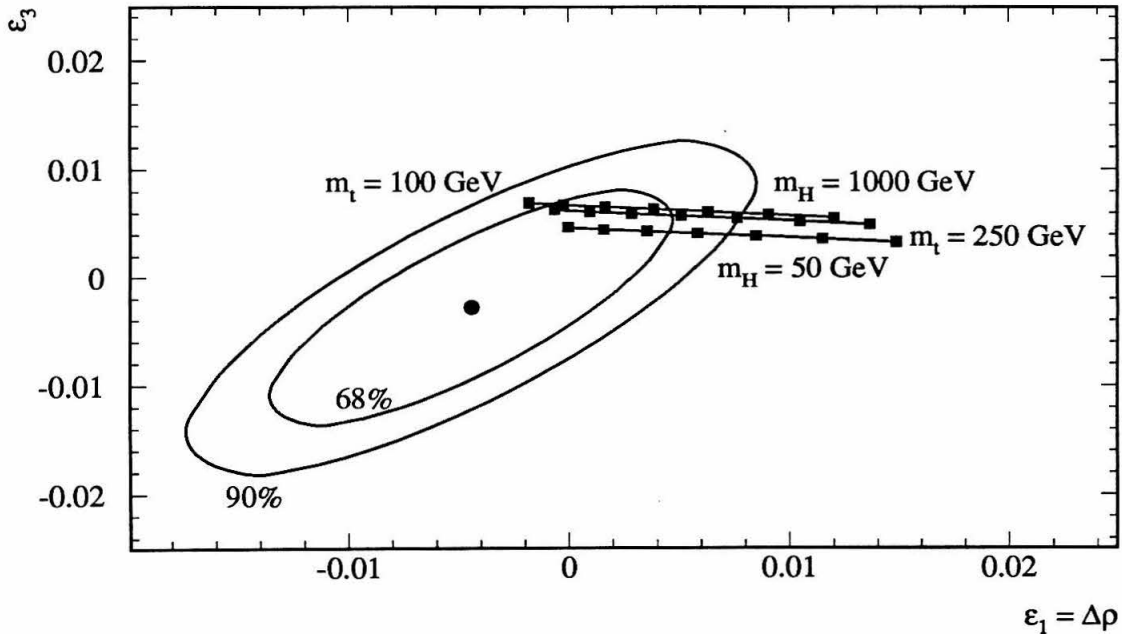
Figure 8.12: Correlation between ϵ_1 and ϵ_3 derived from the electroweak data of L_3. The central value and the 68% and 90% confidence level contours are shown. The three horizontal lines mark MSM predictions for Higgs masses of 1000 GeV (top line), 300 GeV (middle line), and 50 GeV (bottom line). The solid squares mark top quark masses from 100 GeV (left) to 250 GeV (right) in steps of 25 GeV.

Chapter 9

Summary and Conclusion

This thesis has presented in detail the measurement by $\mathbf{L_3}$ of the production cross section and forward-backward charge asymmetry of the process $e^+e^- \to \tau^+\tau^-(\gamma)$ at center-of-mass energies $\sqrt{s}$ around the Z° resonance (88 GeV $< \sqrt{s} <$ 94 GeV). At the peak of the Z° resonance ($\sqrt{s} = m_Z$), the cross section σ and forward-backward charge asymmetry A_{fb} are:

$$\sigma(e^+e^- \to \tau^+\tau^-(\gamma)) = 1.481 \pm 0.019 \pm 0.013 \text{ nb} \tag{9.1}$$

$$A_{fb}(e^+e^- \to \tau^+\tau^-(\gamma)) = 0.014 \pm 0.017 \pm 0.006 \quad , \tag{9.2}$$

where the first errors are statistical and the second systematic. The measurements for each center-of-mass energy point, including statistical and systematic errors, are listed in Tables 6.2 and 6.10, respectively. The entire body of measurements increases the confidence that the charged τ lepton behaves like a sequential lepton with the properties predicted by the Minimal Standard Model of particle physics (MSM).

The systematic error of the cross section measurement is 0.9%, and is mainly due to selection criteria (0.6%) and luminosity (0.6%). The main contribution to the total systematic error of 0.006 in the measurement of charge asymmetry arises from background corrections (0.005). Future improvements in the event selection are possible by making more use of the central tracking chambers and by extending the fiducial volume to the endcap region of the $\mathbf{L_3}$ detector.

These measurements, together with other measurements performed by the L_3 collaboration on Z° decay channels, have been used to determine the properties of the Z° boson, many parameters of the MSM including the coupling constants, and to search for new physics beyond the MSM.

The parameters of the MSM which have been measured by L_3 include:

- the strong coupling constant at the mass of the charged τ lepton:
  $\alpha_s(m_\tau) = 0.35 \pm 0.06 \ (exp.) \pm 0.03 \ (theor.)$,

- the mass of the Z° boson: $m_Z = 91.195 \pm 0.006 \pm 0.007 \ (LEP)$ GeV,

- the total width of the Z° boson: $\Gamma_Z = 2.490 \pm 0.010 \pm 0.005 \ (LEP)$ GeV,

- the partial decay width of the Z° boson into τ pairs: $\Gamma_\tau = 84.6 \pm 1.2$ MeV,

- the effective axial-vector and vector coupling constants of the neutral weak current for charged τ leptons: $g_A^\tau = -0.5032 \pm 0.0037$ and $g_V^\tau = -0.037 \pm 0.008$,

- the effective weak mixing angle: $\sin^2 \overline{\theta}_W = 0.2328 \pm 0.0013$,

- the strong coupling constant at the mass of the Z° boson:
  $\alpha_s(m_Z) = 0.124 \pm 0.005$,

- the mass of the top quark: $m_t = 152^{+36}_{-46} \pm 20 \ (Higgs)$ GeV.

All measurements up until now are in agreement with the Standard Model of particle physics in its minimal realization. Several tests of the MSM have been carried out by comparing electroweak parameters measured in different reactions. Values for the effective weak mixing angle $\sin^2 \overline{\theta}_W$ determined in different processes agree well within errors. The same holds for the effective vector and axial-vector neutral current coupling constants of the charged lepton species, thus confirming charged lepton universality of the neutral current.

The observed agreement of all measurements with the Minimal Standard Model leads to stringent limits on effects arising from possible new physics beyond it. No indication of deviations from the MSM has been found, up to the present.

Further improvements in the calibration of the **LEP** beam energy are clearly desirable. For all channels, the statistical error is still larger than the systematic error. The systematic error also will continue to decrease with increased statistics, due to improved understanding of the detector. An increase by a factor of 10 in the amount of data, as anticipated by the end of the **LEP I** program, therefore will lead to substantially increased sensitivity to new physics, or to higher precision in the determination of fundamental parameters in the MSM.

Appendix A

Radiative Corrections

For a given process of interest, the Feynman rules derived from the MSM Lagrangian allow one to calculate the corresponding matrix elements and hence differential cross sections, which can be compared with experimental measurements. For a given final state, however, the most simple (Born) diagram does not always suffice for precise measurements. It is necessary to incorporate more complicated diagrams leading to the same final state observed in the experiment, in order to get a more precise theoretical prediction.

Changes intrinsic to the diagrams, such as additional internal particle propagators, do not modify the particle content of the observed final state, but do change the functional form of the differential and total cross section relative to the lowest-order result. Other changes corresponding to diagrams adding radiative photons or light fermion pairs to the final state, must be taken into account because of limited resolution of any measurement device: event topologies with additional photons not resolved in the detector will be identified with and counted for the process itself.

All such corrections involve additional vertices, hence these diagrams contain higher powers of the coupling constant than the lowest-order Born term. This is the reason for naming them higher-order corrections. In fact, one can view the sequence of increasingly more complicated diagrams as a perturbation series expansion in powers of the coupling constants.

A.1   Renormalization

Problems arise when calculating higher-order corrections: divergences show up, which would give infinite, thus meaningless results for physical observables. This is related to the interpretation of the parameters in the MSM Lagrangian: for example, coupling constants such as the electromagnetic charge are naively interpreted as the measured ones. However, this need not necessarily be true: the charge observed in experiments is related to theoretical expressions *including* the full perturbation series expansion.

A consistent mathematical procedure has to be used to redefine the ingredients of the Lagrangian – such as the coupling constants, wave functions, and propagators – in order to recover finite expressions. The application of such procedures to a quantum field theory is called renormalization. If this procedure yields finite results for all observables to all orders of perturbation theory, the theory is called renormalizable. In this respect, only renormalizable theories are sensible ones having predictive power.

The MSM is an example of a renormalizable theory, whereas the four-fermion theory (see Chapter 2) is not.

There are two widely used schemes of renormalization:

1. Modified minimal-subtraction ($\overline{\text{MS}}$) scheme:
   The "minimal" subtraction scheme is minimal in the sense that all parameters are defined at a certain renormalization mass scale μ. This scheme is the preferred one of QCD, where there is no preference for a specific mass scale in the renormalization procedure, due to the absence of free fundamental particle states.

2. On-shell renormalization:
   The situation is different in QED and electroweak theory. Here, preferred scales exist for the electromagnetic charge via the classical Thomson scattering (low energy limit of Compton scattering) and for masses via the measured masses (*on-shell*) of e, μ, τ, etc. These values are used as input parameters for the

on-shell scheme of the full electroweak theory, together with the masses of the intermediate vector bosons Z° and $W^\pm$. The renormalization conditions for masses are, that the propagators of particles have poles at their physical masses.

All renormalization schemes are equivalent, and one can always switch from one scheme to another. Results should not depend on the renormalization scheme adopted in the calculation. It can be proven that the results agree, when the perturbation series is summed up to all orders. However, in calculations truncated at finite order in the perturbative expansion, the results do depend on the renormalization scheme. The size of the effect is that of the missing higher-order terms.

A.2 On-Shell Scheme

The Born-type expressions for fermion production $e^+e^- \to f\bar{f}$ at energies near the Z° resonance are modified due to the inclusion of electroweak and QCD higher-order corrections [80]. The procedure adopted in renormalizing infinities arising in higher-order calculations of electroweak theory is the on-shell renormalization scheme. The advantages of on-shell renormalization listed below:

- All parameters have a clear intuitive and physical meaning and can (in principle) be measured directly in suitable experiments.

- All of them are in fact known by measurement, with exception of the masses of top quark and Higgs boson.

- At the one-loop level, higher-order corrections to $e^+e^- \to f\bar{f}$ can be separated naturally into QED and non-QED (weak) corrections, and the latter are sensitive to new physics.

- The weak mixing angle θ_W is no longer a free parameter, but is defined by the condition:

$$\sin^2\theta_W \equiv 1 - \frac{m_W^2}{m_Z^2} \quad . \tag{A.1}$$

QED Corrections

Some diagrams contributing to the class of QED corrections, i.e., those containing an additional photon line (either virtual or real) are given in Figure A.1. The characteristic features of such QED corrections are as follows:

- They are dependent on experimental details, for example the spatial and energy resolution for resolving radiative photons in the final state. Their effect in actual experiments thus must be calculated by Monte Carlo simulation of the specific detector and selection procedure.

- They are independent of the detailed structure of the non-QED part of the theory, i.e., they need only the global parameters m_Z and Γ_Z, and the neutral current vector and axial-vector coupling constants g_V and g_A as input. Hence they are not in themselves of great physics interest.

- They are gauge invariant (which means that their separation from the rest is sensible in the first place).

- They are large around the Z° resonance. For example, the cross section at the peak of the resonance is reduced by 25% due to these corrections. An exhaustive treatment including (leading) higher-order corrections is therefore required.

QED corrections are treated theoretically by convoluting the (improved) Born cross section σ_0 with a radiator function R:

$$\sigma(s) = \int_{4m_f^2/s}^{1} dz\ \sigma_0(zs) R(z,s) \tag{A.2}$$

$$R(z,s) = \delta(1-z) + \sum_{n=1}^{\infty} \left(\frac{\alpha}{\pi}\right)^n \sum_{i=0}^{n} a_{ni} \ln\left(\frac{s}{m_e}\right)^i \ . \tag{A.3}$$

At $\sqrt{s}$ values near the peak of the Z° resonance, the largest effect arises from initial state radiation due to the rapidly varying cross section. Final state radiation exhibits a much smaller effect, which corresponds to an overall normalization factor of

$$R_{QED} = 1 + \frac{3}{4}\frac{\alpha}{\pi}q_f^2 + \mathcal{O}(\alpha^2) \ . \tag{A.4}$$
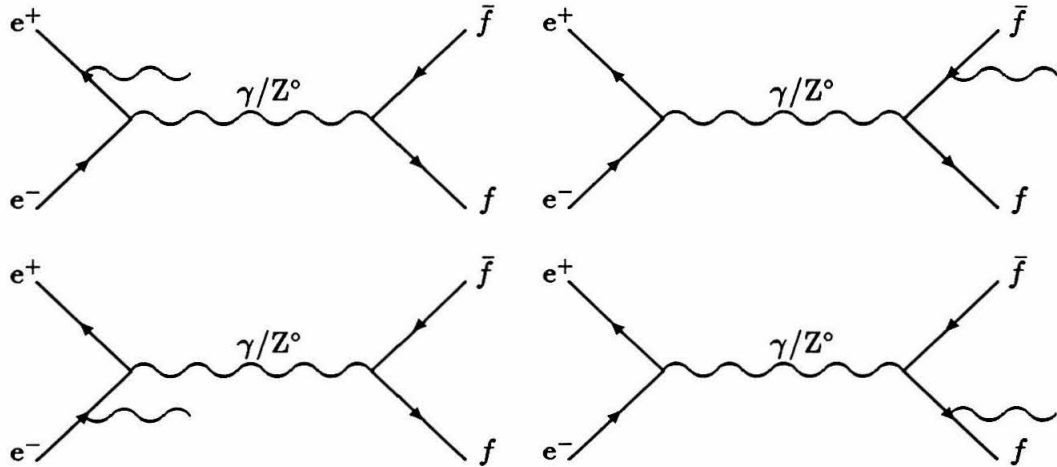
Figure A.1: Diagrams contributing to QED corrections: Initial state radiation (left) and final state radiation (right) of photons.

To allow for an arbitrary number of additional radiative photons in a specific final state, a bracketed γ is added as in $e^+e^- \to \tau^+\tau^-(\gamma)$.

Weak Corrections

Weak corrections arise from non-photonic, i.e., genuine weak higher-order diagrams. The characteristic features of weak corrections are, that:

- they are small;

- they are independent of the experimental set-up;

- they are dependent on the detailed structure of the theory, in particular its particle content, and are therefore sensitive to the as yet unknown masses of the Higgs and the top quark (and hence they are very interesting).

There are three groups of weak corrections:
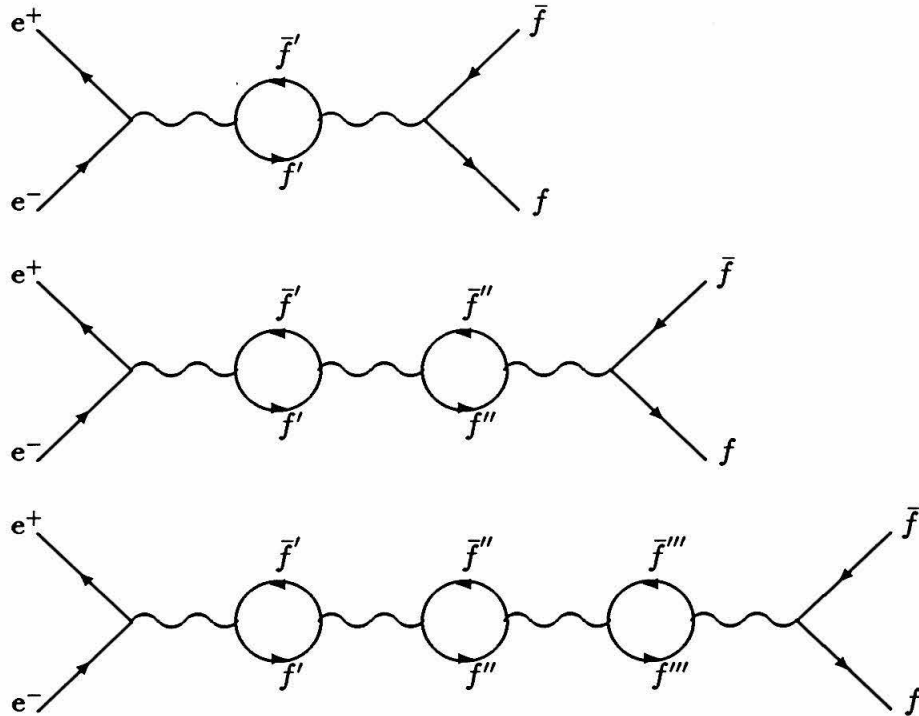
Figure A.2: Diagrams contributing to propagator corrections. There is an infinite number of diagrams forming a series of loop insertions. The propagating gauge boson may change from a γ to a Z° and vice versa before and after a loop insertion. The particle within the loop may also be a $W^\pm$. In addition, the loops may show internal structure, i.e., internal propagators.

1. Propagator (also called self-energy) corrections (Figure A.2):
   Incorporating the series of these corrections in the boson propagators (referred to as dressing of the propagators), makes the width of the propagating heavy gauge boson $\sqrt{s}$ dependent. The corrections are universal, which means that they do not depend on the flavor of the initial or final state fermions.

2. Vertex corrections (Figure A.3):
   Provided the masses of the initial and final state fermions are small, vertex corrections can be summarized by introducing a $\sqrt{s}$-dependence in the usual
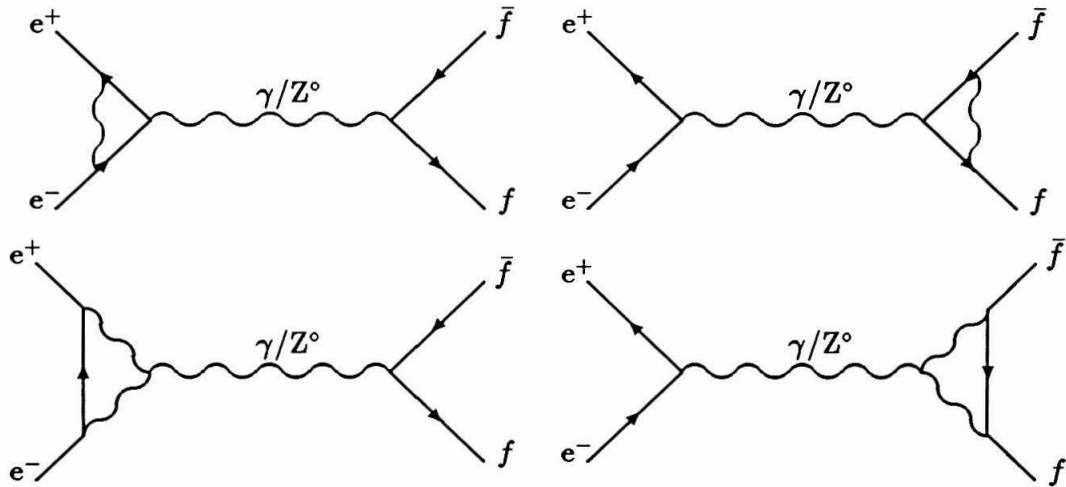
Figure A.3: Diagrams contributing to vertex corrections. In the two top diagrams, the additional boson may be any of γ, Z° or $W^\pm$. In the two bottom diagrams, the additional bosons must be $W^\pm$.

vector and axial-vector coupling constants. The corrections are not universal, but depend on the fermion species.

This is especially true for the b quark, where large corrections arise from top quark effects at the vertex due to the high top quark mass (Figure A.4). The reason for these large corrections in the case of the $b\bar{b}$ production lies in the fact that the top quark is the weak isospin partner of the b quark. Therefore, these diagrams are not suppressed by off-diagonal elements of the Cabibbo-Kobayashi-Maskawa matrix.

3. Box contributions (Figure A.5):
The genuine weak box diagrams are those containing WW and ZZ exchange. Their contributions are non-resonant, hence their effect is small for energies close to the Z° resonance.

QCD Corrections
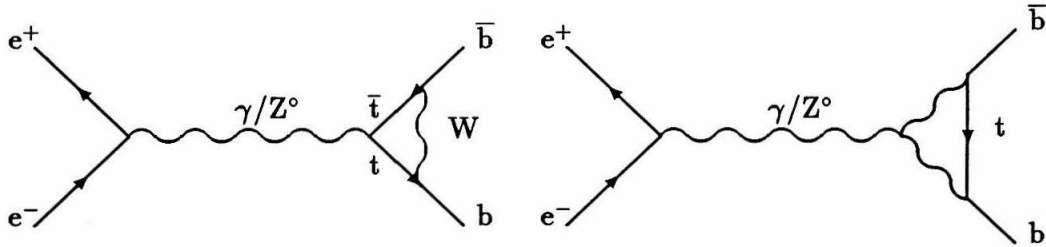
Figure A.4: Diagrams contributing to vertex corrections in b$\overline{\text{b}}$ production involving the top quark.
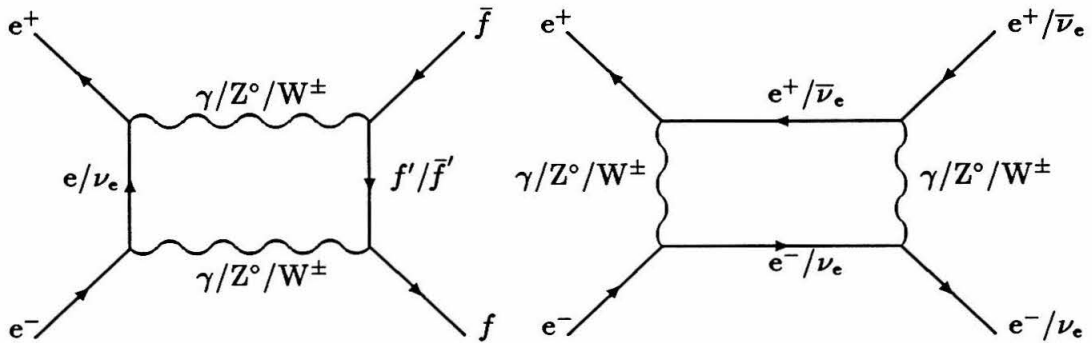
Figure A.5: Box diagrams. The s-channel-exchanged vector bosons must be either both neutral or of opposite charge.

Diagrams contributing to the class of QCD corrections are given in Figure A.6. The characteristic features of these QCD corrections are, that:

- they affect only the final state;

- they appear in $q\bar{q}$ production only.

The final-state QCD correction is a multiplicative factor, which can be expanded in a series in powers of α_s/π [81, 82], in a manner which is analogous to the case of final-state photon radiation in QED. For leptonic final states, the QCD correction
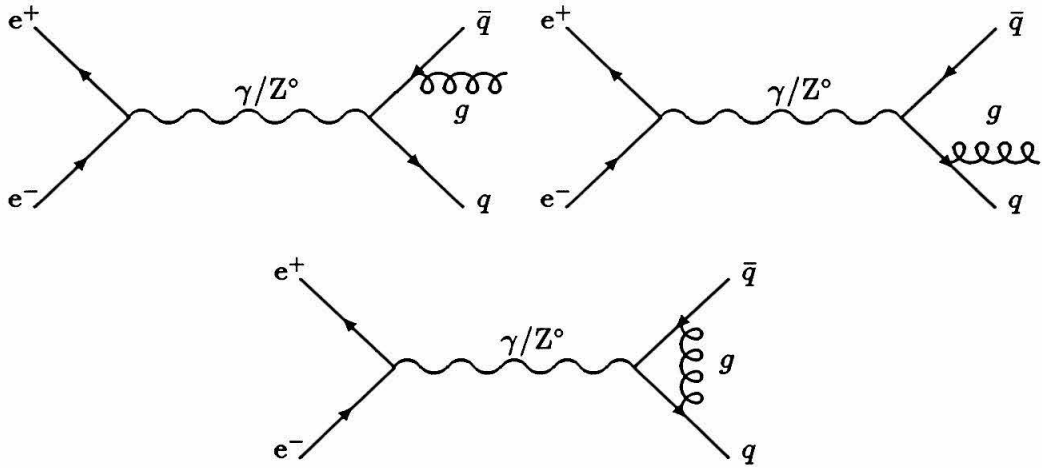
Figure A.6: Diagrams contributing to final-state QCD corrections involving gluons (g) in quark-pair production.

factor is of course 1. Hence the ratio R_Z, defined as:

$$R_Z \equiv \frac{\Gamma_{had}^Z}{\Gamma_\ell^Z} = R_Z^0(1 + \delta_{QCD}) \quad , \tag{A.5}$$

where

$$\delta_{QCD} = 1.05 \cdot \frac{\alpha_s}{\pi} + (0.9 \pm 0.1) \cdot \left(\frac{\alpha_s}{\pi}\right)^2 - 13 \cdot \left(\frac{\alpha_s}{\pi}\right)^3 + \mathcal{O}(\alpha_s^4) \quad , \tag{A.6}$$

(which also includes quark mass effects [83]), is sensitive to the value of the strong coupling constant α_s. The use of R_Z to test the MSM has the advantage that all other corrections, especially those depending on the unknown parameters of the theory, m_t and m_H, are largely suppressed, because they cancel in the ratio:

$$R_Z^0 \equiv R_Z(\alpha_s = 0) = 19.949 \pm 0.017 \quad , \tag{A.7}$$

where the uncertainty arises from a variation of m_t from 100 GeV to 200 GeV, and m_H from 60 GeV to 1000 GeV. In fact, a measurement of R_Z at **LEP** has been used to determine α_s (see Chapter 8).

A.3   Improved Born Approximation

Most of the weak corrections can be absorbed in the lowest-order Born-term formulae
by an adjustment of the coupling constants, yielding the so-called improved Born
approximation. In this framework, the coupling constants and the Z° width entering
in the propagator become $\sqrt{s}$ dependent [84]:

$$\alpha \quad \longrightarrow \quad \alpha(s) = \frac{\alpha}{1 - \Delta\alpha(s)} \tag{A.8}$$

$$\Gamma_Z \quad \longrightarrow \quad \Gamma_Z(s) = \frac{s}{m_Z^2}\Gamma_Z \tag{A.9}$$

$$g_A^f \quad \longrightarrow \quad g_A^f(s) = \sqrt{\rho_f(s)} \cdot T_3^f \tag{A.10}$$

$$g_V^f \quad \longrightarrow \quad g_V^f(s) = \sqrt{\rho_f(s)} \cdot (T_3^f - 2\kappa_f(s)Q_f \sin^2\theta_W) \quad . \tag{A.11}$$

The first equation shows the running of the electromagnetic fine structure "constant"
α with $\sqrt{s}$ (see Chapter 8) due to the photonic vacuum polarization (fermion loops
in the photon propagator):

$$\Delta\alpha = \Delta\alpha_{\text{leptons}} + \Delta\alpha_{\text{hadrons}} \tag{A.12}$$

$$\Delta\alpha_{\text{leptons}}(m_Z) = \frac{\alpha}{3\pi}\sum_{\ell=e,\mu,\tau} q_\ell \left[\ln\left(\frac{m_Z}{m_\ell}\right) - \frac{5}{3}\right] \tag{A.13}$$

$$\Delta\alpha_{\text{hadrons}}(m_Z) = -\frac{\alpha m_Z^2}{3\pi}\Re\left[\int_{4m_\pi^2}^\infty ds \frac{\sigma(e^+e^- \to \text{hadrons})/\sigma_{\text{QED}}}{s(s - m_Z^2 - i\epsilon)}\right] \quad . \tag{A.14}$$

The uncertainty of the hadronic part of the photonic vacuum polarization ($\Delta\alpha_{\text{hadrons}} =
0.0288 \pm 0.0009$ at $s = m_Z^2$ for five quark flavors) is the dominant uncertainty for the
theoretical predictions of otherwise very accurately predicted quantities such as the
various asymmetries or the anomalous magnetic moment of the electron [85].

Higher-order corrections and phase-space effects let the total width of the Z°
boson vary linearly with s, yielding the second equation. For energies around the Z°
resonance, the s dependent factors ρ and κ can be approximated by s-independent
effective constants by setting $s = m_Z^2$, yielding ρ_{eff} and κ_{eff}. This leads in turn to
the *effective* vector and axial-vector coupling constants of the weak neutral current.

Correspondingly, the *effective* weak mixing angle is defined by:

$$\sin^2 \overline{\theta}_W \;\equiv\; \kappa_{\text{eff}} \sin^2 \theta_W \quad. \tag{A.15}$$

Both ρ and κ, although in principle dependent on the fermion species f, are to a good approximation equal for all fermions with the exception of the b quark. Here, large vertex corrections involving the top quark arise (see above).

Effects of Radiative Corrections

The effect of higher-order electroweak corrections is most visible in the relationship between G_F, which is precisely determined from the lifetime of the μ, and the masses of the heavy gauge bosons. Equation 2.29 is modified to:

$$\sin^2 \theta_W \cos^2 \theta_W m_Z^2 \;=\; \sin^2 \theta_W m_W^2 \;=\; \frac{\pi \alpha / (\sqrt{2} G_F)}{1 - \Delta r} \quad, \tag{A.16}$$

where the quantity Δr [86] is a directly observable quantum-correction (zero to lowest order), which is rather sensitive to all kinds of new physics, including the unknown Higgs mass m_H and top mass m_t. It incorporates QED and weak effects:

$$1 - \Delta r \;=\; (1 - \Delta \alpha)(1 + \frac{\cos^2 \theta_W}{\sin^2 \theta_W} \Delta \rho) - \Delta r_H - \Delta r_{\text{remainder}} \quad. \tag{A.17}$$

The first part ($\Delta \alpha$) arises from the running of the electromagnetic coupling constant α. The other parts contain the genuine weak corrections, which are sensitive to m_t and m_H. Evaluating in the leading terms, one has:

$$\Delta \rho_{\text{top}} \;=\; \frac{3 G_F m_t^2}{8 \sqrt{2} \pi^2} \tag{A.18}$$

$$\Delta r_H \;=\; \frac{G_F m_W^2}{8 \sqrt{2} \pi^2} \left[\frac{11}{3} \left(\ln \frac{m_H^2}{m_W^2} - \frac{5}{6} \right) \right] \quad, \tag{A.19}$$

where the latter equation holds for a heavy Higgs boson. Hence, precise measurements of cross sections and asymmetries can be used to constrain these as yet unknown masses.

Figure A.7 shows how the total cross section $\sigma_0(e^+ e^- \rightarrow \tau^+ \tau^-)$ and forward-backward charge asymmetry $A_{fb}(e^+ e^- \rightarrow \tau^+ \tau^-)$ are modified by higher-order radiative corrections.

Tau-pair production
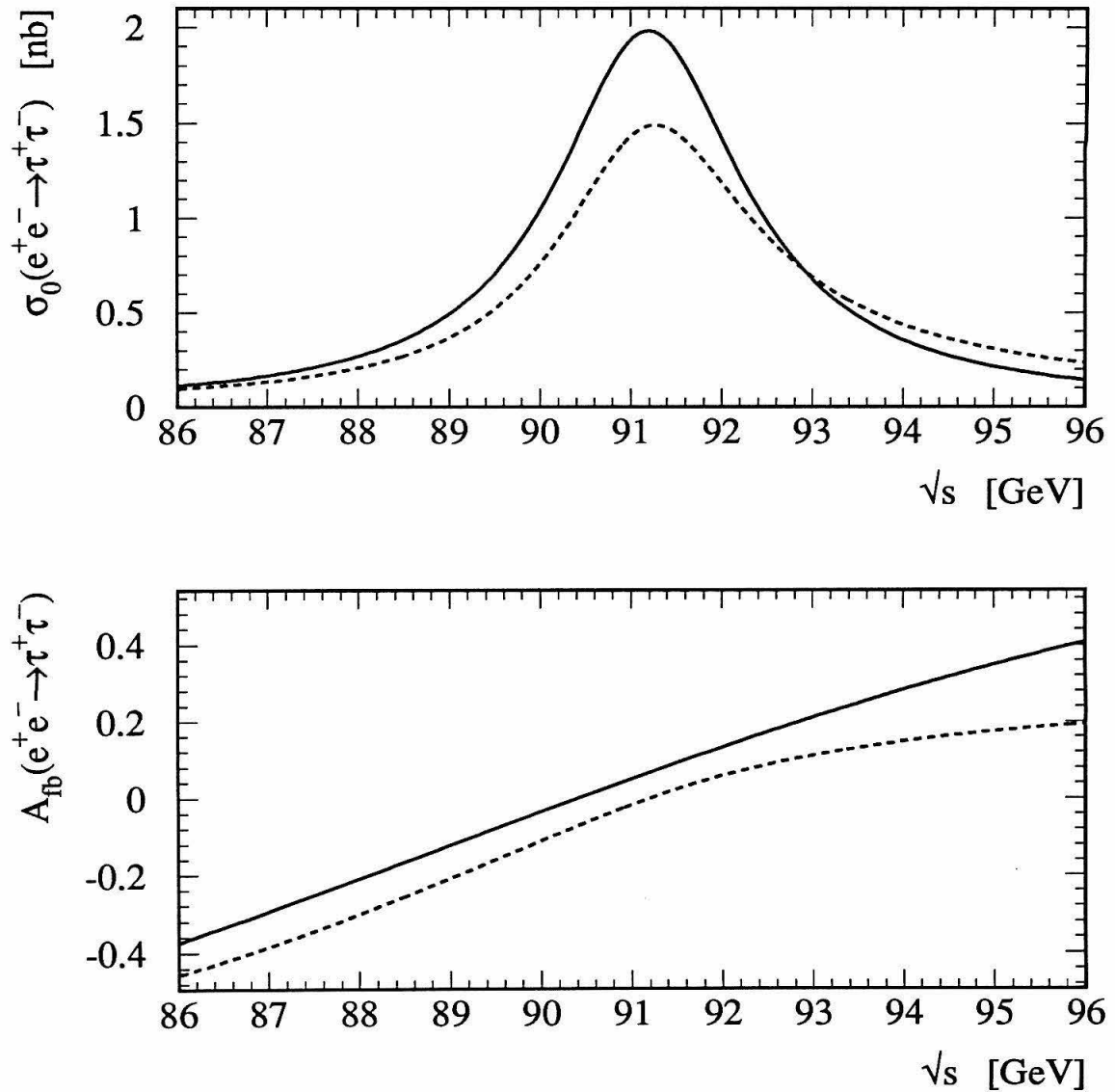
Figure A.7: Effect of radiative corrections on the total cross section $\sigma_0(e^+e^- \to \tau^+\tau^-)$ and the forward-backward charge asymmetry $A_{fb}(e^+e^- \to \tau^+\tau^-)$ in the energy range near the Z° resonance. The solid line is Born term only. The dashed line includes higher-order corrections (calculated by ZFITTER, see Appendix F).

Appendix B

The Decay of the τ Lepton

Within the group of charged leptons, the τ represents a special case, due to the fact that it decays before being detected. Although the decay makes it harder to isolate $\tau^+\tau^-(\gamma)$ events experimentally, it provides additional insights into the weak interactions: Whereas the production of $f\bar{f}$, including $\tau^+\tau^-$ pairs, at e^+e^- colliders such as **LEP** probes the neutral current sector of the **MSM** at an energy scale characterized by m_Z, the decay of the charged τ lepton probes the charged current sector at the much lower scale characterized by m_τ. Figure B.1 shows the decay of the charged τ lepton within the **MSM**.
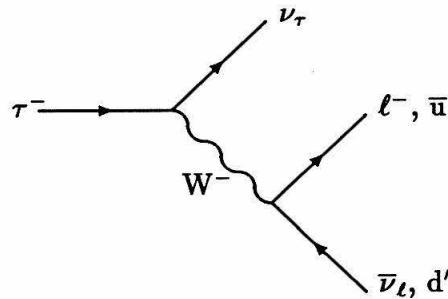
Figure B.1: The decay of the charged τ lepton within the **MSM** ($\ell = e, \mu$; $d' = d\cos\theta_C + s\sin\theta_C$).

B.1   Leptonic τ Decays and τ Lifetime

The decays of the charged τ lepton to a lighter charged lepton ℓ ($\ell = \mathrm{e}, \mu$) are purely electroweak in nature. They can be calculated using the hypothesis of a universal $V - A$ structure of the charged weak current [87]:

$$\Gamma_\ell^\tau \equiv \Gamma(\tau \to \ell\nu_\ell(\gamma)\nu_\tau) = \frac{\mathrm{G}_\mathrm{F}^2 m_\tau^5}{192\pi^3} F_m(y_\ell) F_W F_{rad} \quad , \tag{B.1}$$

where the simple four-fermion term is corrected by:

1. a phase space factor $F_m(y_\ell)$ taking into account the finite mass m_ℓ of the charged lepton ℓ [1]:

$$y_\ell = m_\ell^2/m_\tau^2 \approx \begin{cases} 0.8270 \cdot 10^{-7} & \text{for } \ell = \mathrm{e} \\ 0.3536 \cdot 10^{-4} & \text{for } \ell = \mu \end{cases} \tag{B.2}$$

$$\begin{aligned} F_m(y) &= 1 - 8y + 8y^3 - y^4 - 12y^2 \ln y \\ &\approx \begin{cases} 1.0000 & \text{for } y = y_\mathrm{e} \\ 0.9726 & \text{for } y = y_\mu \end{cases} \quad , \end{aligned} \tag{B.3}$$

2. a factor for the correction due to W propagator effects:

$$F_W = 1 + \frac{3}{5}\frac{m_\tau^2}{m_\mathrm{W}^2} \approx 1.0003 \quad , \tag{B.4}$$

3. a factor expressing QED radiative corrections:

$$F_{rad} = 1 - \frac{\alpha(m_\tau)}{2\pi}\left(\pi^2 - \frac{25}{4}\right) \approx 0.9957 \quad . \tag{B.5}$$

The numerical values above are calculated using world averages [11] for all particle masses except for m_τ, where the BES result [88], $m_\tau = 1.7769^{+0.0004}_{-0.0005}(\text{stat.}) \pm 0.0002(\text{syst.})$ GeV, is used.[2] The running coupling constant of QED at the τ mass is [91]:

$$\alpha(m_\tau) = 1/133.29 \quad , \tag{B.6}$$

---

[1] In case of a massive neutrino ν_τ and neglecting the mass m_ℓ of the charged lepton, the correction is given by $F_m(y_{\nu_\tau})$.

[2] This measurement of m_τ has been confirmed by the ARGUS [89] and CLEO-II [90] collaborations.

incorporating virtual photon corrections as well as the emission of real photons and light fermion pairs. The ratio of the leptonic decay widths is thus given by *phase space* considerations:

$$\frac{\Gamma_\mu^\tau}{\Gamma_e^\tau} \;=\; \frac{B_\mu^\tau}{B_e^\tau} \;=\; \frac{F_m(y_\mu)}{F_m(y_e)} \;\approx\; 0.9726 \quad, \tag{B.7}$$

where the leptonic branching fractions B_ℓ^τ of τ decays are defined as:

$$B_\ell^\tau \equiv \frac{\Gamma_\ell^\tau}{\Gamma_{\text{tot}}^\tau} \qquad (\ell = e, \mu) \quad, \tag{B.8}$$

and where Γ_{tot}^τ is the total τ decay width:

$$\Gamma_{\text{tot}}^\tau \;=\; \Gamma_e^\tau + \Gamma_\mu^\tau + \Gamma_{\text{had}}^\tau \quad. \tag{B.9}$$

The τ lifetime τ_τ is of interest because it establishes another relation between the leptonic branching fractions, which are measured, and the leptonic decay widths, which are calculated with high precision (see above) via the following relation:

$$\tau_\tau \;\equiv\; \frac{1}{\Gamma_{\text{tot}}^\tau} \;=\; \frac{B_\ell^\tau}{\Gamma_\ell^\tau} \quad. \tag{B.10}$$

Consistency and Universality

Consistency within the charged weak interaction sector requires that the lifetime and leptonic branching fractions are proportional to each other, with exactly known proportionality factors (see Chapter 7 for experimental results).

Lepton universality of the *charged* weak current requires the coupling constants A and V to be identical for the three generations of leptons e, μ and τ. Chapter 8 gives experimental results on the lepton universality of the *neutral* weak current.

B.2 Hadronic τ Decays and QCD

The theory of hadronic τ decays [92] is much less developed due to the difficulties introduced by the strong interaction, which confines quarks in hadrons. To zeroth order, one could just use free quark currents in a calculation along the lines used for

the leptonic decay modes. However, using free quark wave functions is not correct, because quarks are bound inside hadrons. On the other hand, one cannot compute reliably the actual quark density functions reliably from first principles, because the QCD perturbative expansion cannot be used directly in this low-Q^2 region.

From general arguments, the decay width of the charged τ lepton into a particular hadronic system h has the form [87]:

$$
\begin{aligned}
\Gamma_h^\tau &\equiv \Gamma(\tau \to h\nu_\tau) \qquad\qquad\qquad\qquad\qquad\qquad\qquad\quad \text{(B.11)}\\
&= 12\pi\Gamma_e^\tau \int_0^{m_\tau^2} \frac{\mathrm{d}s}{m_\tau^2}\left(1 - \frac{s}{m_\tau^2}\right)^2 \\
&\quad \left\{ \cos^2\theta_C \left[\left(1 + 2\frac{s}{m_\tau^2}\right)[v_1(s) + a_1(s)] + (v_0(s) + a_0(s))\right]\right.\\
&\quad \left. + \sin^2\theta_C \left[\left(1 + 2\frac{s}{m_\tau^2}\right)[v_1^S(s) + a_1^S(s)] + (v_0^S(s) + a_0^S(s))\right]\right\} \quad , \quad \text{(B.12)}
\end{aligned}
$$

where s is the invariant mass squared of the hadronic system h. The v's and a's, called spectral functions, depend on h. The hadronic system may have either spin 0 or 1, in which case only the spectral functions with index either 0 or 1 are non-vanishing. Also, h may be either non-strange or strange, in which case only the spectral functions without or with superscript S are non-vanishing. The corresponding Cabibbo angle terms are explicitly separated out of the spectral functions. Finally, the letters v and a refer to spectral functions connected to the vector (V) and axial-vector (A) parts of the weak charged current. The possibilities for spin J and parity P assignments for h are $J^P = 0^+, 1^-$ for V, and $J^P = 0^-, 1^+$ for A. The conserved-vector-current principle (CVC) excludes 0^+ and hence requires the non-strange v_0 to vanish. Hence for any hadronic system of definite spin, parity and strangeness, only one of the above spectral functions is non-zero.

As already said, there is no general way to calculate the spectral function for a specific hadronic system h. However, it is possible to calculate the spectral functions summed over all possible hadronic final states which are associated with specific quark currents, i.e., vector, axial-vector and strange currents. This provides expressions for the following semi-inclusive hadronic decay widths (using N_C to denote the

number of colors in QCD):

- non-strange vector current contribution:

$$\Gamma_{\mathrm{V}}^{\tau} = \sum_{h=(2n)\pi} \Gamma(\tau \to h\nu_{\tau}) \approx \frac{N_{\mathrm{C}}}{2} \cos^2 \theta_C \cdot \Gamma_{\mathrm{e}}^{\tau} \quad , \tag{B.13}$$

- non-strange axial-vector current contribution:

$$\Gamma_{\mathrm{A}}^{\tau} = \sum_{h=(2n+1)\pi} \Gamma(\tau \to h\nu_{\tau}) \approx \frac{N_{\mathrm{C}}}{2} \cos^2 \theta_C \cdot \Gamma_{\mathrm{e}}^{\tau} \quad , \tag{B.14}$$

- strange current contribution:

$$\Gamma_{\mathrm{S}}^{\tau} = \sum_{h=(n)\mathrm{K}} \Gamma(\tau \to h\nu_{\tau}) \approx N_{\mathrm{C}} \sin^2 \theta_C \cdot \Gamma_{\mathrm{e}}^{\tau} \quad . \tag{B.15}$$

These three contributions add up to the total hadronic width:

$$\Gamma_{\mathrm{had}}^{\tau} = \Gamma_{\mathrm{V}}^{\tau} + \Gamma_{\mathrm{A}}^{\tau} + \Gamma_{\mathrm{S}}^{\tau} \approx N_{\mathrm{C}} \cdot \Gamma_{\mathrm{e}}^{\tau} \quad , \tag{B.16}$$

which provides evidence for colored QCD, when compared with the measured result. The approximations quoted in the above equations use the naive free quark currents in the calculations, and are therefore rather crude.

Strong Coupling Constant

Similar to the case of Z° decays, where the quantity R_Z is introduced, one defines an analogous quantity called R_τ:

$$R_\tau \equiv \frac{\Gamma_{\mathrm{had}}^{\tau}}{\Gamma_{\mathrm{e}}^{\tau}} = R_{\tau,\mathrm{V}} + R_{\tau,\mathrm{A}} + R_{\tau,\mathrm{S}} \quad . \tag{B.17}$$

To zeroth order, R_τ is obviously given by the number N_{C} of colors in QCD:

$$R_\tau^0 = N_{\mathrm{C}}(\sin^2 \theta_C + \cos^2 \theta_C) = N_{\mathrm{C}} \quad . \tag{B.18}$$

Large corrections to this expression arise in perturbative QCD, which implies sensitivity of R_τ to the value of the strong coupling constant α_s at the scale m_τ. Corrections due to Cabibbo-Kobayashi-Maskawa quark mixing, electroweak corrections,

both non-perturbative and perturbative QCD as well as corrections for finite quark masses can be incorporated [93, 65, 66]:

$$R_\tau = N_C C_{CKM} S_{EW} \left(1 + \Delta_{EW} + \Delta_{non-pert} + \Delta_{pert}\right) \quad , \tag{B.19}$$

where the various correction terms are explained below:

- C_{CKM} is the term arising from the Cabibbo-Kobayashi-Maskawa matrix elements:

$$C_{CKM} = |V_{ud}|^2 + |V_{us}|^2 \approx 1.0000 \quad . \tag{B.20}$$

- S_{EW} is the renormalization-group improved electroweak correction in the leading logarithm approximation (assuming $m_t > m_Z$):

$$S_{EW} = \left(\frac{\alpha(m_b)}{\alpha(m_\tau)}\right)^{9/19} \left(\frac{\alpha(m_W)}{\alpha(m_b)}\right)^{9/20} \left(\frac{\alpha(m_Z)}{\alpha(m_W)}\right)^{36/17} \tag{B.21}$$

$$\approx 1.0194 \quad . \tag{B.22}$$

- Δ_{EW} is the next-to-leading-logarithm electroweak correction:

$$\Delta_{EW} = \frac{5}{12} \frac{\alpha(m_\tau)}{\pi} \approx 0.0010 \quad . \tag{B.23}$$

- $\Delta_{non-pert}$ contains the QCD non-perturbative corrections plus the corrections for finite quark masses. These corrections are not well known (relative error of 50%), but fortunately rather small:

$$\Delta_{non-pert} = -0.0080 \pm 0.0040 \quad . \tag{B.24}$$

- Δ_{pert} is the perturbative QCD correction, which can be expanded in a series in α_s/π, the coefficients of which are known up to third order:

$$\Delta_{pert} = \sum_{i=1} K_i \left(\frac{\alpha_s(m_\tau)}{\pi}\right)^i \tag{B.25}$$

$$\approx \frac{\alpha_s(m_\tau)}{\pi} + 5.2023 \left(\frac{\alpha_s(m_\tau)}{\pi}\right)^2 + 26.366 \left(\frac{\alpha_s(m_\tau)}{\pi}\right)^3 \quad . \tag{B.26}$$

The coefficients K_i are in fact related to those of the corresponding series expansion of R_Z. The great sensitivity of Δ_{pert} to α_s, and the fact that Δ_{pert} is larger ($\mathcal{O}(20\%)$) than all other corrections ($\mathcal{O}(1\%)$), make R_τ a sensitive tool to determine the value of the strong coupling constant α_s at the mass of the charged τ lepton.

Experimentally, it is sufficient to measure either one or both leptonic branching fractions or the lifetime to determine R_τ:

$$R_\tau = \frac{1 - B_e^\tau - B_\mu^\tau}{B_e^\tau} = \frac{1/\tau_\tau - \Gamma_e^\tau - \Gamma_\mu^\tau}{\Gamma_e^\tau} \quad . \tag{B.27}$$

B.3 Polarization

The energy spectrum of the τ decay products carries information about the polarization of the τ. For a given longitudinal polarization $\mathcal{P}_\tau$, the differential decay rate to lowest order reads:

$$\frac{1}{\Gamma}\frac{d\Gamma(u; \mathcal{P}_\tau)}{du} = h_0^x(u) + \mathcal{P}_\tau \cdot h_1^x(u) \quad , \tag{B.28}$$

where $u = E_x/E_\tau$ is the scaled energy of the charged decay product x as observed in the $\tau^+\tau^-$ center-of-mass frame. To lowest order, the functions $h_{0,1}^x(u)$ are simple polynomials in u, and depend on the τ decay mode x:

- three body decays $\tau \to \ell\nu_\ell\nu_\tau$, where $\ell = e, \mu$:

$$h_0^\ell(u) = \frac{1}{3}(5 - 9u^2 + 4u^3) \tag{B.29}$$

$$h_1^\ell(u) = \frac{1}{3}(1 - 9u^2 + 8u^3) \quad , \tag{B.30}$$

- two body decays $\tau \to x\nu_\tau$, where $x = \pi, K, \rho, a_1$:

$$h_0^x(u) = 1 \tag{B.31}$$

$$h_1^x(u) = \alpha_x \cdot (2u - 1) \quad , \tag{B.32}$$

where α_x is a constant depending on the mass and spin of the decay product x. In the case of spin-0 particles (π, K), $\alpha_x = 1$. The sensitivity of the decay energy

spectrum to $\mathcal{P}_\tau$ is reduced in the case of decays to spin-1 hadrons (ρ, a_1):

$$\alpha_x = \frac{m_\tau^2 - 2m_x^2}{m_\tau^2 + 2m_x^2} < 1 \quad . \tag{B.33}$$

It can be recovered by a spin-analysis of the hadron by examining the kinematics of the decay products of the hadron itself [94].

Polarization at e^+e^- Colliders

By combining appropriately Equations 2.34 and B.28, the double differential cross section in u and $\cos\theta$ is obtained:

$$\frac{d^2\sigma_0(e^+e^- \to \tau^+\tau^-)}{d\cos\theta \, du} = \frac{3}{8}\left[\left\{A(1+\cos^2\theta) + B\cos\theta\right\} h_0^x(u) \right. \\ \left. - \left\{C(1+\cos^2\theta) + D\cos\theta\right\} h_1^x(u)\right]\sigma_{\mathrm{QED}} \quad . \tag{B.34}$$

The polarization asymmetry (or averaged helicity) as a function of the polar scattering angle θ is given by:

$$\mathcal{P}_\tau(\cos\theta) \equiv \frac{\frac{d\sigma(h_f=+1)}{d\cos\theta} - \frac{d\sigma(h_f=-1)}{d\cos\theta}}{\frac{d\sigma(h_f=+1)}{d\cos\theta} + \frac{d\sigma(h_f=-1)}{d\cos\theta}} = -\frac{C(1+\cos^2\theta) + D\cos\theta}{A(1+\cos^2\theta) + B\cos\theta} \tag{B.35}$$

$$\approx \frac{\mathcal{P}_\tau + \frac{2\cos\theta}{1+\cos^2\theta}\mathcal{P}_e}{1 + \frac{2\cos\theta}{1+\cos^2\theta}\mathcal{P}_e\mathcal{P}_\tau} \quad , \tag{B.36}$$

where the approximation holds at the peak of the Z° resonance ($\sqrt{s} = m_Z$). The quantity $\mathcal{P}_e$ is also measured at SLC with polarized beams. The left-right asymmetry A_{lr} is given by:

$$A_{lr} = \frac{\sigma_l - \sigma_r}{\sigma_l + \sigma_r} = -\mathcal{P}_e \quad , \tag{B.37}$$

where σ_l (σ_r) is the total cross section for Z° production from a left-handed (right-handed) e^+e^- system. The measurement of $\mathcal{P}_e$ at **LEP** suffers from a large loss in statistics (identified τ decays) compared to the measurement of A_{lr} using polarized beams (all Z° decays).

Appendix C

Determination of LEP Beam Energy

The mass m_Z and width Γ_Z of the Z° boson are fundamental parameters of the electroweak theory. The experimental determination of these quantities at **LEP** is based on measurements of the e^+e^- annihilation cross section as a function of the center-of-mass energy. In order to make use of the high statistics and hence very accurate cross-section measurements of the four **LEP** experiments, a precise knowledge of the beam energy for each **LEP** fill is essential.

In the combined analysis of the four **LEP** experiments on the data collected in 1989+1990 [95], the imperfect knowledge of the absolute **LEP** energy scale introduced an error on the Z° mass of 20 MeV. Energy-point-to-energy-point uncertainties and fill-to-fill non-reproducibilities resulted in an error on the Z° width of 6 MeV. These errors have to be compared with the statistical precision of the data of the four **LEP** experiments: the experimental errors on the combined **LEP** result for the 1989+1990 data on Z° mass and width are 5 MeV and 9 MeV, respectively.

Standard magnetic measurements yielded the errors quoted above for 1990, and it is clear that a more precise energy calibration was needed. The new method of resonant spin depolarization was used for the 1991 **LEP** running [96].

This appendix summarizes the various methods which were used to obtain a pre-

cise energy calibration of **LEP** for the 1991 data-taking period [97], and it discusses how the 1990 energies were recalibrated.

C.1   Measurements

Several basic measurements are performed in order to obtain information about the **LEP** beam energy.

Standard magnetic and orbit measurements: A particle with charge q and momentum p in a magnetic field B is bent by the Lorentz force on a circular path of definite radius R. Measurement of the magnetic field B created by the **LEP** dipole magnets, together with the knowledge of the central orbit, therefore gives the particle momentum p according to $p = qRB$. In practice, the product RB has to be "averaged" to high precision along the ideal orbital path through the dipole magnets as described below.

Another method, independent of the **LEP** magnetic fields, utilizes the observation of transverse spin polarization of the **LEP** beams to measure their energies.

All measurements are used in a combined analysis to arrive at a precise calibration of the **LEP** energy.

Field Display

The knowledge of the magnetic field created by the **LEP** dipole magnets is an essential ingredient, and serves as a starting point for a precise energy calibration. For this purpose, the field in a reference dipole, which is powered in series with the ring magnets, is monitored with a flipping coil. The energy estimated from this measurement, called E_{FD}, is continuously available. All additional corrections (see below) are made with respect to this measurement. One drawback is, however, that the reference dipole magnet is different from the **LEP** concrete-iron dipoles, and it is situated in different temperature and humidity conditions.

A correction has to be made to account for non-linearities of the magnets. Initially in 1989, the relation between E_{FD} and the magnetic field in the dipole magnets

was linear. Remnant fields of the dipole magnets and the permeability of their laminations at a given temperature have changed with time. Therefore, the transfer function has become slightly non-linear, so that a local linear scale correction has to be applied.

Flux Loop

A more direct measurement of the field generated by the ring dipole magnets can be obtained by cycling the magnets and measuring the induced current in a closed electrical loop embedded in the **LEP** dipoles. However, this method cannot be applied while beams circulate, and it does not take into account the dipole components of other magnets, e.g., in orbit correctors and quadrupole magnets.

The following effects must be corrected for:

- Aging of the flux-loop:
  There is a continuous change in the response of the flux-loops embedded in the **LEP** dipoles due to shrinkage of the concrete-iron dipoles with dehydration.

- Temperature dependence of the flux-loop measurement:
  There is a correlation between flux-loop measurements and the measured temperature of the dipole magnets, which can be reproduced by laboratory measurements.

- Earth's magnetic field:
  The magnetic field of the earth changes the effective field seen by the **LEP** beams. Because the flux-loop measurements are not sensitive to this constant additional field, they have to be corrected for.

Proton Orbit

The particle momentum corresponding to the central orbit in **LEP** can be measured at injection energy (20 GeV) using protons. The method is based on the fact, that protons at 20 GeV are not yet ultrarelativistic. Their velocity β_p is therefore different from the speed of light and can be used to determine the momentum.

The central orbit, with an average radius R, has a revolution frequency f_e and a central RF frequency f_{RF_e} for electrons:

$$f_e = \frac{\beta_e c}{2\pi R} \tag{C.1}$$

$$f_{RF_e} = h_e f_e \quad , \tag{C.2}$$

where h_e is the so-called harmonic number (an integer) for electrons and positrons. Protons are injected into **LEP** with the same magnetic lattice settings, and are then trapped with the RF system, but on a harmonic number h_p different from h_e and an RF frequency f_{RF_p}. Using $\beta_e(20\text{ GeV}) = 1$, the velocity of the protons is given by:

$$\beta_p = \frac{h_e f_{RF_p}}{h_p f_{RF_e}} \quad , \tag{C.3}$$

and hence the particle momentum corresponding to the central orbit in **LEP** at 20 GeV beam energy setting is determined. However, uncertainties arise due to the necessary extrapolation of this result to a beam energy of 45 GeV.

Polarization

A transverse beam polarization of approximately 10% was reproducibly created in **LEP** in 1991. With polarized beams, it is possible to measure the spin precession frequency by inducing a controlled spin-depolarizing resonance. An artificial depolarizing resonance occurs when a superimposed radial magnetic field oscillates at the spin precession frequency $\omega_{dep} = 2\pi\nu_s f_e$. The spin tune ν_s, i.e., the number of spin precessions per revolution, is related to the beam energy via:

$$\nu_s = a_e \gamma = a_e \frac{E_{\text{Beam}}}{m_e} = N_s + \delta\nu_s \quad , \tag{C.4}$$

where $a_e = (g_e - 2)/2$ is the anomalous magnetic moment of the electron. N_s and $\delta\nu_s$ are the integer and fractional part of the spin tune ν_s, respectively. The standard magnetic measurements are precise enough to provide N_s without ambiguity. At the Z° resonance, the integer part of the spin tune ν_s is $N_s = 103$. A measurement of

the depolarizer frequency at the resonance $f_{dep}^{res} = f_e \delta \nu_s$ gives the non-integer part $\delta \nu_s$ of the spin tune, and defines the mean beam energy:

$$E_{\text{Beam}} = \frac{m_e}{a_e} \nu_s = 0.4406486 \cdot \left(N_s + \frac{f_{dep}^{res}}{f_e} \right) \text{ GeV} \quad . \tag{C.5}$$

Since at the Z° resonance, the spin tune is of order 100, the measurement of the non-integer part of ν_s to an accuracy of 0.001 determines E_{Beam} with a precision of 1 in 10^5.

A sweep of f_{dep} around the estimated values is performed, while measuring the beam polarization. Eventually, depolarization is observed at a certain setting f_{dep}^{res}. During the 1991 data taking period, polarization measurements were done repeatedly at 46.5 GeV beam energy ($N_s = 105$), the most promising energy to induce polarization.

A spread in the data of ± 3 MeV was observed for measurements in the same fill and over a period of two months. This was originally interpreted as the short- and long-term stability of the **LEP** machine in agreement with expectations. The spread of ± 3 MeV is reduced to ± 1 MeV, if a correction for tidal effects is applied. Tidal forces from the moon and to a smaller extent from the sun distort the shape of the earth. The local change of the earth's radius induces a small expansion/contraction of the solid surfaces of the earth crust. The 4.25 km radius of **LEP** is expected to change by 0.15 mm, which shifts the center-of-mass energy by about 8 MeV between the two extremes. Both the polarization measurements and the physics runs of the **LEP** machine, and hence the data-acquisition periods of the experiments sample the tidal phases in an unbiased way.

C.2 Calibration Results

In addition to the measurements described above, which result in a determination of the overall **LEP** beam energy, the following interaction-point-specific effect has to be taken into account: The RF units compensating the energy loss due to synchrotron radiation are placed to the left and right of interaction regions 2 (**L₃**) and 6

(OPAL). Because of this asymmetric setting of the RF cavities around the **LEP** ring, interaction-region-dependent shifts occur, which are time dependent due to the status of the RF (high voltage trips etc.). These shifts are significant for **L₃** and OPAL ($\Delta\sqrt{s} \approx +14$ MeV), and nearly zero for ALEPH and DELPHI ($\Delta\sqrt{s} \approx \mp 0.2$ MeV, respectively).

The calibration of the absolute energy scale is obtained as follows:

1. For each fill the field in the reference dipole was measured with the field display system.

2. The absolute energy scale correction at the +2 energy point (nominal beam energy 46.5 GeV) relative to the field display value is determined by the resonant depolarization method. At $\sqrt{s} = 93$ GeV:

$$\left(\frac{\Delta E}{E}\right)_{\mathrm{abs}} = (-73.0 \pm 5.7) \cdot 10^{-5} \quad . \tag{C.6}$$

3. A local linear scale correction (α_0) determined from flux-loop measurements is applied to derive this energy difference for the other six energy scan points:

$$\Delta\sqrt{s} = \alpha_0(\sqrt{s} - 93 \text{ GeV}) \tag{C.7}$$

$$\alpha_0 = (-2.0 \pm 1.5) \cdot 10^{-3} \quad . \tag{C.8}$$

4. A linear temperature correction (C_T) is applied on a fill-by-fill basis. The temperature coefficient is obtained by flux-loop measurements and from dedicated laboratory experiments.

$$C_T = (1.00 \pm 0.25) \cdot 10^{-4} \text{ K}^{-1} \quad . \tag{C.9}$$

5. Interaction-point-dependent corrections $\delta_{RF}(\text{IP})$ varying in time are applied. They arise from alignment errors of the RF cavities and the voltage distribution in these cavities, the latter varying in time due to high voltage trips.

Correction of Energies

The full set of corrections for energy point i and fill f is given by the following formula:

$$\sqrt{s}_f^i = 2E_{f,FD}^i \left[1 + \left(\frac{\Delta E}{E}\right)_{\mathrm{abs}} + \alpha_0 \frac{2E_{f,FD}^i - 93\ \mathrm{GeV}}{2E_{f,FD}^i} \right.$$
$$\left. + C_T(T_f^i - \langle T_f^i \rangle) + \delta_{RF}(\mathrm{IP}) \right] \quad . \tag{C.10}$$

Treatment of Errors

The uncertainties in the determination of the absolute energy are divided into four different categories:

1. the uncertainty in the absolute energy scale:

$$\delta\left(\frac{\Delta E}{E}\right) = 5.7 \cdot 10^{-5} \quad , \tag{C.11}$$

2. the uncertainty in the local energy scale:

$$\delta\alpha_0 = 1.5 \cdot 10^{-3} \quad , \tag{C.12}$$

3. uncorrelated energy-point-to-energy-point errors (zero at 93 GeV):

$$\left(\frac{\delta E}{E}\right)_{\mathrm{ptp}}^{\mathrm{setting}} = 3 \cdot 10^{-5} \quad , \tag{C.13}$$

4. fill-to-fill non-reproducibility errors:

$$\left(\frac{\delta E}{E}\right)_{\mathrm{rep}} = 1 \cdot 10^{-4} \quad , \tag{C.14}$$

each of which requires a different treatment in lineshape[1] studies. Introducing the effective number of fills $\bar{N}_{\mathrm{fills}}^i$ per energy point i:

$$\bar{N}_{\mathrm{fills}}^i = \frac{\left(\sum_{f=\mathrm{fills}(i)} \mathcal{L}_f\right)^2}{\sum_{f=\mathrm{fills}(i)} \mathcal{L}_f^2} \quad , \tag{C.15}$$

---

[1] The Z° resonance cross section as a function of $\sqrt{s}$.

where $\mathcal{L}_f$ is the luminosity in fill f, one can combine the last two errors into one energy-to-energy error:

$$\left[\left(\frac{\delta E}{E}\right)^i_{\text{ptp}}\right]^2 = \left[\left(\frac{\delta E}{E}\right)^{\text{setting}}_{\text{ptp}}\right]^2 + \frac{1}{\bar{N}^i_{\text{fills}}}\left[\left(\frac{\delta E}{E}\right)_{\text{rep}}\right]^2 \quad . \tag{C.16}$$

Defining nine random variables X, all with zero mean and unit variance, the fluctuations of each energy point around the luminosity-weighted mean of its various fills are then:

$$\frac{\delta E^i}{E^i} = X_{\text{abs}}\left(\frac{\delta E}{E}\right)_{\text{abs}} + X_\alpha \frac{2E^i - 93 \text{ GeV}}{2E^i}\delta\alpha_0 + X_i\left(\frac{\delta E}{E}\right)^i_{\text{ptp}} \quad . \tag{C.17}$$

The above equations can be used to calculate the correlations between the lineshape fit parameters and the correlation matrix between the various scan points.

The error in the calibration of the LEP beam energy, as discussed above, leads to an uncertainty in the m_Z and Γ_Z of 6.3 and 4.9 MeV, respectively (also see Chapter 8). The forward-backward charge asymmetry on the peak is affected by an absolute error of 0.0008.

Calibration for Data Taken in 1991 before August 14

The cooling system of the LEP dipole magnets was changed on August 14, 1991, which induced an effect on the calibration of the flux-loop measurements. It is difficult to extrapolate back the absolute energy scale from the end of 1991, where the energy scan and polarization measurements were performed, to the period before August 14. Thus, the absolute energy scale of the data taken until that date is a factor of four more uncertain, $20 \cdot 10^{-5}$ compared to $5.7 \cdot 10^{-5}$ for data taken after that date.

Calibration for Data Taken in 1990

The working group on LEP energy recommended to use the 1990 Z° mass to recalibrate the 1990 beam energy, by applying the local linear scale correction mentioned above and then rescaling the energies such that the 1990 and 1991 fitted Z° masses

coincide. This has the effect, that only the *shape* of the 1990 lineshape, but not its *position*, will add information to the determination of electroweak parameters. This is reflected in the quoted uncertainty of the energy scale of data taken in 1990 of $29 \cdot 10^{-5}$, which is large compared to 1991.

Future Improvements

For further improvement of the **LEP** energy calibration (1992+), the following items are foreseen:

- polarization measurements at more or all energy points,

- further investigation of tidal effects,

- better control and understanding of temperature effects.

It is anticipated to reach an ultimate accuracy of less than 2 MeV in the center-of-mass energy.

C.3   Energy Spread

The energy distribution of particles in the **LEP** beams is not a δ-function, but has a finite width σ_E. The relative spread σ_E/E scales linearly with the beam energy:

$$\frac{\sigma_{E_{Beam}}}{E_{Beam}^2} = 0.157 \cdot 10^{-4} \text{ GeV}^{-1} \quad . \tag{C.18}$$

The resulting spread in the center-of-mass energy $\sqrt{s}$ is not simply $\sqrt{2}\sigma_{E_{Beam}}$, but approximately $1.55\sigma_{E_{Beam}}$, due to finite dispersion at the interaction point. This corresponds to a spread of about 51 MeV in the center-of-mass energy of the peak, with an error of 5 MeV mainly due to variation of the central frequency of the RF system.

Hence measured quantities such as cross sections and asymmetries are effectively averaged over a small but non-vanishing range of center-of-mass energies, even within a fill. The data of **L3**, summarized in Appendix G, have been corrected for this

effect. The correction is largest on top of the peak ($\sqrt{s} \approx m_Z$), where it amounts to an increase in cross section of 0.14%.

Appendix D

Upgrades of the LEP Machine and the L$_3$ Experiment

D.1 Upgrades of the LEP Accelerator

Future plans for the **LEP** machine include the beam energy upgrade, improvements in luminosity and possibly introduction of longitudinal polarized beams.

Energy

The **LEP** energy upgrade to more than 80 GeV beam energy has been planned from the very beginning of the construction program [98]. The development to reach this second phase is already under way. The installation of 192 additional superconducting RF cavities is scheduled to take place during the shutdown periods of the years 1990 until 1994. The **LEP** running from 1994/1995 onwards will therefore concentrate on the physics of W$^\pm$-pair production.

Luminosity

A substantial increase in **LEP** luminosity is possible by increasing the number of bunches in the electron and positron beam, which was 4 + 4 for the first years of

LEP running. In November 1992, after several tests, the mode was changed to $8+8$ bunches for physics runs.

Increasing the number of bunches automatically increases the number of unwanted collisions along the particle path, thus lowering the gain in luminosity from the naive factor of 2 due to additional beam-beam effects. Therefore, the bunches of both beams are separated at the empty collision points by means of a "pretzel" scheme, where the beams are folded around the central path in form of a pretzel in such a way as to avoid each other.

An increase in luminosity by as much as a factor of 9 could be possible by operating with 36 bunches per beam. However, this mode of LEP operation requires major changes in the trigger and data acquisition systems of all four experiments due to an increase in bunch-crossing rate by a factor of 9.

Polarization

As discussed in Appendix C, transverse spin polarization of the LEP beams at the 10% level was reproducibly observed under special running conditions at the end of the 1990 data taking period. In 1991, this effect was exploited to calibrate the beam energy of LEP by means of resonant depolarization of the observed polarization.

Longitudinal spin polarization can be obtained from transverse polarization by rotating the polarization through 90° using spin rotators. This form of polarized beams allows some additional precise studies of electroweak couplings at the Z° peak (left-right asymmetry A_{lr}), which currently can be done only at the SLC.

D.2   Upgrades of the L$_3$ Detector

Five major upgrades of the L$_3$ detector are foreseen in the period from 1992 to 1994:

1991/92: Trigger

The change from $4+4$ to $8+8$ bunches doubles the bunch crossing rate and hence leaves only half the time to arrive at a level-1 trigger decision. As always, negative

level-1 decisions must not introduce significant dead time. For this purpose, the level-1 subtriggers had to be upgraded using faster hardware. In case of the energy trigger, nearly 90% of the hardware had to be changed. Tests made in $4 + 4$ bunch mode helped with the early debugging of the hardware, so that **LEP**'s first $8 + 8$ bunch run under physics conditions was quite successful for L_3. An additional level-0 trigger has been introduced for the energy and muon level-1 subtriggers by running effectively a more coarse-grained but faster version of the corresponding level-1 algorithm.

1992: RFQ Calibration System

In order to exploit fully the high intrinsic resolution of electromagnetic crystal calorimeters, a precise calibration of each crystal is necessary. The standard calibration method of the L_3 BGO calorimeter, described in Chapter 3, has some clear disadvantages:

- Precise absolute calibration of each crystal with particles has been done in a test beam, but cannot be repeated.

- A calibration with cosmic rays requires about a month of dedicated cosmic data taking, to obtain the necessary statistics for each crystal. However, because of a high workload for detector maintenance during the **LEP** shutdown periods, it is virtually impossible to get enough data-taking time.

- The Xenon light system measures only the transparency of the crystals, and thus is insensitive to scintillation processes.

In order to overcome these drawbacks, and to reach the highest possible resolution, a novel calibration technique developed by Caltech [25, 26] will be applied, which allows *in situ* absolute calibration of all crystals of the L_3 BGO calorimeter within hours.

The idea of the calibration is to create a source of photons with definite energy inside the L_3 detector. It is then a matter of statistics to get a precise relative calibration of each crystal. Knowing the material in front of each crystal with respect to the

position of the photon source allows one to make small systematic corrections [25], and thus to obtain an absolute calibration.

Copious monochromatic photons are created most easily by a nuclear reaction. The reaction chosen yields the highest photon energies possible under the experimental constraints of feasibility and intensity:[1]

$$H^0 + {}^7_3Li \longrightarrow \gamma + {}^8_4Be \quad . \tag{D.1}$$

Radiative capture of protons in a Lithium target yields Beryllium plus a highly energetic photon of 17.65 MeV. In order to excite the appropriate resonance of 12 keV width, the incoming protons must have an energy of 450 keV. The experimental constraint of the L_3 detector operating within a magnetic field leads to the following setup for the RFQ calibration system:

1. 30 keV RF-excited H^- ion source,

2. low-energy beam transport system,

3. 1.85 MeV RFQ ion accelerator,

4. high-energy beam transport system including four focusing quadrupole magnets and a steering magnet,

5. beam neutralizer ($H^- \rightarrow H^0$) consisting of a differentially pumped gas cell,

6. beam pipe of 12 m length pointing upwards at an angle of 21.6° with respect to the LEP beam line,

7. molybdenum foil of 12.5 μm thickness to protect the target and to degrade the hydrogen kinetic energy to the excitation energy of the nuclear resonance,

8. lithium crystal target of 2 cm diameter and 2 mm thickness positioned within the outer layer of the FTC.

---

[1] Within the RFQ context, H denotes the hydrogen atom and not the Higgs boson.

The 425 MHz RFQ itself needs a 250 kW RF power system. A soft iron cover is used to protect the low energy beam of H^- ions from the stray field of the L_3 magnet. To guarantee the vacuum within the RFQ and the long beam pipe, special vacuum systems including pressure gauges together with cryogenic and NEG pumps are installed. Locally, the system is controlled and monitored by a stand-alone PC. However, the system also is interfaced to the general L_3 control and monitoring system.

The idea of a calibration run is to stay as close as possible to the standard procedure of running the L_3 detector during normal data taking. For this purpose, the time gate of the beam crossing is simply replaced by the RFQ signal. The low-level readout of the digitized BGO data from barrel, endcap and luminosity monitor is done in the usual way. However, histogramming of the energies deposited in each crystal will be done online in order not to write every event to tape, so that the trigger rate during a calibration run can be increased to the maximum of 150 Hz. To obtain a calibration, it is only necessary to know the energy distribution of the photons for each crystal. On the offline side, various corrections are applied, and a fit to the spectrum yields the calibration constants.

The first RFQ run in L_3 took place during November 1992, and analysis of the data is underway to determine precisely the corrections for each region of the BGO calorimeter. The first RFQ calibration, and a database permitting routine *in situ* calibrations in 1993, is expected to be completed during 1992.

1992/93: Luminosity Monitor

As discussed in Chapter 5, the systematic error introduced to the luminosity measurement due to imperfect knowledge of the location of the edge of the BGO crystals is the dominant contribution to the experimental systematic error. In order to reduce this uncertainty to 0.2%, the drift chambers in front of the luminosity calorimeters will be replaced by layers of silicon strips for precise impact-point reconstruction. The installation has started during the technical LEP stop in September 1992, and will be finished during the 1992/1993 winter shutdown.

1992/93: Silicon MicroVertex Detector

Starting with the 1991 run, all **LEP** experiments have operated with a new vacuum beam pipe of reduced radius (5.3 cm instead of 9 cm). This opens up the possibility to install a high precision silicon strip microvertex detector (SMD).

As the last of the four **LEP** experiments to do so, **L₃** will install its version of an SMD (see Figure D.1) during the 1992/1993 shutdown. This detector will enlarge the lever arm for track measurements in the crucial direction towards the interaction point, thus helping to maintain the current charge determination capabilities at **LEP 200** energies, as well as improving the resolution for vertex reconstruction. For example, the resolution in the distance of closest approach of a track to the vertex is expected to improve by a factor of 6. It is necessary to have this detector operational for at least one year of high statistics **LEP** running at the Z° resonance before entering into the **LEP 200** physics program in order to perform precision alignment with the other tracking detectors TEC, Z-detector and FTC.

1993/94: Forward-Backward Muon Chambers

The current angular acceptance for dimuons is restricted to the barrel region, which is given by the angular acceptance of the muon chamber system, where the muon tracks pass through at least two of the three chamber layers of the muon spectrometer (see Chapter 3). In order to increase this acceptance, forward-backward muon chambers are currently under construction. These chambers will be installed during the 1993/94 shutdown, and will be ready for the **LEP 200** program, allowing **L₃** to make reliable measurements of muonic W decays over the angular range $|\cos\theta| < 0.95$. The forward-backward muon chambers also will be valuable for further measurements with high luminosity at $\sqrt{s} \approx m_Z$, from 1994 onwards.

L3 Inner Tracking System
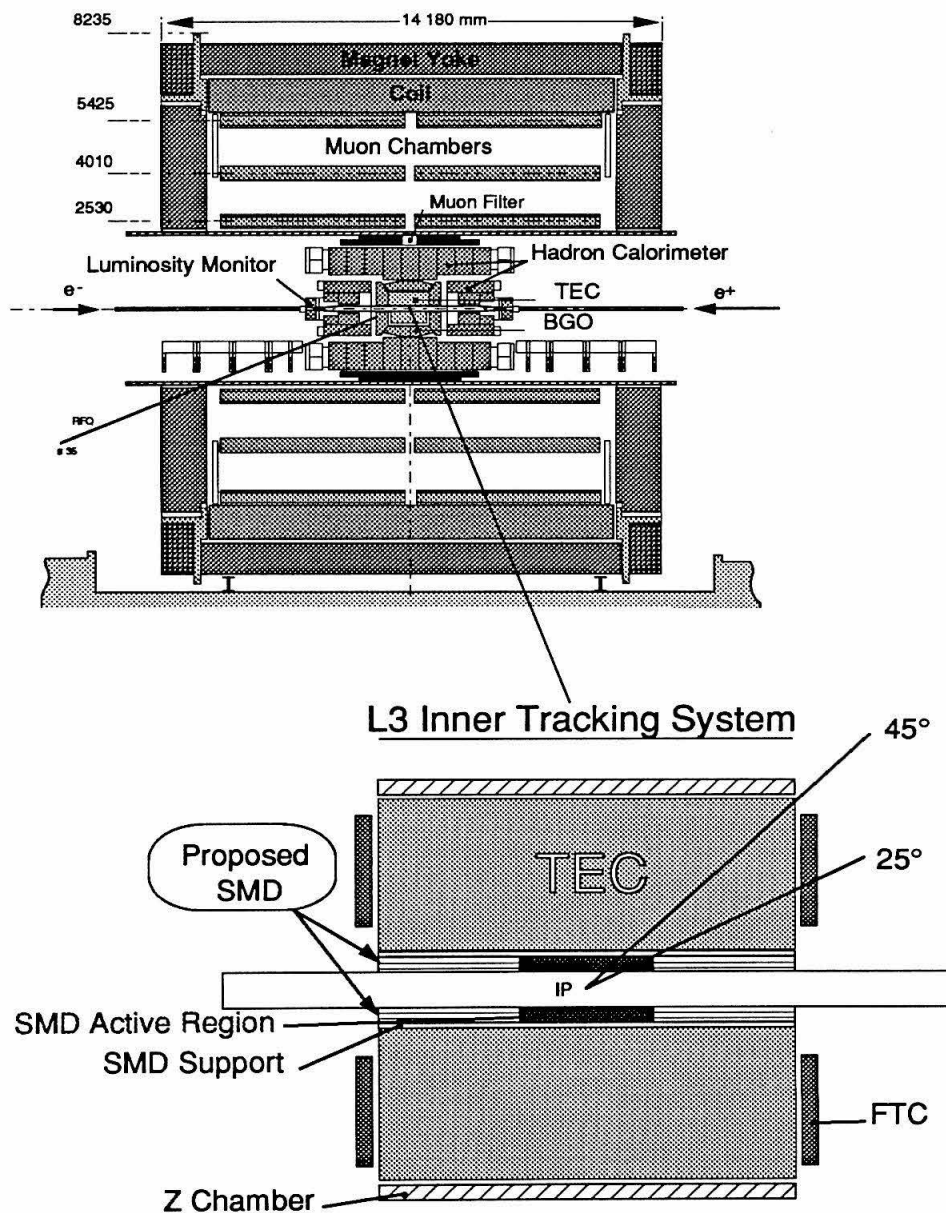
View of the SMD location in the L3 Experiment with 5 cm beam pipe

Figure D.1: Silicon microvertex detector (SMD) for **L3**.
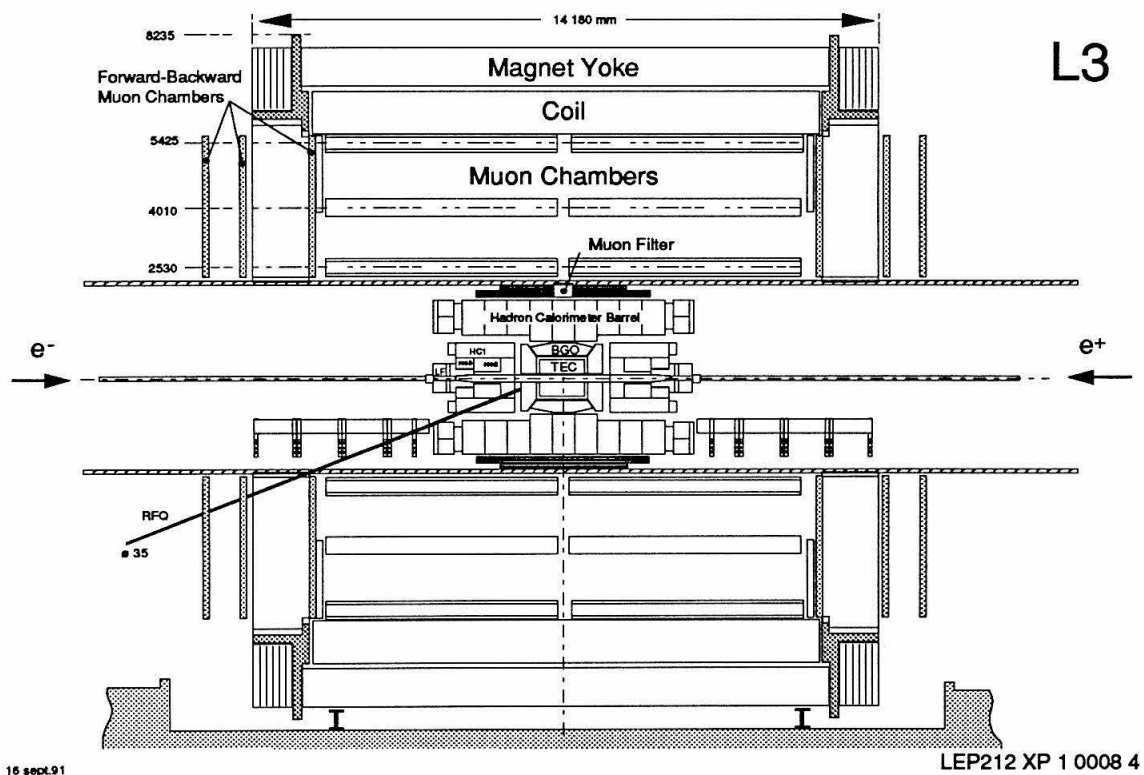
Figure D.2: Forward-backward muon chambers for **L3**.

Appendix E

Simulation of the L₃ Detector

This appendix describes in some detail the simulation of the L₃ detector using the general purpose detector simulation packages GEANT [47] and GHEISHA [48]. After an introduction to the technical realization of the simulation process, the development of the L₃ detector simulation program during the years 1989 until 1993 will be discussed. At the end, an overview on the current status and remaining problems is given.

E.1   GEANT and GHEISHA

GEANT groups particles into six different tracking types according to their interaction with matter, which have to be simulated during the tracking phase. The tracking types are:

1. photon γ,

2. positron/electron e^+e^-,

3. muon $\mu^+\mu^-$,

4. neutral hadron h^0,

5. charged hadron $h^\pm$,

6. "geantino."

Geantinos are special artificial GEANT particles, having the advantage that they do not undergo any interaction at all. A geantino can be generated at a given position and sent off into any direction the user likes. During tracking, the traversed detector materials are summed up in units of radiation and absorption lengths, so that a detailed study of the detector in terms of these quantities is possible.

Physics processes simulated by the GEANT package fall in three classes:

1. decays of unstable particles,

2. electromagnetic processes,

3. hadronic interactions.

By keeping track of the time of flight for each particle, GEANT is able to decay unstable particles properly. For this purpose, decay tables for long-lived hadrons, listing decay products and branching fractions, are included.

Electromagnetic processes are simulated using three different methods. They can be regarded as purely discrete processes, continuous processes or a mixture of both. The decision on which method to use depends on a process specific energy cutoff E_{cut} for the energies of created secondaries, which can be set by the user. For a certain process, the differential cross section as a function of the energy of a created secondary has the form:

$$\frac{\mathrm{d}\sigma}{\mathrm{d}E} = f(E) \quad , \tag{E.1}$$

where this differential cross section usually diverges for $E \to 0$ (infrared divergences typical for QED). Its integral from zero to E_{cut}, weighted by E, however, must be finite, so that Equation E.1 can be interpreted in terms of a continuous energy loss:

$$\frac{\mathrm{d}E}{\mathrm{d}x} = n \int_0^{E_{cut}} E f(E) \mathrm{d}E \quad , \tag{E.2}$$

where n is the density of scatterers in the medium through which the particle is tracked. Therefore, this part of the cross section is treated as a continuous energy

loss dE/dx of the particle during tracking from one discrete interaction to the next along its path, without simulating the low-energy secondaries with energies less than E_{cut} at all.

The remaining part of the cross section is finite everywhere, and is treated like any other discrete process. The mean free path λ between interactions in the material through which the particle is tracked is calculated:

$$1/\lambda \; = \; n \int_{E_{cut}}^{\infty} \frac{d\sigma}{dE} dE \quad . \tag{E.3}$$

The distribution of distances a particle will travel before undergoing the discrete interaction is given by:

$$\Delta x \; = \; -\lambda \cdot \ln R \quad , \tag{E.4}$$

using random numbers R distributed uniformly between 0 and 1. After each tracking step, the value of Δx is reduced by the length of the step. As soon as Δx is reduced to zero, an interaction is simulated by sampling the multi-differential cross sections to generate the kinematics after the interaction. Then, a new Δx is calculated using a new random number. In practice, many different processes with different mean free paths compete with each other. Their distances to the next interaction are maintained in parallel for each step. The higher the threshold E_{cut} is placed, the longer the mean free path becomes, and the shorter the computer time spent to simulate the process.

The following processes are implemented in GEANT:

- Continuous processes:

    - multiple scattering: Gaussian or Molière theory.

- Continuous and discrete processes:

    - bremsstrahlung: The energy cut-off E_{cut} is the energy of the bremsstrahlungs photon.

    - Moeller or Bhabha scattering: The energy cut-off E_{cut} is the energy of the generated secondary electron (δ-ray or knock-on electron).

- Discrete processes:

  - Rayleigh effect,

  - photoelectric effect,

  - Compton scattering,

  - pair production induced by photons and muons,

  - positron annihilation,

  - photo-fission,

  - hadronic interactions (via GHEISHA).

The purely continuous processes are applied after a tracking step to the position of the next discrete interaction has been taken. However, if it turns out that this step is so large that the continuous approximation is no longer valid, the step will be shortened by an appropriate amount before the particle is transported. Thus, beside the basic requirement of a step being longer than a minimal and shorter than a maximal step size, the following conditions limit the size of a tracking step:

- displacement due to multiple scattering,

- fractional energy loss,

- turning angle in magnetic field,

- crossing boundaries between different media,

- distance to next discrete interaction.

Switches allow each process to be deactivated by the user. Additionally, in the case of discrete processes, there exists the possibility to suppress the explicit generation of secondary particles. Instead, the sum of their kinetic energies will be released at the place of the interaction, and only the initial particle has to be tracked further, thus also shortening the computer time needed for simulation.

A particle will be tracked by GEANT as long as its kinetic energy is above a threshold, which can be set by the user to different values for each tracking type.

If during tracking the kinetic energy falls below this threshold, the particle will be stopped and its total kinetic energy deposited at its current position. The only physics process which still can take place once a particle has stopped, is its decay. It is very important to pick up the decay products and consider them for further tracking by GEANT. Finally, tracking is suspended when the tracked particle leaves the geometrical volume enclosing the experimental setup, or when its accumulated time of flight exceeds a specified limit.

Thus, the GEANT program provides many tracking parameters and cut-off energies at the disposal of the user, all of which require the assignment of a value. In principle, all the thresholds discussed above should be set as low as possible in order to have the simulation as accurate as possible. However, the price to pay for low thresholds is a dramatic increase in computer time for simulating the event. Compromises between what is important and what is negligible have to be found. To aid the user in this respect, newer versions of GEANT calculate sensible values for these parameters from the material description of the detector. The suggested values are valid for quick studies and can serve as a starting point for the user to go ahead with tuning. However, tuning of tracking parameters is almost always necessary. For the L_3 detector, extensive studies and tuning had to be made, and are still being made, in order to further improve the accuracy of the detector simulation.

E.2 Development of the Simulation 1989-1993

The Monte Carlo simulation program SIGEL3 was first confronted with real Z° decays recorded by the L_3 detector in August 1989. At that time, the simulation was based on GEANT 3.13. Severe deficiencies were found in the simulation of the hadronic shower development, most notably the transverse shower width and the energy depositions (50% too low) in the wire chambers of the hadron calorimeter. Several problems with the original GEANT 3.13 code were found. Therefore, it was decided to introduce a private GEANT version for the L_3 collaboration, containing all the necessary corrections and improvements to the original GEANT 3.13. The most

Visible energy

Missing energy

Thrust
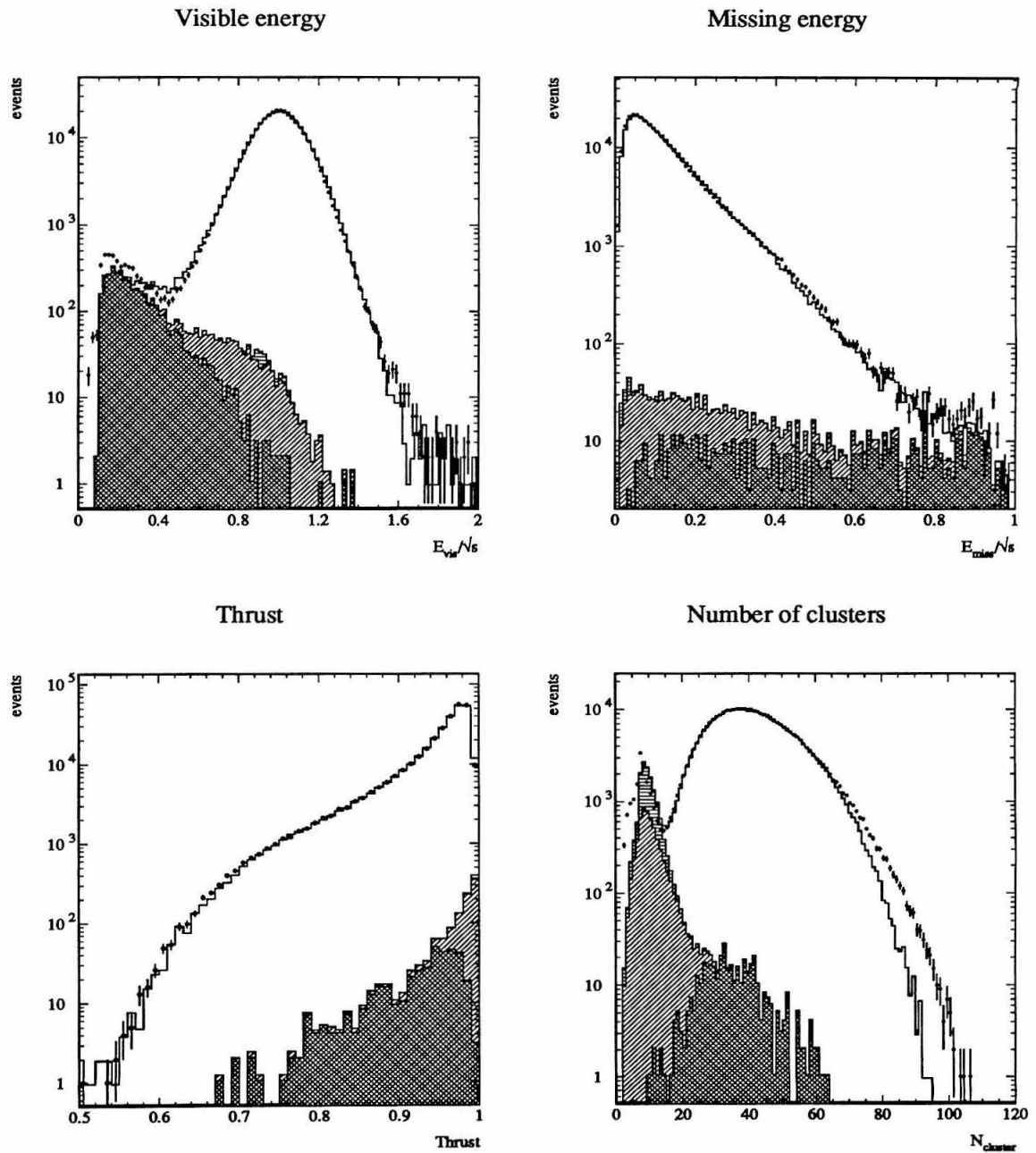
Number of clusters

Figure E.1: Distribution of visible energy E_{vis}, length E_{miss} of missing energy vector, thrust, and number $N_{cluster}$ of clusters in the calorimeter for hadronic events. Dots with error bars are data, solid histogram is total Monte Carlo, hatched part is background Monte Carlo: two-photons (cross hatched), Bhabhas (horizontal lines), and τ pairs (sloped lines).

important changes were:

- change from stepwise linear to logarithmic binning in the energy loss tables,

- technical corrections to erroneous tracking at boundaries between very small volumes (such as gas cells enclosed by brass sheets in the hadron calorimeter),

- corrections to the hadronic shower generation in the areas of photon-nuclei and neutron-nuclei interactions, photo-fission and photo-absorption, as well as in the process of slowing-down neutrons,

- careful tuning of tracking parameters, especially the energy cut-off parameters.

The 1990 Monte Carlo production[1] was based on this version called GEANT 3.31. Significant improvements in the precision of hadronic shower simulation were obtained by this tuning. The energy response of the hadron calorimeter increased to 90% of the measured values. However, some discrepancies in the hadronic shower width and the punch-through rate still remained. Further modifications in handling of volumes during tracking were subsequently incorporated to form GEANT 3.32. Version 3.33 contains additional corrections of minor bugs.

For CERN's successor version to GEANT 3.13, GEANT 3.14, most of the L_3 modifications have been in fact incorporated by the team of GEANT authors. These and other improvements implemented in GEANT 3.14, the basis for the L_3 Monte Carlo simulation in 1991, lead to a much better description of the data, especially in the simulation of electromagnetic showers within the BGO calorimeter [99]. A detailed comparison between simulated data using GEANT 3.14 and selected real data events for the reaction $e^+e^- \rightarrow \tau^+\tau^-(\gamma)$ was carried out [100]. The decays of τ's into hadrons are free from uncertainties in the fragmentation model, and are thus an ideal tool to study showers created by a few light hadrons with energies up to

---

[1]Large-scale production of simulated events to support all phases of the L_3 physics analysis, carried out on large numbers of workstations at CERN, and at computer centers accessed over networks in the US and Europe. This activity is coordinated by the Caltech group.

the beam energy. The study concentrated especially on punch-through and cluster-multiplicity studies. The results from this study led to the following modifications of GEANT 3.14:

- reduction of the cross section for particle-uranium interactions by 10% (except for neutrons),

- corrections to the energy-loss tables for muons in gaseous materials,

- continued tracking of decay products of stopped particles,

- further tuning of tracking parameters, especially the energy cutoff for neutrons (10 keV).

These modifications were incorporated into the L$_3$ private version, GEANT 3.41.

By the middle of the 1991 running period, a lot more data had been accumulated, and more detailed checks were possible. A major problem was still the simulation of L$_3$'s complicated hadron calorimeter. The ratio of energies deposited in the BGO and hadronic calorimeter were different in data and Monte Carlo. For this reason, a *major* modification was introduced in the tracking of charged particles through the hadron calorimeter gas: the treatment of the particles energy loss was changed from restricted Landau fluctuations plus explicit generation of δ-rays (mixed process) to pure, but unrestricted Landau fluctuations (continuous process). This immediately resulted in comparable energy depositions in data and Monte Carlo, so that thresholds applied in the reconstruction had the same effect on data and Monte Carlo events. Another problem showed up in the simulation of the hadron calorimeter itself: energy depositions of muons relative to jets were different in data and Monte Carlo. The response to muons has to be scaled down by a 35%. The resulting GEANT 3.42 version is the basis of the detector simulation for both 1991 and beginning of 1992.

In April 1992, CERN released a new version, GEANT 3.15. It is considered a consolidation version, basically a GEANT 3.14 including corrections to all known bugs. Comparisons between GEANT 3.42 and GEANT 3.15 made for the L$_3$ set-up do not show any significant differences [101]. However, the simulation of particle energy

loss in case of restricted Landau fluctuations plus explicit generation of secondaries has been modified. Using this option, the muon response still has to be scaled down by 29%, but the width of the minimum ionizing signal has much improved, and the quality of hadronic shower simulation in the hadron calorimeter is retained. Thus, **L3**'s private version GEANT 3.51 reverts to this kind of tracking of particles in the hadron calorimeter gas. Apart from the values of tracking parameters, which differ from the defaults, the only remaining modification with respect to GEANT 3.15 is currently the reduction of 10% in the cross section between particles (except neutrons) and uranium. Further Monte Carlo production in 1992 and beginning of 1993 is based on GEANT 3.51.

E.3   Current Status

A remaining problem in the Monte Carlo program is the discrepancy between data and Monte Carlo in the cluster-multiplicity distribution of $e^+e^- \rightarrow \tau^+\tau^-(\gamma)$ events (see Chapter 6). A comparison of different τ decay modes between the data and Monte Carlo shows that it is the simulation of charged pions interacting in the BGO which is at fault. This leads to fewer BGO clusters in the Monte Carlo on average, compared to data. Nevertheless, the current version of the detector simulation based on GEANT 3.14 shows a significant improvement in the multiplicity distributions compared to the 1990 detector simulation based on GEANT 3.13 [102].

In order to further reduce the systematic error , and to exploit fully the expected increase in statistics in the future, further studies of showers created by single charged pions within the BGO geometric setup have to be made. Continued studies of test-beam data, as well as Monte Carlo studies using the newly available hadronic shower generators FLUKA, HADRIN and NUCRIN within the latest GEANT 3.15 framework, are planned or under way.

A second problem is the accurate simulation of insensitive ("dead") material within the detector. Although the sensitive volumes are entered into the code with great care, the exact position and properties of some dead material, such as cable

Missing longitudinal energy

Missing transverse energy

Number of clusters (barrel events)

Number of clusters (endcap events)
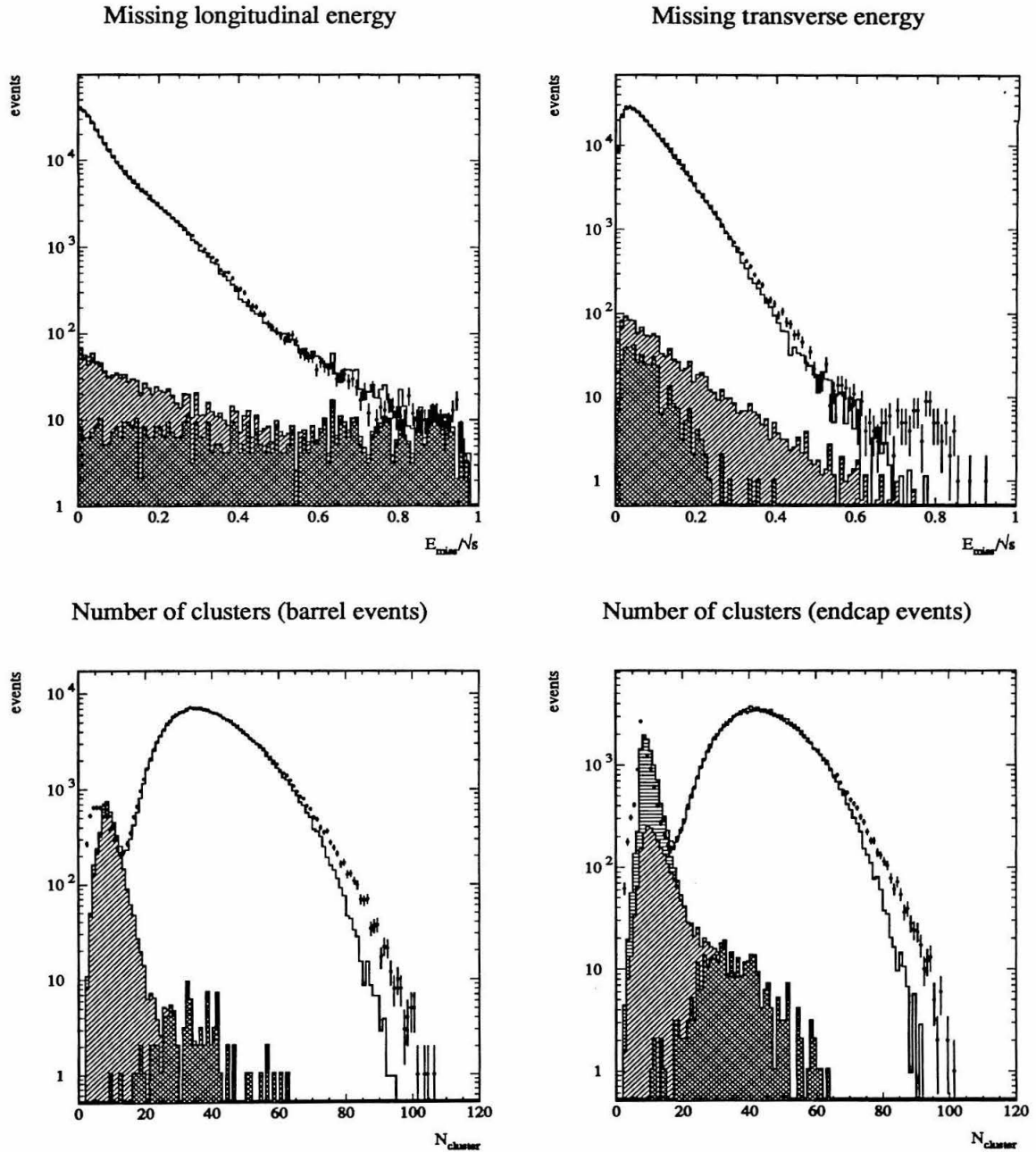
Figure E.2: Distribution of missing longitudinal and transverse energy (E_{miss}), and number of clusters $N_{cluster}$ for barrel and endcap events in the calorimeter, for hadronic events. Dots with error bars are data, solid histogram is total Monte Carlo, hatched part is background Monte Carlo: two-photons (cross hatched), Bhabhas (horizontal lines), and τ pairs (sloped lines).

bundles, pipes and support structures, is only approximately included in the *Monte Carlo* description of the detector. Two examples are given below:

1. The two endflanges of the TEC are covered with a different amount of material: on one side, there are the numerous read-out cables of the signal wires (signal side), on the other side, there is the distribution of the chamber high voltage (HV side). An azimuthally averaged medium between the TEC endflanges and the FTC as well as between the BGO barrel and endcap was included in the simulation program to account for this dead material. This drastically improved, for example, the agreement between the data and Monte Carlo for the $\cos\theta$ distributions of the event-axis for $\tau^+\tau^-(\gamma)$ events.

2. The wires of the precision muon chamber segments (P segments) are partially inefficient in small regions near the internal supporting bridges and the endflanges. This leads to a slightly incorrect prediction of efficiency in that region of the muon chamber.

Whereas the first problem is solved, the solution to the second must still be fully implemented in the simulation program. These considerations make it obvious that the effort of improving the simulation program must go on continuously, and in close contact with the physics analysis, when taking more and more data which reveals more and smaller discrepancies.

A third problem is the general validity, accuracy and limitation of the model used for simulating the detector response. As an example, the simulation of charged particles traversing the TEC is considered.

During tracking, the coordinate of the particles are known, so that using the geometry of the TEC, drift distances to the corresponding signal wire are easily calculated, and converted into drift times as measured by the L_3 detector. This conversion could be modeled at several levels of precision, e.g., one can simulate the complete drift process including diffusion, gas amplification at the anode wire, pulse shaping amplifiers, FADC digitization and calculation of the actual drift time using the center-of-gravity method. On the other hand, one can use a faster parameterization calculating the drift time directly from the known drift distance, appropriately

smeared to account for the above effects. It is then a question of the accuracy of this parameterization, whether the Monte Carlo prediction agrees with the data.

Another aspect arises from chamber calibration: in reality, the wires are not at their ideal position, electric fields are slightly inhomogeneous etc. The magnitude of these effects is not known, and thus a calibration of the drift-distance versus drift-time relation for each wire and half-sector is required. The TEC simulation, however, is ideal in this respect: perfectly aligned sectors and perfect fields. Since the calibration obtained from real data is not of infinite precision, problems in TEC performance, such as momentum resolution and probability for charge mismeasurement, are larger in the data than predicted by Monte Carlo.

Since the detailed effects and their magnitudes are not (exactly) known, they can in principal not be simulated in the Monte Carlo. In this respect, there will always be a discrepancy between data and Monte Carlo. A crude way out is an *a posteriori* additional smearing of hit positions or track parameters, where the amount of smearing is determined by the requirement of agreement between data and Monte Carlo after smearing.

One area of the L$_3$ simulation which requires further improvement is the trigger simulation. The trigger simulation currently consists of external programs which are not integrated into the L$_3$ simulation framework, and not all triggers are simulated. According to the trigger design and trigger thresholds, the trigger efficiency is virtually 100% for all Z$^\circ$ decay modes to charged fermions, which has been verified by analyses of trigger and event data for all those runs declared as good from the trigger point of view. However, special physics event signatures exist, e.g., the neutrino counting process $e^+e^- \rightarrow \nu\bar{\nu}\gamma$, where the efficiency is less than this ideal value. In such cases, additional information coming from a complete trigger simulation taking malfunctioning trigger channels into account would be very useful, in order to reduce systematic errors further.

Appendix F

Fitting using Analytical Programs

F.1 Analytical Programs

Many analytical programs for specialized applications in e^+e^- annihilation are available. In the following, only the two most widely used programs for **LEP I** physics will be presented. These analytical programs are used to fit for parameters of the assumed model, typically the (minimal) **SM**. The input to the fit consists of cross sections and asymmetries measured at a series of $\sqrt{s}$ values, corrected for detector effects using Monte Carlo simulations. One of the program packages written by members of the **L₃** collaboration to actually perform these fits, taking into account correlations in the input data and their errors, also is presented below.

ALIBABA

The name **ALIBABA** stands for "A (semi) analytical leading log improved Bhabha scattering calculation." The program **ALIBABA** [103] calculates cross sections and forward-backward charge asymmetries for Bhabha scattering $(e^+e^- \rightarrow e^+e^-(\gamma))$. It is possible to impose cuts on the minimum and maximum scattering angle, and also on the minimum energies of both the electron and the positron in the final state. A cut on the acollinearity of the final-state leptons can be imposed as well. The program is intended for large-angle scattering, i.e., the minimal scattering angle should

be larger than approximately $10°$. A complete first-order electroweak treatment is implemented, plus the following important QED corrections:

- first- and second-order initial-state leading-log corrections plus exponentiation,

- second-order final-state leading-log corrections,

- first-order non-log corrections.

Since ALIBABA is rather time-consuming in computation, it cannot be used directly in a fit to the $e^+e^- \to e^+e^-(\gamma)$ data. There are two possibilities to circumvent this drawback. One either subtracts the t-channel and the s+t-interference parts, and then treats Bhabha scattering as a standard s-channel scattering in the fit, or one uses a fast parameterization of ALIBABA, called MIBA [104].

ZFITTER

The analytical program ZFITTER 4.5 [45] performs calculations for fermion-pair production in e^+e^- annihilation. The following options for cuts in phase space are possible (corresponding to "chains" in the ZFITTER language):

- no cuts at all,

- cut on the minimum invariant mass of the $f\bar{f}$ pair, and optionally a cut on the maximum production angle of the outgoing anti-fermion,

- cut on energies and acollinearity of final-state fermions, and optionally a cut on the maximum production angle of the outgoing anti-fermion.

The following models are implemented in ZFITTER (called "branches"):

- analytic MSM formulae with higher-order corrections,

- model independent ansatz using effective axial-vector and vector couplings of fermions to the $Z°$ boson,

- model independent ansatz using partial decay widths of the Z° boson to fermion species f,

- S-matrix ansatz using S-matrix theory for a global description of the hard scattering process.

ZFITTER calculates the following observables (via callable "interfaces"):

- MSM cross sections (σ) and forward-backward asymmetries (A_{fb}) as functions of m_Z, m_t, m_H and α_s,

- MSM τ-polarization (A_{pol}) and forward-backward τ-polarization (A_{pol}^{fb}) as functions of m_Z, m_t, m_H and α_s,

- model-independent cross sections and asymmetries as functions of the normalization form factors (ρ) and the effective vector and axial-vector coupling constants (g_V^f, g_A^f), respectively,

- model-independent final-state polarization in τ-pair production as a function of the normalization form factors and effective vector and axial-vector couplings,

- model-independent cross sections as functions of the partial (Γ_f) and total (Γ_Z) Z width,

- model-independent cross sections, based on an S-matrix-inspired ansatz, as functions of m_Z, Γ_Z, etc.

ZFITTER is thus a very flexible program offering many possibilities to fit to the data and to interpret the results. Constant development by the group of authors ensures that the program incorporates the latest developments in analytical calculations. ZFITTER 4.5 contains a complete $\mathcal{O}(\alpha)$ electroweak treatment using the DIZET 4 [44] weak library, including:

- soft photon exponentiation,

- higher-order QED corrections for initial-state radiation,

- complete m_t-dependent $\mathcal{O}(\alpha)$ terms,

- leading $\mathcal{O}(\alpha^2 m_t^4)$ terms,

- complete $\mathcal{O}(\alpha\alpha_s)$ terms plus leading parts in $\mathcal{O}(\alpha\alpha_s m_t^2)$.

ZFITTER is the standard analytical program used by three LEP collaborations, including L3, to make fits of parameters of interest to the data.

There exists the supplement ZEFIT 2.0 [105] for ZFITTER, which incorporates the effects of an additional neutral heavy gauge boson (Z') predicted in extensions of the SM. Thus, experimental data may also be analyzed in that respect.

FUNPLO

The analytical programs described above calculate observables measured at LEP as functions of interesting parameters of the underlying model. A fit has to be performed in order to determine the best values of these parameters, i.e., those, which best reproduce the measured data. For this purpose, fit programs like FUNPLO [106] have been written, which calculate the appropriate χ^2 or likelihood function for the dataset used and minimize it by calling the CERN program MINUIT [107] in order to extract the best parameter values. A detailed description of the function to be minimized is given below. FUNPLO takes into account common and correlated systematic errors, effects of the beam-energy calibration of LEP (see Appendix C) and effects of the beam-energy spread.

F.2   Fitting Function

The program package FUNPLO (see above) is used to perform various fits to the data in order to obtain the parameters of the assumed model, usually the MSM. The fit is performed by minimizing a χ^2 quantity. The χ^2 quantity contains measurements obtained from data in channels f at center-of-mass energy points i of year n, usually measured values for cross sections, $\sigma(f, i, n)$, and asymmetries (forward-backward and polarization), $A(f, i, n)$. In the case of quarks, the hadronic cross section is

summed over all quark flavors. The data considered are that of the years 1990 and 1991, with seven energy points i in each year.

The fit variables form a vector $\vec{x}$ with components x_j, which contain two sets: First, there are the variables which have a physical meaning within the theoretical model, e.g., the mass and width of the Z° in the MSM. Second, there are the variables which are of a more technical nature. They are also called correction terms, because they implement common correlated errors between several measurements used in the fit. Variables of both sets can be constrained to a mean $\overline{x}$ within a range $\delta\overline{x}$.

Furthermore, "external" measurements, giving additional constraints $y_k \pm \delta y_k$, e.g., measurements of the ratio of W and Z° mass from collider experiments, can be taken into account in the fit.

The χ^2 function now has the following form:

$$
\begin{aligned}
\chi^2 = \quad & \sum_{f,i,n} \alpha(f,i,n) \left[\frac{\sigma'(f,i,n) - \sigma_{\text{th}}(f,i,n,\vec{x})}{\delta\overline{\sigma}(f,i,n,\vec{x})} \right]^2 \\
+ \ & \sum_{f,i,n} \beta(f,i,n) \left[\frac{A'(f,i,n) - A_{\text{th}}(f,i,n,\vec{x})}{\delta\overline{A}(f,i,n,\vec{x})} \right]^2 \\
+ \ & \sum_j a_j \left[\frac{x_j - \overline{x}_j}{\delta\overline{x}_j} \right]^2 + \sum_k b_k \left[\frac{y_k - y_{\text{th}}(\vec{x})}{\delta y_k(\vec{x})} \right]^2 \quad ,
\end{aligned}
\tag{F.1}
$$

where the subscript "th" denotes the theoretical prediction.

The factors α, β, a and b are set either to 0 or 1 to determine whether the term they multiply is included in the χ^2 function or not. The factors α and β decide whether the fit will make use of the corresponding measurement or not. This is helpful in the case only a subset of the measurements is to be taken into account, or in case some measurements are not available (yet). If a factor a is 1, it implements a constraint on the corresponding fit parameter, e.g., constraining some model parameter or constraining the correlated error terms within their quoted variance to their mean. If a factor b is 1, the corresponding "external" constraint on the corresponding y variable is taken into account.

The cross sections $\sigma'(f,i,n)$ and asymmetries $A'(f,i,n)$ entering the χ^2 contain

the above mentioned correction terms x, taking the correlated part of the *total* measurement errors, i.e., common systematic errors, into account:

$$\sigma'(f,i,n) = x_{Lum}(n) \cdot x_{sys}^{\sigma}(f,n) \cdot \sigma(f,i,n) \tag{F.2}$$

$$A'(f,i,n) = A'(f,i,n) + x_{sys}^{A}(f,n) \quad . \tag{F.3}$$

The correction terms x are treated as Gaussian distributed random variables with mean $\overline{x}$ either 0 or 1 for additive or multiplicative corrections, respectively, and a sigma $\delta\overline{x}$ corresponding to the value of the correlated error they describe. Usually, for a given channel f, the correction terms expressing systematic errors are identical for all $\sqrt{s}$ points i of a given year n.

The correction terms x_{sys} refer to the systematic errors of event selection. In the case of fitting a cross section, an additional common systematic error arises from the luminosity measurement, corresponding to x_{Lum}. This error consists of two parts, one due to the common theoretical error in the Bhabha cross section determination, and another from the systematic error in luminosity event selection.

The theoretical predictions $\sigma_{th}(f,i,n,\vec{x})$ and $A_{th}(f,i,n,\vec{x})$, calculated by the analytical program ZFITTER, depend of course only indirectly on i,n via the corresponding center-of-mass energy $\sqrt{s}(i,n)$. The values of $\sqrt{s}(i,n)$ are given by the **LEP** beam energy calibration discussed in Appendix C. They in turn depend on the nine random variables X (see section C.2) describing the fluctuations around the luminosity weighted mean energy of the fills belonging to energy point i. These nine variables are therefore included in the vector $\vec{x}$. The finite spread of the **LEP** beam energy of about 51 MeV (Appendix C) is included by convoluting the theoretical cross section as a function of $\sqrt{s}$ with a normalized Gaussian of 51 MeV width around the mean center-of-mass energy.

The errors $\delta\overline{\sigma}$ and $\delta\overline{A}$ contain the uncorrelated parts of the total error of each measurement. The experimental errors are corrected by a factor to obtain the error

as expected by the theoretical prediction for the measurement:

$$\delta\overline{\sigma}(f,i,n) = \delta\sigma(f,i,n)\cdot\sqrt{\frac{\sigma_{\text{th}}(f,i,n,\vec{x})}{\sigma(f,i,n)}} \tag{F.4}$$

$$\delta\overline{A}(f,i,n) = \delta A(f,i,n)\cdot\sqrt{\frac{1-A_{\text{th}}^2(f,i,n,\vec{x})}{1-A^2(f,i,n)}}\cdot\sqrt{\frac{\sigma(f,i,n)}{\sigma_{\text{th}}(f,i,n,\vec{x})}} \quad . \tag{F.5}$$

Treatment of Bhabha Scattering

The reaction $e^+e^- \to e^+e^-(\gamma)$ is distinguished from the other channels by the property that it proceeds via γ/Z° t-channel scattering, in addition to the γ/Z° s-channel "annihilation". This has two consequences:

1. The Bhabha cross section diverges for scattering angles approaching zero. The measured cross section therefore can not be extrapolated to the full solid angle, as is usually done for s-channel processes. Using a Monte Carlo, one can only correct for detector and selection effects (efficiency, background) within a certain fiducial volume, i.e., within a certain range of scattering angle θ. Bhabha cross sections are always quoted with respect to a restricted fiducial volume.

2. The calculation necessary to obtain the same precision as in pure s-channel scattering is much more involved. This has consequences of a technical nature: precision analytical programs for Bhabha scattering take much more computer time to arrive at an answer than analytical programs for pure s-channel scattering with the same precision. The effect is sometimes so drastic that programs like ALIBABA are not directly suitable for fitting purposes.

Thus, a special treatment of the electron data is needed in a fit. Possible procedures include:

- subtraction of the effects of t-channel and (s+t)-interference from the measured value using ALIBABA,

- scaling of the measured data by the ratio of the theoretical prediction of s-channel and total given by ALIBABA,

- direct fitting of the measured data using ALIBABA to give t-channel and (s+t)-interference effects.

Since only the s-channel part is actually fitted and the ALIBABA contributions are fixed during a fit, the fitting procedure has to be iterated using new ALIBABA predictions resulting from fitted parameters. Of course, all three methods should give equivalent results, if the errors and correlations have been treated correctly.

Standard Fits

Usually, the following three types of fits are performed to extract as much information as possible from the data:

1. a model independent fit to the cross section data alone, to determine the mass m_Z as well as the total width Γ_Z and the various partial widths Γ_f of the Z° boson;

2. a model independent fit to the combined cross section and asymmetry data, to determine the effective coupling constants of the neutral weak current, g_A^f and g_V^f;

3. a MSM fit to the combined data set to determine the as yet unknown parameters of the MSM: m_t and m_H, along with α_s and m_Z.

These fits may or may not impose lepton universality (see below) or use "external" constraints.

Lepton Universality

The experimental data used in these fits contain measurements for each of the charged lepton species separate. Thus, a test of lepton universality is possible. After having verified lepton universality, one can assume lepton universality in the fit in order to arrive at an improved determination of electroweak parameters.

Appendix G

Summary of Electroweak Measurements from L_3

The following sections summarize the cross section and asymmetry measurements from L_3 used as input to the analysis described in Chapter 8. The data of 1990 has been reanalyzed; for example the luminosity has been reevaluated. Thus, the values quoted in the tables for 1990 and their errors differ slightly from those published earlier [50].

The accuracy of the **LEP** beam energy calibration of 1991 is different for data taken before and after August 14, 1991 (see Appendix C). Since the energy scan had just started at that date, essentially only the data on the peak is affected. For this reason, the tables for the 1991 data quote two cross section and asymmetry values for this center-of-mass energy point. The data have been corrected for the effect of the spread in beam energy (see Appendix C).

G.1   Cross Sections

Quoted cross sections are total cross sections extrapolated to the full solid angle of 4π. The one exception is Bhabha scattering, for which the cross section is quoted within a restricted fiducial volume.

Hadrons

1990 Data			
$\sqrt{s}$ [GeV]	N_{events}	$\mathcal{L}$ [nb^{-1}]	σ_{tot} [nb]
88.231	1776	393.3	4.53±0.11
89.236	3841	453.7	8.50±0.14
90.238	6725	364.0	18.60±0.25
91.230	83835	2784.8	30.38±0.12
92.226	8637	399.5	21.78±0.26
93.228	6368	518.3	12.36±0.16
94.223	3915	480.0	8.20±0.14
Totals	115097	5393.6	

1991 Data			
$\sqrt{s}$ [GeV]	N_{events}	$\mathcal{L}$ [nb^{-1}]	σ_{tot} [nb]
91.254	155091	5130.8	30.43±0.10
88.480	4050	782.9	5.17±0.09
89.470	8528	847.9	10.08±0.12
90.228	14333	794.3	18.12±0.18
91.222	90618	3014.8	30.26±0.13
91.967	16059	658.5	24.51±0.24
92.966	10864	759.2	14.36±0.16
93.716	7945	794.6	10.02±0.13
Totals	307488	12783.0	

Table G.1: Total cross section $\sigma(e^+e^- \rightarrow$ hadrons) measured with L_3 in 1990 and 1991. Quoted errors are statistical only. The systematic error is estimated to be 0.3% for the 1990 data and and 0.2% for the 1991 data (excluding the 0.6% luminosity uncertainty).

Electrons

1990 Data				
$\sqrt{s}$ [GeV]	N_{events}	$\mathcal{L}$ [nb^{-1}]	σ_{tot} [nb]	σ_{tot}^{s} [nb]
88.231	120	380.1	0.334±0.030	0.188±0.053
89.236	237	466.3	0.532±0.034	0.473±0.057
90.238	310	359.3	0.894±0.050	1.034±0.082
91.230	3020	2960.9	1.052±0.019	1.462±0.031
92.226	276	397.4	0.715±0.043	1.135±0.071
93.228	198	505.5	0.405±0.029	0.660±0.048
94.223	104	485.7	0.223±0.022	0.348±0.037
Totals	4265	5555.2		

1991 Data				
$\sqrt{s}$ [GeV]	N_{events}	$\mathcal{L}$ [nb^{-1}]	σ_{tot} [nb]	σ_{tot}^{s} [nb]
91.254	5422	5244.3	1.031±0.014	1.437±0.023
88.480	316	783.5	0.400±0.023	0.291±0.040
89.470	498	862.3	0.573±0.026	0.528±0.044
90.228	632	795.0	0.792±0.032	0.866±0.053
91.222	3295	3080.8	1.067±0.019	1.484±0.030
91.967	591	731.7	0.798±0.033	1.239±0.054
92.966	336	759.9	0.430±0.024	0.701±0.040
93.716	261	832.1	0.302±0.019	0.486±0.032
Totals	11351	13089.6		

Table G.2: Total cross section $\sigma(e^+e^- \rightarrow e^+e^-(\gamma))$ measured with **L3** in 1990 and 1991. Quoted errors are statistical only. The acceptance corrected cross section σ_{tot} is for $44° < \theta < 136°$ and $\zeta_{\text{acol}} < 25°$. The s-channel corrected cross section σ_{tot}^{s} is extrapolated to the full solid angle. The systematic error is estimated to be 0.4% for σ_{tot} and 0.5% for the s-channel cross section σ_s (excluding the 0.6% luminosity uncertainty).

Muons

1990 Data			
$\sqrt{s}$ [GeV]	N_{events}	$\mathcal{L}$ [nb^{-1}]	σ_{tot} [nb]
88.231	66	388.6	0.268±0.033
89.236	104	421.0	0.387±0.038
90.238	217	364.9	0.929±0.063
91.230	2675	2822.4	1.476±0.028
92.226	282	394.8	1.115±0.066
93.228	160	496.6	0.505±0.040
94.223	123	480.4	0.404±0.036
Totals	3627	5368.7	

1991 Data			
$\sqrt{s}$ [GeV]	N_{events}	$\mathcal{L}$ [nb^{-1}]	σ_{tot} [nb]
91.254	5425	5041.9	1.497±0.020
88.480	130	780.4	0.235±0.021
89.470	290	851.1	0.478±0.028
90.228	492	794.3	0.866±0.039
91.222	2912	2933.8	1.381±0.026
91.967	585	700.9	1.165±0.048
92.966	372	759.2	0.686±0.036
93.716	282	830.9	0.478±0.028
Totals	10488	12692.4	

Table G.3: Total cross section $\sigma(e^+e^- \to \mu^+\mu^-(\gamma))$ measured with $\mathbf{L_3}$ in 1990 and 1991. Quoted errors are statistical only. The systematic error is estimated to be 0.8% for the 1990 data and 0.5% for the 1991 data (excluding the 0.6% luminosity uncertainty).

Taus

1990 Data			
$\sqrt{s}$ [GeV]	N_{events}	$\mathcal{L}$ [nb^{-1}]	σ_{tot} [nb]
88.231	36	337.8	0.228±0.037
89.236	83	404.7	0.439±0.047
90.238	138	319.9	0.920±0.077
91.230	1868	2721.3	1.463±0.033
92.226	188	366.3	1.095±0.078
93.228	132	472.2	0.599±0.051
94.223	95	477.4	0.427±0.043
Totals	2540	5099.6	

1991 Data			
$\sqrt{s}$ [GeV]	N_{events}	$\mathcal{L}$ [nb^{-1}]	σ_{tot} [nb]
91.254	3720	4909.1	1.505±0.025
88.480	95	780.4	0.236±0.024
89.470	229	851.1	0.531±0.035
90.228	359	794.3	0.885±0.047
91.222	2102	2886.1	1.447±0.032
91.967	425	690.2	1.224±0.059
92.966	248	759.2	0.641±0.041
93.716	225	830.9	0.535±0.036
Totals	7403	12501.3	

Table G.4: Total cross section $\sigma(e^+e^- \rightarrow \tau^+\tau^-(\gamma))$ measured with $\mathbf{L_3}$ in 1990 and 1991. Quoted errors are statistical only. The systematic error is estimated to be 1.5% for the 1990 data and 0.7% for 1991 the 1991 data (excluding the 0.6% luminosity uncertainty).

G.2   Asymmetries

Polarization of the Charged τ Lepton

The τ polarization on the peak of the Z° resonance has been measured to be [61]:

$$\mathcal{P}_\tau \; = \; -0.132 \pm 0.026 \pm 0.021 \quad , \tag{G.1}$$

where the first error is statistical and the second systematic.

Forward-Backward Charge Asymmetry of Heavy Flavors

The forward-backward charge asymmetry on the peak of the Z° resonance for c and b quarks has been measured to be [67]:

$$A_{fb}^c \; = \; +0.083 \pm 0.038 \pm 0.027 \tag{G.2}$$

$$A_{fb}^b \; = \; +0.086 \pm 0.015 \pm 0.007 \quad , \tag{G.3}$$

where the first errors are statistical and the second systematic. The b quark asymmetry is corrected for $B^0 \leftrightarrow \bar{B}^0$ mixing [108].

Electrons

1990 Data			1991 Data		
$\sqrt{s}$ [GeV]	A_{fb}	A_{fb}^{s}	$\sqrt{s}$ [GeV]	A_{fb}	A_{fb}^{s}
			91.254	0.118±0.014	0.001±0.020
88.231	0.520±0.095	-0.034±0.276	88.480	0.504±0.055	-0.013±0.157
89.236	0.296±0.070	-0.205±0.161	89.470	0.312±0.048	-0.126±0.099
90.238	0.155±0.064	-0.111±0.107	90.228	0.206±0.045	-0.100±0.075
91.230	0.101±0.021	-0.023±0.028	91.222	0.129±0.019	0.019±0.027
92.226	0.040±0.069	0.042±0.085	91.967	0.161±0.047	0.103±0.055
93.228	0.083±0.081	0.053±0.094	92.966	0.107±0.064	0.098±0.072
94.223	0.144±0.118	0.129±0.148	93.716	0.185±0.070	0.165±0.085

Table G.5: Forward-backward charge asymmetry $A_{fb}(e^+e^- \rightarrow e^+e^-(\gamma))$ measured with **L3** in 1990 and 1991. Quoted errors are statistical only. The asymmetry A_{fb} is determined by counting events in the angular range of $44° < \theta < 136°$ and for $\zeta_{acol} < 25°$. The asymmetry A_{fb}^{s} is the s-channel contribution to the asymmetry extrapolated to the full solid angle. The systematic error is estimated to be 0.004 for the measured asymmetry, and 0.005 for the extrapolated s-channel asymmetry.

Muons

1990 Data		1991 Data	
$\sqrt{s}$ [GeV]	A_{fb}	$\sqrt{s}$ [GeV]	A_{fb}
		91.254	0.018±0.015
88.231	-0.391±0.117	88.480	-0.148±0.102
89.236	-0.044±0.109	89.470	-0.202±0.067
90.238	-0.184±0.074	90.228	-0.041±0.052
91.230	0.006±0.021	91.222	0.013±0.021
92.226	0.110±0.066	91.967	0.060±0.045
93.229	0.095±0.091	92.966	0.122±0.058
94.223	0.134±0.099	93.716	0.084±0.067

Table G.6: Forward-backward charge asymmetry $A_{fb}(e^+e^- \rightarrow \mu^+\mu^-(\gamma))$ measured with L_3 in 1990 and 1991 ($\zeta_{acol} < 15°$). Quoted errors are statistical only. The systematic error is estimated to be 0.005.

Taus

1990 Data		1991 Data	
$\sqrt{s}$ [GeV]	A_{fb}	$\sqrt{s}$ [GeV]	A_{fb}
		91.254	0.037 ± 0.021
88.231	-0.42 ± 0.20	88.480	-0.106 ± 0.129
89.236	-0.09 ± 0.15	89.470	-0.152 ± 0.083
90.238	-0.18 ± 0.11	90.228	-0.137 ± 0.070
91.230	0.07 ± 0.03	91.222	-0.032 ± 0.029
92.226	-0.04 ± 0.10	91.967	0.042 ± 0.063
93.228	0.11 ± 0.12	92.966	0.161 ± 0.079
94.223	0.02 ± 0.13	93.716	0.058 ± 0.082

Table G.7: Forward-backward charge asymmetry $A_{fb}(e^+e^- \rightarrow \tau^+\tau^-(\gamma))$ measured with $\mathbf{L_3}$ in 1990 and 1991 ($\zeta_{acol} < 0.25$ rad). Quoted errors are statistical only. The systematic error is estimated to be less than 0.01 for the 1990 data and 0.006 for the 1991 data.

Bibliography

[1] S. Glashow, *Partial-Symmetries of Weak Interactions*, Nucl. Phys. **22** (1961) 579;

S. Weinberg, *A Model of Leptons*, Phys. Rev. Lett. **19** (1967) 1264;

A. Salam, *Weak and Electromagnetic Interactions*, in: Elementary Particle Theory, ed.: N. Svartholm, Almqvist and Wiksell, Stockholm (1968) 367.

[2] C. Yang and R. Mills, *Conservation of Isostopic Spin and Isotopic Gauge Invariance*, Phys. Rev. **96** (1954) 191.

[3] The Gargamelle Collaboration, F. Hasert *et al.*, *Search for Elastic Muon-Neutrino Electron Scattering*, Phys. Lett. B **46** (1973) 121.

[4] *Standard Model Lagrangian*, see any good textbook on particle physics.

[5] P. Higgs, *Broken Symmetries, Massless Particles and Gauge Fields*, Phys. Lett. **12** (1964) 132; *Broken Symmetries and the Masses of Gauge Bosons*, Phys. Rev. Lett. **13** (1964) 508; *Spontaneous Symmetry Breakdown without Massless Bosons*, Phys. Rev. **145** (1966) 1156.

[6] M. Gell-Mann, *The Eightfold Way*, CALTECH CTSL-20 (1961).

[7] E. Fermi, *Versuch einer Theorie der β-Strahlen*, Z. Phys. **88** (1934) 161.

[8] M. Gell-Mann and R. Feynman, *Theory of the Fermi Interaction*, Phys. Rev. **109** (1958) 193.

[9] J. Sakurai, *Invariance Principles and Elementary Particles*, Princeton University Press (1964).

[10] L. Rolandi, *Precision Tests of the Electroweak Interaction*, talk given at the XXVI ICHEP 1992, Dallas, USA, CERN-PPE/92-175.

[11] Particle Data Group, K. Hikasa *et al.*, *Review of Particle Properties*, Phys. Rev. D **45** (11, pt. 2) (1992) 1.

[12] E. Gross and P. Yepes, *SM Higgs Boson Hunting at LEP*, CERN-PPE/92-153.

[13] A "top candidate" event has been presented by the CDF collaboration at the November 1992 APS/DPF meeting in Chicago, USA.

[14] *Z Physics at LEP 1, Vol.1: Standard Physics, and Vol.2: Higgs Search and New Physics*, ed.: G. Altarelli, R. Kleiss and C. Verzegnassi, CERN yellow report 89-08.

[15] The L3 Collaboration, *L3 Technical Proposal*, CERN-LEPC (1983).

[16] The L3 Collaboration, B. Adeva *et al.*, *The Construction of the L3 Experiment*, Nucl. Instr. Meth. A **289** (1990) 35.

[17] The MARK II Collaboration, *The MARK II Detector for the SLC*, Nucl. Instr. Meth. A **281** (1989) 55.

[18] The SLD Collaboration, *SLD Design Report*, SLAC 273 (1984).

[19] The ALEPH Collaboration, *ALEPH: A Detector for Electron-Positron Annihilations at LEP*, Nucl. Instr. Meth. A **294** (1990) 121.

[20] The DELPHI Collaboration, *The DELPHI Detector at LEP*, Nucl. Instr. Meth. A **303** (1991) 233.

[21] The OPAL Collaboration, *The OPAL Detector at LEP*, Nucl. Instr. Meth. A **305** (1991) 275.

[22] *SLAC Linear Collider Conceptual Design Report*, SLAC-PUB-229 (1980).

[23] C. Camilleri *et al.*, *Physics with Very High Energy* e^+e^- *Colliding Beams*, CERN 76-18 (1976).

[24] Martin W. Grünewald, *Test einer Nachweisstruktur für eine hochauflösende Vertexkammer: Bestimmung der Ortsauflösung entlang des Signaldrahtes*, RWTH Aachen, PITHA 87-39.

[25] H. Akbari *et al.*, *Calibration of the L3 BGO Electromagnetic Calorimeter with a Radiofrequency Quadrupole Accelerator*, Nucl. Instr. Meth. A **274** (1989) 112.

[26] H. Ma, H. Newman, R. Zhu and R. Hamm, *Calibration of Electromagnetic Calorimeters in High-Energy Experiments with a Radiofrequency Quadrupole Accelerator*, Nucl. Instr. Meth. A **281** (1989) 469.

[27] Martin W. Grünewald, *Event Generators and L3 Software*, L3 Note 1264.

[28] *Z Physics at LEP 1, Vol.3: Event Generators and Software*, ed.: G. Altarelli, R. Kleiss and C.Verzegnassi, CERN yellow report 89-08.

[29] T. Sjöstrand, *The Lund Monte Carlo for Jet Fragmentation and* e^+e^- *Physics – Jetset Version 6.2*, Comp. Phys. Comm. **39** (1986) 347;

T. Sjöstrand and M. Bengtsson, *The Lund Monte Carlo for Jet Fragmentation and* e^+e^- *Physics – Jetset Version 6.3 – an Update*, Comp. Phys. Comm. **43** (1987) 367;

T. Sjöstrand, *PYTHIA 5.6 and JETSET 7.3: Physics and Manual*, CERN-TH.6488/92 (revised).

[30] G. Marchesini, B. Webber, G. Abbiendi, I. Knowles, M. Seymour and L. Stanco, *HERWIG 5.1 – a Monte Carlo Event Generator for Simulating Hadron Emission Reactions with Interfering Gluons*, Comp. Phys. Comm. **67** (1992) 465.

[31] B. Anderson, G. Gustafson and C. Peterson, *A Semiclassical Model for Quark Jet Fragmentation*, Z. Phys. C **1** (1979) 105.

[32] A. Ali, B. van Eijk and E. Pietarinen, unpublished;

B. van Eijk, PhD thesis, University of Amsterdam, 1987, unpublished;

A. Ali, B. van Eijk and I. ten Have, *Heavy Flavor Production in Large Transverse Momentum Proton-Antiproton Collisions*, Nucl. Phys. B **292** (1987) 1;

B. van Eijk, *EURODEC User Manual*, DELPHI Report 89-39; *EURODEC Reference Manual*, in preparation.

[33] A. Bassetto, M. Ciafaloni and G. Marchesini, *Jet Structure and Infrared Sensitive Quantities in Perturbative QCD*, Phys. Rep. 100 (1983) 201.

[34] G. Fox and S. Wolfram, *A Model for Parton Showers in QCD*, Nucl. Phys. B **168** (1980) 285.

[35] D. Amati and G. Veneziano, *Preconfinement as a Property of Perturbative QCD*, Phys. Lett. B **83** (1979) 87.

[36] F. Berends, P. Daverveldt and R. Kleiss, *Complete Lowest-Order Calculations for Four-Lepton Final States in Electron-Positron Collisions*, Nucl. Phys. B **253** (1985) 441.

[37] J. Hilgart, R. Kleiss and F. LeDiberder, *An Electroweak Monte Carlo for Four Fermion Production*, CERN-PPE/92-115.

[38] S. Jadach, E. Richter-Was, B. Ward and Z. Was, *Monte Carlo Program BH-LUMI 2.01 for Bhabha Scattering at Low Angles with Yennie-Frautschi-Suura Exponentiation*, Comp. Phys. Comm. **70** (1992) 305.

[39] D. Yennie, S. Frautschi and H. Suura, *The Infrared Divergence Phenomena and High-Energy Processes*, Annals of Physics **13** (1961) 379.

[40] M. Böhm, A. Denner and W. Hollik, *Radiative Corrections to Bhabha Scattering at High Energies (I). Virtual and Soft Photon Corrections*, Nucl. Phys. B **304** (1988) 687;
F. Berends, R. Kleiss and W. Hollik, *Radiative Corrections to Bhabha Scattering at High Energies (II). Hard Photon Corrections and Monte Carlo Treatment*, Nucl. Phys. B **304** (1988) 712.

[41] J. Field and T. Riemann, in preparation.

[42] S. Jadach, B. Ward and Z. Wąs, *The Monte Carlo Program KORALZ, Version 3.8, for the Lepton or Quark Pair Production at LEP/SLC Energies*, Comp. Phys. Comm. **66** (1991) 276.

[43] S. Jadach and B. Ward, *YFS2 - The Second-Order Monte Carlo Program for Fermion Pair Production at LEP/SLC, with the Initial State Radiation of Two Hard and Multiple Soft Photons*, Comp. Phys. Comm. **56** (1990) 351.

[44] The weak library DIZET 4 is to some extent described in reference [45].

[45] D. Bardin *et al.*, *ZFITTER: An Analytical Program for Fermion Pair Production in e^+e^- Annihilation*, CERN-TH.6443/92.

[46] S. Jadach, J. Kühn and Z. Wąs, *TAUOLA - a Library of Monte Carlo Programs to Simulate Decays of Polarized τ Leptons*, Comp. Phys. Comm. **64** (1991) 275.

[47] R. Brun *et al.*, *GEANT 3 Users Guide*, CERN DD/EE/84-1.

[48] H. Fesefeldt, *The Simulation of Hadronic Showers: Physics and Applications*, RWTH Aachen PITHA 85-02.

[49] E. Fahri, *Quantum Chromodynamics Test for Jets*, Phys. Rev. Lett. **39** (1977) 1587.

[50] The L3 Collaboration, B. Adeva *et al.*, *Measurement of Electroweak Parameters from Hadronic and Leptonic Decays of the Z^0*, Z. Phys. C **51** (1991) 179.

[51] The L3 Collaboration, *Luminosity Measurement with L3*, to be submitted to Z. Phys. C (1993).

[52] The L3 Collaboration, *Results from the L3 Experiment at LEP*, CERN-PPE/93-31, submitted to Physics Reports.

[53] The ALEPH Collaboration, D. Decamp *et al.*, *Improved Measurements of Electroweak Parameters from Z Decays into Fermions*, Z. Phys. C **53** (1992) 1.

[54] The ALEPH Collaboration, D. Decamp *et al.*, *Update of Electroweak Parameters from Z decays*, to be published in Phys. Lett. B (1993).

[55] The DELPHI Collaboration, P. Abreu *et al.*, *Determination of Z^0 Resonance Parameters and Couplings from its Hadronic and Leptonic Decays*, Nucl. Phys. B **367** (1991) 511.

[56] The DELPHI Collaboration, P. Abreu *et al.*, *Measurements of the Lineshape of the Z and Determination of Electroweak Parameters from its Hadronic and Leptonic Decays*, to be published in Phys. Lett. B (1993).

[57] The OPAL Collaboration, G. Alexander *et al.*, *Measurement of the Z^0 Lineshape Parameters and the Electroweak Couplings of Charged Leptons*, Z. Phys. C **52** (1991) 175.

[58] The OPAL Collaboration, P. Acton *et al.*, *Precision Measurements of the Neutral Current from Hadron and Lepton Production at LEP*, CERN-PPE/93-03.

[59] M. Pohl, private communication.

[60] The L3 Collaboration, B. Adeva *et al.*, *Decay Properties of Tau Leptons Measured at the Z^0 Resonance*, Phys. Lett. B **265** (1991) 451.

[61] The L3 Collaboration, O. Adriani *et al.*, *A Measurement of τ Polarization in Z^0 Decays*, Phys. Lett. B **294** (1992) 466.

[62] T. Hebbeker, *QCD Correction to Hadronic τ Decays*, March 1991, unpublished.

[63] Martin W. Grünewald, *Determination of the Strong Coupling Constant α_s using the Leptonic Branching Fractions of τ-Decay*, April 1991, unpublished; α_s *from τ Decays*, L3 Note 1022.

[64] T. Hebbeker, τ *Decays and α_s*, L3 Note 1177 and update 1177.1.

[65] E. Braaten, S. Narison and A. Pich, *QCD analysis of the Tau Hadronic Width*, Nucl. Phys. B **373** (1992) 581.

[66] F. LeDiberder and A. Pich, *The Perturbative QCD Prediction to R(Tau) Revisited*, Phys. Lett. B **286** (1992) 147; *Testing QCD with Tau Decays*, Phys. Lett. B **286** (1992) 165; Fortran program to calculate R_τ (1992).

[67] The L3 Collaboration, O. Adriani *et al.*, *Measurement of the $e^+e^- \to b\bar{b}$ and $e^+e^- \to c\bar{c}$ Forward-Backward Asymmetries at the Z^0 Resonance*, Phys. Lett. B **292** (1992) 454.

[68] The L3 Collaboration, O. Adriani *et al.*, *Determination of the Number of Light Neutrino Species*, Phys. Lett. B **292** (1992) 463.

[69] S. Ganguli and A. Gurtu, *Results on Electroweak Parameters from L3*, L3 Note 1343.

[70] The L3 Collaboration, O. Adriani *et al.*, *Determination of α_s from Hadronic Event Shapes Measured on the Z^0 Resonance*, Phys. Lett. B **284** (1992) 471 .

[71] The CHARM Collaboration, J. Dorenbusch *et al.*, *Experimental Results on Neutrino-Electron Scattering*, Z. Phys. C (1989) 567;

K.Abe *et al.*, *Determination of* $\sin^2 \theta_W$ *from Measurements of Differential Cross Sections for Muon-Neutrino and -Antineutrino Scattering by Electrons*, Phys. Rev. Lett. **62** (1989) 1709;

The CHARM II Collaboration, D. Geiregat *et al.*, *A New Determination of the Electroweak Mixing Angle from Muon-Neutrino-Electron Scattering*, Phys. Lett. B **232** (1989) 539;

F. Avignone *et al.*, *Interpretation of* $\overline{\nu}$-e^- *Scattering with Reactor Antineutrinos*, Phys. Rev. D **16** (1977) 2383;

U. Amaldi *et al.*, *Comprehensive Analysis of Data Pertaining to the Weak Neutral Current and the Intermediate-Vector-Boson Masses*, Phys. Rev. D **36** (1978) 1385.

[72] S. Banerjee and S. Ganguli, *Estimation of the QED Coupling Constant* α *at* $\sqrt{s} = M_Z$, Z. Phys. C **57** (1993) 229.

[73] Martin W. Grünewald and M. Sachwitz, *Looking for TOP at LEP in 1991*, in: Proceedings of the XIV International Warsaw Meeting on Elementary Particle Physics; ed.: Z. Ajduk, S. Pokorski and A. Wroblewski (World Scientific, Singapore, 1992) 101.

[74] The CDF Collaboration, F. Abe *et al.*, *Lower Limit on the Top-Quark Mass from Events with Two Leptons in* $p\overline{p}$ *Collisions at* $\sqrt{s} = 1.8$ *TeV*, Phys. Rev. Lett. **68** (1992) 447; *A Limit on the Top-Quark Mass from Proton-Antiproton Collisions at* $\sqrt{s} = 1.8$ *TeV*, Phys. Rev. D **45** (1992) 3921.

[75] A. Leike, S. Riemann and T. Riemann, *ZZ′ Mixing and Radiative Corrections at LEP I*, Phys. Lett. B **291** (1992) 187.

[76] S. Ganguli, *Determination of Rho-tree from LEP*, unpublished.

[77] G. Altarelli and R. Barbieri, *Vacuum Polarization Effects of New Physics on Electroweak Processes*, Phys. Lett. B **253** (1990) 161.

[78] G. Altarelli, R. Barbieri and S. Jadach, *Toward a Model-Independent Analysis of Electroweak Data*, Nucl. Phys. B **369** (1992) 3.

[79] G. Altarelli, *The Standard Electroweak Theory and its Experimental Tests*, CERN-TH.6305/91.

[80] *Z Physics at LEP 1, Vol.1: Standard Physics*, ed.: G. Altarelli, R. Kleiss and C. Verzegnassi, CERN yellow report.

[81] L. Surguladze and M. Samuel, *Total Hadronic Cross Section in* e^+e^- *Annihilation at the Four-Loop Level of Perturbative QCD*, Phys. Rev. Lett. **66** (1991) 560.

[82] S. Gorishny, A. Kataev and S. Larin, *The* $O(\alpha_s^3)$ *Corrections to* $\sigma_{tot}(e^+e^- \to$ hadrons) *and* $\Gamma(\tau \to \nu_\tau + $ hadrons) *in QCD*, Phys. Lett. B **259** (1991) 144.

[83] T. Hebbeker, *QCD Corrections to* Γ_{had}, RWTH Aachen PITHA 91/08 (revised version).

[84] D. Bardin, M. Bilenky, G. Mitselmakher, T. Riemann and M. Sachwitz, *A Realistic Approach to the Standard Z Peak*, Z. Phys. C **44** (1989) 493.

[85] D. Treille, *Review of the Standard Model*, CERN-PPE/92-107.

[86] G. Burgers *et al.*, Δr, *or the Relation between the Electroweak Couplings and the Weak Vector Boson Masses*, in: Z Physics at LEP 1, Vol.1: Standard Physics, ed.: G. Altarelli, R. Kleiss and C. Verzegnassi, CERN yellow report 89-08.

[87] M. Perl, *The Tau Lepton*, Rept. Prog. Phys. **55** (1992) 653.

[88] The BES Collaboration, J. Bai *et al.*, *Measurement of the Mass of the* τ *Lepton*, Phys. Rev. Lett. **69** (1992) 3021.

[89] The ARGUS Collaboration, H. Albrecht *et al.*, *A Measurement of the Tau Mass*, Phys. Lett. B **292** (1992) 221.

[90] The CLEO-II Collaboration, R. Ballest *et al.*, *A Measurement of the Tau Lepton Mass*, CLNS-93-1194, CLEO-93-2.

[91] W. Marciano and A. Sirlin, *Electroweak Radiative Corrections to Tau Decay*, Phys. Rev. Lett. **61** (1988) 1815.

[92] H. Thacker and J. Sakurai, *Lifetimes and Branching Ratios of Heavy Leptons*, Phys. Lett. B **36** (1971) 103.

[93] S. Narison and A. Pich, *QCD Formulation of the Tau Decay and Determination of Lambda(MSbar)*, Phys. Lett. B **211** (1988) 183;
E. Braaten and C. Li, *Electroweak Radiative Corrections to the Semihadronic Decay Rate of the Tau Lepton*, Phys. Rev. D **42** (1990) 3888;
E. Braaten, *The Perturbative QCD Corrections to the Ratio R for Tau Decay*, Phys. Rev. D **39** (1989) 1458;
M. Samuel and L. Surguladze, *On the Renormalization Group Ambiguity of Perturbative QCD for R(s) in* e^+e^- *Annihilation and R(tau) in Tau Decay*, Phys. Rev. D **44** (1991) 1602.

[94] K. Hagiwara, A. Martin and D. Zeppenfeld, *Tau Polarisation Measurements at LEP and SLC*, Phys. Lett. B **235** (1990) 198;
A. Rouge, *Polarisation Observables in the* $3\pi\nu$ *Decay Mode of the* τ, Z. Phys. C **48** (1990) 75; *Tau Decays as Polarization Analysers*, Talk given at the first workshop on tau lepton physics, Orsay, France, 1990.

[95] The LEP Collaborations: ALEPH, DELPHI, L3 and OPAL, *Electroweak Parameters of the* Z^0 *Resonance and the Standard Model*, Phys. Lett. B **276** (1992) 247.

[96] The LEP Polarization Collaboration, L. Arnaudon *et al.*, *Measurement of LEP Beam Energy by Resonant Spin Depolarization*, Phys. Lett. B **284** (1992) 431.

[97] The working group on LEP energy, L. Arnaudon *et al.*, *The Energy Calibration of LEP in 1991*, CERN-PPE/92-125, CERN-SL/92-37(DI).

[98] *LEP Design Report*, CERN-LEP/84-01.

[99] H. Chen, *The Detector Simulation of the L3 Experiment*, L3 Note 1046.

[100] H. Fesefeldt, private communication.

[101] M. Pieri *et al.*, private communication.

[102] Martin W. Grünewald, *Oral Candidacy Examination*, California Institute of Technology, December 1990.

[103] W. Beenakker, F. Berends and S. van der Marck, *Large Angle Bhabha Scattering*, Nucl. Phys. B **349** (1991) 323; *Higher Order Corrections to the Forward-Backward Asymmetry*, Phys. Lett. B **251** (1990) 299;

W. Beenakker and W. Hollik, *Electroweak One-Loop Corrections to Heavy-Fermion Pair Production*, ECFA workshop on LEP 200, ed.: A. Böhm and W. Hoogland, CERN green report 87-08 (1987) 185;

W. Hollik, *Radiative Corrections in the Standard Model and their Role for Precision Tests of the Electroweak Theory*, Fort. Phys. **38** (1990) 165.

[104] M. Martinez and R. Miquel, *Fitting the* $e^+e^- \to e^+e^-$ *Lineshape*, Z. Phys. C **53** (1992) 115.

[105] A. Leike, S. Riemann and T. Riemann, *ZZ′ Mixing in Presence of Standard Weak Loop Corrections*, Univ. Munich LMU-91/06, L3 Note 1074.

[106] T. Hebbeker and J. Rose, *FUNPLO User's Guide and Reference Manual*, unpublished.

[107] F. James, *MINUIT Function Minimization and Error Analysis*, CERN Program Library Entry and Long Writeup D506 MINUIT.

[108] The L3 Collaboration, B. Adeva *et al.*, *An Improved Measurement of* $B^0 - \bar{B}^0$ *Mixing in* Z^0 *Decays*, Phys. Lett. B **288** (1992) 395.